Direct measurement of coating thermal noise in the AEI 10 m prototype

Von der Fakultät für Mathematik und Physik
der Gottfried Wilhelm Leibniz Universität Hannover

zur Erlangung des akademischen Grades
Doktor der Naturwissenschaften
Dr. rer. nat.

genehmigte Dissertation von

M.Sc.
Janis Wöhler

2023

Referent:	Prof. Dr. Karsten Danzmann
Korreferent:	Apl. Prof. Dr. Benno Willke
Korreferent:	Prof. Dr. Joshua Smith
Tag der Promotion:	13. Januar 2023

MAX-PLANCK-GESELLSCHAFT

The work presented in this thesis was carried out at the

Max Planck Institute for Gravitational Physics (Albert Einstein Institute)
and Institute for Gravitational Physics, Leibniz Universität Hannover,
Callinstraße 38, 30167 Hannover, Germany

Abstract

GW150914 marked the beginning of gravitational wave astronomy with the first direct observation of the merger of two black holes. Two years later, the observation of GW170817, a binary neutron star merger, by LIGO and Virgo, marked the beginning of multimessenger astronomy, demonstrating the full potential of gravitational wave detection. The coincident gamma-ray burst was observed by the Fermi and Integral satellites, triggering a follow-up campaign, involving more than 70 telescopes across the electromagnetic spectrum. Over several months, details of the associated kilonova have been recorded.

These observations have been made possible by continuously increasing the sensitivity of the gravitational wave detectors. To continue this trend into the next generation of earth-bound gravitational wave detectors, the main research focus lies on improving quantum noise and thermal noise in the most sensitive frequency band. Part of the research effort to surpass quantum limits is the AEI 10 m prototype in Hannover, commissioning a small-scale Fabry-Perot-Michelson interferometer. To ensure that this experiment and future gravitational wave detectors are not suffering from thermal noise, a large effort is underway to understand, model and measure mirror thermal noise.

Part of this effort is the Thermal Noise Interferometer (TNI), a 10 cm Fabry-Perot cavity with suspended mirrors, which is the subject of this thesis. The hemispherical design of the TNI ensures that the readout is dominated by mirror thermal noise of a flat test mirror. By using the infrastructure of the AEI 10 m prototype the low noise environment necessary is provided.

Successful integration of the TNI in the AEI 10 m prototype required significant changes and improvements from the initial version. For these changes to be implemented, the TNI was moved to an optical table outside of the vacuum chamber. This facilited access to implement and test changes. Part of this effort was to revise the triple suspensions used to seismically isolate the cavity mirrors, reaching the required seismic isolation performance while allowing fast mirror exchanges. The suspensions were characterized using optical levers and shadow sensors. This setup was also used to install and test cavity length actuators and test lock acquisition procedures.

The TNI was subsequently moved back into the vacuum system onto a seismic pre-isolation system and commissioned to reach its design sensitivity. A photon pressure calibrator setup was built to calibrate the TNI error signal and judge the progress of commissioning. Several steps of exchanging mirrors and mirror holders due to increased levels of absorption and mechanical loss led to a stably working setup, allowing for highly sensitive measurements.

The measurements performed agree with coating Brownian thermal noise of the end mirror together with substrate thermal noise from the input mirror, from frequencies of 60 Hz to 10 kHz, reaching a noise floor close to $1 \cdot 10^{-18}\mathrm{m}/\sqrt{\mathrm{Hz}}$. This is the first demonstration of a direct thermal noise measurement in the audio-band in Europe. From these results, mechanical loss angles of the coating were extracted in agreement with literature values. This demonstrates the capabilities of the TNI to test and characterize the coating thermal noise of high reflectivity mirrors used in precision interferometry.

Keywords: *Gravitational-wave detection, thermal noise, interferometry*

Kurzzusammenfassung

GW150914 war die erste direkte Beobachtung von verschmelzenden schwarzen Löchern und markierte den Beginn der Gravitationswellenastronomie. Zwei Jahre beobachteten LIGO und Virgo GW170817, das Verschmelzen zweier Neutronensterne, und das Zeitalter der Multi-messenger Astronomie startete. In Koinzidenz wurde ein Gammastrahlenausbruch von den Fermi- und Integral-Satelliten detektiert, was eine Beobachtungskampagne mit mehr als 70 Teleskopen in allen Bereichen des elektromagnetischen Spektrums initiierte. Über mehrere Monate wurden die Details der dem Gammastrahlenausbruch assoziierten Kilonova aufgezeichnet.

Diese Beobachtungen wurden durch eine kontinuierlich steigende Sensitivität der Gravitationswellendetektoren ermöglicht. Um diese Entwicklung in die nächste Generation der erdgebundenen Gravitationswellendetektoren fortzusetzen, liegt das Hauptaugenmerk auf dem Quantenrauschen und dem thermischen Rauschen. Ein Teil der Bemühungen, das Standardquantenlimit zu unterschreiten, findet am AEI 10 m Prototypen in Hannover statt, wo eine kleine Version eines Fabry-Perot-Michelson Interferometers aufgebaut wird. Damit dieses Experiment sowie zukünftige Gravitationswellendetektoren nicht durch thermisches Rauschen limitiert sind, gibt es weitreichende Anstrengungen, thermisches Rauschen zu verstehen, modellieren und verringern.

Teil dieser Bemühungen ist das Thermal Noise Interferometer (TNI), ein 10 cm Fabry-Perot Resonator mit aufgehängten Spiegeln, der das Thema dieser Arbeit darstellt. Die hemisphärische Geometrie des Resonators stellt sicher, dass die Längensensitivität durch das thermische Rauschen des flachen Testspiegels dominiert ist. Die nötige rauscharme Infrastruktur wird dabei durch den AEI 10 m Prototypen bereitgestellt.

Die erfolgreiche Integration des TNI in den AEI 10 m Prototypen erforderte signifikante Veränderungen und Verbesserungen von der initialen Ausführung. Dafür wurde das TNI zunächst auf einen optischen Tisch außerhalb der Vakuumkammer platziert. Dies ermöglichte einfachen Zugang, um Verbesserungen zu implementieren und testen. Teil dieser Prozedur war die Erneuerung der Dreifachaufhängung, die zur seismischen Isolation der Resonatorspiegel benutzt wird. Dabei wurde sowohl die benötigte seismische Isolation erreicht als auch eine kurze Zeit für Spiegelwechsel. Die Aufhängungen wurden dabei mit Hilfe von optischen Hebeln und Schattensensoren. Dieser Testaufbau wurde weiterhin verwendet, um die Längenaktuatoren des Resonators zu installieren und testen und damit die Stabilisierungsprozeduren zu testen.

Anschließen wurde das TNI in das Vakuumsystem auf einen seismisch isolierten Tisch überführt und dort bis zur Zielsensitivität optimiert. Ein Strahlungsdruckkalibrationssystem wurde aufgebaut, mit dessen Hilfe das Fehlersignal des TNI kalibriert wurde. Dies erlaubte, den Fortschritt der Optimierung der Sensitivität des TNI zu überwachen. Nach einigen Spiegel- und Spiegelhalterwechseln auf Grund von erhöhter optischer Absorption und mechanischem Verlust erreichte das TNI einen Zustand, in dem zuverlässig hochsensitive Messungen durchgeführt werden konnten.

Die durchgeführten Messungen lassen sich durch das thermische Rauschen der Spiegelschichten des Endspiegels zusammen mit thermischem Rauschen des Eingangsspiegelsubstrats in einem Frequenzbereich von 60 Hz bis 10 kHz erklären, und erreichen eine maximale Sensitivität von etwa $1 \cdot 10^{-18} \mathrm{m}/\sqrt{\mathrm{Hz}}$. Dies ist die erste Realisierung einer direkten Messung von thermischem Rauschen im Audiofrequenzbereich in Europa. Aus diesen Resultaten wurden die mechanischen Verluste der Spiegelschichten extrahiert, in Übereinstimmung mit Literaturwerten. Dies demonstriert das Potenzial des TNI, das thermische Rauschen von hochreflektiven Spiegeln für hochpräzise Interferometer zu testen und charakterisieren.

Schlagwörter: *Gravitationswellendetektion, Thermisches Rauschen, Interferometrie*

Abstrakt

GW150914, prvé pozorovanie kolízie binárnej diery, bolo začiatok astronómie gravitačných vĺn. O dva roky neskôr, LIGO a Virgo detegovali GW170817, splynutie dvoch neutrónových hviezd. To bol začiatok multi-kanálnej astronómie. Simultánny záblesk gama žiarenia bol pozorovaný satelitmi Fermi a Integral, čo spustilo nasledujúce pozorovania, do ktorého sa zapojilo viac ako 70 teleskopy skrz celé elektromagnetické spektrum. Podrobnosti s tým spojenej Kilonovy sa zaznamenávali počas niekoľkých mesiacov.

Tieto pozorovania boli umožnené kontinuálnym zlepšením citlivosť detektorov gravitačných vĺn. Aby sa pokračovalo v tomto vývoji do ďalšej generácie pozemných detektorov gravitačných vĺn, je treba zmenšiť kvantový a tepelný šum. Časť vedeckej snahy o prekonanie štandardnej kvantovej hranice je AEI 10 m Prototyp v Hannoveri, uvadzajúci do prevádzky máloobjemový Fabry-Perot-Michelsonov interferometer. Aby sa zaistilo, že tento experiment a budúce detektory gravitačných vĺn nebudú sužované tepelným šumom, pracuje sa na pochopení, na vypočitaní a na meraní povrchového tepelného šumu.

Časť tej snahy je Thermal Noise Interferometer, 10 cm Fabryho-Perotov rezonátor so zavesenými zrkadlami, čo je téma tejto dizertačnej práce. Pologuľovitý návrh TNI zaistuje, že tepelný šum plochého testovného zrkadla dominuje citlivosť. Použitím infraštruktúry AEI 10 m Prototypa sa umožni potrebné prostredie nízkého šumu.

Úspešná integrácia TNI do AEI 10 m prototypu si vyžadovala signifikantné zmeny a vylepšenia v porovnaní s pôvodnou verziou. Aby tieto zmeny mohli byť implementované, TNI bola premiestnená na opticky stôl mimo vakuovej komory. To umožnilo prístup nutný na implementáciu a testovanie zmiem. Časť týchto snáh spočivala v prepracovaní trojitých zavesení používaných na seizmuckú izoláciu zrkadiel vo vákuovej komore, tak aby sa dosiahla vyžadovaná seizmická izolácia, ktorá by zároveň umožnila rýchlu výmenu zrkadiel. Zavesenia boli charakterizované použitím optických pák a tieňových senzorov. Tieto nastavenia boli tiež použité na nainštalovanie a otestovanie aktuátorov merajúcich dĺžku komory a na otestovanie stabilizčné procedúry.

Následne bol TNI premiestnený naspäť do vákuového systému na systém predseizmickej izolácie a uvedený do fungovanie tak, aby dosiahol plánovanú senzitivitu. Na kalibráciu odchylky signálu a posúdenie pokroku v senzitivite a nastavení TNI bol nainštalovaný systém kalibráciu svetelného tlaku. Po niekoľkých výmenách zrkadiel a držiakov zrkadiel kvôli zvýšeným hodnotám absorbcie a mechanyckým strátam boli dosiahnuté stabilné nastavenia umožňujúce vysoko citlivé merania.

Výsledky merania sa zhodujú s povrchovým tepelným šumom koncového zrkadla spolu s tepelným šumom substrátu z inputového zrkadla vo frekvenciách 60 Hz až 10 kHz, s najnižším šumom zhruba pri $1 \cdot 10^{-18}\mathrm{m}/\sqrt{\mathrm{Hz}}$. To je prvá demonštrácia priameho merania povrchového tepelného šumu v audio pásme v Európe. Z týchto výsledkov boli extrahované mechanické stratové uhly povrchu, ktoré sa zhodujú s referenčnými hodnotami z literatúry. Týmto boli demonštrované schopnosti TNI testovať a charakterizovať povrchový tepelný šum vysoko reflektívnych zrkadiel používaných v vysoko presnej interferometrii.

Kľúčové slová: *pozorovanie gravitačných vĺn, tepelný šum, interferometria*

Contents

Figures and tables

List of figures

List of tables

Glossary

Abbreviations

10m PT	10m prototype facility
a.u.	arbitrary units
ADC	analogue-to-digital converter
AEI	Albert Einstein Institute
AEI-SAS	AEI seismic attenuation system
AlGaAs	aluminium gallium arsenide
AOM	acousto-optic modulator
AR	anti-reflective
ASD	amplitude spectral density
BOSEM	Birmingham optical sensor and electro-magnetic actuator
BS	beamsplitter
CCD	charge-coupled device
CDS	LIGO Control and Data Acquisition System
cts.	counts (CDS digitization unit)
DAC	digital-to-analogue converter
DC	direct current (used to describe the 0 Hz part of a general signal)
DTT	diagnostic test tools
DWS	differential wavefront sensing
EOM	electro-optic modulator
EPICS	Experimental Physics and Industrial Control System
ESD	Electrostatic drive
ETM	end test mass
FI	Faraday isolator
Foton	filter online tool
FSR	free spectral range
FWHM	full width at half maximum
GRB	gamma-ray burst
GUI	graphical user interface
GW	gravitational wave
HOM	higher-order mode
HR	highly reflective
HWP	half-wave plate
IFO	interferometer
IM	intermediate mass
IR	infrared
ISS	intensity stabilization servo
ITM	input test mass
KAGRA	Kamioka gravitational wave detector
LED	light-emitting diode
LIGO	Laser Interferometer Gravitational-Wave Observatory

LVC	LIGO-Virgo Scientific Collaboration
MEDM	Motif Editor and Display Manager (graphical user interface for CDS)
Nd:YAG	neodymium-doped yttrium aluminium garnet (Nd:$Y_3Al_5O_{12}$)
NPRO	non-planar ring oscillator
p-pol.	p-polarization (here linearly polarized in horizontal direction)
PBS	polarizing beamsplitter
PCal	photon pressure calibrator
PD	photodiode, photodetector
PDH	Pound-Drever-Hall
PMC	pre-mode cleaner
PUM	penultimate mass
PZT	lead zirconate titanate (piezoelectric transducer)
QPD	quadrant photodetector
QWP	quarter-wave plate
RC	reference cavity
RCG	real-time code generator
RF	radio frequency
RIN	relative intensity noise
RMS	root mean square (square root of the mean square of a time series)
RPN	radiation pressure noise
s-pol.	s-polarization (here linearly polarized in vertical direction)
SAT	single-arm test
SM	steering mirror
SN	shot noise
SNR	signal-to-noise ratio
SPI	suspension platform interferometer
SQL	standard quantum limit
TE	thermo-elastic
TEM	transverse electromagnetic mode
TM	test mass
TNI	thermal noise interferometer
TO	thermo-optic
TR	thermo-refractive
TTFSS	table top frequency stabilization servo

Reoccurring mathematical symbols

c	speed of light, $c = 2.998 \times 10^8\,\mathrm{m/s}$
E	electric field
$\mathcal{F}$	finesse of a cavity
f	frequency
$h(t)$	gravitational-wave strain
$\hbar$	reduced Planck constant, $\hbar = 1.055 \times 10^{-34}\,\mathrm{J\,s}$
$i(t)$	photo current
L	cavity length
l	optical loss
m	mass
P	light power

t	time
λ	wavelength
ω, ω_0	angular frequency
$\langle \hat{X} \rangle$	expectation value of operator $\hat{X}$
$\mathrm{Var}(\hat{X})$	variance of operator $\hat{X}$
$\overline{x}$	mean of $x(t)$
$\tilde{x}_{\mathrm{RMS}}$	root mean square value of $x(t)$
$S_x(f)$	single-sided power-spectral density of $x(t)$
$\tilde{x}(f)$	single-sided amplitude-spectral density of $x(t)$

CHAPTER 1

Introduction

Gravitational waves have played an integral role in expanding the knowledge about our universe since the LIGO observatories in the USA first directly detected them in 2015 [Abb+16b]. This first detection showed clearly, that black hole binaries exist, can coalesce in the lifetime of the universe, and radiate a substantial amount of energy as gravitational waves. Gravitational wave detectors of the second generation, such as Advanced LIGO and Advanced Virgo, thereby opened up new possibilities to observe highly energetic cosmic events as well as test our understanding of gravity and cosmology. The full potential of this network of gravitational wave detectors, which further includes GEO600 in Hannover and KAGRA in Japan, was demonstrated when their simultaneous observation of a binary neutron star merger (see figure 1.1) coincident with a gamma-ray burst, observed by the Fermi and Integral satellites [Abb+17n][Abb+17o], enabled accurate sky localization of the source (see figure 1.2) and triggered an observation campaign including more than 70 astronomical observatories. These included earth-bound and satellite-based telescopes and detectors looking for a counterpart in the radio, infrared, optical, UV, X-ray, and gamma-ray parts of the electro-magnetic spectrum; and even Neutrino detectors were searching for signals coincident with the event [Alb+17a].

This was the first example of a successful multi-messenger campaign, which led to new insights into the phenomena of gamma-ray bursts and kilonovae. The association of the observed gamma-ray burst with the binary neutron star merger inferred from the gravitational wave signal gave a clearer picture about the processes involved in short gamma-ray bursts and Kilonovae. It is now believed that a class of short gamma-ray bursts originate, when neutron stars collide and produce neutron rich ejecta [Met19]. An artist's impression of this process is shown in figure 1.3.

When part of these ejecta are accreted by the merger remnant - either a supermassive neutron star or a black hole they produce a powerful jet, which generates synchroton radiation in the gamma part of the electro-magnetic spectrum. This directed emission, when pointed towards earth, is registered as a gamma-ray burst. Interaction of the isotropic part of the ejecta with the interstellar medium creates shock fronts, providing the conditions to breed heavy r-process elements, which decay subsequently. These decay processes create an afterglow, which is referred to as kilonova. The kilonova emissions are distributed over the whole electro-magnetic spectrum, shifting the emission peak towards the infrared on a timescale of days and towards radioemissions over several months. From details of this afterglow, as shown in figure 1.4, and estimates of the mass of ejecta and rate of mergers, it could be estimated that most of the heavier elements such as gold present on earth today most likely stem from such events [Abb+17e].

These encouraging results only mark the beginning of gravitational wave astronomy with more and more precise detections being promised by the third generation gravitational wave detectors in development. Projects such as Einstein Telescope in Europe and Cosmic Explorer in the US will place more stringent constraints on general relativity, improve measurements of the expansion history of the universe and catalogue populations of neutron stars, black holes and possibly unknown exotic objects. These goals require an increase in the sensitivity of the detectors at all frequencies, with the highest sensitivity reached around a few hundred hertz. At higher frequencies,

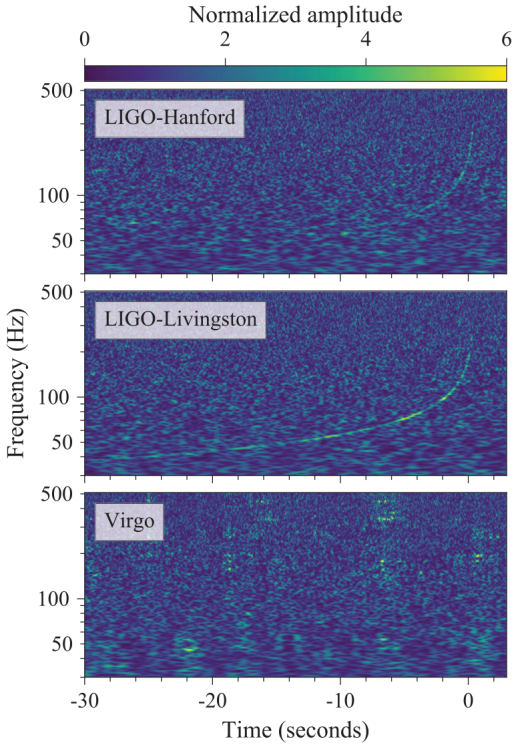

Figure 1.1: Spectrograms of the strain amplitude as measured by LIGO Hanford, LIGO Livingston and Virgo during the binary neutron star merger producing GW170817. [Abb+17n]

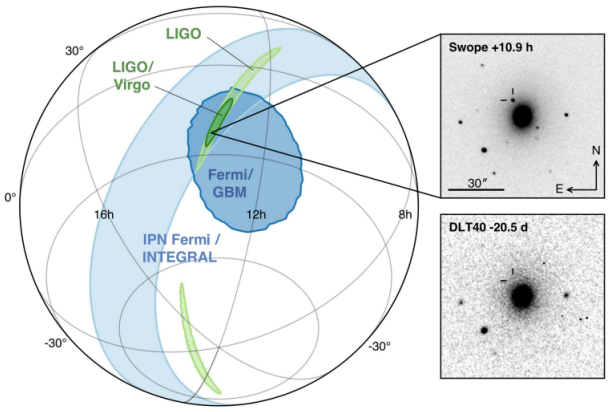

Figure 1.2: Projected skymap showing the localization of the gravitational wave source in conincidence with a short gamma ray burst. The upper inset shows the appearance of a kilonova in the electromagnetic spectrum, absent in an earlier observation of the host galaxy in the lower inset. [Abb+17o]

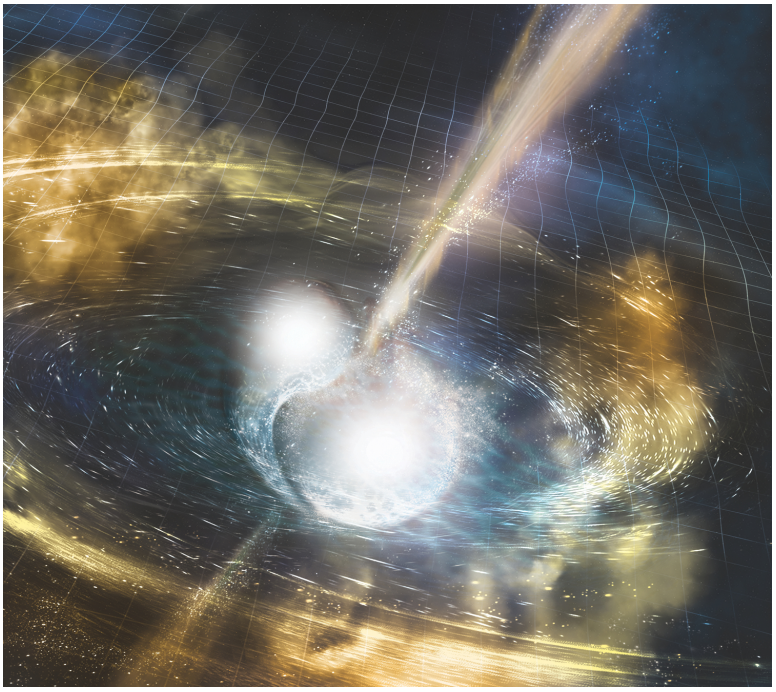

Figure 1.3: An artist's impression of a binary neutron star merger. When the neutron stars collide, a strong jet is observed, generating the characteristic gamma ray emission. A disc of ejecta is created in the orbital plane. (Courtesy NSF/LIGO/Sonoma State University/A. Simonnet)

the detectors are mostly limited by shot noise. Improvements can be achieved using higher laser power and novel quantum techniques reducing the fundamental uncertainty in phase measurements using light. Some of these new techniques enabling measurements below the standard quantum limit will be tested in the AEI 10 m prototype based in Hannover. At low frequencies, seismic motion of the ground is the limiting factor, calling for better seismic isolation and even bringing detectors underground. Quantum radiation pressure noise, dominating when seismic motion is sufficiently reduced, will be dealt with using again novel quantum techniques.

This leaves the most sensitive frequency band around a few hundred hertz, where the limiting noise source apart from quantum noise will be thermal noise of the mirror coatings and substrates (see figure 1.5). Fundamentally, thermal noise arises from losses present in the system, which couple mechanical and thermal degrees of freedom of the components involved to the heat bath, thereby introducing random fluctuations. These fluctuations limit the ultimate sensitivity of gravitational wave detectors by manifesting as an effective motion of the test mass mirrors, masking any gravitational wave signal. This detrimental influence on the length sensitivity of the optical setup is not restricted to gravitational wave detectors, but also shows up in high precision optical experiments such as atomic clocks, which use ultrastable lasers as the master oscillator probing atomic transitions [Jia+11][Kes+12]. Optomechanical experiments, which study the interaction of light and matter, are also prone to suffering from excess motion of their mechanical components driven by thermal noise [Col12][Neb+12].

Since the debilitating influence of thermal noise in interferometric experiments has first been calculated thirty years ago [Sau90], several approaches have been established to reduce thermal noise. These approaches utilize knowledge and manipulation of the variables influencing thermal noise in mirrors. Among these variables are temperature and readout laser beam spot size, which influence all the different kinds of thermal noise. Other variables can be summed up as material

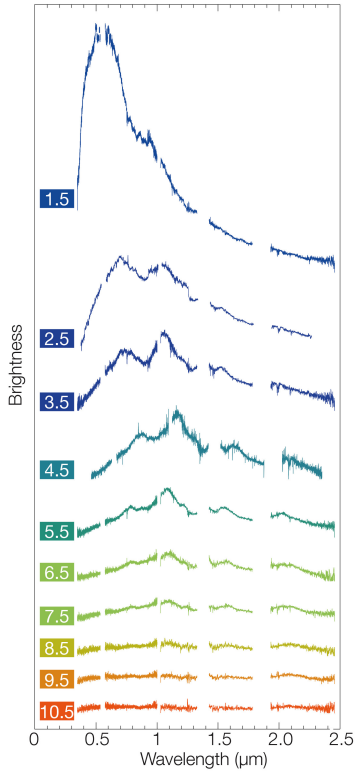

Figure 1.4: Lightcurves showing the spectrum of electromagnetic emission during the kilonova associated with GW170817. The spectra are labelled by the time (in days) they were taken after the merger.(Courtesy ESO/E. Pian et al./S. Smartt & ePESSTO)

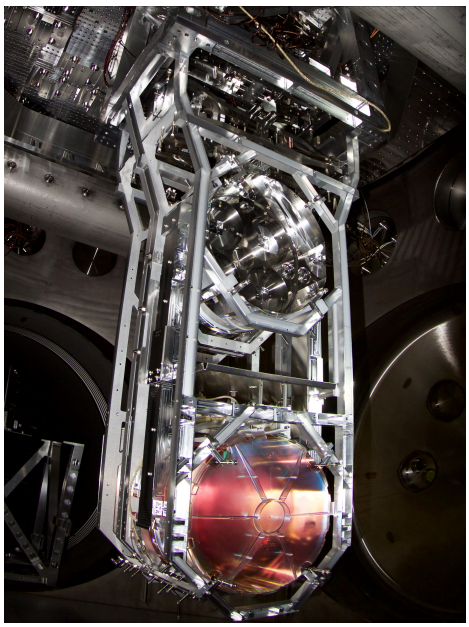

Figure 1.5: One of the main suspensions in a LIGO observatory, where the 40 kg HR-mirror at the bottom is hanging to the fused silica mass in the upper part of the picture. (Courtesy Caltech/MIT/LIGO Lab)

properties, among which the mechanical loss (ϕ) is the main contribution factor for Brownian thermal noise, itself the dominating thermal noise contribution in most current high-sensitivity laser interferometric experiments [GHD12].

A straightforward method used whenever possible is increasing the readout laser beam size on the mirror, that way averaging out surface fluctuations caused by thermal noise. This method is only useful until diffraction losses start to become non-negligible when a significant portion of the beam will not fit on the mirror anymore. In gravitational wave detectors, this leads to beam radii of 6 cm on mirrors of diameter 35 cm.

Producing larger mirrors with suitable reflective coatings fulfilling the requirements in homogeneity and surface roughness is technologically challenging. Alternatively, laser beam geometries other than the fundamental gaussian TEM00 mode, for example the Laguerre-Gauss type LG33 mode can be an option [GHD12], although this leads to an increase in the complexity of the optical design.

Another obvious approach is decreasing the temperature. This approach comes with significant challenges, including reaching low temperatures without introducing vibrations from cryo-systems, growing of ice layers on the coating, and an unfavourable increase in the mechanical loss for materials such as silica. A further challenge is dissipating the heat introduced from residual laser absorption, leading to compromises in the seismic isolation system design. KAGRA, the Japanese underground gravitational wave detector currently in the commissioning phase, pursues this idea by cooling sapphire test masses to a temperature of 20 K, and are encountering ice growth problems [SM19].

The materials approach, which also forms the basis for this thesis, revolves around studying and improving the material properties of the mirror substrates and coatings. Mainly focussing on the mechanical loss to improve Brownian thermal noise, other parameters such as optical loss and and thermal coefficients also have to fulfil stringent requirements.

The influence of material properties can further be reduced by developing intricate coating structures having either more than two materials and or a non-uniform distribution of layer thicknesses. They can be designed to redistribute the light power in the coating such that most of the light sees a thin layer of mechanically lossy, but optically low-loss material. As coating thermal noise is proportional to the thickness of the lossy material, this gives a small noise contribution while keeping optical losses small. The thick rest of the coating can then be optically worse, but mechanically less lossy, making the coating highly reflective while keeping the thermal noise low [YGE15][Tai+20].

Another example is a proposal by Khalili, where the end mirror of a Fabry-Perot cavity consists of two separate mirrors forming an anti-resonant cavity, where a thin layer on the first mirror provides most of the reflectivity, but very little thermal noise. The thicker layers of the second mirror raise the reflectivity to a typical level of 0.9999 or more, while only weakly interacting with the light because of the anti-resonance of the cavity [Kha05]. The thermal noise sensed is therefore reduced significantly.

Further improvements also rely on finding and characterizing new materials and material processing procedures. One set of such procedures currently employed for gravitational wave detector test mirrors consists of doping the tantala, which is an amorphous high-refractive index material used in HR silica/tantala-coatings, with titania [Har+06a] and annealing the coating at temperatures up to 600 °C [Mar+10].

Among promising new coating materials under investigation are crystalline AlGaAs/GaAs-heterostructures, which possess significantly reduced intrinsic mechanical loss [Col+13b], thereby reducing the level of coating Brownian thermal noise. These crystalline coatings are intended to be used in the AEI 10 m prototype sub-SQL Fabry-Perot-Michelson interferometer, which is designed to reach the standard quantum limit and study quantum noise reduction schemes surpassing it [Goß+10]. To achieve the required thermal noise performance in crystalline coatings, not only mechanical losses have to be dealt with, but thermal properties of the material play an important role as well. Elevated levels of thermorefractive and thermoelastic noise, influenced by thermal

coefficients of the material, have to be dealt with by designing a coating structure which cancels these contributions. The resulting thermooptic noise can be pushed below Brownian thermal noise, making full use of the lower mechanical loss levels [Cha+16].

The search for and characterization of these new materials and coating designs is assisted by experimental setups built to extract coating material properties and measure the thermal noise itself. Among the first and most widely used setups are ringdown experiments. In these, the mechanical modes of coated discs [Cro+02] or cantilevers [Mar+09] are excited and their ringdown time is tracked. From this time constant, the quality factor respectively the mechanical loss of the excited modes can be extracted. These results are then used to gauge the success of different material choices, coating procedures and coating treatments. Additionally, they provide input for computer-based atomic structure simulations, which enhance the understanding of the origins of thermal noise and help guide the search for new material candidates [Bas+13].

The more direct characterization of complete coating structures is done using so called thermal noise interferometers. These are, as the TNI presented in this thesis, optical resonators designed to directly measure the impact of coating thermal noise on their displacement readout. Different configurations have been employed, ranging from rigid spacer cavities and breadboard based cavities ([Gra+17][Cha+14]) to completely suspended interferometers ([Num+03][Bla+04a]). While the former rely on cancellation of common noise sources such as seismic, suspended cavities, like the TNI of this thesis, are built to be directly limited by thermal noise in their readout.

The first thermal noise interferometer to directly measure coating thermal noise was built in Tokyo, reaching the sensitivity required in 2003 [Num+03]. Two cavities of 1 cm length consisting of individually suspended mirrors were probed simultaneously, providing cancellation of common noise. A second experiment, using a similar setup, was conducted shortly after in 2004 at Caltech, again showing coating thermal noise limited performance [Bla+04a]. Ten years later, a modified version based on this setup was commissioned, where the suspended mirrors were replaced by suspended fixed spacer cavities [Cha+14]. A recent addition to direct thermal noise measurements came from the MIT, where a single cavity operating with TEM_{20} and TEM_{02} modes in unison with the fundamental Gaussian mode shows coating thermal noise limited performance, even though standard mirror mounts without any additional seismic isolation are used [Gra+17][GE18]. Further attempts to build a TNI were made, but either failed, were abandoned or did not produce published results [Gra00][Leo+04][Tay08][Eic][Cia].

The latest addition to the small squad of thermal noise interferometers, the AEI 10 m prototype TNI (shown in figure 1.6), is presented in this thesis. Only having a single cavity made up of individually suspended mirrors, and only probing the fundamental Gaussian mode, this is the most direct measurement of mirror thermal noise in the audio-band to date.

This thesis details the efforts involved in bringing the TNI to its design sensitivity. Chapter 2 lays the foundation for the understanding of thermal noise. The Fluctuation-Dissipation-Theorem is the fundamental tool for understanding and calculating all kinds of thermal noise encountered in interferometry, and based on this the most relevant types of thermal noise are derived.

Formulas derived are then employed to simulate the expected level of thermal noise for arbitrary coating structures, which in turn is used in optimization procedures to get coating structures with minimal thermal noise.

Chapter 3 takes the resulting expected thermal noise as the requirement for all other noise sources encountered in the TNI. These requirements are compared to the noise present in the laboratory and highlight the necessity of using the AEI 10 m prototype infrastructure in an effort to suppress this noise. Relevent subsystems of the AEI 10 m prototype and their noise suppression are discussed, in turn setting the requirements for the TNI itself.

Chapter 4 details the design of the TNI, both optical and mechanical, taking the requirements derived in the chapter before as the basis. This mainly places constraints on the seismic isolation performance of the TNI.

For the working TNI to give useful results, the output has to be calibrated, which is shown in detail in chapter 6. Chapter 6 takes the calibrated output of the TNI and compares it to measured

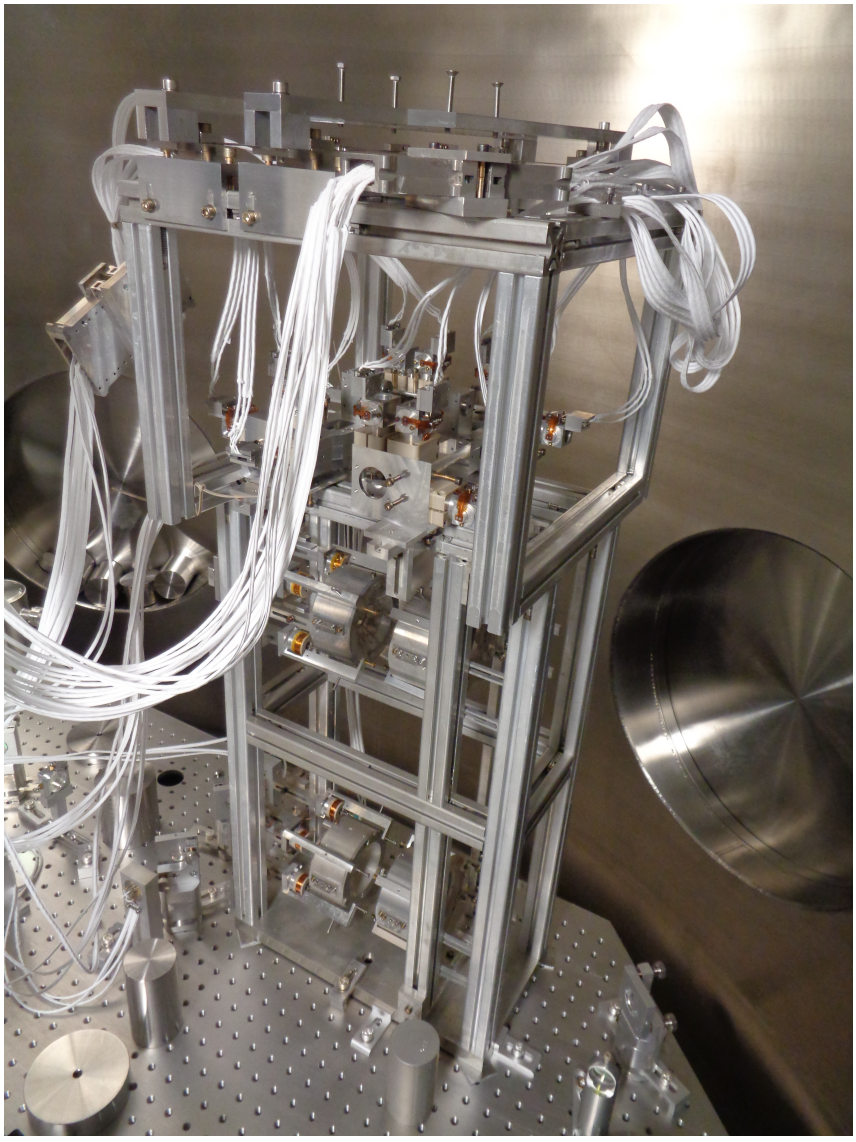

Figure 1.6: TNI inside the vacuum chamber of the AEI 10 m prototype.

and projected noise sources, creating a noise budget.

This provides the basis for claiming in chapter 7, that the measurements are dominated by mirror thermal noise over a wide frequency band. Further tests of this claim are being shown, which increase confidence.

The thesis closes in chapter 8 by giving a summary and an outlook, detailing plans for future upgrades to the TNI, so it will serve its purpose as a testbed for coating thermal noise of different coating materials and structures.

CHAPTER 2

Thermal noise in mirrors

This chapter provides the minimal theoretical basis needed to understand and calculate thermal noise of mirrors. In the first part, the dielectric coating is discussed, which provides the tools to calculate the reflectivity and thermal noise of any HR-coating, given the structure in terms of layers of different materials and their thicknesses.

The second part discusses the most relevant kinds of thermal noise, highlighting the most influential parameters. This leads to formulaic expressions for each thermal noise, allowing the calculation given a specific coating geometry.

The last part applies these principles to test optimization procedures for crystalline HR-coatings intended to be used for the AEI 10 m prototype sub-SQL interferometer.

2.1 Dielectric mirrors

Most HR-mirrors used in precision experiments today are dielectric mirrors, usually consisting of alternating high and low refractive index layers. The properties of these layers not only determine the reflectivity of the coating, but also influence the level of thermal noise observed. It is therefore necessary to understand how each layer couples to reflectivity and thermal noise, and this formalism is used in subsequent chapters to calculate and optimize thermal noise.

Dielectric mirrors work by exploiting the fact that light is able to interfere. Furthermore, the Fresnel equations state that light encountering a boundary between two media of different refractive indices will be partly reflected, the amount reflected depending on the refractive indices and the angle of incidence as well as the polarization. Increasing the reflectivity to the high levels needed is then achieved by stacking multiple layers of different refractive indices, where each boundary contributes according to the Fresnel equations. The contributions from each boundary interfere with each other, and depending on the optical thickness of each layer, this can result in constructive or destructive interference.

High reflectivity mirrors are created by choosing the layer thicknesses such that when looking at the reflected light, the contribution from each layer are in phase to create as much constructive interference as desired. There are two approaches commonly used to get the reflectivity and phase upon reflection of a given coating structure. The method briefly presented here relies on calculating the amplitude reflectivity at each boundary iteratively starting from the substrate interface, until ending at the total reflectivity of the coating at the coating-air interface, based on [GHD12].

From the amplitude reflectivity, the power reflectivity can easily be calculated. The other method uses two-dimensional matrices describing reflection and propagation of light inside the coating. Multiplication of the collection of matrices then gives the reflectivity. The amplitude reflection coefficient for normal incidence at the boundary of layers i with refractive index $n^{(i)}$

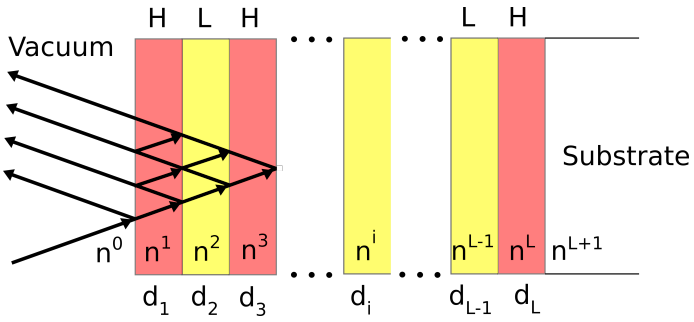

Figure 2.1: The structure of an HR-coating, consisting of layers of refractive index $n^{(i)}$ and thickness d_i. In this example, alternating layers of high index of refraction (H; red) and low index of refraction (L; yellow) are shown. At each interface, partial reflection takes place, as indicated for the three topmost layers.

and $i-1$ with refractive index $n^{(i-1)}$ is given by

$$\gamma_{i-1,i} = \frac{n^{(i-1)} - n^{(i)}}{n^{(i-1)} + n^{(i)}}\,, \tag{2.1}$$

where the layer next to the substrate has index N_L (number of layers) and the topmost layer has index 1. A schematic of such a coating structure is shown in figure 2.1.

This assumes normal incidence, which is fulfilled for Fabry-Perot cavities. The ratio between the electric field coming from the left and the electric field going to the left is then defined as

$$\Gamma_{i-1} = \frac{\gamma_{i-1,i} + \Gamma_i \exp(-2\imath\Psi_i)}{1 + \gamma_{i-1,i}\Gamma_i \exp(-2\imath\Psi_i)}\,. \tag{2.2}$$

Here, $\Psi_i = \frac{4\pi d_i n^{(i)}}{\lambda}$ is the phase acquired while traversing layer i, which corresponds to the optical thickness. The total reflection coefficient for the coating is then calculated by recursion to $\Gamma_c = \Gamma_1$, using $\Gamma_{N_L} = \gamma_{N_L,N_L+1}$ as the starting condition. Taking the absolute square $|\Gamma_c|^2$ gives the power reflectivity and calculating the phase of the complex number Γ_c gives the phase of the reflected electric field at the coating surface. This phase Φ is equivalent to an expansion of the total coating (or alternatively to a shift of the coating surface) Δ_c, by

$$\Phi = \frac{\Delta_c}{\partial^z_\Phi}\,, \tag{2.3}$$

with $\partial^z_\Phi = \frac{-\lambda}{4\pi}$.

Several coating thermal noise calculations require knowledge of the dependence of the phase Φ on the individual layer phases Ψ_i. In the case of Brownian thermal noise, the change in optical thickness is solely caused by a change in physical thickness (neglecting photoelasticity). For thermooptic noise, the optical thickness change has a physical component driven by temperature fluctuations through the thermoelastic coefficient and a purely optical component where the refractive index changes through the thermorefractive coefficient. The corresponding formulas can be found for example in [Eva+08].

The simplest choice of layer thicknesses for an HR-coating is $\frac{\lambda}{4}$ for each layer. Light reflected from the second boundary then acquires a round-trip phase correspoding to half a wavelength when traversing the first layer twice (a quarter wavelength per transition), interfering constructively with the light directly reflected from the first boundary aquires the same phase by reflection off a denser medium. For coatings of this type the total transmission solely depends on the number of

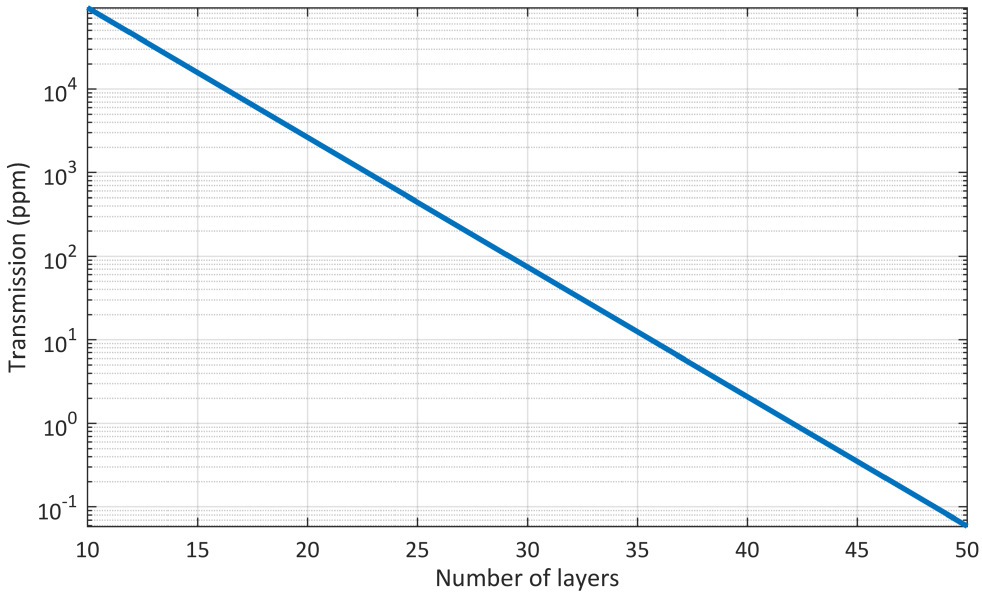

Figure 2.2: The transmission of a $\frac{\lambda}{4}$ HR-coating, depending on the number of layers.

layers and the refractive index contrast (as shown in figure 2.2 for Silica and Tantala).

2.2 Thermal noise

Thermal noise is a fundamental noise source present in all precision experiments, and currently limiting the most sensitive frequency band of large ground-based gravitational wave detectors such as LIGO and Virgo. Improving the understanding of the exact mechanisms responsible for different kinds of thermal noise is an ongoing effort, and in this thesis an experiment for the measurement and characterization of optical coatings and their thermal noise is presented.

To provide a basis for decisions made in planning and commissioning, and a means to calculate the expected thermal noise of mirrors, this chapter gives a short introduction to the fundamentals of thermal noise in general, and concise explanations of the different kinds of thermal noise found in optical precision experiments.

2.2.1 Fluctuation-dissipation theorem

The fluctuation-dissipation theorem, first derived mathematically by Callen and Welton in 1951 [CW51], serves as the basis for all calculations of thermal noise. It connects the amount of energy lost in a system, which experiences a cyclic excitation by a generalized force, to the amplitude of fluctuations of the same generalized force driven by thermal energy. This does not only apply to mechanical or thermal degrees of freedom, as it will be used throughout this chapter, but for example also to electrical currents experiencing resistance resulting in Johnson noise, and to accelerated charges experiencing bremsstrahlung resulting in an alternative derivation of Planck's law of radiation.

The derivation done by Callen and Welton starts by calculating the dissipation present in a

linear and dissipative system, which absorbs the energy delivered by a periodic perturbation and where the power dissipated is proportional to the square of the amplitude of the perturbation. These conditions are fulfilled for systems containing densely distributed energy states and for small perturbations. Quantum mechanical perturbation theory then allows to make the connection between the driving perturbation and the power dissipated. A more detailed derivation is given in A.1. The result of the derivation of the fluctuation-dissipation theorem is

$$\langle V^2 \rangle = \frac{2}{\pi} \int_0^\infty R(\omega) E(\omega, T) d\omega \,, \tag{2.4}$$

with

$$E(\omega, T) = \frac{1}{2}\hbar\omega + \hbar\omega \left[\mathrm{e}^{\frac{\hbar\omega}{kT}} - 1 \right]^{-1}, \tag{2.5}$$

which can be approximated at high temperatures by

$$\langle V^2 \rangle \simeq \frac{2}{\pi} kT \int_0^\infty R(\omega) d\omega \,. \tag{2.6}$$

Here, V is the fluctuating force, T the temperature, E the energy of eigenstates of the system and R the resistance of the system to perturbations.

This derivation shows the origin of the temperature dependence of thermal noise. It is directly proportional to the temperature in the power spectral density because of the Boltzmann factor (kT), relating the energy present in the system to its temperature. This energy then drives the fluctuations manifesting as noise. Furthermore, it becomes clear that the coupling strength from the thermal energy to the fluctuations is the generalized resistance, which can be seen as a loss when the system is driven. These are the two fundamental properties of thermal noise, and the resulting level of thermal noise then only depends on how loss is realized in the system under consideration, and which readout variable is taken into account.

2.2.2 Levin's approach

Early on, the importance of thermal noise of the test masses of LIGO for the readout sensitivity has been realized, and efforts to calculate the expected levels of noise were based on formulas derived for suspension thermal noise. Saulson [Sau90] solved the problem for a damped harmonic oscillator using a Langevin approach as well as the fluctuation dissipation theorem, obtaining the simple expression for the power spectral density of displacement

$$\langle x^2(\omega) \rangle = \frac{4 k_B T f}{(k - m\omega^2)^2 + f^2 \omega^2} \,, \tag{2.7}$$

with the angular frequency ω, k_B the Boltzmann constant, T the temperature, k the spring constant, m the mass and f is connected to the Q-factor via $f = \frac{m\omega_0}{Q}$ with the resonance frequency ω_0.

As this approach can be used for any lossy harmonic oscillator, it was straightforward to apply this formula to the modes of the mirrors, requiring only the knowledge of the Q-factors of each mode. The thermal noise read out by the laser being reflected off the mirror then depends on the overlap with the modes calculated, and assumptions about the amplitde of higher order modes and convergence of the approach as well as orthogonality of the modes had to be made.

As this was unsatisfactory, Levin [Lev98] found a more direct approach to the calculation of mirror thermal noise, getting analytic expressions for the thermal noise under investigation. This approach involved application of the fluctutation-dissipation theorem directly to the readout

variable $x(t) = \int ff(\vec{r})y(\vec{r},t)d^2r$, which most commonly is the location of the test mass surface probed by a gaussian beam, having the lateral form factor $ff(\vec{r}) = \frac{1}{\pi r_0^2}\mathrm{e}^{-\frac{r^2}{r_0^2}}$ with the position vector $\vec{r}$ in polar coordinates. A generalized oscillating force is then applied at different frequencies, having the shape of this gaussian readout beam, giving rise to the oscillatory pressure

$$P(\vec{r},t) = F_0 cos(2\pi ft) ff(\vec{r})\,. \tag{2.8}$$

The fluctuation-dissipation theorem then states, that the spectral density corresponding to this readout variable is

$$S_x(f) = \frac{4k_BT}{\pi^2 f^2}|\Re[Z(f)]|\,, \tag{2.9}$$

where

$$Z(f) = 2\pi\imath\frac{x(f)}{F(f)} \tag{2.10}$$

is the complex impedance of the system associated with the readout variable. This impedance can be linked to the energy dissipated during the application of the oscillating force, which is given by

$$|\Re[Z(f)]|= \frac{2W_{diss}}{F_0^2} \tag{2.11}$$

and therefore the resulting spectral density has the form

$$S_x(f) = \frac{4k_BT}{\pi^2 f^2}\frac{2W_{diss}}{F_0^2}\,. \tag{2.12}$$

The problem thus has been reduced to calculating the dissipated energy under an oscillatory generalized force, and in the case of a mechanical force acting on a homogeneously lossy material used in Brownian thermal noise calculations, this energy is of the form

$$W_{diss} = 2\pi f U_{max}\phi(f)\,. \tag{2.13}$$

with the loss angle $\phi(f)$ being defined as the imaginary part of the Young's modulus $Y = Y_0[1 + \imath\phi(f)]$ and the maximum elastic energy stored U_{max}.

2.2.3 Brownian thermal noise

Brownian thermal noise is the thermally driven mechanical motion of the constituents of a system, in the case of advanced gravitational wave detectors a mirror or a suspension wire. It has the same frictional origin as found in the famous observation by Robert Brown, where he discovered that small particles suspended in a viscous fluid not only experience drag when being pulled, but also move about randomly, driven by thermal energy [Bro28].

2.2.3.1 Mechanical loss

The microscopic realisation of the friction causing energy loss and thereby coupling the thermal bath to the motion of the constituents depends on the system under investigation and only recently there has been progress in modelling the loss mechanisms in amorphous solids such as fused silica commonly employed in high reflectivity mirrors and suspension wires. A heuristic description involves double well potentials with differing barrier heights and asymmetries (shown in figure 2.3), commonly referred to as a two-level system (TLS), where tunneling can occur between eigenstates of energy E_1 and E_0, leading to loss [GHD12].

In the case of fused silica, the minima of the double well potentials are assumed to correspond

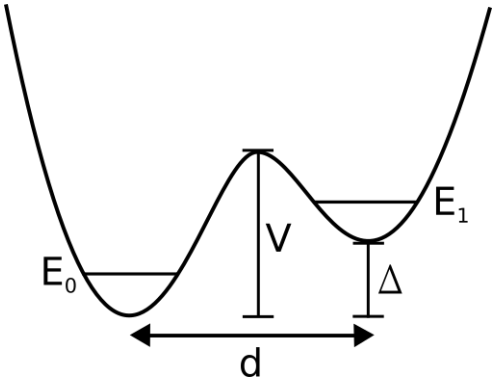

Figure 2.3: Two-level system in a double well potential (adapted after [GP81]). The parameters Δ and V describe the asymmetry and the barrier height of the double well potential. The spatial separation of the minima is d, and the energy of the corresponding minimal energy eigenstates is E_0 and E_1 respectively. Such model systems can describe configurations in amorphous solids.

to different configurations of tetrahedra [LDK17]. Transitions involve the displacement of oxygen atoms and flipping of bond angles between two silica atoms and the oxygen atom.When going from the higher local minimum to the lower one in a double well potential, energy is effectively lost. The presence of such two-level systems and their properties then influence the level of thermal noise observed. Changing the different configurations involved is a way to reduce thermal noise, for example annealing the coating after deposition or doping the material with atoms such as Titania.

2.2.3.2 Substrate Brownian thermal noise

Substrate Brownian thermal noise was among the earlier mirror thermal noise sources to be calculated, using an infinite half-space made up of the substrate material as an approximation of the mirror. In [BHV98], the starting point is the general expression for the spectral density of the readout variable according to Levin's approach

$$S_x(f) = \frac{4k_BT}{\pi f} U\phi(f)\,. \tag{2.14}$$

Here, the dissipated energy is expressed as the product of the loss angle $\phi(f)$ of the substrate material and the strain energy U stored in the substrate caused by the oscillatory pressure with a spatial distribution corresponding to a Gaussian beam. The assumption of an infinite half plane as a model for the mirror substrate allows to use analytical expressions for the displacement, strain and resulting elastic energy. Only one boundary condition has to be considered, resulting in the expression

$$S_x(f) = \frac{4k_BT}{\pi f} \frac{1-\sigma^2}{2\sqrt{\pi} Y w_0} \phi(f)\,, \tag{2.15}$$

with Young's modulus Y, Poisson's ratio σ and Gaussian beam waist size w_0.

A more sophisticated approach is required to analytically solve the elastic equations and find the stored energy in the case of a finite sized test mass. For simple geometrical shapes such as cylinders, this is still a straightforward, but rather lengthy calculation, involving expansion of the displacements into Bessel functions and boundary conditions for each surface. The result can be expressed as a correction factor to the infinite half plane calculation, becoming significant in the case of mirror diameters not being much larger than the beam radius. Furthermore, the noise of

the finite mirror depends on the aspect ratio $\frac{h}{a}$ of the mirror with the mirror height h and the mirror diameter a, favouring rod shaped mirror geometries over gong shaped geometries.

2.2.3.3 Coating Brownian thermal noise

Brownian thermal noise does not only appear in the substrate as described above, but also in the coating. At first glance it seems that because of the larger amount of material present in the substrate compared to the coating, the contribution of the substrate would dominate the total thermal noise [Cro+02][Har+02]. Measurements showed early on that indeed the coating Brownian thermal noise is the dominant contribution in high reflectivity mirrors [Num+03][Bla+04a]. This is mainly attributed to the fact that the mechanical loss in the thin coating layers is several orders of magnitude higher than in the bulk of the substrate, even for the same chemical composition.

Typical loss values for bulk material and thin layers are 10^{-8} and 10^{-4} respectively. Investigations showed, that those excess losses do not arise from the interfaces of the coating layers with each other or with the substrate, but indeed from the coating material inside each layer [Har+06a]. Furthermore, the coating is the part of the mirror directly interacting with the light used to read out the test mass position. Losses in the coating thus have a larger influence compared to losses at the edge of the substrate.

Over the last years, there have been discussions about the most adequate treatment of losses in coating Brownian thermal noise calculations, and the following discussion follows [Hon+13] in splitting the mechanical loss contributions into bulk and shear loss, instead of loss in strains parallel or perpendicular to the mirror surface. This is achieved by making the bulk modulus and shear modulus of the coating layer materials complex, where the imaginary part corresponds to the mechanical loss of the type of deformation in question.

Brownian coating thermal noise can then be calculated starting with the fluctuation-dissipation theorem in the form of equation 2.14, where U represents the elastic energy stored in the coating upon deformation by a force with a Gaussian profile, and $\phi(f)$ stands for the mechanical loss. The elastic energy stored now has to be split in contributions from bulk deformations and shear deformations, and each contribution is associated with its individual mechanical loss, ϕ_B and ϕ_S. For most calculations, both losses are assumed to be equal, but future measurements could show a difference between both loss channels.

Formal descriptions of each of the contributions can be found by solving the elastic equations in the presence of a driving force. As the readout beam is usually small compared to the mirror, finite-size effects can be neglected and an infinite substrate and layer can be assumed. Solving the elastic equations gives the time-dependent stress and strain in the coating. For the frequencies of interest to the TNI and gravitational wave detectors, a quasi-static approximation can be used, as those frequencies are below the internal resonance frequencies. It is then enough to take the maximum deflection of the coating and calculate the stored energy in this state. The loss is then calculated by multiplying the stored energy with the loss angle $\phi(f)$.

Not much is known so far about the frequency dependence of the loss, but measurements support the assumption, that the loss is frequency-independent [Cro+06][Li+14] or has a very small frequency dependence [Kaj+99][GE18], which so far is being neglected in calculations. Frequency independent loss is characteristic for structural damping, in contrast to viscous damping, which increases in strength with increasing frequency.

Assuming constant loss in every material, several levels of complexity can be chosen in the thermal noise calculation. The simplest way, and most often employed, is treating the coating as a single layer with averaged parameters. A slightly more complicated approach bundles the contributions from each coating material into one layer of that material, neglecting any effects of the distribution of layer thicknesses in the coating. Taking this into account leads to results, which resemble the calculations for thermo-refractive noise. As now the light penetrates the coating and layers, it not only interacts with a moving coating surface, but also experiences changes in the

optical path length in each layer. This leads to a change in the reflected light phase. Another effect, coming from the photoelastic properties of the coating, changes the optical thicknesses of the layers through the coupling of elastic deformations to the refractive index.

Additionally, the effect of one of the shear modes being opposite to all other deformations, can cancel part of the thermal noise. For most purposes, including this thesis, the single layer or double layer approximations suffice, creating errors on the order of 2 % [KGG11]. The simplified formula used is then

$$S_x(f) = \frac{4k_BT}{\pi^2 w_0^2 f}\left[\phi_B \frac{(1-2\sigma_c)d}{3}\left(\frac{Y_c}{Y_s^2}\frac{(1-2\sigma_s)^2(1+\sigma_s)^2}{(1-\sigma_c)^2} + \frac{1}{Y_s}\frac{2(1-2\sigma_s)(1+\sigma_s)(1+\sigma_c)}{(1-\sigma_c)^2} + \frac{1}{Y_c}\frac{(1+\sigma_c)^2}{(1-\sigma_c)^2}\right) + \phi_S \frac{2d}{3}\left(\frac{Y_c}{Y_s^2}\frac{(1-\sigma_c+\sigma_c^2)^2(1+\sigma_s)^2(1-2\sigma_s)^2}{(1-\sigma_c^2)^2(1+\sigma_c)} - \frac{1}{Y_s}\frac{(1+\sigma_c)(1-2\sigma_c)(1-2\sigma_s)(1+\sigma_s)}{(1-\sigma_c)^2} + \frac{1}{Y_c}\frac{(1-2\sigma_c)^2(1+\sigma_c)}{(1-\sigma_c)^2}\right)\right], \tag{2.16}$$

with the coating (c) and substrate (s) parameters Young's modulus Y and Poisson's ratio σ. These parameters, as well as the loss angles ϕ_S and ϕ_B, come with significant uncertainties. This is one of the main motivations for experiments like the TNI.

2.2.4 Thermoelastic and thermorefractive noise

Thermoelastic and thermorefractive noise share a common fluctuation mechanism, which then couples into the measured displacement differently. The source is fluctuations in the local temperature inside the substrate and coating, powered by energy from the thermal bath. The derivation and formal description of these temperature fluctuations and successively the coupling mechanisms resulting in the different forms of thermal noise explained below is based on [Eva+08].

2.2.4.1 Coating thermoelastic noise

The basis for coating thermoelastic noise and closely related coating thermorefractive noise is the calculation of fluctuations of the temperature inside the coating. In agreement with Levin's approach and following [Eva+08], a fluctuating power (P) per volume element (δV) in the shape of the Gaussian readout variable (Gaussian laser beam in the fundamental TEM00 mode ($q(\vec{r})$)) is applied to the surface of the mirror under investigation.

$$\frac{P}{\delta V} = TF_0 \sin(\omega t) q(\vec{r})\,. \tag{2.17}$$

F_0 is a scale factor and ω the angular frequency of the fluctuating power. This is equal to introducing a fluctuating entropy, which is used in some publications. This power introduced leads to a flow of energy or heat following the diffusion equation

$$C\frac{\partial \delta T}{\partial t} = \kappa \nabla^2 \delta T\,, \tag{2.18}$$

with the thermal conductivity κ and the heat capacity per volume C. The boundary condition that heat flow is directed only inwards through neglecting radiative losses is applied. Assuming further that the thermal diffusion length $r_T = \sqrt{\frac{\kappa}{2\pi C f}}$ is significantly smaller than the radius of the applied power injection leads to the solution of the diffusion equation.

This solution represents the temperature gradient, which leads to heat flow and thereby to a

change in entropy, which in turn leads to dissipation of energy, written as

$$W \simeq \langle \oint \frac{\kappa_s}{T} \left(\frac{\partial \delta T}{\partial z} \right)^2 \rangle \,, \tag{2.19}$$

The fluctuation-dissipation theorem then gives the spectral density of temperature fluctuations

$$S_T(f) = \frac{2}{\sqrt[3]{\pi}} \frac{k_B T^2}{w_0^2 \sqrt{\kappa C f}} \,, \tag{2.20}$$

These temperature fluctuations couple into displacement fluctuations of the coating surface via the thermoelastic coefficient. This coupling has to be calculated by summing the contributions from each layer given their thermal material properties.

Writing the resulting effective thermal expansion coefficient as $\overline{\alpha}_c = \sum_k \overline{\alpha}_k \frac{d_k}{d}$ with the layer thickness d_k, total thickness d and the individual thermoelastic coefficients

$$\overline{\alpha}_k = \alpha_k \frac{1+\sigma_s}{1-\sigma_k} \left[\frac{1+\sigma_k}{1-\sigma_k} + (1-2\sigma_s) \frac{E_k}{E_s} \right] , \tag{2.21}$$

with the layer specific Poisson ratios σ_k and the Young's modulus E_k, gives the spectral density of coating thermoelastic noise

$$S_x(f) = \frac{2}{\sqrt[3]{\pi}} \frac{k_B T^2}{w^2 \sqrt{\kappa C f}} (\Delta \overline{\alpha} d)^2 \,. \tag{2.22}$$

2.2.4.2 Coating thermorefractive noise

Coating thermorefractive noise calculations start from the same temperature fluctuations as in the case of coating thermoelastic noise, and then using a different coupling path into phase fluctuations of the reflected light. Similar to the case of coating Brownian thermal noise, the temperature fluctuations in each layer cause a change of the optical layer thickness through the thermoelastic coefficient (α) for mechanical deformation and the thermorefractive coefficient (β) changing the refractive index and thereby the optical thickness.

The naming of coating thermorefractive and coating thermoelastic noise is misleading, as the defining difference is taking the internal coating structure change into account (single layer contributions versus whole coating expansion), not the coupling mechanism (refractive versus elastic). As a result, following [GHD12], the spectral density for coating thermorefractive noise is given by

$$S_x(f) = \frac{2 k_B T^2}{\sqrt[3]{\pi}} \frac{\beta_{eff}^2 \lambda^2}{w^2 \sqrt{\kappa \rho C f}} \,, \tag{2.23}$$

where

$$\beta_{eff} = \frac{1}{2\pi} \frac{\pi n_L^2 (\beta_L + \beta_H) + \beta_L (\phi_c - \sin(\phi_c))(n_H^2 - n_L^2)}{(n_H^2 - n_L^2)(n_L^2 + 1 + (n_L^2 - 1)\cos(\phi_c))} \,, \tag{2.24}$$

and n_L and n_H are the refractive indices of the low index material and high index material respectively, and ϕ_c is the phase associated with the topmost part of the coating with thickness d_c by $\phi_c = \frac{4\pi d_c n}{\lambda}$.

2.2.4.3 Coating thermooptic noise

Coating thermooptic noise is the coherent combination of coating thermoelastic noise and coating thermorefractive noise. Both types of noise are correlated because they originate from the same temperature fluctuations in the coating, the only difference being the way they change the phase

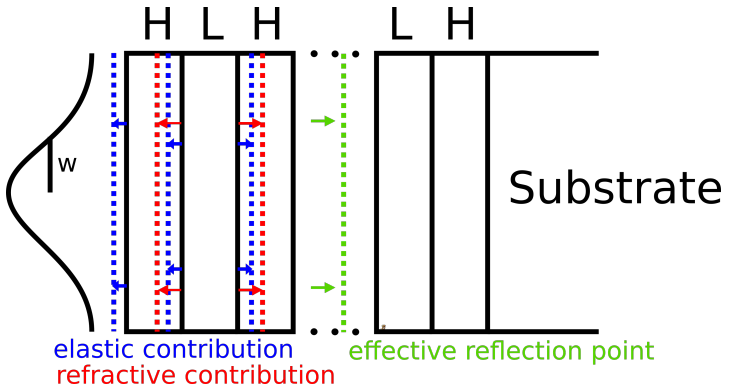

Figure 2.4: The coherent contributions from thermoelastic noise and thermorefractive noise to thermooptic noise partially cancel. Thermoelastic noise moves the coating surface, whereas thermorefractive noise shifts the effective reflection point inside the coating in the opposite direction. The thermorefractive noise consists of contributions from thermoelastic and thermorefractive thickness changes of each layer.

of the reflected light. As thermoelastic noise describes the motion of the coating surface caused by the thermal expansion of the coating stack, an expansion of the coating will lead to a negative phase change in the reflected light as the coating surface moves toward the source of the light.

Thermorefractive noise on the other hand describes the change of optical path length inside each layer independently, which in turn changes the phase of the reflected light, and an expansion of each layer causes a positive phase change of the light making a round trip in this layer. The change of the optical path length is driven by temperature fluctuations coupling via the thermoelastic and thermorefractive coefficient. The effect of a change in the optical thickness of layers can be visualized as a change in the effective penetration depth of the light in the coating, and for an optimized coating design, the effective point of reflection corresponding to the penetration depth will move in the opposite direction as the mirror surface driven by thermoelastic noise (shown in figure 2.4).

Thus, a certain level of cancellation is possible and for crystalline materials envisioned as future materials for the coatings of test masses, this canecellation is needed as their thermal properties cause the thermoelastic noise and thermorefractive noise to be higher than Brownian thermal noise. The simplified formula for coating thermooptic noise, taking the coherent sum of coating thermoelastic and coating thermorefractive noise, is given by

$$S_x(f) = \frac{2}{\sqrt[3]{\pi}} \frac{k_B T^2}{w^2 \sqrt{\kappa C f}} \left(\overline{\alpha}_c d - \overline{\beta} \lambda - \overline{\alpha}_s d \frac{C_c}{C_s} \right)^2 , \tag{2.25}$$

where the subscripts s and c stand for the substrate and the coating. This is based on the assumptions, that the thermal diffusion length is much larger than the coating thickness, removing the coating from the heat flow calculations, and that the gaussian beam size is much larger than the thermal diffusion length, neglecting lateral heat flow.

As coatings are getting thicker to increase the reflectivity of high reflectivity mirrors, the first assumption might break down and this can be accounted for by introducing a so called thick coating correction. This is done by modifying the power injection and the diffusion equation. The solution involves a transformation into a second order differential equation, and finally arriving at the dissipated energy, from which the correction factor for the spectral density of coating thermooptic noise can be derived [Eva+08].

2.2.4.4 Substrate thermoelastic noise

Substrate thermoelastic noise is calculated using the fluctuation-dissipation theorem as above, requiring the solution of the heat diffusion equation, from which the dissipated power through heat flow can be derived [GHD12]. The temperature fluctuations resulting are then coupled to surface displacement of the substrate by the thermoelastic coefficient and the elastic properties of the material.

Substrate thermoelastic noise can thus be represented by the power spectral density

$$S_x(f) = \frac{4k_B T^2 \alpha^2 (1+\sigma)^2 \kappa}{\sqrt{\pi^5}(C\rho)^2 w_0^3 f^2}\,, \tag{2.26}$$

with the thermal expansion coefficient α, specific heat capacity per unit mass C, density ρ, thermal conductivity κ and Gaussian beam waist w_0. This noise is in part coherent with coating thermoelastic noise, and partial compensation should be possible.

2.2.4.5 Substrate thermorefractive noise

The starting point for substrate thermorefractive noise is the flucutation-dissipation theorem [GHD12], applied to the phase of the light transmitted through the mirror translated into a displacement

$$\delta z = \int\limits_V d^3\vec{r} a\beta\delta T(\vec{r}) q(\vec{r})\,, \tag{2.27}$$

as the readout variable. Here, $\beta = \frac{\partial n}{\partial T}$ is the thermorefractive coefficient, a is the optical pathlength through the substrate and $q(\vec{r})$ is the form factor corresponding to a Gaussian beam. Injecting entropy into a small volume

$$\frac{\delta S(\vec{r},t)}{dV} = F_0 \cos(\omega t) a\beta q(\vec{r})\,, \tag{2.28}$$

with the amplitude of entropy injection F_0, solving the heat equation

$$C\rho\frac{\partial \delta T}{\partial t} - \kappa\nabla^2\delta T = T\frac{\partial}{\partial t}\frac{\delta S(\vec{r},t)}{dV}\,, \tag{2.29}$$

given this input and deriving the dissipated power through heat flow by

$$W_{diss} = \int\limits_V d^3\vec{r}\frac{\kappa}{T}\langle(\nabla\delta T)^2\rangle\,, \tag{2.30}$$

gives the resulting power spectral density

$$S_x(f) = \frac{4k_B\kappa T^2\beta^2 a}{4\pi^3(C\rho r_0^2 f)^2}\,, \tag{2.31}$$

An extra factor of

$$1 + \frac{2k^2 r_0^2}{1+(2kl_{th})^4}\,, \tag{2.32}$$

can be added to account for standing light waves inside the substrate, where $k = \frac{2\pi n}{\lambda}$ is the wavevector of the light and $l_{th} = \sqrt{\frac{\kappa}{2\pi C\rho f}}$ is the thermal diffusion length. In most high sensitivity interferometers, substrates are only traversed once or twice, compared to the repeated interaction with coatings in high finesse cavities, which makes the contribution of substrate thermorefractive

noise often negligible.

2.2.4.6 Photothermal noise

Photothermal noise describes those types of thermal noise, which are caused by temperature fluctuations coupling to the light phase through the thermorefractive and thermoelastic mechanism, but where the source of the temperature fluctuations is not coupling to the heat bath via the fluctuation-dissipation theorem, but the absorption of laser light by the mirror [GHD12].

The absorbed power leads to a local increase in temperature and subsequent heat flow. This resulting temperature distribution gets translated into surface fluctuations via the thermoelastic coefficient for the substrate, resulting in the power spectral density

$$S_x(f) = \frac{S_{abs}\alpha^2(1+\sigma)^2}{\pi^4\rho^2C^2w_m^4f^2}\,. \tag{2.33}$$

For the coating, the same calculations apply, using the thermoelastic and thermorefractive mechanism, resulting in the expressions for the photothermoelastic contribution

$$S_x(f) = \frac{4S_{abs}(1+\sigma)^2\alpha_f^2d_N^2}{\pi^3\rho C\kappa w_m^4 f}\,, \tag{2.34}$$

and the photothermorefractive contribution

$$S_x(f) = \frac{S_{abs}\beta_{eff}^2\lambda^2}{\pi^3\rho C\kappa w_m^4 f}\,, \tag{2.35}$$

which are correlated and can be combined into photothermooptic noise. In properly commissioned interferometers using active power stabilization, the spectral density of power fluctuations of the light S_{abs} will correspond to shot noise, having the form

$$S_{abs} = 2h\frac{c}{\lambda}W_{abs}\,, \tag{2.36}$$

with the absorbed power W_{abs}. Excess power noise on the laser light increases the contribution of photothermal noise, which has been used to assess the thermooptic noise cancellation properties of coatings in [Cha+16].

2.2.5 Other thermal noise

All thermal noise sources illustrated above give more or less significant contributions to the noise budget of the TNI and of gravitational wave detectors. The materials used as substrates and coatings increase or reduce the importance of some kinds of thermal noise. There exist a few more thermal noise sources which are further away from being limiting in the near future, but nonetheless interesting examples of the variety of noise sources which are present.

2.2.5.1 Stefan-Boltzmann noise

When calculating the spectrum of temperature fluctuations used for thermooptic noise simulations, only the loss associated with heat flow inside the material is taken into account [GHD12]. As the fluctuation-dissipation theorem can be used with any loss mechanism, radiative loss from the surface governed by the Stefan-Boltzmann law can be studied. In most cases this noise is neglected as it is strongly temperature dependent and effectively suppressed at room temperature.

It can nevertheless be useful to calculate the expected contribution by this radiative process

following the Stefan-Boltzmann law for blackbody radiation. As it originates from the surface, the resulting temperature fluctuations will affect the mirror expansion in the same way as photothermal noise, so the formula for Stefan-Boltzmann noise is based on photothermal noise, where the spectral density of the absorbed power is exchanged by the expression

$$S_{abs} = 8\sigma_B k_B T^5 \pi w_m^2 \,, \tag{2.37}$$

with the Stefan-Boltzmann constant σ_B.

2.2.5.2 Coating photoelastic noise

Another correction to a thermal noise evaluation described above can be considered for the case of coating Brownian thermal noise, where the photoelastic tensor p_{ij} introduces coupling from the thermally induced mechanical deformation of the coating layers to a change in the refractive index according to [GHD12]

$$\delta n = -\frac{n^3}{2} p_{ij} \frac{\delta d}{d} \,. \tag{2.38}$$

The result behaves similar to the case of thermooptic noise, where the change of the refractive index of each layer changes the phase of the reflected light and is correlated to the elastic changes of layer thicknesses.

In the case of Brownian thermal noise, however, the contribution of photoelasticity is very small, causing a correction on the order of 1 % [GV10], which is not enough to properly cancel Brownian thermal noise, as is possible in the thermooptic case.

2.2.5.3 Cosmic Ray noise

A rather curious form of thermal noise acts similar to photo-thermoelastic noise, but in this case the heat introduced into the test mass does not stem from the laser impinging on the mirror, but from cosmic ray showers produced in the upper atmosphere [BRV06a][BRV06b]. Mainly composed of Muons, these showers interact with the test masses of gravitational wave detectors by imparting momentum, charging and heating up the material along their trace through the mirror.

For higher energy particles around 1 TeV, the occurence is rare at rates of 10 to 100 per year, making veto processes possible to remove the signal created. Lower energy particles at 0.2 GeV and above appear at rates of 14 particles each second passing through test masses of size used in advanced gravitational wave detectors, creating a background noise.

The approximate formula for cosmic ray noise,

$$S_x(f) = \frac{2J_\mu}{\pi^2} \frac{\alpha^2}{f^2 \rho^2 C^2} \left(\frac{dE}{dx} \right)^2 \,, \tag{2.39}$$

with the thermal expansion coefficient α, the heat capacity C, the density ρ, the angular intensity distribution of muons J_μ and the stopping power $\frac{dE}{dx}$ gives a level of noise of 10^{-26} in strain for advanced gravitational wave detectors, ensuring that being limited by this type of noise requires the removal of many other thermal noise sources.

2.2.5.4 Thermochemical noise

Recently, another form of thermal noise has been proposed [BL09], which originates from the lossy drifting motion of impurities such as hydroxyl ions in fused silica. The fluctuation-dissipation theorem then predicts random fluctuations of the concentration of these impurities, which influences the refractive index of the material, thereby changing the optical phase of light traversing the

mirror. Example calculations for the beam splitter of GEO600 show, using the expression

$$S_x(f) = \frac{4DP\alpha^2 k^2 a'}{4\pi^2 r_0^2 \eta f^2}\,, \tag{2.40}$$

that this noise lies far below the measurement sensitivity. Depending on the size, material and purity of optics for future gravitational wave detectors, it might become relevant.

2.3 Thermal Noise Simulation and Optimization

Calculating the level of thermal noise for different coating geometries using a variety of materials is the goal of a large effort across the LVK-collaboration [Cha+14]. Uncertainties in material parameters, which are necessary inputs for calculations, especially the mechanical loss of thin layers of coating material, led to the development of several experiments dedicated to extract these parameters [Cro+02].

Confirmation of the formulas used in coating thermal noise calculations has been the other focus, so that calculations using the aforementioned parameters result in correct predictions of coating thermal noise at all frequencies and beam sizes.

In this thesis, the results of thermal noise simulations using numerical tools such as MATLAB are used for creating a noise budget for the TNI. A second focus was optimizing the coating structure for AlGaAs-coatings planned to be used for the AEI 10 m prototype Fabry-Perot-Michelson interferometer.

2.3.1 Thermal noise simulation

The basis for all thermal noise calculations used in chapter 6 and in the coating optimization have been three MATLAB codes written by Sean Leavey, Kentaro Somiya and Rana Adhikari. Modifications have been introduced to the thermooptic calculations based on [Eva+08], which mostly remove simplifying assumptions.

Starting from the stack geometry, given as optical thicknesses in units of the optical wavelength for each layer, and the corresponding refractive indices, the code calculates the reflectivity as described in 2.1. To include optical losses, refractive indices have been modified by adding an imaginary part [GHD12]. The total loss of the coating is then calculated by adding the loss in each layer, which in turn depends on the electric field amplitude present in this layer.

Calculations for coating Brownian noise neglect penetration of light into the coating and use layer-thickness-weighted effective parameters. The calculations for thermo-optic noise include light penetration, as this is essential in the coherent cancellation of thermo-elastic and thermo-refractive noise. Other than serving as the basis for the optimization procedures for the sub-SQL interferometer AlGaAs-mirrors, the code has been used to design coating structures which could be used to measure contributions from Brownian, thermo-elastic and thermo-refractive noise individually.

A coating design being limited by coating Brownian noise is shown in figure 2.5. It consists of 28 pairs of quarter-wave layers of AlGaAs and GaAs with a GaAs-cap of 1.25λ thickness and a bottom layer of half-wave thickness. GaAs is commonly used as the topmost layer, as it is more durable. This coating design focuses on thermooptic compensation, thereby increasing the separation between coating Brownian noise and thermooptic noise.

For being limited by thermoelastic noise, a coating with 36 pairs of quarter-wave layers with a cap of quarter-wave thickness and the third lowest layer having a thickness of 50.25λ is chosen. The thick layer deep in the coating increases thermo-elastic noise while not seeing much light, therefore

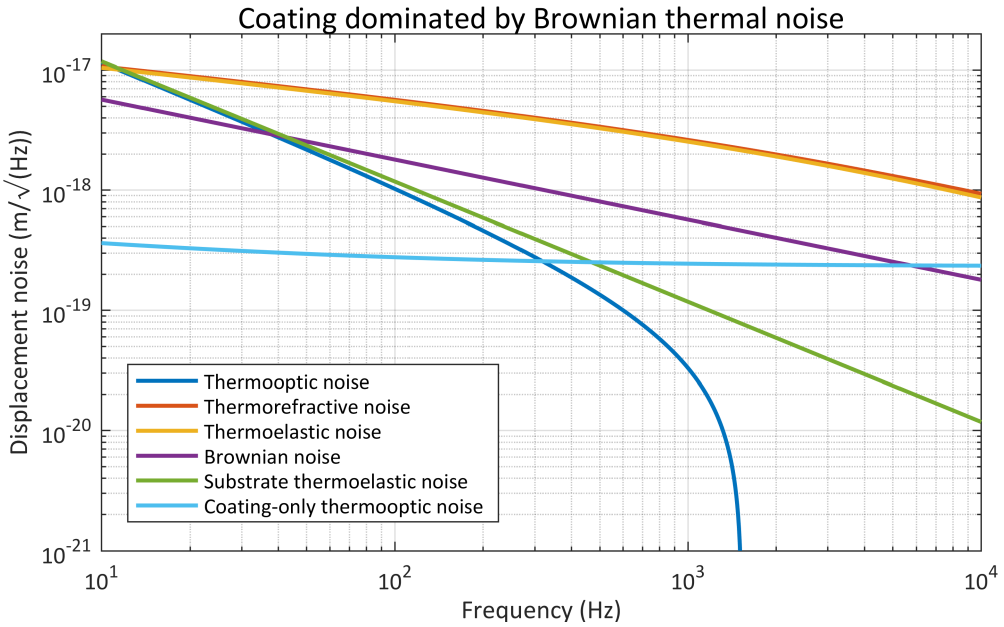

Figure 2.5: A coating design being limited by Brownian thermal noise. Proper cancellation makes the contribution from thermooptic noise negligible.

not enabling coherent cancellation. The resulting predicted spectrum is shown in figure 2.6.

Achieving a coating limited by thermorefractive noise is possible using 36 pairs of quarter-wave layers, with a half-wave bottom layer giving a large margin to the coating Brownian noise contribution. The resulting spectrum is shown in figure 2.7.

Another question that arose during work on the TNI is, if there is a thermoelastic noise contribution from part of the substrate which is coherent with the coating thermooptic noise. This can be tested by designing a coating which shows a different level of noise for a coherent and non-coherent contribution. The non-coherent calculation is the standard calculation, summing coating thermo-optic noise and substrate thermo-elastic noise in quadrature. Coherently summing substrate thermoelastic noise from a region of the size of the thermal diffusion length gives the coherent contribution. This would show up as a significant difference in the total thermal noise (as shown in figure 2.8).

2.3.2 Coating stack optimization

The MATLAB scripts used for calculating coating thermal noise were furthermore used to find possible coating structures for high-reflectivity AlGaAs-coatings, planned to be used in the AEI 10 m prototype sub-SQL interferometer. The choice of these coatings is based on the significantly reduced mechanical loss angle of the crystalline heterostructure of AlGaAs and GaAs compared to an amorphous silica/tantala coating. The difference in loss angle directly translates into a difference in coating Brownian thermal noise, which allows for measurements well below the SQL (as shown in figure 2.9).

The starting point for the optimization is a collection of boundary conditions to be met. In general, the planned coatings consist of alternating layers of GaAs and AlGaAs with variable thicknesses. Deviating from the standard quarter-wave thicknesses for the layers leads to a reduction in reflectivity, necessitating an increase in layer number. Optimizing layer thicknesses while keeping the total number of layers as another variable complicates the optimization problem

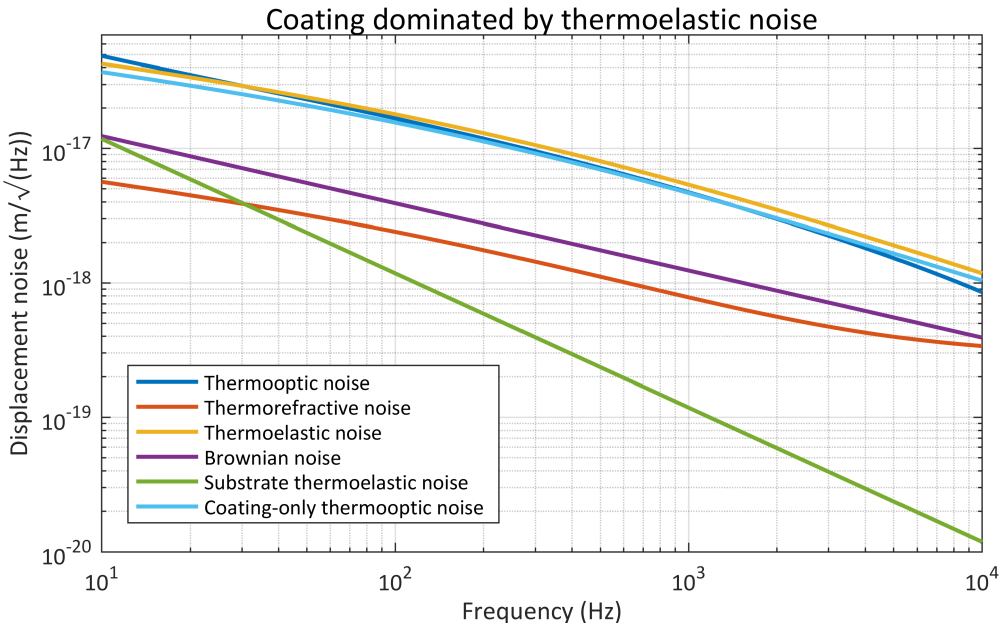

Figure 2.6: A coating design limited by thermoelastic noise. A 50.25λ thick layer close to the bottom of the coating raises thermoelastic noise far above Brownian thermal noise.

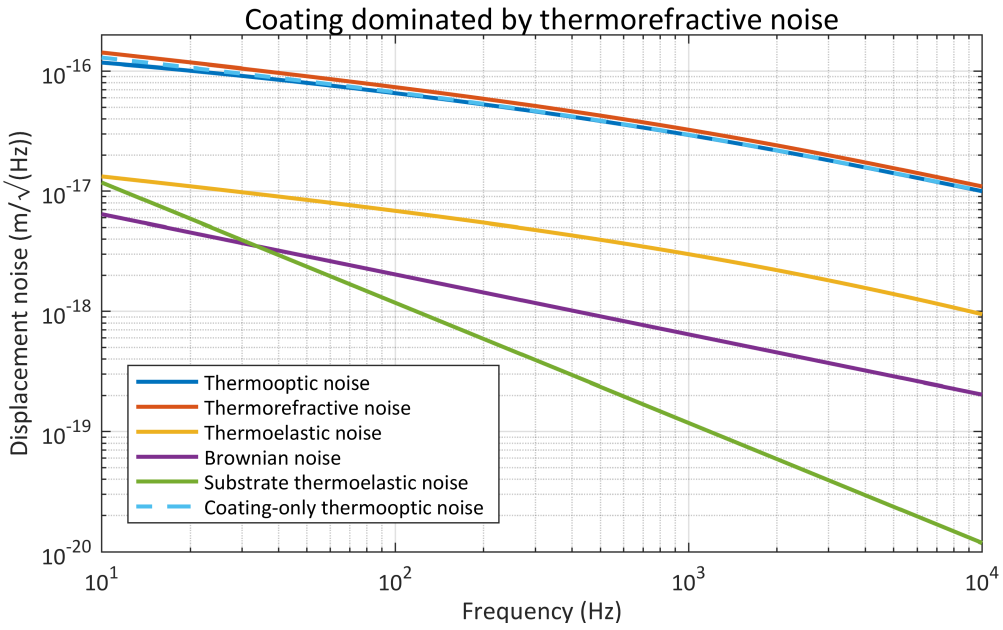

Figure 2.7: A coating design limited by thermorefractive noise. A half-wave thick bottom layer raises thermorefractive noise far above Brownian thermal noise.

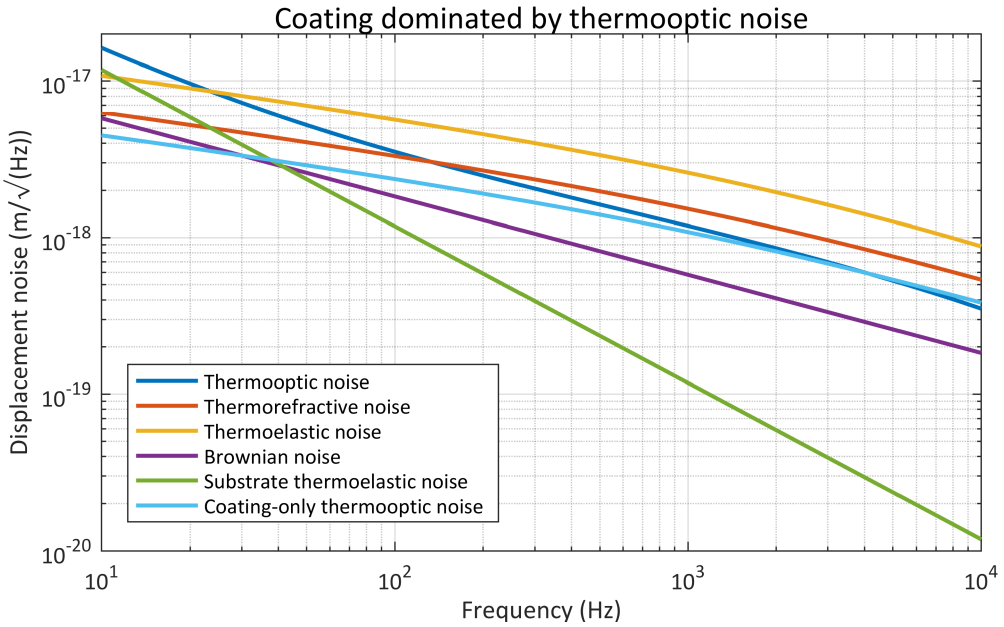

Figure 2.8: A coating design limited by thermo-optic noise. This makes it possible to test whether part of the substrate thermoelastic noise contributes coherently to coating thermo-optic noise.

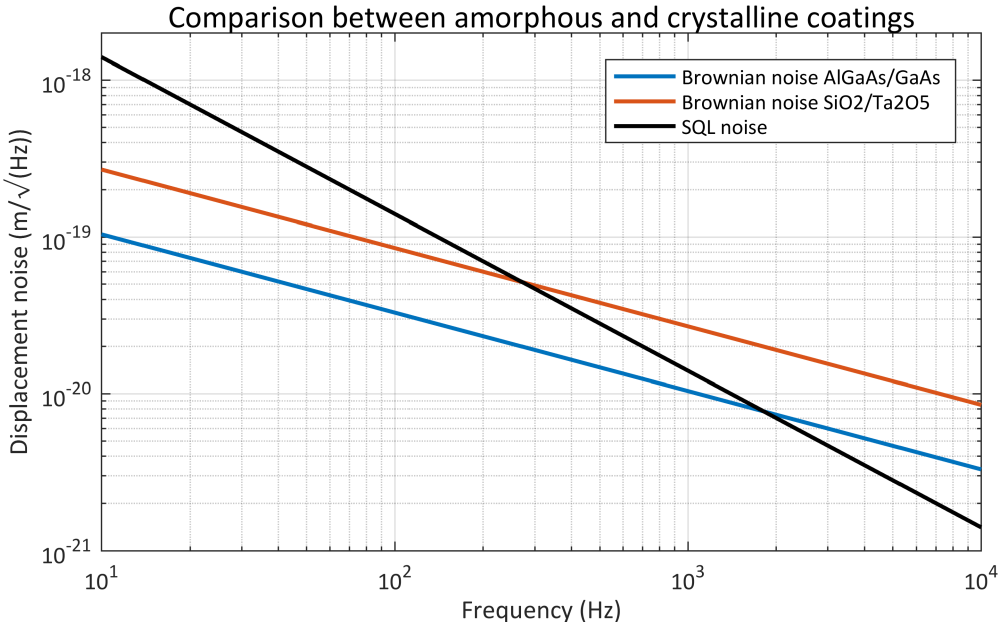

Figure 2.9: Comparison of Brownian coating thermal noise for an amorphous silica/tantala coating and a crystalline AlGaAs coating. The coating design is done for the AEI 10 m prototype sub-SQL interferometer and has to show coating noise lower than the SQL.

significantly. The layer structure has to ensure that the mirrors have reflectivities at or slightly below 1000 ppm for the ITM and 50 ppm for the ETM. Furthermore, the electric field present at the surface has to be as low as possible to prevent damage by attracting and burning-in dust particles. For that purpose, the phase of the electric field in reflection with respect to the incoming field is assumed to be below 10°. The top layer is chosen to be GaAs as this is less susceptible to environmental influences, especially to oxidization in contrast to AlGaAs. Lastly, the total absorption of the coating has to be below 5 ppm.

Imposing these boundary conditions, the coating structure giving the lowest incoherent sum of Brownian coating thermal noise and thermo-optic coating thermal noise has to be found. Other thermal noise sources are negligible when using low-loss fused silica substrates, monolithically suspended from fused silica PUMs. Several approaches, based on MATLAB scripts, have been tested, among them a genetic algorithm, a particle swarm optimization and a manual reduction of the search domain with subsequent manual optimization.

For the genetic algorithm, a MATLAB based script by Holger Wittel has been adapted to fit the needs for coating thermal noise optimization. Several optimization runs have been performed, where for each run, a fixed number of coating layers has been chosen as well as the minimal and maximal thickness allowed for the layers. With a population size of 2000 trial coatings, the code ran for at most 100 generations to find optimal values for coating Brownian noise and coating thermo-optic noise while meeting the boundary conditions. The fitness function, which guides the selection of the fittest individuals of each generation, has been varied between runs, and was chosen, for example, to be linear in the thermal noise terms and exponential in the surface field and transmissibility.

The result is a magnitude of different coating structures with low coating Brownian and coating thermooptic noise. A similar procedure was tried with particle swarm optimization, giving comparable results. All these results (shown for five trial runs with 20 trials each using the genetic algorithm in figure 2.10), although possessing low coating thermooptic noise, showed higher coating Brownian thermal noise than the generic quarter wave coating stack.

This can be explained by the fact that reducing the thermo-optic noise requires deviation from quarter wave-thick layers. Dephasing between light fields reflected at different depths in the coating results, which leads to a lower reflectivity. This can be compensated by thickening individual layers when others have been made thinner, or adding more layers. The effect on the reflectivity is shown in figure 2.11, deviating in some cases significantly from the goal of 50 ppm. Overall, the total coating thickness will increase, thereby raising coating Brownian noise. As the total noise performance of the mirrors does not only rely on the best coating thermo-optic noise possible, but is limited by the highest noise contribution, these resulting coating stacks are not optimal for the intended use. As there was no example where the coating Brownian noise was below the quarter wave stack, it was assumed as a working hypothesis that the thinnest and thereby lowest Brownian noise coating is indeed the quarter wave stack.

Thermooptic noise can then be brought down below the coating Brownian noise with a minimal penalty in thickness by tuning a few of the uppermost layers. Changing for example only the uppermost layer, called cap, leads to an oscillatory behaviour in the coating thermorefractive noise and thereby also in the coating thermo-optic noise, while only barely changing coating thermoelastic and coating Brownian noise. This is shown in figure 2.12 for a stack of 62 layers corresponding to the case of 50 ppm and in figure 2.13 for 28 layers corresponding to 1000 ppm. The transmission is unchanged when the cap thickness is an odd multiple of 0.25λ and can be reduced by up to a factor 11 for 62 layers when the cap thickness is a multiple of 0.5λ.

For the case of 50 ppm there is a tradeoff between having minimal coating thermooptic noise, for example close to a cap of size 0.1λ or 0.4λ, which would have a significant electric field at the coating surface, or at 1.25λ with a slight increase in coating Brownian noise, and minimizing the electric field as well as coating Brownian noise at 0.25λ or 0.75λ with a slightly higher contribution from coating thermo-optic noise. A coating design with a cap of thickness 1.25λ and with 62 layers in total would improve the thermooptic noise contribution by a factor of 5.7, leaving coating

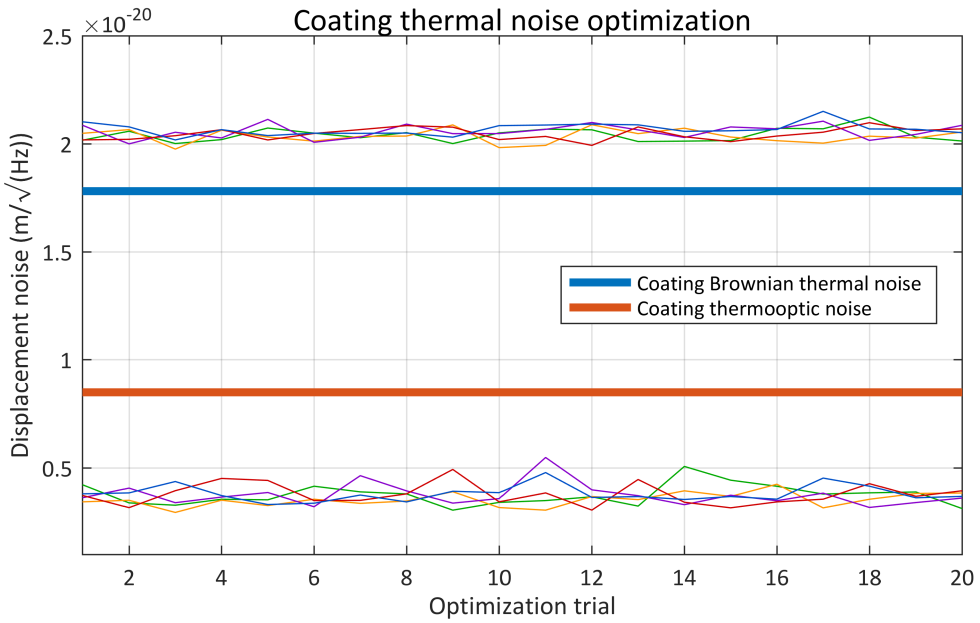

Figure 2.10: Power spectral densities of coating Brownian thermal noise (blue line and above) and coating thermooptic noise (red line and below) at 100 Hz. Thick lines are calculated using a standard quarter wave coating with an optimized cap, while the thin lines are the results of five runs of 20 genetic algorithm optimization trials. While coating thermooptic noise can be improved, the dominant coating Brownian noise does get worse.

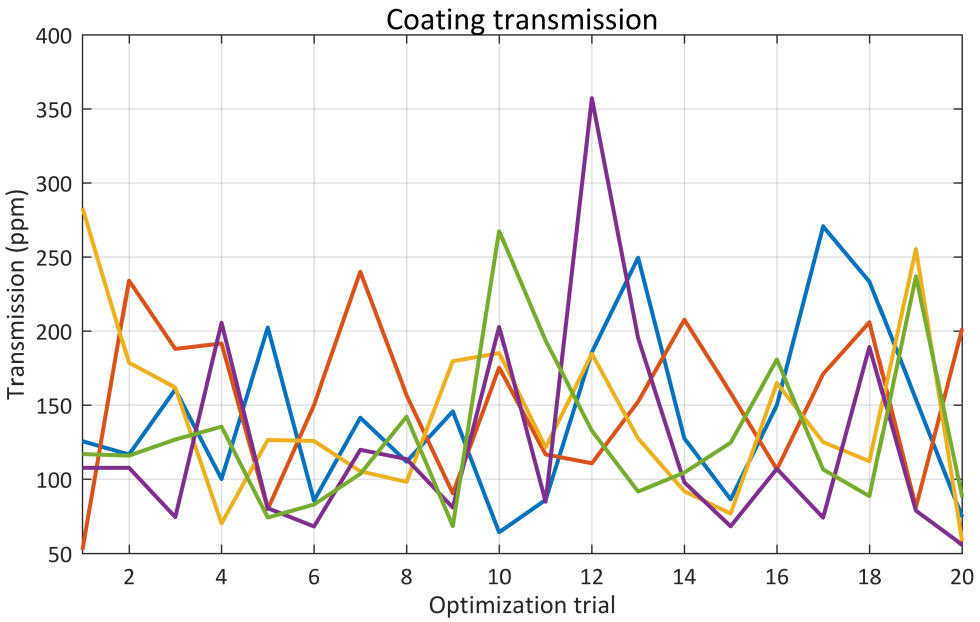

Figure 2.11: Transmission values for the coating structures found in the genetic algorithm optimization trials used for coating thermal noise optimization (figure 2.10). All coating structures have a higher transmission than the value of 50 ppm aimed for.

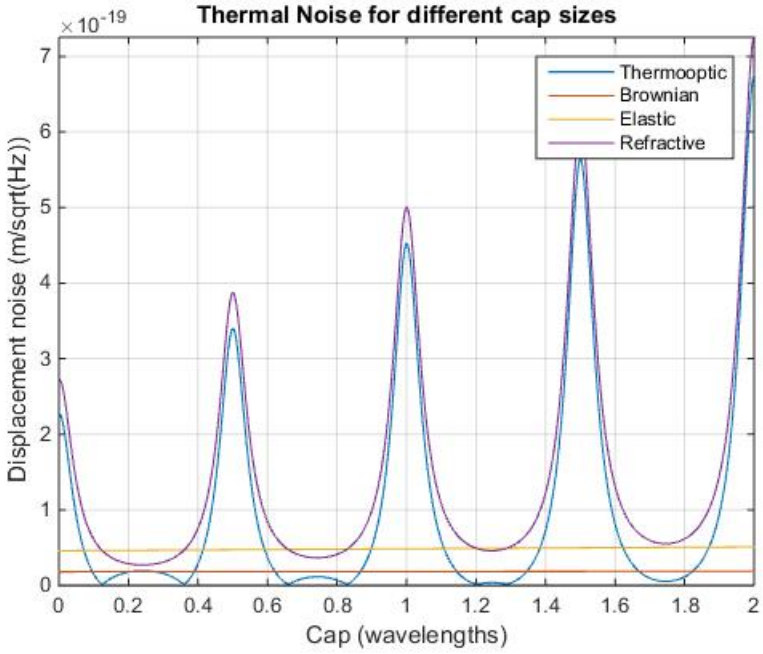

Figure 2.12: Coating thermal noise contributions for the ETM of the AEI 10 m prototype sub-SQL interferometer (transmission of 50 ppm at 62 layers), depending on the thickness of a cap layer. For thicknesses around $\frac{\lambda}{4}$ and $\frac{3\lambda}{4}$, coherent cancellation in thermooptic noise occurs, and Brownian thermal noise becomes the limiting contribution.

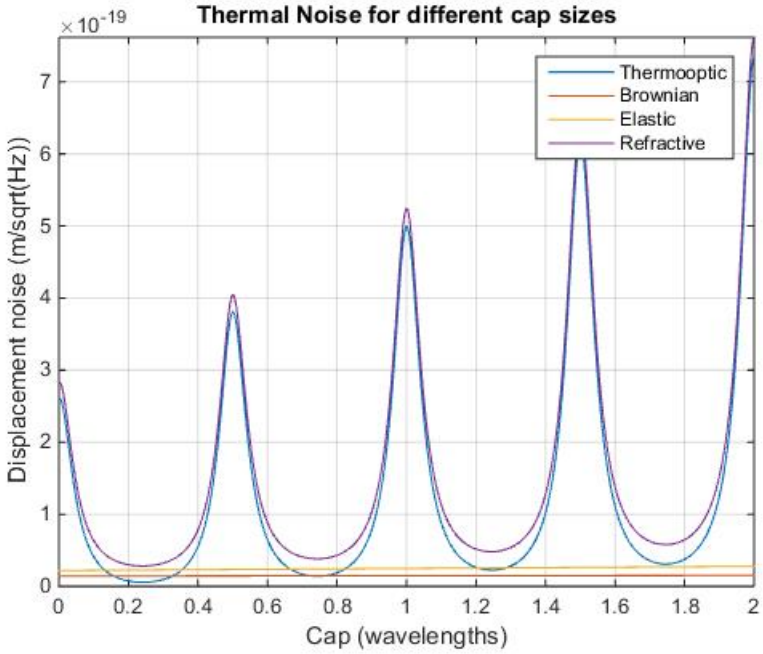

Figure 2.13: Coating thermal noise contributions for the ITM of the AEI 10 m prototype sub-SQL interferometer (transmission of 1000 ppm at 28 layers), depending on the thickness of a cap layer. For a thickness of $\frac{\lambda}{4}$, coherent cancellation in thermooptic noise occurs, and Brownian thermal noise becomes the limiting contribution.

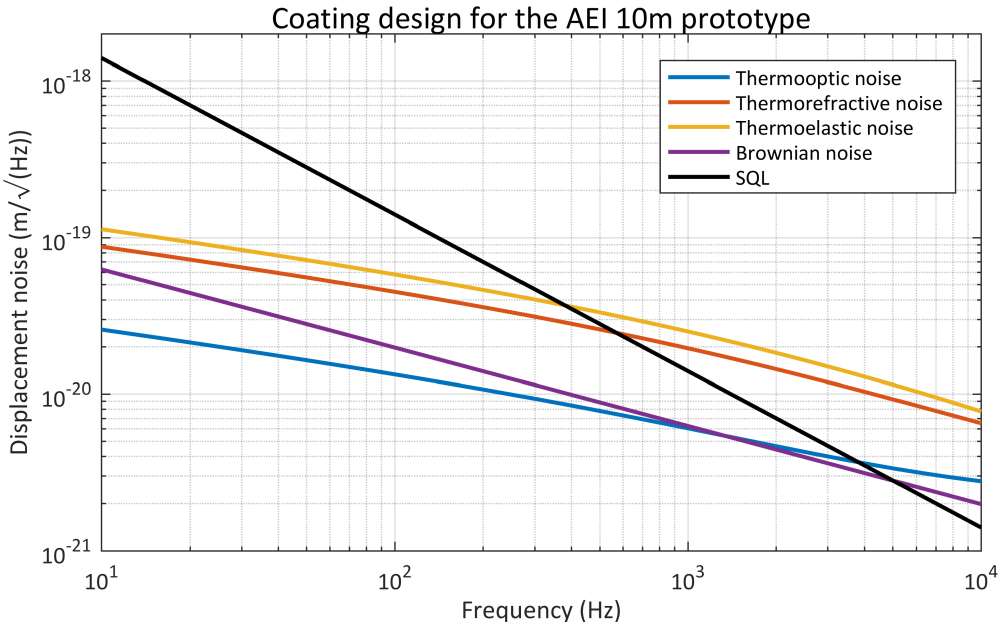

Figure 2.14: Contributions to coating thermal noise in the coating design of a single end test mass for the AEI 10 m prototype sub-SQL interferometer. Coherent cancellation reduces thermooptic noise to a level comparable to Brownian thermal noise, and gives a large margin to the SQL.

Brownian noise as the dominant noise source.

In the case of 1000 ppm, this tradeoff does not apply as the double well structure in the coating thermooptic noise vanishes for thinner coatings and a choice of 0.25λ is optimal. The code has been used to verify that these resulting coating stack designs show losses of less than 5 ppm. For the sub-SQL interferometer, the contribution from the ETM of the arm cavities is larger because of the thicker coating, and the final thermal noise, including thermo-optic compensation, can then be compared to the SQL, as shown in figure 2.14.

2.3.3 Final coating choices

After the coating design and optimization described above, another round of coating design was initiated and conducted by David Wu. The results were close to the ones presented here, being based on a number of quarterwave layers with a variable cap to reduce thermooptic noise. For the ITM, the result were 26 quarterwave layers plus a quarterwave cap. For the ETM, 66 quarterwave layers plus a $\frac{5}{4}\lambda$ cap resulted. These were subsequently purchased, but could not be bonded onto the substrates because during an unknown handling step the surfaces were scratched. These defects would prevent proper bonds from forming, leading to voids and bumps under the coating, thereby changing the surface properties, which have to meet stringent requirements in terms of flatness and roughness.

Until new substrates are available, the damaged substrates are IBS-coated with amorphous silica and titania-doped tantala coatings. For these, another optimization procedure was performed by David Wu, taking into account the higher loss of tantala. Reducing the total cumulative thickness of the tantala layers reduces the overall coating Brownian noise, while thermooptic noise is not limiting for these coating materials. This is achieved by deviating from the quarterwave structure, instead using nine doublets of 0.189λ tantala and 0.311λ silica with a bottom tantala layer of

0.174λ for the 8220 ppm ITM and nineteen doublets of 0.183λ tantala and 0.317λ silica with a bottom tantala layer of 0.165λ for the 16 ppm ETM. This optimized design improves the coating Brownian noise by approximately 5 %.

These optics have been delivered and are now being characterized in terms of surface roughness and scattering. Small sample optics, if available, can then be characterized by the TNI for their level of coating thermal noise.

CHAPTER 3

Thermal noise interferometer in the AEI 10 m prototype

It is no conincidence that the TNI is built inside the AEI 10 m prototype facility. The high sensitivity required to measure thermal noise can only be achieved in a suitable environment. Sufficient isolation against seismic and acoustic as well as a stabilized light source have to be provided.

The first section in this chapter compares the expected level of thermal noise with measurements done without the AEI 10 m prototype infrastructure, showing the level of suppression required. The second section then introduces the subsystems of the AEI 10 m prototype, discussing their function and performance relevant for the TNI.

3.1 Thermal noise interferometer noise requirements

The main future goal of the TNI is the measurement of coating Brownian thermal noise, especially in crystalline AlGaAs-coatings. This level, calculated for a nominal spot size of 86 µm (corresponding to a stable cavity with a length of 0.095 m), is compared with the sensitivity of the TNI in situations, where subsystems of the AEI 10 m prototype were not used. They all clearly show the need for these subsystems to perform as intended in order to properly measure coating thermal noise.

3.1.1 Seismic and acoustic

The devastating influence of seismic and acoustic on the TNI, although having its own seismic isolation, can be seen from its sensitivity while it was placed on an optical bench outside the vacuum system (shown in figure 3.1). This bench has no seismic isolation, and the laser locked to the cavity was unstabilized in frequency and power. Except for transparent curtains, no restrictions to acoustics and air-flow are present. Even conversations could be extracted from recorded spectra. A typical noise spectrum, together with the predicted thermal noise, is shown in figure 3.2.

This clearly shows the limitations in measuring thermal noise stemming from the seismic and acoustic disturbances. While seismic is mostly problematic at low frequencies, impeding lock acquisition, acoustic noise directly acts in the most sensitive frequency range of the TNI. This is shown in figure 3.3, displaying a spectrum measured while the TNI was sitting on the seismic isolation system, but in air.

Figure 3.1: The TNI sitting outside the vacuum chamber on the south detection bench. This table has no seismic isolation, and the tent only keeps dust away, but does not protect against air currents and acoustic.

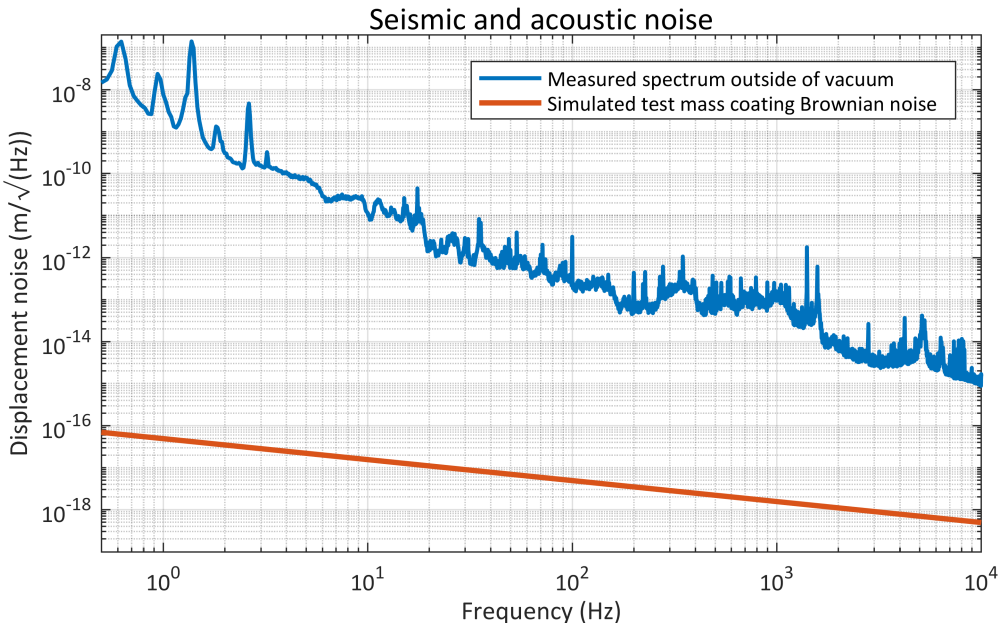

Figure 3.2: Spectrum of the TNI taken out of vacuum. The missing seismic isolation shows up at low frequencies as strongly excited suspension resonances. Frequencies above 10 Hz are dominated by acoustics and bury the expected coating thermal noise.

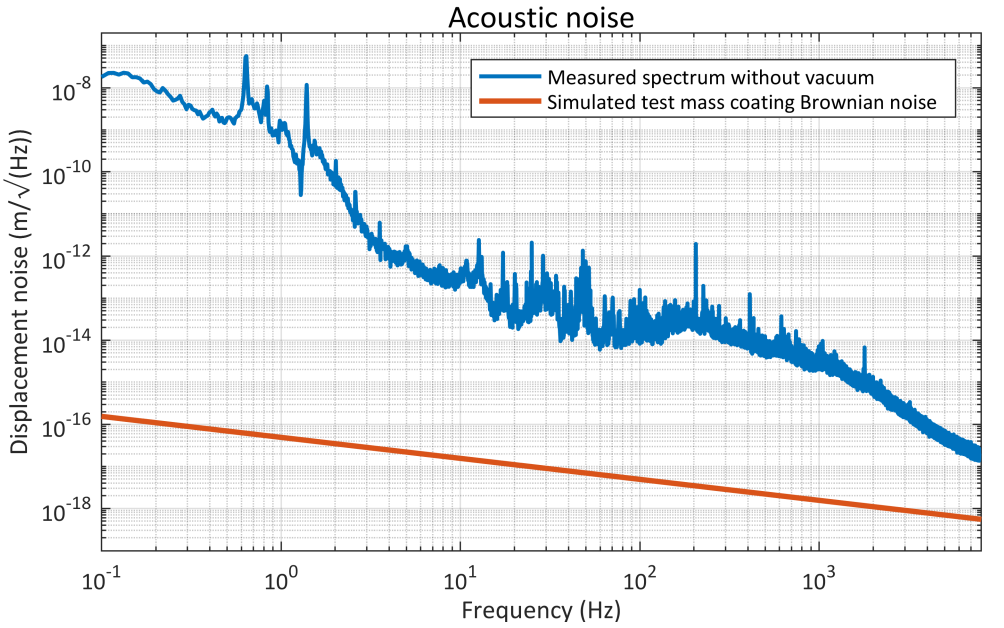

Figure 3.3: Spectrum of the TNI taken with seismic isolation. The acoustic disturbances prohibit the measurement of thermal noise.

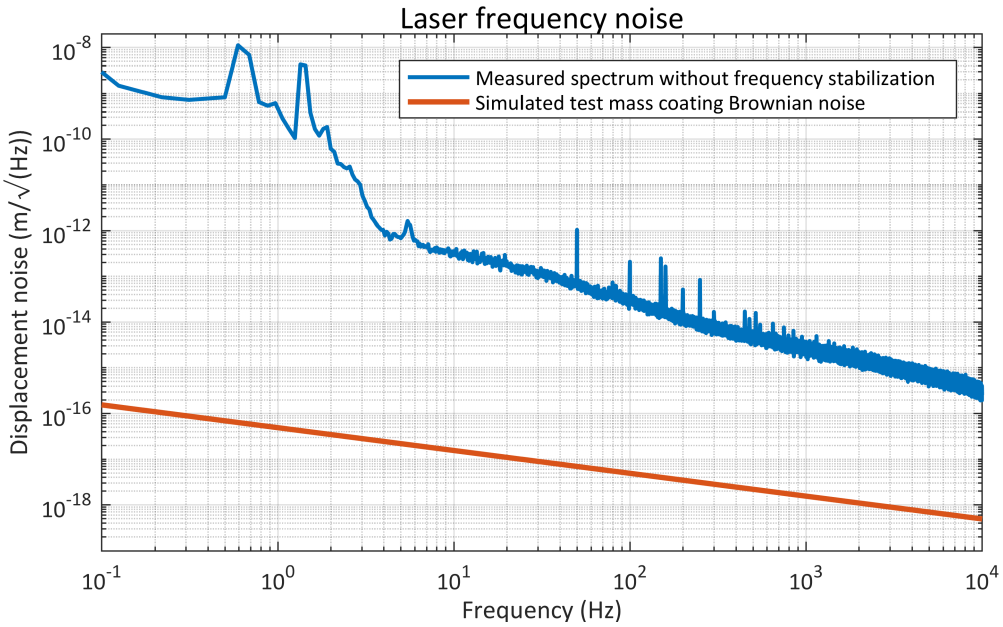

Figure 3.4: Spectrum of the TNI while the frequency reference cavity is turned off. The characteristic $\frac{1}{f}$-noise of the NPRO laser dominates the spectrum at frequencies above 5 Hz.

3.1.2 Laser frequency noise

The main laser, although having an intrinsic stability of $100\,\mathrm{Hz}/\sqrt{\mathrm{Hz}}$ at 100 Hz, falling with f^{-1} [Mep], is too noisy for the TNI. As can be seen in figure 3.4, several orders of magnitude of laser frequency noise suppression are required to meet the sensitivity requirements of the TNI.

3.1.3 Laser intensity noise

Laser intensity does not couple strongly into the TNI, but still shows a level too high to measure thermal noise when the intensity stabilization is not engaged, as can be seen in figure 3.5.

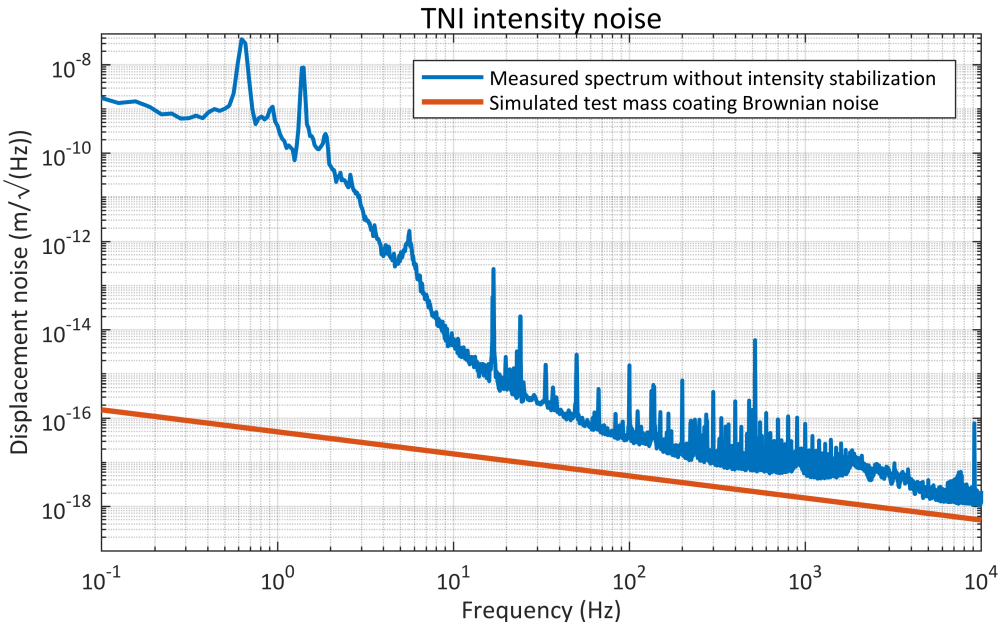

Figure 3.5: Spectrum of the TNI while the intensity stabilization is turned off. At frequencies above 10 Hz, intensity noise dominates the spectrum, masking mirror thermal noise.

3.2 AEI 10 m prototype facility

In order to reach the required sensitivity to measure coating thermal noise, the TNI is placed inside the AEI 10 m prototype facility. This facility consists of a 100 m^3 L-shaped vacuum chamber which houses seismic isolation and light stabilization systems to provide the environment needed to commission a Fabry-Perot-Michelson interferometer which will be operated at and below the standard quantum limit. To gain experience and test subsystems, a single 10 m Fabry-Perot cavity, called the single arm test (SAT), is operated before commissioning the Fabry-Perot-Michelson interferometer.

The scope of this infrastructure also encompasses being used for other high sensitivity experiments like the TNI. The individual subsystems, which are relevant to fulfill the noise requirements of the TNI as detailed in 3.1, and their performance are detailed in the following sections of this chapter.

3.2.1 Vacuum system

Optical precision experiments suffer from the presence of density fluctuations, translated into index of refraction fluctuations, while travelling through a gaseous medium such as air or water vapour. Even more limiting for the experiments in the AEI 10 m prototype, where cavities with suspended optics are employed, is the interaction of gas molecules with the mirrors transferring momentum and thereby shaking the optics.The resulting effect is called residual gas noise.

To reduce these effects to a level where measurements at the standard quantum limit of interferometry are possible, it is necessary to remove as much gas as possible. This is achieved by placing the experiment in a vacuum chamber, pumped down to the lowest pressure achievable on a time scale of one week. The ultimate pressure, typically 10^{-7}mbar, is limited by the presence of outgassing materials. The TNI would only require the pressure to be below 10^{-4}mbar to have the residual gas noise an order of magnitude below the expected level of coating Brownian noise, but other experiments are more susceptible to these disturbances, setting the requirements for the

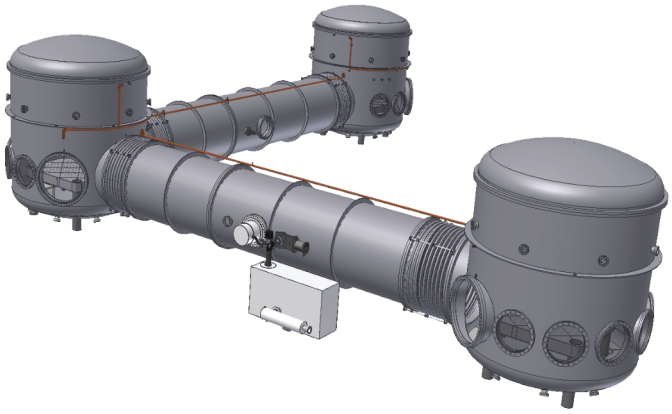

Figure 3.6: A CAD drawing showing the main vacuum system of the AEI 10 m prototype (Courtesy K. Mossavi). It consists of three steel tanks housing the optical tables, connected by large steel tubes, having arm lengths of 10 m.

AEI 10 m prototype vacuum chamber.

For the AEI 10 m prototype, the vacuum chamber consists of three tanks of heigth 3.9 m and diameter 3 m connected by tubes of diameter 1.69 m, arranged in an L-shape (shown in figure 3.6) to facilitate the setup of a typical Michelson interferometer. The total volume is close to 100 m^3, mainly driven by the need to have large seismically isolated optical tables accessible in each tank, and have the tubes large enough to send a variety of spacially separated laser beams simultaneously. Access to the vacuum chamber is provided by a door of diameter 1.5 m at each tank for humans, by a number of viewports for freely propagating laser beams, and by several flanges with feedthroughs for optical fibers and electrical cables.

The pressures reached are close to 1×10^{-6} mbar after 9 d of pumping, first using a large screw pump (Leybold SP630) to get to a pressure below 5×10^{-3} mbar, subsequently using two magnetically levitated turbo pumps (Leybold MAG W 2800) backed by scroll pumps (BOC Edwards XDS35i) to reach the final pressure of 1.9×10^{-7} mbar after 90 d(pressure shown in figure 3.7). Furthermore, the lids of the vacuum tanks and the doors as well as the tube connections are pumped differentially to reduce leakage through these large Viton-sealed openings. The final pressure is mostly limited by water vapour, outgassing from the steel of the vacuum chamber as well as installed components, where PEEK plays a major role in storing and releasing water.

3.2.2 Seismic isolation system

Having removed air as a noise source by placing the optical experiments inside a vacuum chamber, the next dominating noise source is seismic noise. Although the mirrors of the cavities are suspended and thereby are provided with proper isolation in the measurement band, low frequency seismic noise reduces the alignment ability as well as burdening the actuators for locking. Expecially the fundamental resonances of the mirror suspensions close to 1 Hz will be excited by ground motion and dominate the relative mirror motion.

The optical tables inside the vacuum chamber, where the experiments are placed upon, are therefore equipped with a seismic pre-isolation system. Furthermore, the relative motion between optical tables is controlled by the suspension platform interferometer (SPI) in the longitudinal degree of freedom and by optical levers in rotational degrees of freedom.

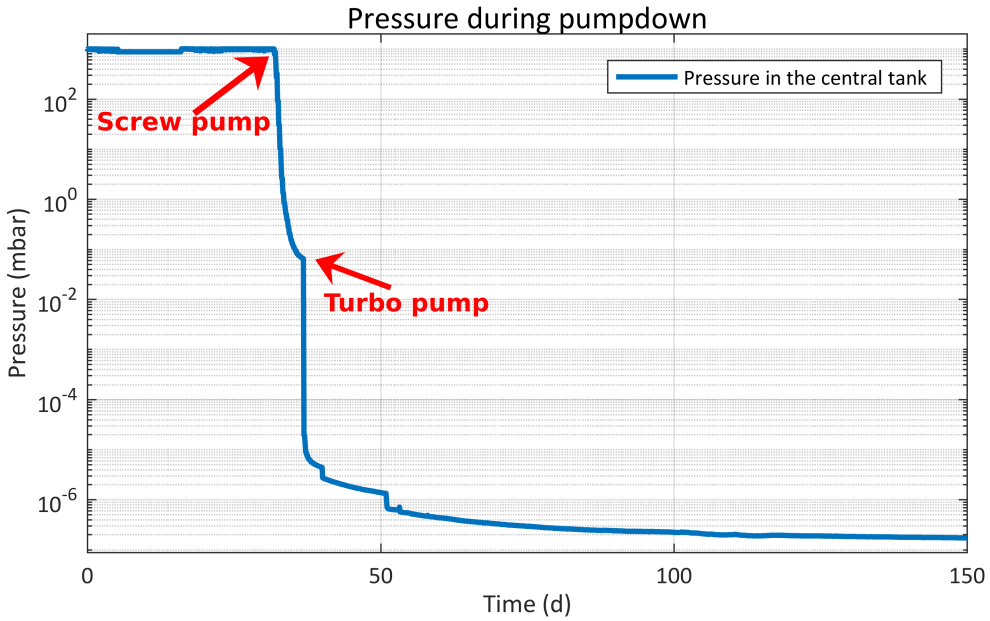

Figure 3.7: Trace of the pressure in the vacuum chamber over 90 d during a pumpdown. An exponential drop is visible, showing a change of rate when additional pumps are switched on. The first hours are pumped with a screw pump before switching to turbo pumps, accelerating the drop in pressure significantly. The other drops in the pressure are measurement artifacts.

3.2.2.1 SAS

Seismic attenuation, especially at low frequencies between 0.1 Hz and 10 Hz, where the fundamental resonances of the mirror suspensions are located, is provided by the seismic attentuation system AEI-SAS [Kir21]. The design is based on the HAM-SAS used in Advanced LIGO and includes three similar optical tables made of stainless steel and weighing approximately 1 t each (shown in figure 3.9 and a schematic drawing in figure 3.8).

The attenuation of seismic motion is passively achieved in vertical and horizontal degrees of freedom. For the horizontal degrees of freedom, inverted pendulum (IP) legs ((5) in figure 3.8) provide a resonance frequency of 100 mHz, acting as a pendulum and therefore providing isolation above the resonance. Low resonance frequencies are achieved by countering the restoring force of the bottom flexure keeping the IP-leg upright with the gravitationally induced tilting motion of the inverted pendulum. The closer the restoring and deflecting forces are, the lower the resulting resonance frequency. Tuning can then be achieved by changing the mass supported by the IP-legs. This also sets limits on the mass allowed to be placed on the optical tables. In total, each table is supported by three IP-legs, providing seismic isolation above the resonance frequency. The isolation reaches roughly 60 dB above 10 Hz, where the measurement band starts.

Isolation in the vertical degree of freedom is realized by geometric anti-spring filters (GAS-filters) ((6) in figure 3.8). The same basic principles as in the IP-legs are used to achieve low resonance frequencies, where here the destabilizing force comes from eight blades being compressed against each other. Resonance frequencies of 300 mHz are realized, providing seismic isolation above. As in the horizontal case, roughly 60 dB are achieved in the measurement band.

This basic passive isolation has to be complemented by passive and active means to damp fundamental and internal resonances and position the tables. Passive damping is achieved by Viton pads ((7) in figure 3.8) and resonant dampers ((12) in figure 3.8). The Viton pads are placed

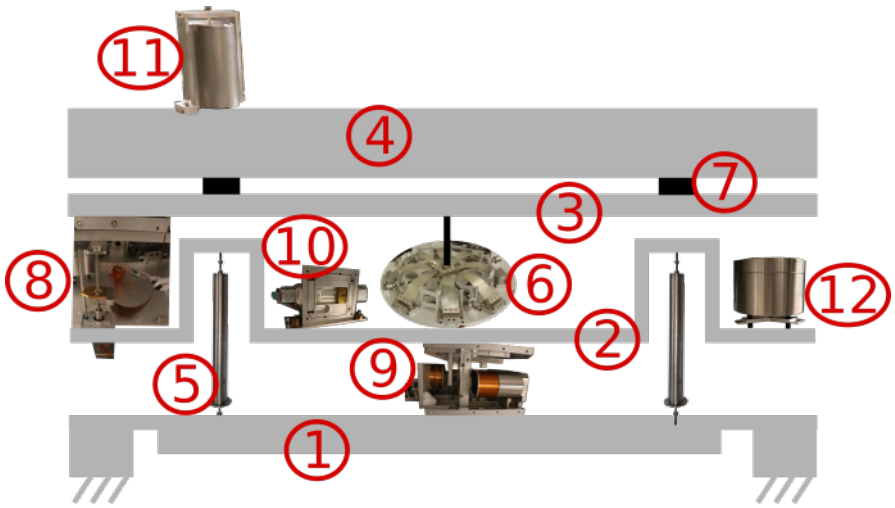

Figure 3.8: Schematic showing the main parts of the AEI-SAS. All the components are discussed in more detail in the text. The uppermost part (4) is the optical table, supporting all experiments, and consists of two large plates welded together with stiffening structures inbetween. This structure sits on the Viton stage (3), separated by Viton pads (7), which introduce additional damping. This stage is supported by the three GAS-filters (6), which sit on the spring box (2). The spring box is held up by three inverted pendulum legs (5), sitting on the base plate (1). The base plate is directly connected to the ground. Sensors (geophones (11), accelerometers (10) and LVDTs (9)) and actuators (LVDTs (9) and motorized springs (8)) are located on several stages, providing damping and control in the horizontal and vertical directions. Additional damping of structural resonances is done by resonant dampers (12).

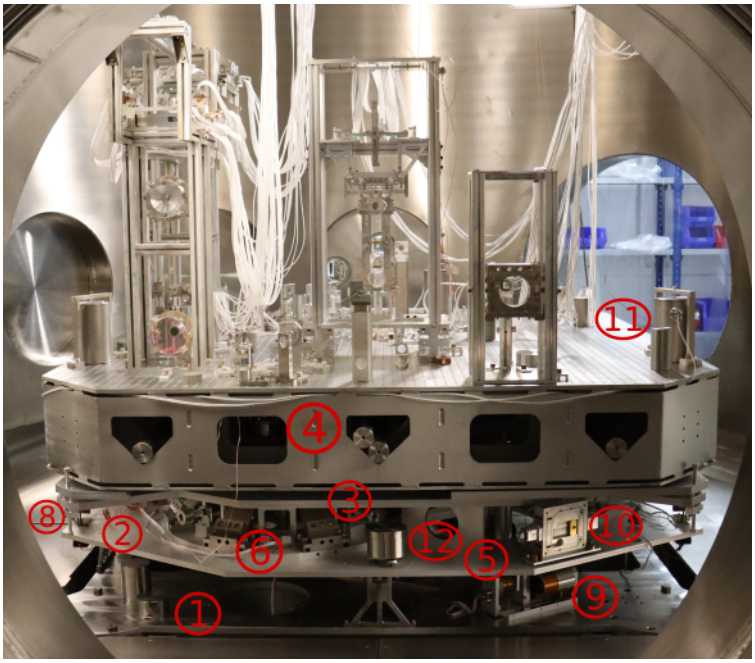

Figure 3.9: AEI-SAS located inside the vacuum chamber of the AEI 10 m prototype. The upper part shows the optical table top, welded to the spring box. Below, the base plate is visible, holding the GAS-filters. Components mentioned in figure 3.8 are marked with their corresponding numbers.

between the spring box sitting on the GAS filters and the optical table, and they provide viscous damping above 10 Hz. Resonant dampers are placed at locations of anti-nodes of internal spring box ((2) in figure 3.8) resonances and are tuned such that their resonance frequency agrees with the mode to be damped. Energy is then transferred from the mode to the resonant damper, which has Viton structures to introduce viscous damping, dissipating the energy to heat. This reduces the amplitude of internal resonances between 30 Hz and 100 Hz, directly in the measurement band of the TNI.

Another measure to reduce the effect of internal resonances is to push the resonance frequency up out of the most critical frequency range. Glue-bolting and stiffening structures were used in the west table to more rigidly connect the two plates making up the spring box, increasing stiffness and thereby pushing resonance frequencies up above 50 Hz. The south table, on which the TNI is located, has not been equipped with these modifications.

Active control utilizes four different kinds of sensors and two different sets of actuators on each table. The sensors are L4-C geophones ((11) in figure 3.8), LVDTs ((9) in figure 3.8), an STS2 and accelerometers ((10) in figure 3.8). Actuators include voice-coil actuators colocated with the LVDTs and motorized springs ((8) in figure 3.8). The Streckeisen STS-2 is a commercial seismometer located on the ground close to the central tank, measuring the ambient seismic motion in a frequency range between 0.1 Hz and 100 Hz.

Linear variable differential transformers (LVDTs) are used as relative position sensors, showing table position and motion relative to ground. The LVDTs consist of an excitation coil and two sensing coils, generating a position-dependent signal through oscillating magnetic fields generated in the excitation coil inducing currents in the sensing coils. Co-located is a voice-coil actuator, which is used for table positioning as well as in feedback-loops damping fundamental table resonances when robust performance is required. LVDT signals and voice-coil actuators are in these cases used from DC to between 0.1 Hz and 0.8 Hz, depending on the degree of freedom.

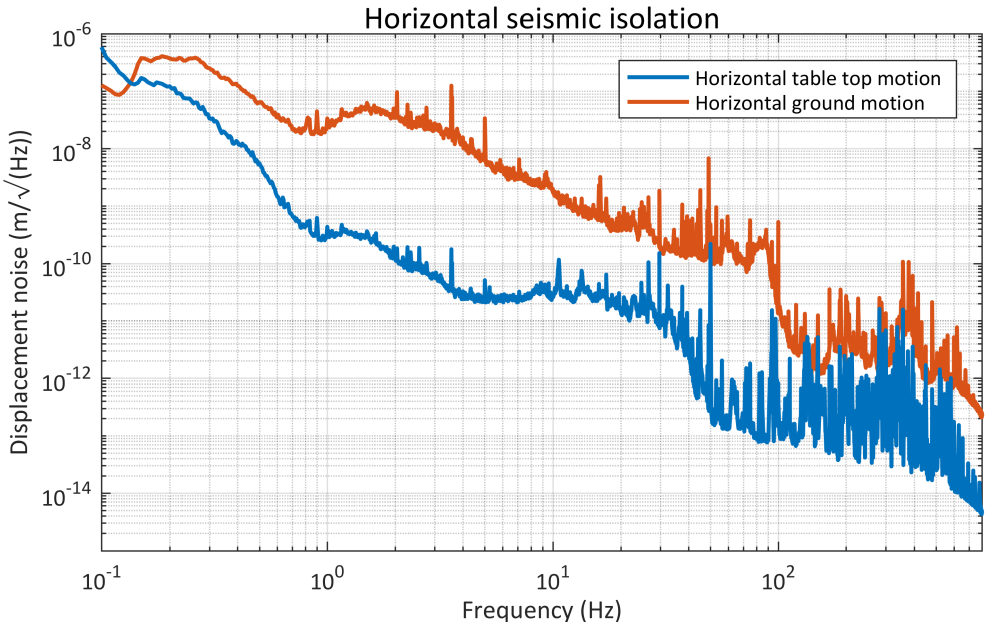

Figure 3.10: Comparison of a horizontal seismic spectrum with the reduced motion of the table-top of the AEI-SAS. A significant difference is visible at frequencies above 1 Hz.

The L4-C geophones are damped masses suspended as one-dimensional harmonic oscillators. Motion of the damped test mass relative to the frame is read out by a magnet-coil pair through the induced voltage. Every table, except the south table, is equipped with three horizontal geophones and three vertical geophones, working as inertial sensors for horizontal and vertical degrees of freedom. Their sensitivity allows the extraction of useful signals from 0.1 Hz on.

Further horizontal inertial sensors are sets of three custom-built accelerometers. These also have a test mass suspended, although by a combination of a pendulum and an inverted pendulum, called Watt's linkage. This provides a low resonance frequency, and the motion is read out by small LVDTs, which also provide feedback to keep the test mass in position. Their inertial signals are used from 0.1 Hz on, but their unfortunate positioning in the soft spring box makes the use of the L4-Cs on the stiffer optical table favourable. Rough positioning of the tables, especially after pump-downs and during temperature changes, is achieved by motorized springs. Stepper motors push a soft spring in the vertical or horizontal direction, moving the table without creating strong seismic shortcuts.

In total, passive and active systems provide seismic isolation of 40 dB at 1 Hz and above for the horizontal degrees of freedom (shown in figure 3.10) and 50 dB above 1 Hz in the vertical direction (shown in figure 3.11). The influence of the residual seismic table top motion on the TNI is discussed in section 6.2.

3.2.2.2 SPI

The AEI 10 m prototype Fabry-Perot Michelson as well as the frequency reference cavity have their cavity mirrors distributed across several tables. In order to reduce the inter-table motion and thereby offload actuation from the cavity feedback loops, an additional interferometer is used. This is the suspension platform interferometer (SPI), which measures the longitudinal motion of the south and west table relative to the central table [Kö18]. The measured motion is then transformed into an error signal which is fed back to table actuators so that the west table and

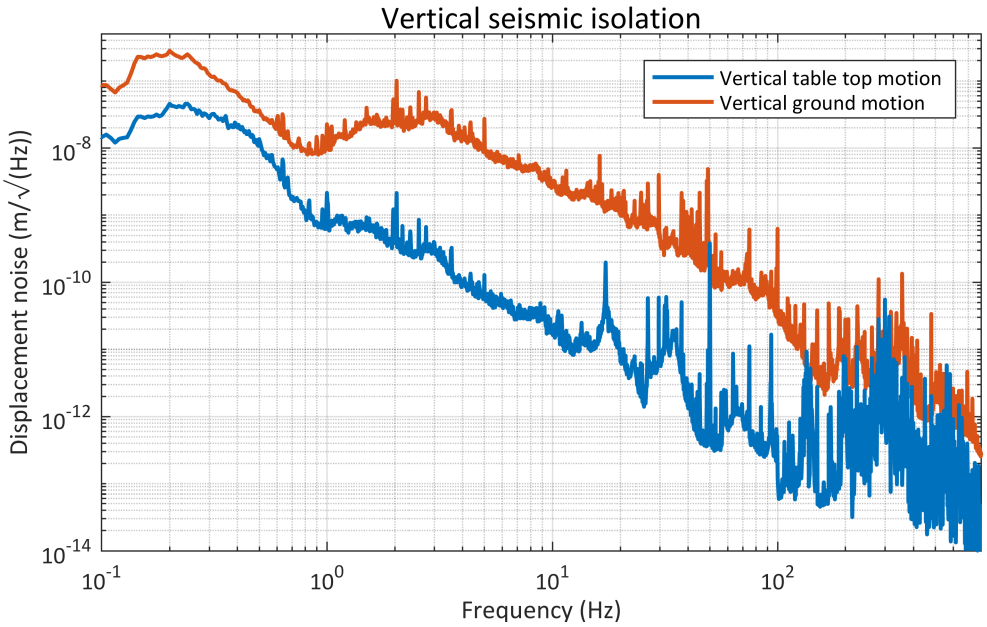

Figure 3.11: Comparison of a vertical seismic spectrum with the reduced motion of the table-top of the AEI-SAS. A significant difference is visible above 1 Hz

south table follow the motion of the central table. This creates a virtual rigid L-shaped platform for the optical experiments.

The basis for the SPI is a heterodyne Mach-Zehnder interferometer with unequal arm lengths. The light is supplied by an InnoLight P2000E NPRO running at 1064 nm and being stabilized externally to an iodine cell. Most optics of the two Mach-Zehnder interferometers including the short arms are monolithically bonded onto a Clearceram baseplate, which is placed in the center of the central table. The mirrors of the long arms are distributed onto the south and west table.

This setup allows the relative table motion to be suppressed to a level of below $100\,\mathrm{pm}/\sqrt{\mathrm{Hz}}$ between 10 mHz and 4 Hz. This suppression not only helps the reference cavity in stabilizing the laser frequency, but also reduces the potential for beam jitter in the input path of the TNI, which is also distributed over the central table and the south table.

3.2.2.3 Optical levers

Optical levers are complementing the SPI by measuring the relative rotational motion of the tables [Kö18]. This is especially important for the cavities having their mirrors distributed on different tables, but it also influences the input path beam jitter of the TNI. The optical levers use light picked off from the SPI for central table attitude measurements and fibre coupled light for south table attitude measurements. The light is then sent to the opposite table and detected using a quadrant photo diode.

This gives signals indicating pitch and yaw motion of the central and south table amplified by the optical lever path length. The achieved performance suppresses rotational motion between 10 mHz and 10 Hz in pitch and yaw, reaching $10\,\mathrm{nrad}/\sqrt{\mathrm{Hz}}$ at 10 mHz and down to $30\,\mathrm{prad}/\sqrt{\mathrm{Hz}}$ at 1 Hz.

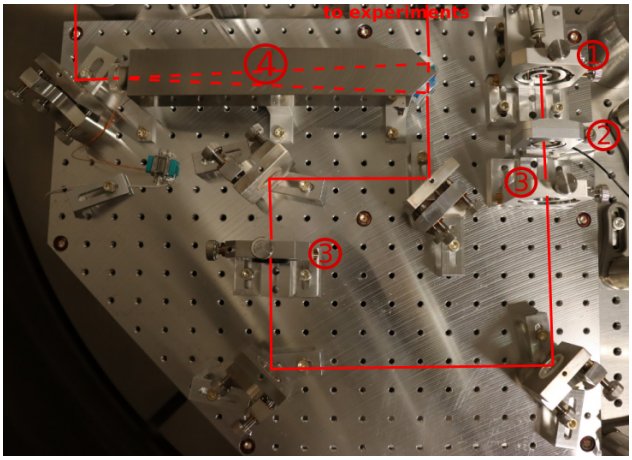

Figure 3.12: The PMC (4), a triangular fixed-spacer cavity, sitting on a dedicated breadboard. Lenses (3) and steering mirrors shape the beam coming from the fiber coupler (1) at the top right. A wave-plate in a piezo rotation mount (2) adjusts the polarization.

3.2.3 Laser, PCF and PMC

In the AEI 10 m prototype, the laser is a master-oscillator power amplifier system running at 1064 nm as used in enhanced LIGO, using an InnoLight Mephisto NPRO having an output power of 2 W as the master oscillator and four diode pumped Yttrium-Vanadat rod amplifiers. The total output power is 35 W [Opp17].

The light of the laser is sent into vacuum through a photonic crystal fibre. As the AEI 10 m prototype Fabry-Perot-Michelson interferometer needs a power of 5 W to reach the standard quantum limit, and the other subsystems need a total of ∼1 W, the fibre has been chosen to couple a total of 8 W into vacuum. This places stringent requirements on the power density handling capacity of the fiber, and for common single-mode fibers with a mode field diameter of ∼5 µm are not an option. Larger mode field diameters are realised by photonic crystal fibres (PCF) consisting of a hexagonal array of air holes inside the silica fibre center. This effectively creates a band-gap like behaviour as observed for electrons in crystalline materials, thereby making the effective guiding core diameter as big as 12.6 µm. Thus the PCF of type LMA-PM-15 by NKT Photonics used in the AEI 10 m prototype keeps the power density inside the fibre low enough to not cause severe distortion or damage.

Furthermore, the geometry restricts guidance of higher order modes, making the PCF effectively a single-mode fiber. This mode filter effect already reduces the residual higher order mode content coming from the laser, but further mode cleaning and polarization definition is still necessary, which is achieved by the pre-mode cleaner (PMC). The PMC is a short triangular fixed spacer cavity (shown in figure 3.12) of round trip length 53 cm and a Finesse of 937 [Ali13]. One mirror is glued onto a PZT, allowing the PMC to be locked to the incoming laser.

The feed back loop has a bandwidth of 3.2 kHz, and the error signal sent to the PZT high voltage actuator is calibrated to µm reference cavity length to serve as a reference for comparisons between different cavities in the AEI 10 m prototype facility. Aligned to only be resonant for the TEM00-mode, the higher order mode content after the PMC is shown in figure 3.13. This corresponds to a suppression of more than 40 dB for higher order modes.

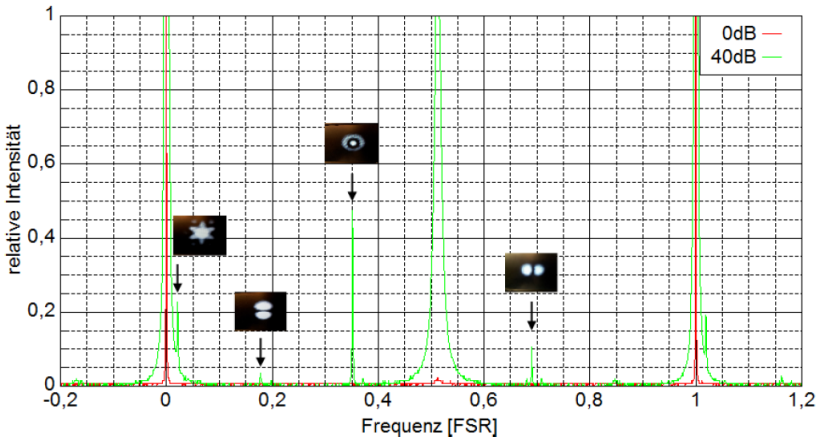

Figure 3.13: A modescan of the PMC, showing the higher-order mode content in comparison to the fundamental TEM00-mode, taken from [Ali13]

Figure 3.14: The two suspension cages of the reference cavity. On the left, the end mirror of the triangular cavity, located on the south table, is visible. On the right, input and output mirrors, making up the short arm of the cavity, are visible on the central table. The separation is 10 m.

3.2.4 Frequency reference cavity

Every laser shows frequency fluctuations which are characteristic of the type of laser. In the AEI 10 m prototype laser the frequency noise at the level of the NPRO seed laser is quoted to be $100\,\mathrm{Hz}/\sqrt{\mathrm{Hz}}$ at 100 Hz, falling with $\frac{1}{f}$ [Mep]. The Fabry-Perot-Michelson interferometer requires laser frequency noise to be seven orders of magnitude lower, so active frequency stabilization is required. The frequency reference cavity was designed for this purpose, built as a triangular cavity consisting of three triple-suspended monolithic optics distributed over two optical tables at a distance of 10 m (shown in figure 3.14). This gives a round trip length of 21.2 m [Han18]. The cavity has a Finesse of 3580, and is being operated at an input power of 120 mW.

A Pound-Drever-Hall scheme in reflection is used to lock the laser to the frequency reference cavity. The TTFSS, a frequency stabilization servo adapted from LIGO is used to feed back to a temperature controlling Peltier, a PZT pushing on the NPRO crystal and an EOM. The Peltier gives the low frequency control, the PZT works in the audio-band and the EOM is used for fast feedback. The locking loop transfer function is shown in figure 3.15, having a unity gain frequency of just above 100 MHz and an expected low frequency gain of 140 dB. The expected performance results in a frequency noise spectrum as shown in figure 3.16.

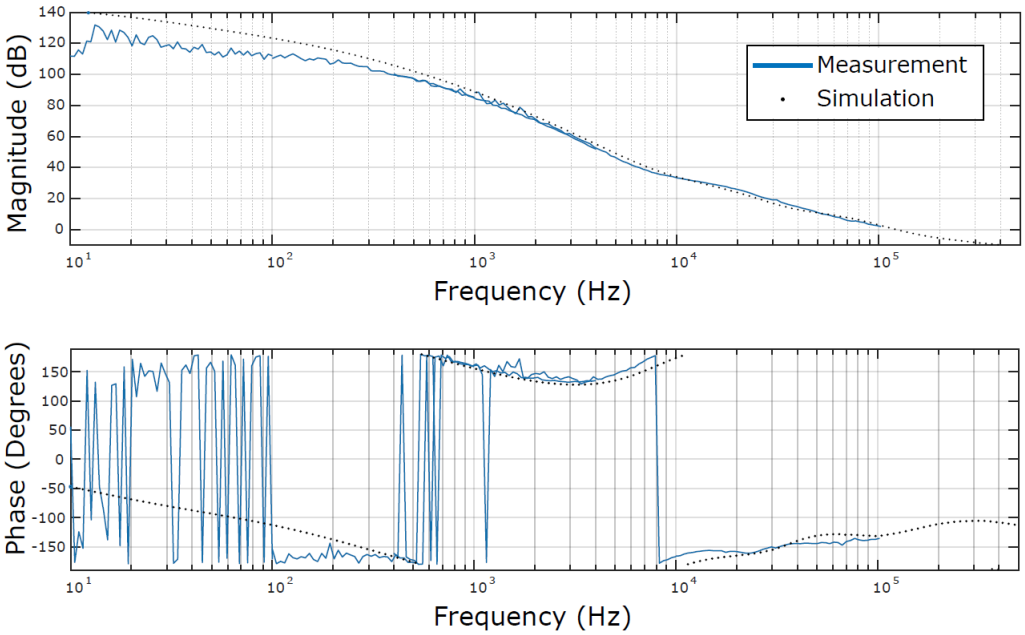

Figure 3.15: Transfer function of the reference cavity locking loop, made up of simulations and measurements, taken from [Han18]. Shown are the contributions from the temperature at low frequencies, the PZT at intermediate frequencies and the EOM at high frequencies up to the unity gain frequency just above 100 MHz.

3.2.5 Intensity stabilization servo

In an experiment like the AEI 10 m prototype Fabry-Perot-Michelson interferometer, where the standard quantum limit of interferometry is to be reached, classical radiation pressure noise has to be below quantum radiation pressure noise, which makes up the low frequency side of the standard quantum limit. Although not as susceptible to classical radiation pressure noise due to the 850 g mirrors, the TNI also benefits from the intensity stabilization.

Classical radiation pressure noise is created by classical laser power fluctuations, which therefore have to be suppressed. This is achieved via a conservative scheme originally used in LIGO consisting of four photodiodes. They are arranged in an array to sense as much power as possible (as show in figure 3.17), which is necessary to reduce the shot noise limit for sensing the laser power fluctuations [Jun16].

More advanced approaches to laser power stabilization are in development, see for example [Ner21]. In the ISS of the AEI 10 m prototype, a total of 140 mW are sensed. The error signal created is then fed back to an AOM inside the main laser, thereby stabilizing the power to a level of $2 \times 10^{-9}\, 1/\sqrt{\text{Hz}}$. A measurement of the residual intensity noise with and without suppression by the ISS is shown in figure 3.18.

The difference in TNI spectra with and without the ISS engaged is shown in section 6.8, showing excess power noise at high frequencies without the ISS. This shows the importance of the ISS for reaching the design sensitivity of the TNI.

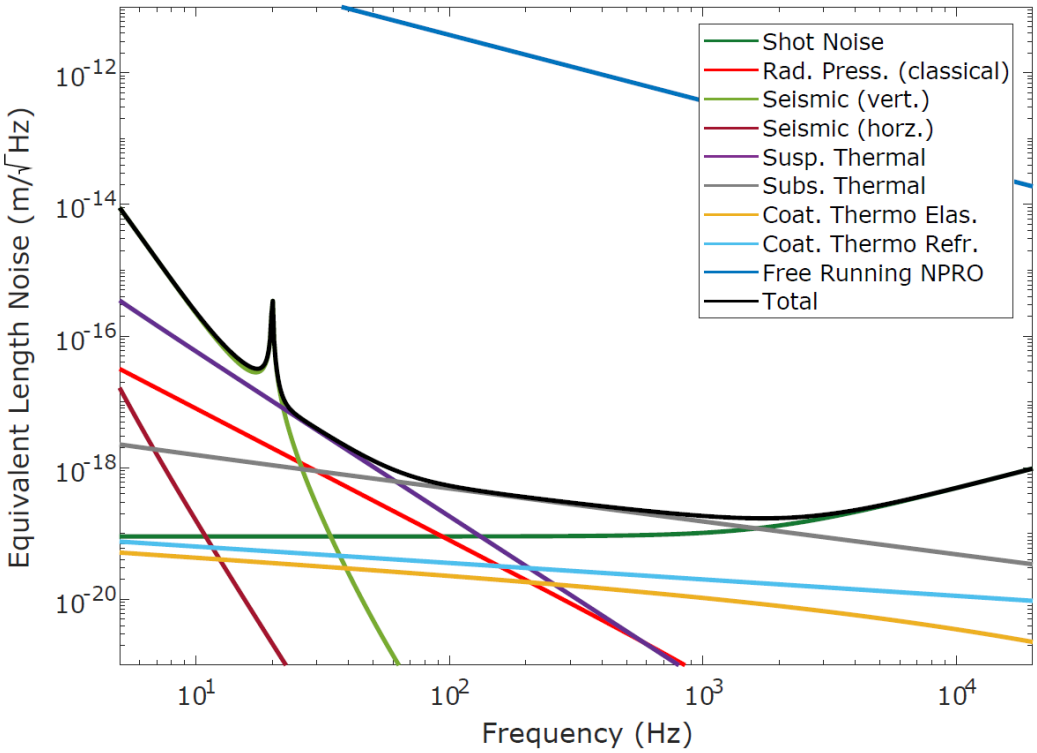

Figure 3.16: A spectrum of the expected performance of the reference cavity, taken from [Han18]. This ideally corresponds to the noise budget of the reference cavity, as the laser is tightly locked to the cavity. Higher frequency noise is expected when the loop gain cannot be chosen sufficiently high to reduce the frequency noise to the reference cavity sensitivity level.

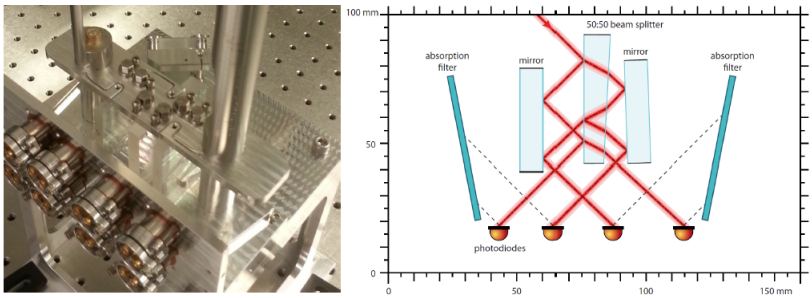

Figure 3.17: On the left, a picture of the inside of the ISS shows the beam splitters and the eight photodiodes. The right shows a schematic, detailing the splitting of the incoming light onto the four photodiodes. [Jun16]

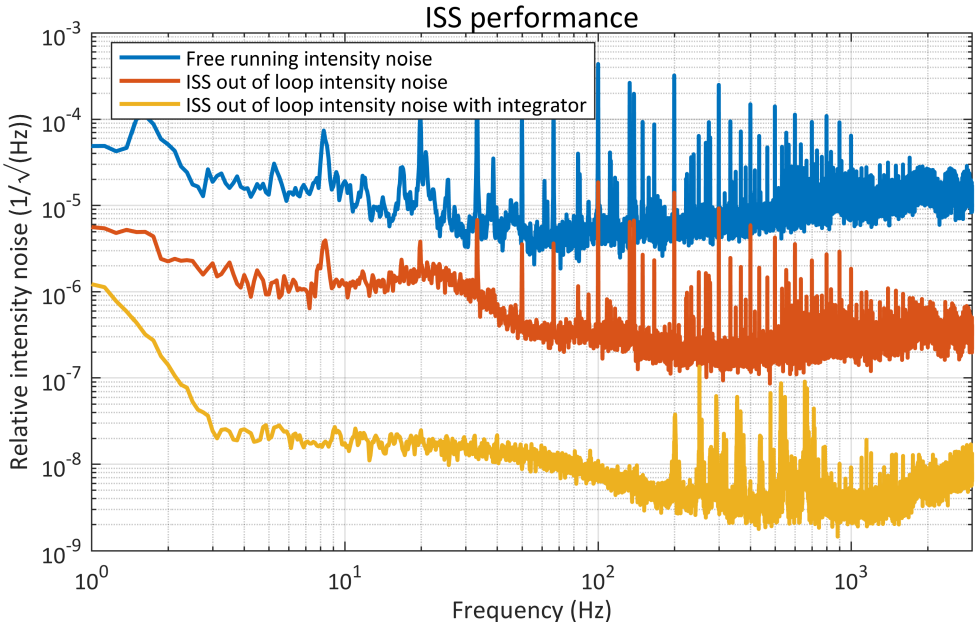

Figure 3.18: Spectra showing the reduction of power noise by employing the ISS. More than three orders of magnitude of reduction are observed between 100 mHz and 1 kHz.

CHAPTER 4

Thermal Noise Interferometer and its commissioning

The thermal noise interferometer (TNI) is a hemispherical Fabry-Perot cavity consisting of mirrors individually suspended by a triple suspension, limited by thermal noise in the audio band. In this chapter, this simple description will be expanded to include all the details which are necessary to understand and characterize the performance of the TNI. Furthermore, some of the steps taken towards measurements at the design sensitivity are shown, highlighting improvements made along the way.

The first section 4.1 details the optical design, which includes an analysis of the cavity length dependence of the spot size as well as a discussion of mirror reflectivity choices. Especially the choice of core optics and improvements concerning optical loss are important steps towards a working TNI.

In the section 4.2, the optical path towards the TNI and its components are described, especially focusing on the mode matching telescope, which ensures high incoupling efficiency into the interferometer.

The focus of section 4.3 is the suspension design, which provides the seismic isolation necessary to measure thermal noise. Proper placement of resonances and coupling of degrees of freedom to provide controllability are important aspects which are evaluated using a MATLAB-based state space model. This is compared to the measured properties of the suspensions, including improvements in the setup process.

The damping of the suspensions, necessary for lock acquisition, is detailed in the fourth section 4.4. This includes a description of the sensors and actuators used in feedback control loops used for damping. A characterization of the damping loops themselves follows.

The section 4.5 goes into detail about the mechanical setup of the TNI, which consists of an aluminum cage holding the suspensions as well as extra structures for support and adjustment of the suspensions and their actuators. Several new features have been introduced into the preexisting raw setup.

In section 4.6, actuators which are used for locking the TNI are described first, which includes coil-magnet pairs at the intermediate mass and test mass. The focus lies on a trade off between actuation strength and noise performance. The photodiode as the most important piece of electronics in terms of noise and sensitivity is described in the second part of this section. The final part then shows, how these actuators are used in a feedback loop used for locking the TNI. Blending of two sets of actuators and offloading to less noise prone actuators were studied as well.

All other electronics including the digital data acquisition system are briefly discussed in Appendix B.

Showing the improvements over time in sensitivity is section 4.7, starting from more than four orders of magnitude above coating thermal noise to finally reaching the thermal noise limit.

4.1 Optical design

The optical design is the most crucial aspect of the TNI, as the goal is to interferometrically measure the displacement of high reflectivity coatings due to thermal noise inside the coating materials. Coating thermal noise scales with the inverse of the spot size on the mirror under investigation (when looking at the amplitude spectral density), so one aspect is to make the spot size on the mirror under investigation small enough to enhance thermal noise above all other noise sources.

This is done by choosing an appropriate cavity geometry defined by the length of the cavity and the radii of curvature of the mirrors, as explained in the first subsection. Amplifying the sensed surface fluctuations above shot noise in the readout requires the choice of a sufficiently high Finesse through appropriate mirror reflectivities, as shown in the second subsection.

4.1.1 Cavity geometry

The cavity geometry is determined by three factors: the cavity length L, and the radii of curvature of the input mirror R_1 and the output mirror R_2. Their choice defines the type of cavity (for example concentric, confocal or hemispherical) as well as the stability, defined as [Mes17]

$$g = g_1 \cdot g_2 = (1 - \frac{L}{R_1})(1 - \frac{L}{R_2}) , \tag{4.1}$$

where g is the cavity g-factor, and g_1 and g_2 are the g-factors for input and output mirror respectively. This factor has to be between 0 and 1 for the cavity to be stable, which can be interpreted as the intracavity beam not growing in size after one round trip, until it is too large to be reflected from the mirrors and therefore lost from the cavity.

For a fixed choice of mirrors, a change in cavity length will change the stability of the cavity. This is important for the TNI, where the choice of the parameters is $R_1 = 0.1\,\mathrm{m}$, $R_2 = \infty$ and a default length of $L = 0.095\,\mathrm{m}$, which is variable between 0.08 m and 0.0999 m. This corresponds to a hemispherical cavity, shown in figure 4.1, where the waist w_2 of the fundamental Gaussian beam inside the cavity is located on the output mirror. The input mirror has a larger spot size w_1, determined by the requirement that the fundamental gaussian mode resonant in the cavity has a curvature of radius R_1 on the surface of the input mirror. The stability is 0.05 in the nominal configuration at 0.095 m with a range of 0.25 for 0.08 m to 0.001 for 0.0999 m. The closer to instability, the smaller the spot size on the flat mirror, leading to a higher thermal noise contribution.

The size of the waist w_2 can be calculated according to the formula [Mes17]

$$w_2(l) = \sqrt{\frac{L \cdot \lambda \cdot \sqrt{\frac{(1-\frac{l}{R_1})}{\frac{l}{R_1}}}}{\pi}} , \tag{4.2}$$

with the wavelength $\lambda = 1064\,\mathrm{nm}$, the radius of curvature of the curved mirror R_1 =0.1 m and the cavity length l. Through the spot size dependence of thermal noise, this explains an increased sensitivity to coating thermal noise of the flat output mirror and a reduced sensitivity to thermal noise contributions from the curved input mirror. The flat mirror thus becomes the mirror under investigation in the TNI, dominating the noise of the TNI. For the parameters given above, the spot size on the flat mirror is 86 µm and the spotsize on the curved mirror is 384 µm, leading to a factor of ≈ 4.5 higher thermal noise contribution from the flat mirror. Thus it is only necessary to produce different flat mirrors with various coatings for investigation of their thermal noise, and the work of exchanging mirrors for measurements is cut in half. Another aspect is a reduction in cost for test mirrors, as only one mirror is needed, and curved coated mirrors are significantly

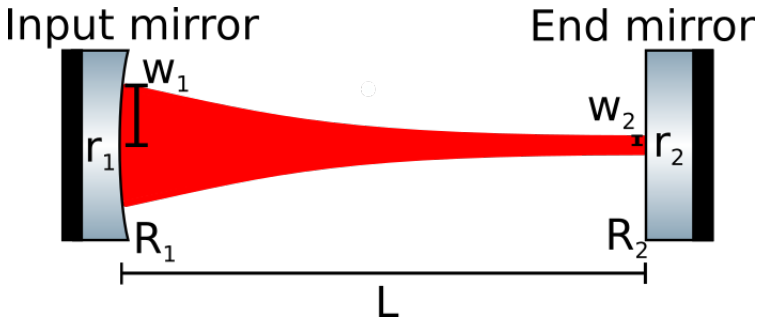

Figure 4.1: A schematic drawing of the hemispherical cavity used in the TNI. It consists of a flat mirror with reflectivity r_2 and a curved mirror with reflectivity r_1 and radius of curvature R =0.1 m, where the radius of curvature corresponds to the mirror separation L. The waist of the fundamental cavity eigenmode w_2 is located on the flat mirror. On the curved mirror, the spot size is w_1.

more expensive than flat mirrors.

A problem can arise, when the flat mirror under investigations has a coating that has significantly lower mechanical losses compared to the input mirror coating. This can be the case for an amorphous coating on the input mirror and a crystalline AlGaAs-coating on the flat test mirror. Then the ratio of the spot sizes has to be adjusted by decrasing the spot size on the flat mirror and increasing the spot size on the curved mirror. This can be achieved by lengthening the cavity closer to instability at 10 cm, reaching spot size ratios greater than 10 at less than 1 mm from instability, as shown in figure 4.2.

For the suspended cavity, the spot size on the flat mirror has been inferred by measuring beam cross sections at different locations along the transmitted beam path, using a beam profiling camera. These measurements have been fitted to the propagation of a Gaussian beam, giving a waist size of 85 µm. The error of this measurement was estimated by applying the fitting procedure to 10000 sets of synthetic data generated including normally distributed errors of 10 % for beam profiling measurements and 0.5 cm for measurement positions. The resulting 1σ-error is 3 µm.

The fact that the TNI is relatively close to the stability limit leads to an increased sensitivity of the spot size on the flat mirror to the cavity length. The dependence of the spot size on the cavity length is shown in figure 4.3 and zoomed in in figure 4.4. The corresponding slope, given as change of spot size per length change depending on the cavity length is shown in figure 4.5. Taking measurements at different spot sizes in a range from 120 µm to 20 µm is then possible, making it feasible to characterize the spot size dependence of coating thermal noise.

4.1.2 Mirror reflectivities and Finesse

The sensitivity, with which the cavity length and thereby thermal fluctuations of the mirror surface can be read out, depends on the amount of light interacting with the cavity mirrors. Two approaches can be chosen to increase the signal strength.

One approach is to use more input light power, but in most cases having a higher Finesse, which is proportional to the power amplification inside the cavity, is the approach taken. This is because in most cases, the input power is limited by the available power, the power handling capabilities of the photodetector used and concerns about stray light and thermal effects from the high power in the input path. The Finesse F is calculated through [Mes17]

$$F = \frac{\pi \cdot \sqrt{\sqrt{r_1 r_2}}}{1 - \sqrt{r_1 r_2}}\,, \tag{4.3}$$

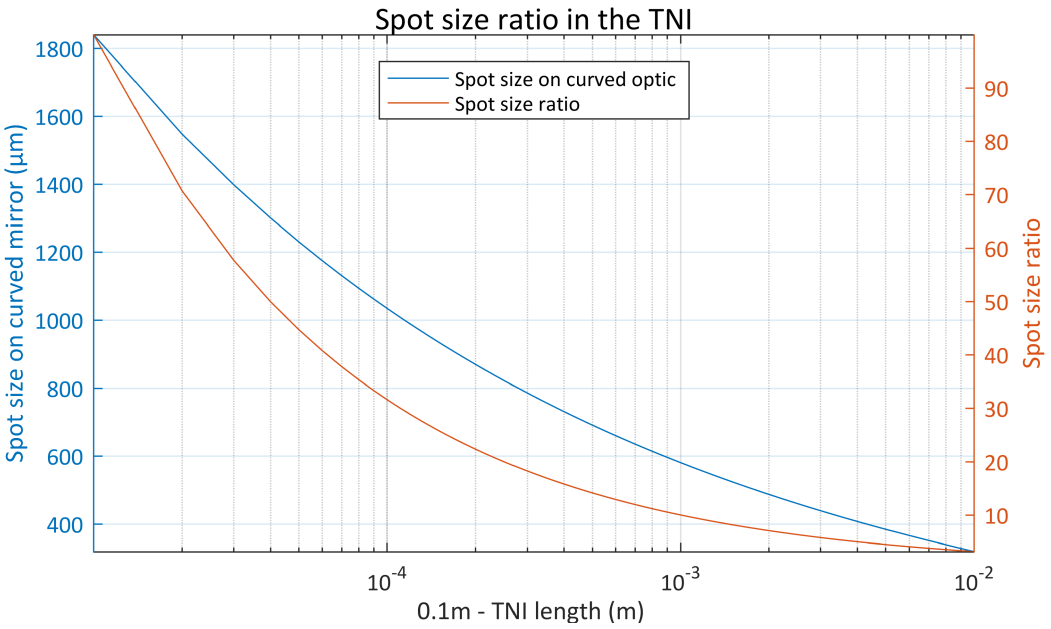

Figure 4.2: The spotsize on the curved mirror of a hemispherical cavity as a function of the distance from instability. The ratio of the spot sizes on the curved mirror and the flat mirror is shown

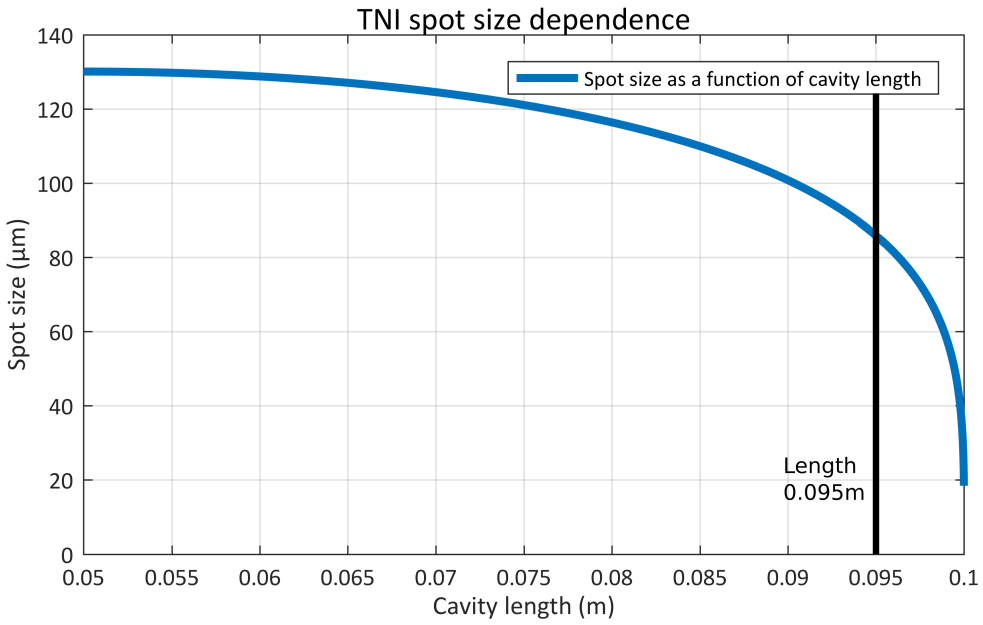

Figure 4.3: The spotsize on the flat mirror of a hemispherical cavity as a function of the cavity length. The radius of curvature of the curved mirror is 10 cm.

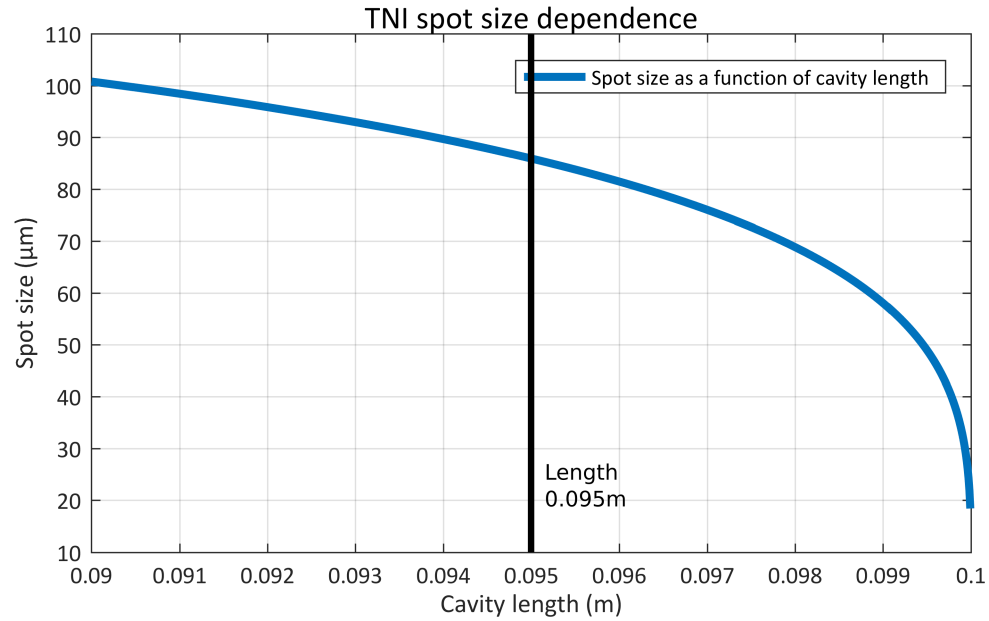

Figure 4.4: A zoomed in view of the spotsize on the flat mirror of a hemispherical cavity as a function of the cavity length. The lengths shown correspond to the range close to instability, which is useful to the TNI.

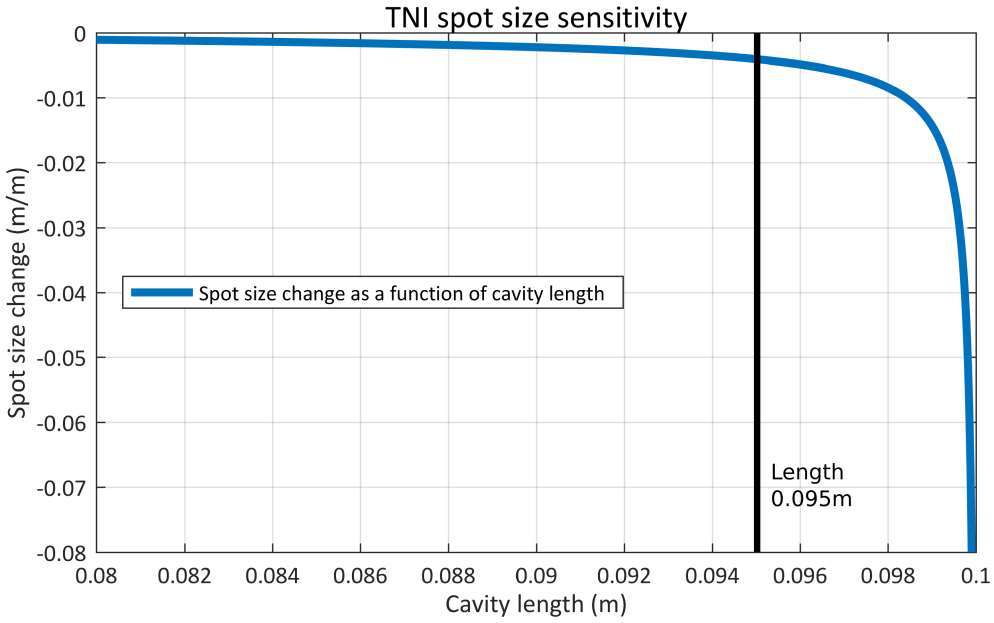

Figure 4.5: The rate of change of the spotsize as a function of cavity length. This shows the sensitivity of the spotsize against changes in the length, which is used for tuning the spotsize.

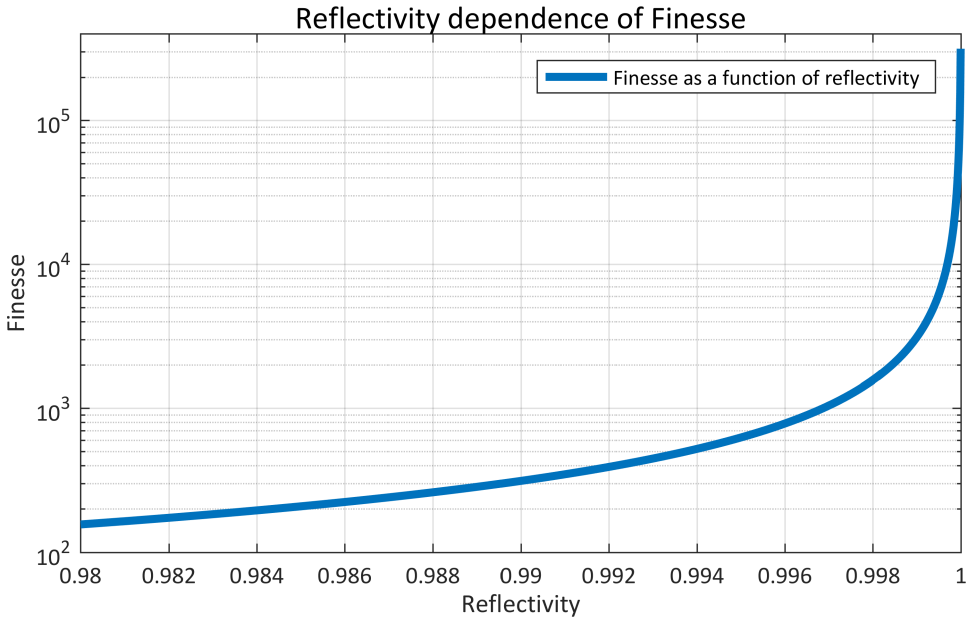

Figure 4.6: The Finesse of a Fabry-Perot cavity as a function of the mirror power reflectivities. Both mirrors are assumed to have the same reflectivity.

where r_1 and r_2 are the power reflectivities of the input mirror and output mirror respectively. This is an approximation in the absence of losses. In case of the TNI, the mirror reflectivities are the same for the input mirror and output mirror in the original configuration:

$$r_1 = r_2 = r = 0.9985\,. \tag{4.4}$$

This is called the impedance matched case, where both reflectivities are the same and when on resonance, all the light will be transmitted. The power on the locking photodiode in reflection is then minimal, avoiding problems with saturation while reducing the shot noise level.

The Finesse depends nonlinearly on the mirror reflectivities as shown in figure 4.6. The case of undercoupling, where the input mirror has a higher reflectivity than the output mirror, is rarely being used. Overcoupled cavities are widely used, for example as arm cavities in gravitational wave detectors, and this configuration will be relevant for some measurements in the TNI, where the mirror under investigation has some reflectivity higher than the input mirror. This is the case for the latest TNI measurements, where a monolithic spare mirror of the reference cavity is used, having a transmission of a few ppm. Many coatings of interest, which are intended for reference cavities and Fabry-Perot Michelson interferometers, also have transmissivities on the order of a few ppm. The influence of impedance-matching on the TNI, especially through shot noise, is detailed in section 6.1.

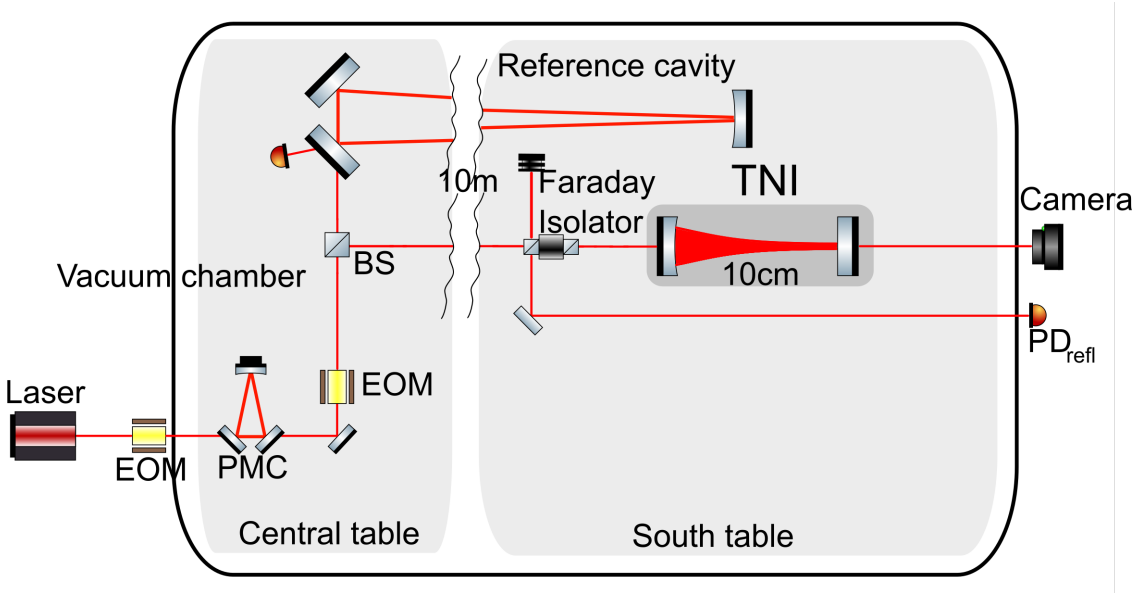

Figure 4.7: Schematic drawing of the main optical setup of the TNI. The light from the laser is mode-filtered by the PMC and subsequently sidebands are imprinted by a resonant EOM. Part of the light is split off for frequency stabilization by the reference cavity. 50 mW are sent to the hemispherical TNI, and the light reflected by the cavity is separated by a Faraday Isolator to be sent to the locking photodiode. A camera in transmission is used to judge the modal content of the resonant light.

4.2 Optical setup

The optical setup of the TNI placed in vacuum is shown in figure 4.7. As few parts as possible are used to reduce jitter coupling and scattering. The light from the main laser of the AEI 10 m prototype is filtered by the PMC and modulated by the EOM imprinting sidebands at 8.047 MHz. All of this happens in the common path, from where light is sent to the single-arm test, the frequency reference cavity and the TNI. A beam splitter is used to split off approximately 50 mW for the TNI, and two lenses on the central table collimate the beam to send it to the south table.

The first optic on the south table is a partly reflective mirror dumping excess power into an in-vacuum beam dump, as only up to 20 mW of the available 50 mW are currently being used. The second component on the south table is the Faraday Isolator which prevents light reflected from the TNI to couple back into other experiments. The reflected port of the Faraday Isolator is used to send the reflected light needed for the PDH-scheme to the locking photodiode. This is done using steering mirrors and lenses, focusing the beam onto the locking PD.

The light transmitted by the Faraday Isolator is sent through two mode matching lenses and steered by four steering mirrors into the TNI. The light transmitted by the TNI expands quickly because of the small waist present on the flat output mirror, and therefore a lens is placed behind the TNI to collimate the beam. This beam is then sent to a large-area silicon photodiode and a Watec WAT-902H2 Ultimate CCD-camera. The photodiode signal is used for alignment, broadening the error signal and triggering lock acquisition, and the camera gives information about the mode content resonant in the TNI. A partly reflective mirror and an in-vacuum beam dump are used in front of the lens to reduce the amount of light leaving the vacuum chamber through a vacuum window, because the interaction with the window causes scattering. This mirror and beam dump assembly was removed while measuring the reference cavity spare mirror, which has a transmissibility of less than 1 ppm. The amount of transmitted light sensed by the photodiode

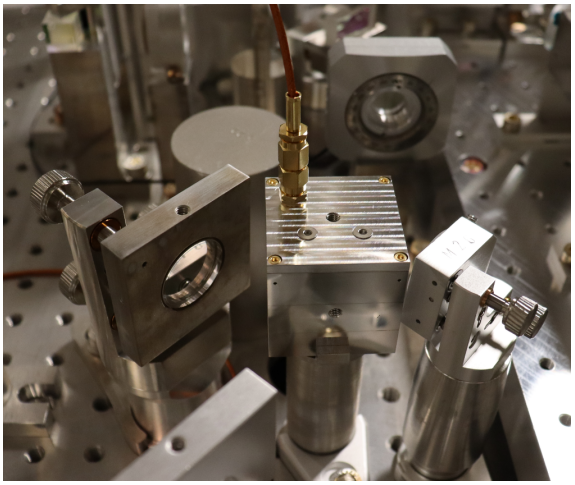

Figure 4.8: The resonant in-vacuum EOM (in the middle between two steering mirrors) is connected to the 8 MHz oscillator via a vacuum compatible capton-coated SMA-cable. In the background, the half-wave plate used to define the input polarization can be seen.

would otherwise have been forbiddingly low.

In the remainder of this section, the optical path is followed starting after the PMC, giving details about the components encountered along the way. The first component described is the EOM used for imprinting sidebands. After that, the Faraday Isolator is briefly discussed, followed by a more in-depth description of the mode matching telescope. The main compontents, the cavity mirrors, are described and characterized in the third section, focussing on their scattering properties and thermal noise associated with their composite mirror holders.

4.2.1 EOM

Locking an optical cavity with the Pound-Drever-Hall scheme requires phase modulation sidebands imprinted on the incoming light. In the AEI 10 m prototype, this is achieved by an EOM made by Qubig, which is shown in figure 4.8. This EOM has a 30 mm long KTP-crystal with a 3 mm quadratic aperture, which is sandwiched between copper foil electrodes connected to a resonant amplification circuit.

The sidebands at 8.047 MHz are used for locking the TNI as well as the reference cavity and the single arm test. As the EOM is located inside the vacuum chamber, vacuum compatibility is critical. The signal to be amplified in the resonant circuit is supplied by a highly stable temperature controlled crystal oscillator made by Wenzel, and is sent through a feedthrough and a vacuum compatible shielded cable to the EOM. Although the EOM is only a very small part in the input path of the TNI, it was responsible for a delay of several months as the crystal of the main EOM and a spare broke.

4.2.2 Faraday isolator

Generating a Pound-Drever-Hall error signal requires detecting the light reflected from the optical cavity. There are two common approaches, both of which have been used in the TNI in the past. The first uses a polarizing beam splitter and a quarter wave plate to convert incoming linearly polarized light into circularly polarized light interacting with the optical cavity and after reflection being converted back to linearly polarized light, but in the other polarization mode. The polarizing beam splitter then reflects the light reflected from the optical cavity and thereby seperates it from

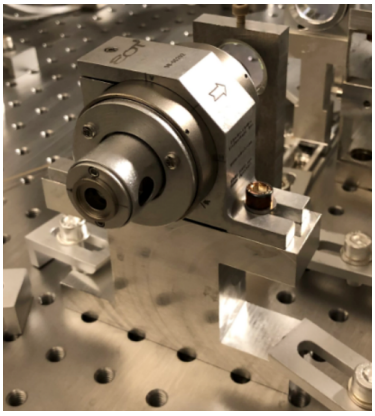

Figure 4.9: The vacuum-compatible Faraday Isolator by EOT. The clear aperture of 8 mm prevents clipping of the beam.

the incoming light.

For some coatings, especially crystalline coatings, it is advantageous to use linearly polarized light inside the cavity because of the presence of birefringence in the coating material. In this case, a second approach using a Faraday isolator is taken. This is currently being done in the TNI after starting with the first version for early tests.

The Faraday isolator is a vacuum compatible model HP-08-I-1045-1080-Vakuum made by EOT, with an aperture of 8 mm(shown in figure 4.9). Through the presence of strong Neodymium Iron Boron magnets around a terbium gallium garnet (TGG) crystal, the polarization inside the Faraday isolator is rotated by 45° upon transmission. As magnetic fields break time-reversal symmetry for optical systems, the rotation on the way back through the Faraday isolator has the same handedness as before, effectively rotating the beam into the orthogonal polarization with respect to the incoming beam. A polarizing beam splitter then separates the light and sends it to the locking PD.

4.2.3 Mode matching

Mode matching is essential to optimize the fraction of light coupled into the cavity. Light being reflected by the cavity contributes to shot noise on the locking photodiode, but does not carry the cavity length signal from interacting with the mirror surfaces. Therefore, any light directly reflected by the cavity needs to be avoided and proper mode matching is needed.

In the TNI, mode matching is achieved using two lenses placed in x-y-adjustable holders on translation rails. This ensures in-situ optimization of the mode matching efficiency by aligning the lenses to be hit in the very center and moving the lenses along the optical axis to find the optimal position. The starting point for the mode matching procedure is the waist of 386 µm located inside the PMC. After split off from the common path, lenses of focal length -51.5 mm and 257.5 mm are located at distances 20.5 cm and 73 cm from the PMC waist such that a collimated beam of size 1086 µm is sent from the central table to the south table.

There, another system of two lenses images the incoming collimated beam onto the waist located on the flat end mirror of the TNI. A simulation of the propagating beam through the setup on the south table is shown in figure 4.10. The design is aided by a MATLAB-based code, which optimizes lens positions given constraints such as available focal lengths, input beam size and position and size of the target waist. Care is taken to ensure that no small waist is present on any optic, as this keeps the power density on the optics low, while also keeping the maximum beam size such that no clipping occurs on the standard 1” optics used. Furthermore, having optics at

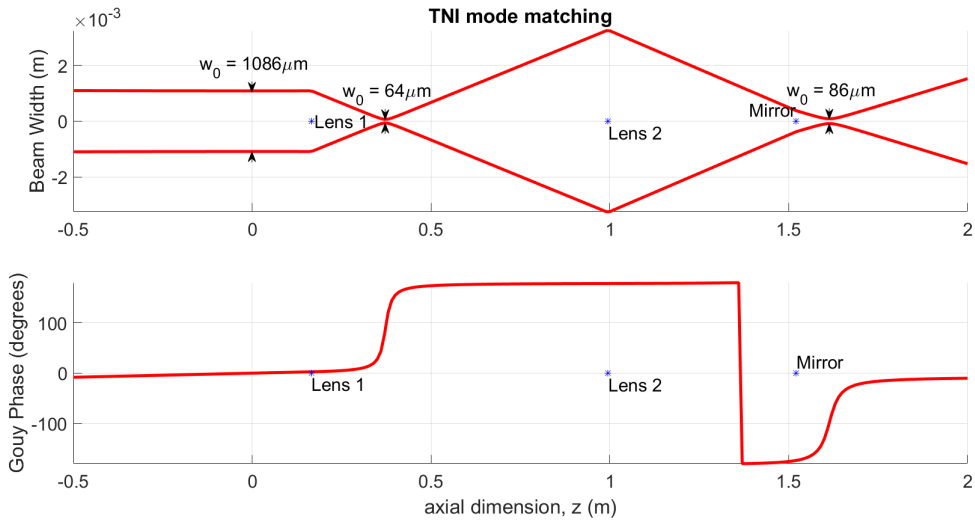

Figure 4.10: MATLAB simulation of the mode matching setup for the TNI. The upper plot shows the beam size as a function of propagation distance. The positions of the two lenses used are indicated as well as the beam waists. The lower plot shows the corresponding Gouy phase shift along the propagation path.

locations of beam waists increases the coupling of scattered light into the optical cavity [Hil07].

Equally important is, that the sensitivity of the mode matching efficiency on the lens positions allows high mode matching efficiency without posing unrealistic requirements for the accuracy of lens positioning. The mode matching efficiency plotted against lens positions for the two lenses is shown in figure 4.11. The position of the first lens has to be adjusted with an accuracy of a few mm, while the position of the second lens is less critical. The overall adjustment range is chosen such that the lenses can be mounted onto sliding rails for ease of positioning.

Other sensitivies which are checked are mode matching efficiency versus the size and position of the waist of the collimated input beam (plotted in figure 4.12 and figure 4.13). It is important that the sensitivity is not too high as the precision with which the large waist size of 1092 µm and its position can be measured is low and the expected position is in front of the optical table. As shown in figure 4.12, there is an approximate change of 2 % over 1 m, fulfilling the requirements.

Comparing the model with reality is done using the DataRay WinCam TaperCamD-UCD23 to measure beam profiles on the south table. The measured beam profiles are fitted by a Gaussian beam evolution. This gives the waist size and position of the Gaussian beam in relation to the table edge. The individual data points consist of beam sizes in x- and y-direction, and the average is taken to get the beam sizes for the fitting procedure. From the results, a value of 1104 µm for the waist at a position 35.88 cm in front of the south table edge is found.

Some measurements show a slightly larger ellipticity, which can be caused by a tilt of the beam profiler. Excluding beam sizes from measurements with an ellipticity of less than 0.98 gives a waist size of 1092 µm at a position of 42.81 cm in front of the south table edge. As shown above, this is within the allowed deviations to not limit the mode matching efficiency substantially. Using an iterative approach shifting lenses and realigning the cavity for maximal power in transmission gives mode matching efficiencies between 95 % and 97 %.

More lenses are needed to image the reflected and transmitted light from the cavity onto photodiodes and cameras on the detection bench. In transmission, a lens of focal length 300 mm placed 318 mm after the waist position is used to convert the strongly divergent beam starting from a waist size of 86 µm to a collimated beam of size 1 mm over a range of at least 3 m. The beam size evolution for different lens positions is shown in figure 4.14.

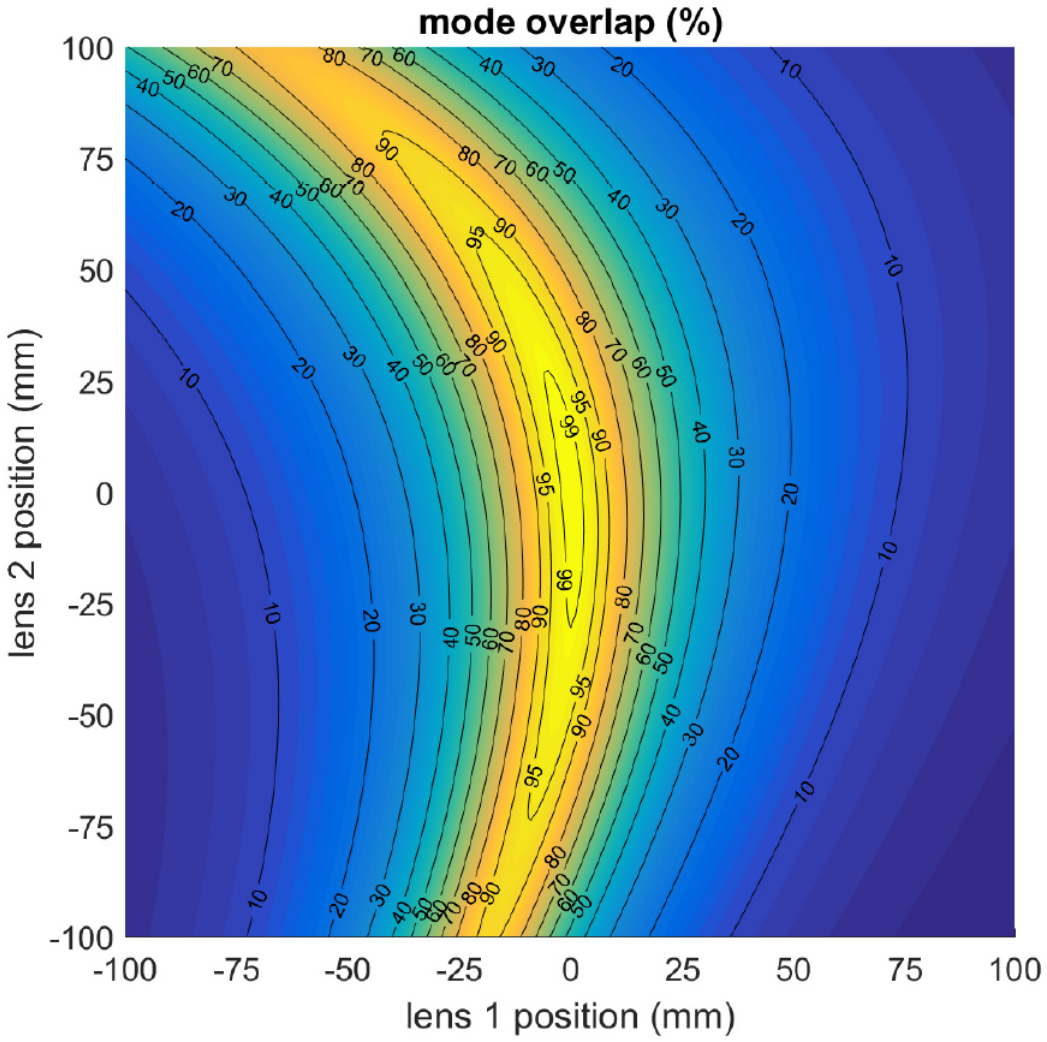

Figure 4.11: The mode matching efficiency is plotted as a function of the positions of the two lenses around the optimum position. A strong dependence on the position of the first lens is apparent, whereas the position of the second lens is less critical.

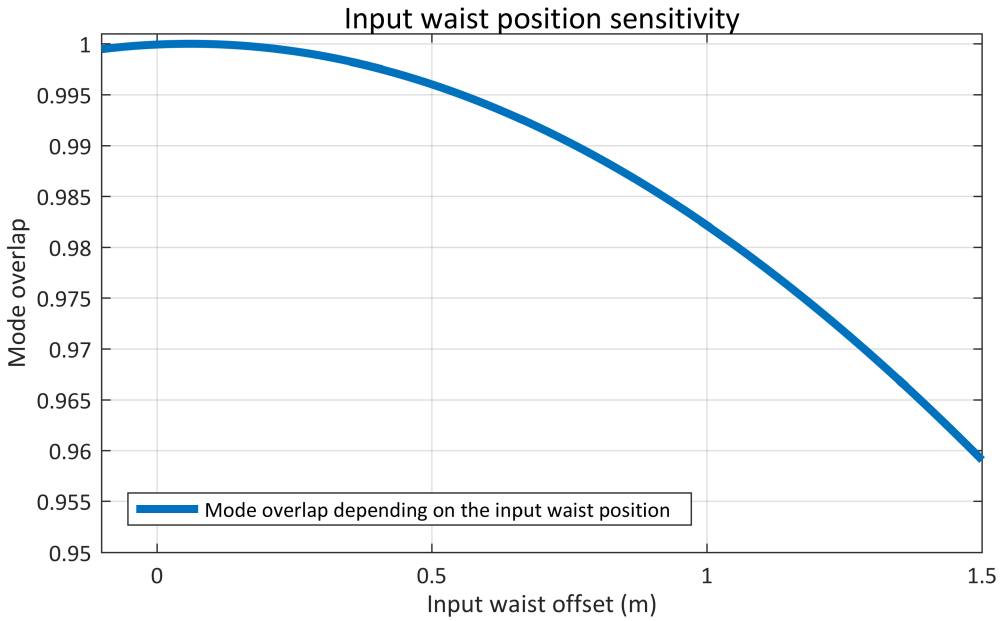

Figure 4.12: The mode matching efficiency is shown as a function of the position of the input waist. As this position is located in front of the optical table, sufficient stability is required. This is achieved with a 2 % change over 1 m.

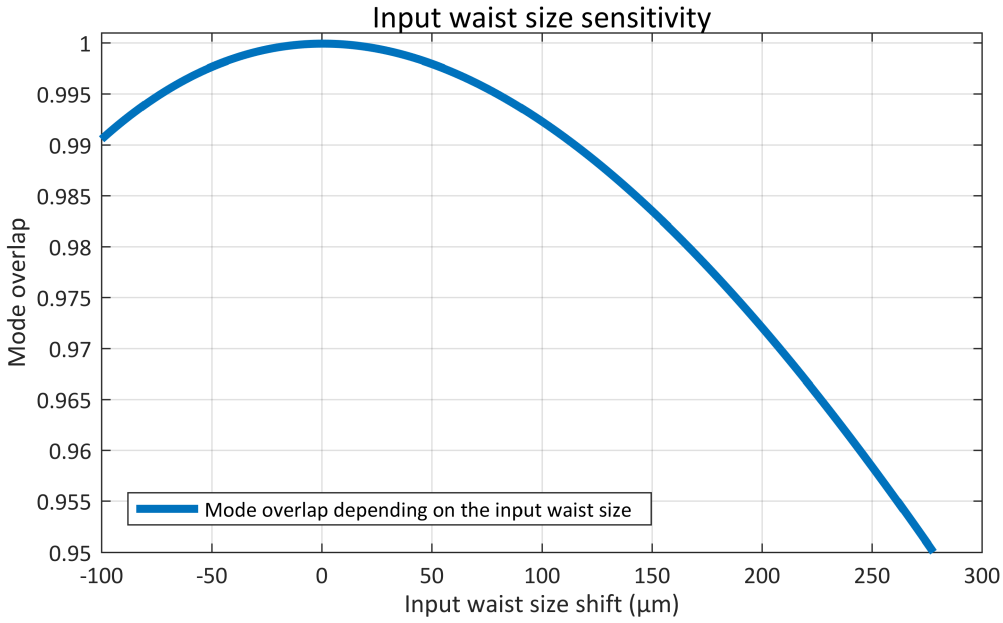

Figure 4.13: The mode matching efficiency is shown as a function of the size of the input waist. As this size can only be tuned and measured to within 5 µm, sufficient stability is required. This is achieved with less than 1 % change over 50 µm.

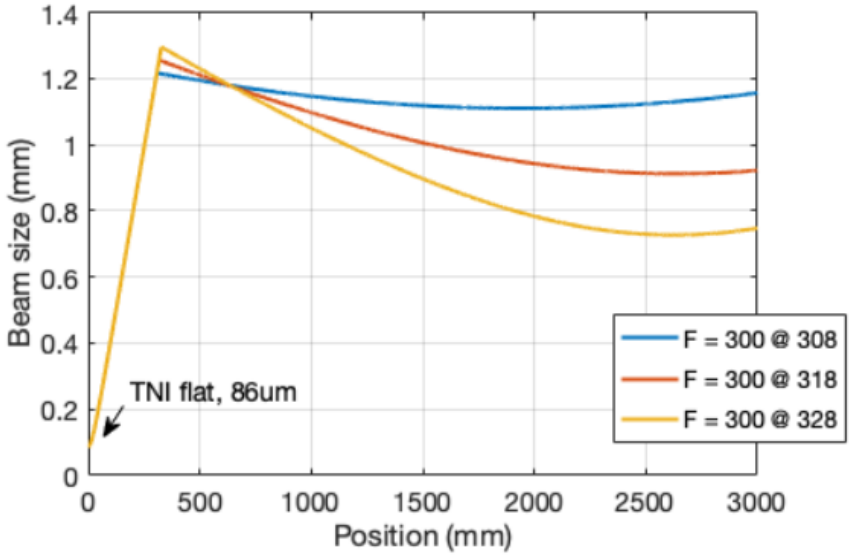

Figure 4.14: The evolution of the transmitted beam of the TNI after passing through a collimating lens. Three different lens positions are considered as the distance between the reflecting surface of the flat TNI mirror and the lens cannot be measured accurately. Within this range of positions, the requirement of a collimated beam of size 1 mm is sufficiently fulfilled.

A simpler approach is taken for the reflected beam, which behaves nearly in the same way as the incoming beam, slowly increasing in beam size over a few metre as shown in figure 4.15. A single lens of focal length 200 mm is then used close to the locking PD in the reflected path to focus the beam down onto the PD of size 1 mm.

4.2.4 Mirrors

The mirrors form the core of the TNI, and measuring their coating thermal noise is the main goal of the experiment. As explained above, the thermal noise of the TNI will be dominated by the coating thermal noise of the flat end mirror. Nevertheless, care has to be taken that the input mirror does not show significantly higher thermal noise, possibly surpassing the contribution of the end mirror. Furthermore, both mirrors have to meet tight specifications concerning scattering and losses.

To meet these requirements, custom made 1” mirrors by Laseroptik Garbsen have been acquired. They have a nominal reflectivity of 99.85 %, achieved by eleven pairs of quarter wave layers and topped with a three-quarter wave low refractive index layer and a 2.089λ high refractive index layer, giving a total thicknesses of 3.613 µm.

Using the layer thickness structure, the levels of thermal noise can be calculated as shown in chapter 2. An issue with mirrors used before in the TNI was scattering at the surface. The flat mirror from Laseroptik Garbsen is superpolished, the curved mirror, having a radius of curvature of 0.1 m, is polished to a level of a few Ångström rms.

A comparison with formerly used mirrors, supplied by Eksma Optics, was done in a dark field illumination experiment called scratchometer. There the mirror is illuminated from the back with a bright white light source under an angle and photographed in the dark field. The experiment shows a dramatic difference in the scattering present (shown in figure 4.16), especially when considering a significantly reduced exposure time for the formerly used mirror, which became necessary

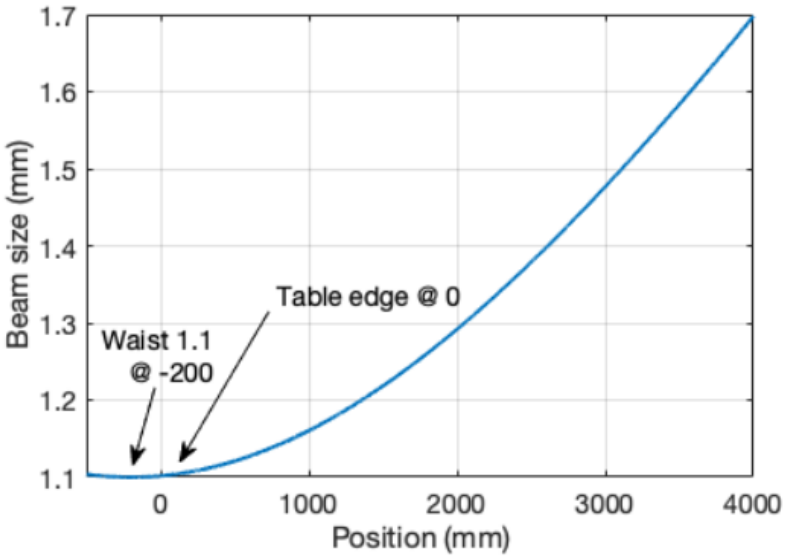

Figure 4.15: The beam size of the reflected beam slowly increases on its way to the detection bench. There a 1" lens is used to focus down the beam onto the locking photodiode.

because of saturation. Further characterization has been done using a scattering experiment called a scatterometer [Koc22], where a 10 mW laser source illuminates a spot on the mirror, and a Basler ace acA2040-55um Monochrome Camera detects scattered light under different angles. Postprocessing then gives a plot of the BRDF of the mirror. The mirror made by Laseroptik Garbsen shows a low level of scattering, two orders of magnitude lower than the Eksma mirror (as shown in figure 4.17), making highly sensitive measurements possible. As a comparison, the level of scattering of an old mirror is shown in figure 4.18.

The mirrors described above are 1" in diameter, but have to be suspended in a triple suspension, requiring a weight of roughly 850 g at the lowest stage, and a mirror diameter of 10 cm. There are several ways in which this can be achieved, and in the beginning the approach using a composite mass was chosen (as shown in figure 4.19). This aluminum mass provides the weight and dynamical properties needed as the lowest mass in the suspension chain. Attached on the sides are breakoff prisms, defining the first point of contact with the steel wires from which the mass is suspended. These breakoff prisms are located 1 mm above the center of mass of the aluminum mass.

In a first iteration, the mirror was clamped into the aluminum mass using a small PEEK grub screw. This turned out to limit the noise level achievable, displaying large resonance peaks above 1 kHz. They most probably stem from thermal excitation of resonances of the PEEK-screw-aluminum mass-mirror system (shown in figure 4.20). Replacing the PEEK screws in the flat mirror aluminum holder with UV-curable glue resulted in the removal of the central peak of the lower triplet close to 3 kHz and the higher frequency peaks around 5 kHz (shown in figure 4.21), and the successive PEEK screw replacement for the curved mirror resulted in the removal of all residual resonances (shown in figure 4.22).

Later measurements showed an elevated noise level, displaying the characeristic frequency dependence of Brownian thermal noise. It is highly unlikely that these mirrors have a coating loss angle ten times higher than comparable mirrors, as the loss angle of these highly pure and homogeneous mirror materials has not shown a significant variation over the last twenty years of research [Pen+03][GE18]. Thus the noise could be explained as substrate Brownian noise, being driven by excess mechanical losses in the composite mass.

To test this hypothesis and increase the sensitivity of the TNI to measure coating thermal

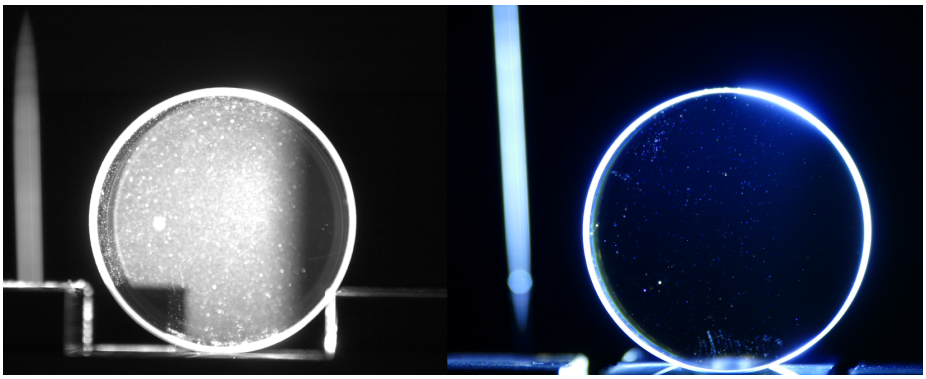

Figure 4.16: Dark-field images of the formerly used Eksma Optics mirror and the custom-made Laseroptik mirror in a setup called Scratchometer. The difference in scattering is evident, especially considering that the left image was taken with an exposure time three times less than the one used for the picture on the right.

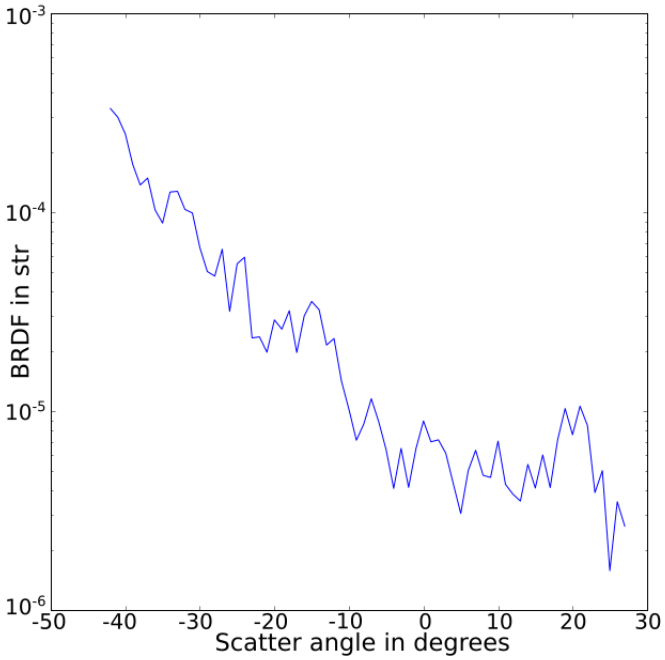

Figure 4.17: BRDF of a custom-made Laseroptik mirror, measured with the Scatterometer experiment.

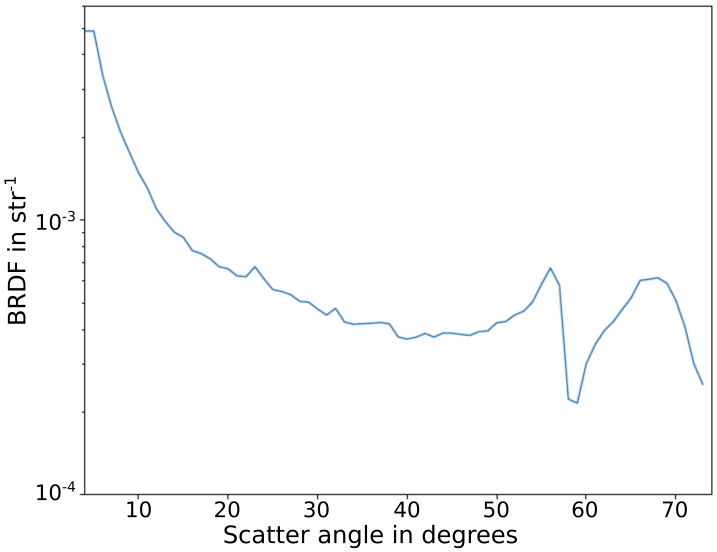

Figure 4.18: BRDF of the formerly used Eksma Optics mirror, measured with the Scatterometer experiment. The significantly elevated level of scattering in comparison to 4.17 is evident.

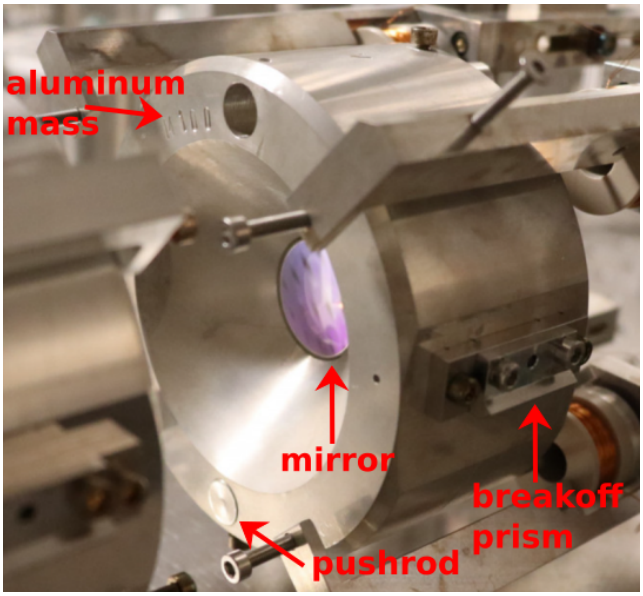

Figure 4.19: Composite mirror suspended in the TNI. The aluminum mass provides the weight and dynamical properties, while the small mirror screwed/glued in the center provides the optical properties. On the side, breakoff prisms are screwed on to define a contact point for the suspension wires. Above and below the mirror, pushrods are inserted to allow pitch adjustment.

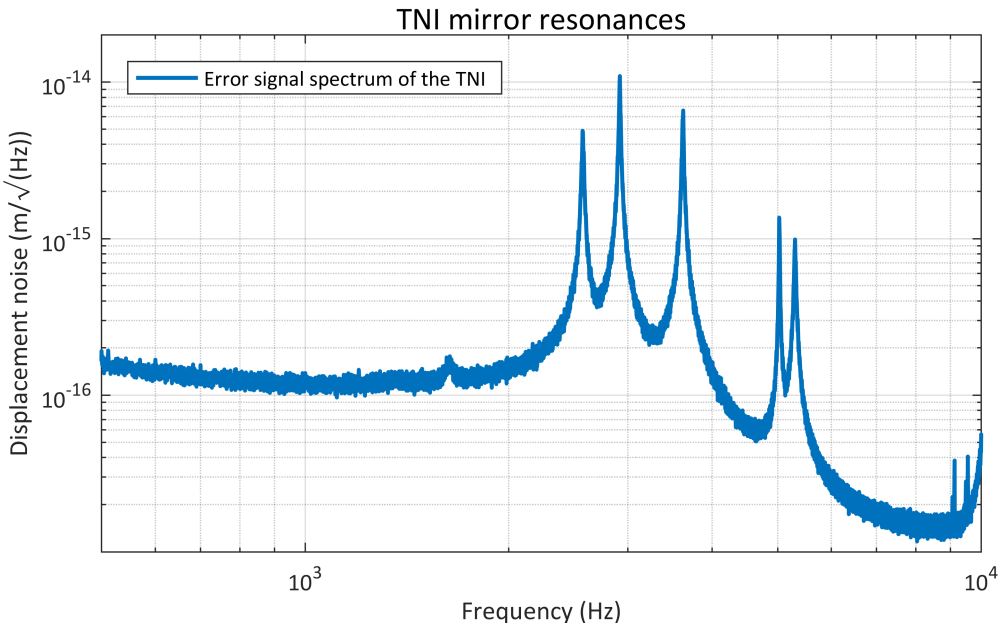

Figure 4.20: A length spectrum of the TNI, showing resonances of the composite mass between 2 kHz and 6 kHz. At this point, the small mirror was clamped into the aluminum mass by a PEEK-screw.

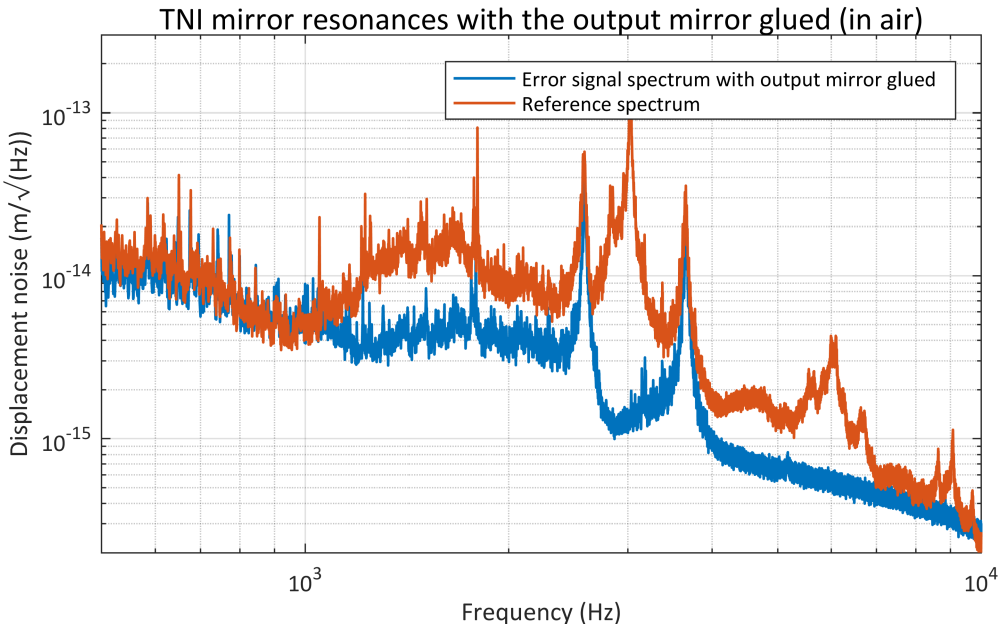

Figure 4.21: A spectrum of the TNI taken after glueing the flat mirror into the aluminum holder. Two resonances between 2 kHz and 4 kHz are left, the other resonances have vanished.

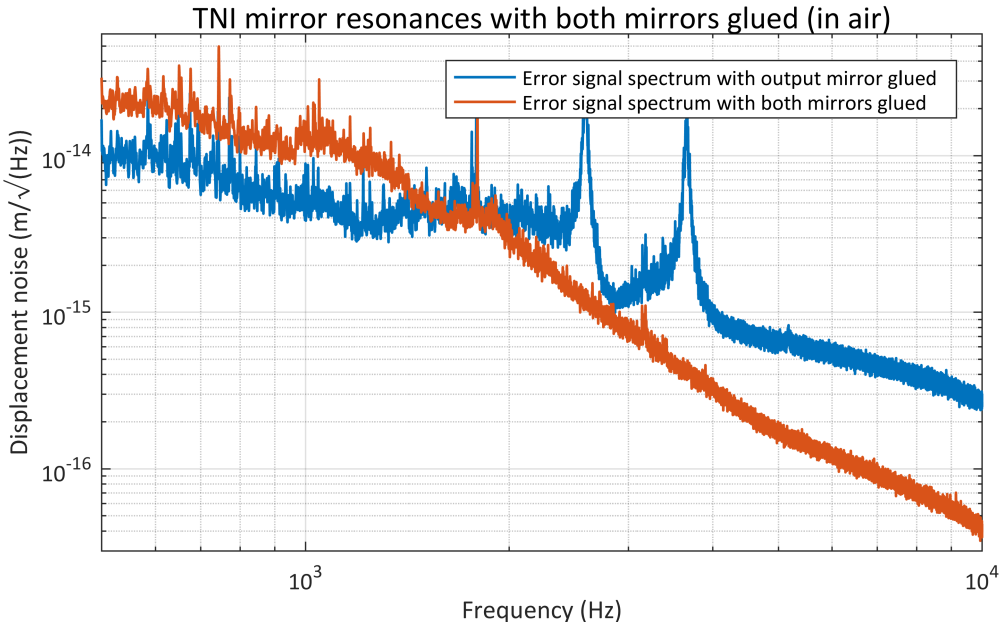

Figure 4.22: After glueing the second mirror into the aluminum holder, all the resonances have disappeared, showing that clamping the mirror with PEEK-screws introduces unwanted resonances in the measurement band between 50 Hz and 10 kHz.

noise, the composite masses are successively replaced by cavity mirrors, which are fabricated as monolithic fused silica masses weighing close to 850 g. The diameter is still 10 cm and the thickness 5 cm. As the flat end mirror of the TNI is dominating the readout noise, this mirror is replaced first by a spare reference cavity mirror (shown in figure 4.23). This mirror meets the aforementioned requirements, having a reflectivity of more than 99.9999 % and a radius of curvature of 37.8 m.

An approximate transmission value for this mirror has been inferred from power measurements while the TNI was locked. In reflection, 14.4 mW are detected, while in transmission 11.7 µW are measured. Using the known reflectivity of 99.85 % of the input mirror and an estimate of 20 ppm for intracavity losses gives a transmissivity for the output mirror of less than 0.5 ppm. This value is taken as the basis for an estimate of the coating structure and thickness, used in the calculations for coating thermal noise.

For future measurements, monolithic input mirrors of 10 cm diameter possessing a radius of curvature of 10 cm have been bought and will be installed to further improve the sensitivity of the TNI. The HR-coatings of these mirror are planned to come with two different reflectivities. This ensures through impedance matching, that for a wide variety of test mirror reflectivities, the shot noise will be low enough that the readout can be dominated by coating thermal noise, as shown in figure 4.24 for reflectivities of 0.999 and 0.9999 and other parameters as in the current iteration of the TNI.

Another issue is the thermal noise of the input mass, as has been seen for the case of the excess substrate thermal noise in the TNI. For thermal noise optimized coatings such as AlGaAs coatings, improvements in the amplitude spectral density of up to a factor 10 are expected, such that the spot size ratio of 4.5 would not be enough to have the test mass noise dominate the TNI readout. One way would be that coatings of similar thermal noise levels are used for the input mass, but a more straightforward is to adapt the spot size ratio by bringing the cavity closer to instability. This is shown in figure 4.2, and ratios of more than 20 are in reach, providing sufficient suppression

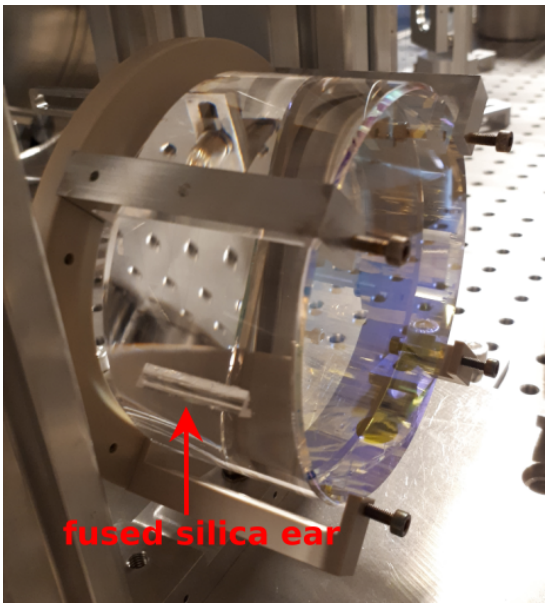

Figure 4.23: A monolithic spare reference cavity mirror has been installed in the TNI. The diameter is 10 cm and the thickness 5 cm, similar to the aluminum composite mass. UV-glued fused silica ears serve as breakoff prisms.

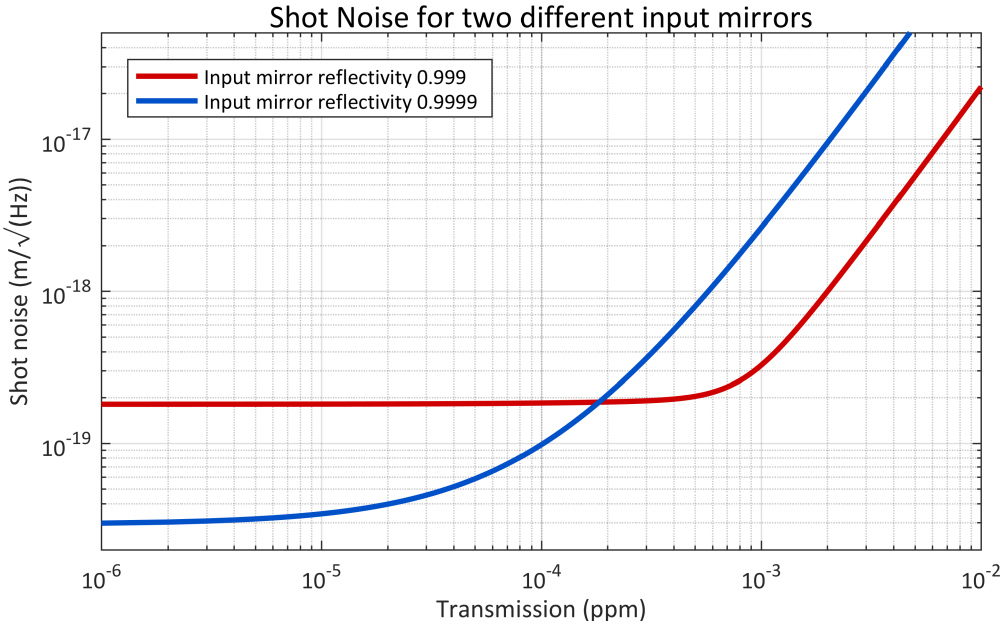

Figure 4.24: Shot noise as a function of the test mirror transmission for two different input mirrors with reflectivities of 0.999 (red) and 0.9999 (blue).

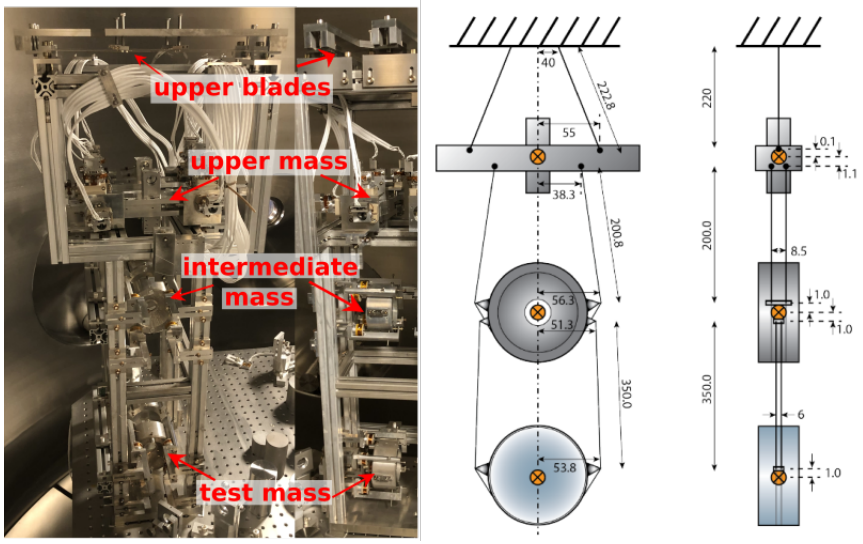

Figure 4.25: Dimensions of the triple suspension as used in the TNI (in mm). The parameters shown determine the horizontal and vertical displacement transfer functions. The center of mass for each mass is marked by a cross on an orange circle. [Wes16]

of the input mirror noise contribution.

For the test mass, small test substrates could be optically contacted to low loss fused silica substrates in the future to increase flexibility in the coated sample size, but this imposes surface quality constraints on the test samples and substrates. The viability of this approach has to be tested in the TNI as one of the next steps.

4.3 Suspension

The suspensions for the two mirrors of the TNI provide the required seismic isolation necessary for reaching the coating thermal noise level. The basic design is similar to the suspensions of the reference cavity [Wes16], and a crude test setup has been assembled in the past. In order to reach the design sensitivity, many additions, changes and modifications were required, along with several rounds of noise hunting in vacuum and out of vacuum.

The basic setup of the triple suspensions is briefly described in the first part, followed by an in-depth discussion of the most important commissioning steps required to achieve the final suspension performance. This performance is evaluated in the third part, looking at the resonance frequencies and transfer functions of the suspension chains.

4.3.1 Setup

The suspension design consists of three wire stages for horizontal passive isolation and two blade stages for vertical passive isolation. The first blade stage consists of two blades, from which the uppermass is suspended by two wires. The second blade stage consists of two blades inside the uppermass, and from these blades the intermediate mass is suspended in two wireslings. Another two wireslings are clamped to the intermediate mass to suspend the test mass. A schematic of the suspension including the dimensions is shown in figure 4.25 next to an annotated picture.

Calculations, which form the basis of the design, have been done in MATLAB using state space modelling, based on [Tor99]. They take the parameters from figure 4.25 to get the theoretical

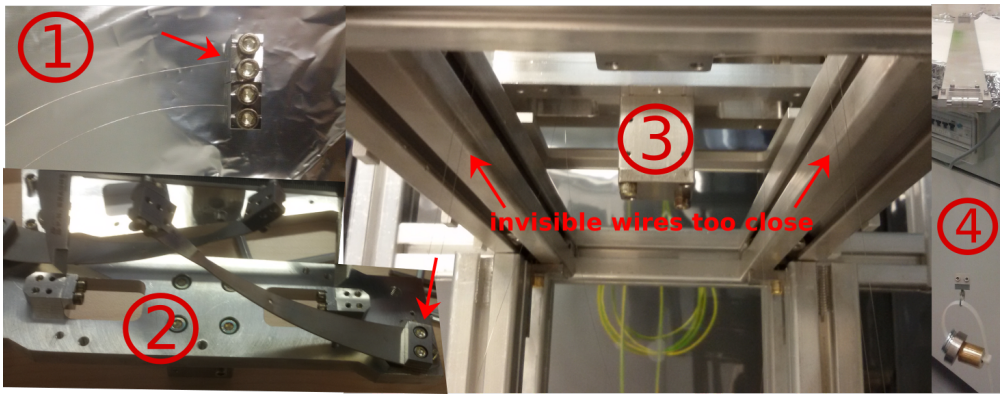

Figure 4.26: (1) shows the angled wire in the uppermass clamp, leading to a pitched uppermass. (2) shows the inside of the uppermass, where the blades holding the intermediate mass are mounted. The base of the blade (red arrow) can be rotated in slot holes, and needs to be properly aligned to avoid the blades touching other parts. (3) shows where the wires suspending the intermediate mass are too close to the ITEM aluminum profiles (red arrows). Moving the ITEM profiles was necessary to provide enough clearance. (4) shows the jig for defining the suspension wire length, with the weight used for tensioning dangling below.

suspension properties, which can then be compared to the final setup. Furthermore, noise projections are based on the transfer functions of the horizontal and vertical stages, taken from the state space model.

4.3.2 Commissioning

The commissioning of the suspension is a crucial step in providing the required seismic isolation for the TNI. Starting with a rough preliminary setup similar to the suspensions of the reference cavity, nearly every part has been disassembled, improved and properly reassambled. Several additions were necessary as well, to provide the setup necessary to measure mirror thermal noise.

At the top of the suspension, the upper steel blades are mounted using newly designed blade holders, described below. These blade holders are then moved laterally to set the nominal cavity length of 9.5 cm. Afterwards, the vertical adjustability of the blade holders is used to set the height of the mirror centers at 10 cm above the table surface.

The wires connecting the upper blades with the upper mass have a thickness of 150 µm and are clamped between steel blocks on both ends. These are then screwed to the blades and to the inside of the upper mass. A source of excess suspension tilt was found and eliminated by ensuring that the breakoff angle of the wire at the clamp was as close to 90° as possible (shown in figure 4.25 picture (1)).

The upper mass has two short blades inside (shown in figure 4.25 picture (2)), which have to be adjusted laterally to ensure that the lower part of the suspension hangs directly underneath the center of mass of the upper mass, thereby not inducing unwanted torque. Additionally, the blade has to be prevented from scratching against other parts inside the uppermass while moving.

Wires with a thickness of 100 µm are clamped between steel blocks connected to these blades and form a sling, in which the intermediate mass is suspended. Adjustments to the cage structure were necessary as these wires were too close to cage aluminum profiles, creating seismic shortcuts (shown in figure 4.25 picture (3)). The intermediate mass consists of an aluminum cylinder of diameter 10 cm and thickness of 5 cm. The middle has a hole inside a conical cutout, such that the total mass is close to the mirror mass of 850 g.

Breakoff prisms screwed to the sides of the intermediate mass ensure a well defined point of

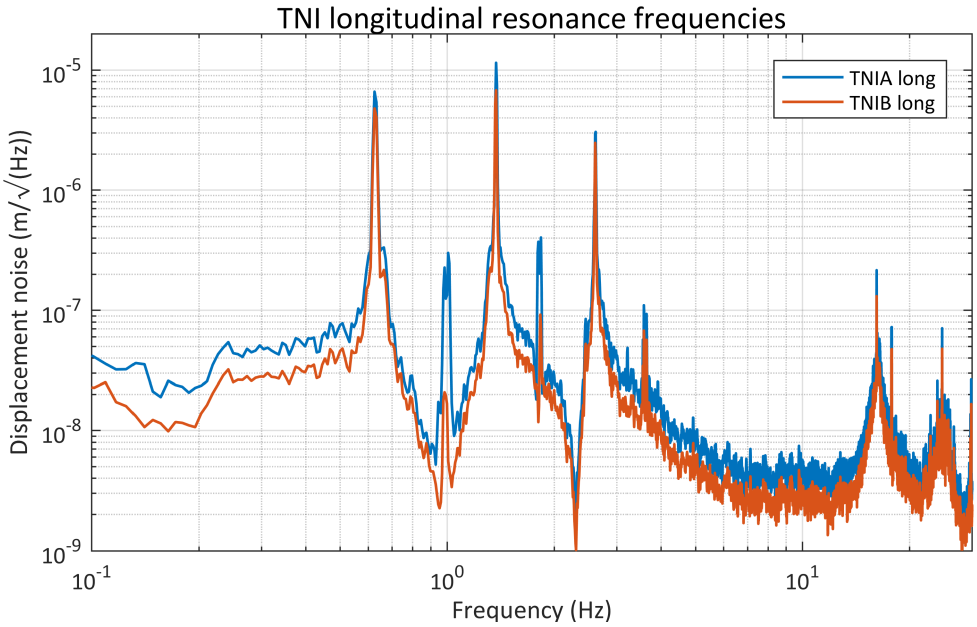

Figure 4.27: Spectra taken from the BOSEMs at each suspension in the longitudinal degree of freedom. The largest resonances at 0.63 Hz,1.39 Hz and 2.61 Hz correspond to the three lowest longitudinal resonances, while smaller peaks arise from cross coupling to pitch and yaw motion.

contact for the wires, reducing excess frictional losses. The breakoff prism structure is also used to clamp the wire, which suspends the test mass. This wire is made by Fort Wayne Metals and has a thickness of 50 µm. Wire lengths are controlled by using a jig, in which the wire is held while being clamped into the clamping structures. To get the correct wire length of the suspended setup, the wires in the jig are loaded with a weight corresponding to the masses in the suspension, attached to the wire by a clamp (shown in figure 4.25 picture (4)).

The test mass aluminum holder has breakoff prisms as well, defining the point of contact with the wires. Alignment is aided by steel or aluminum cylinders, called pushrods, which can be moved inside the suspended masses, so that pitch and roll misalignments can be corrected. Fine adjustments are realized by slightly moving the wire positions at the breakoff prisms iteratively, until the suspension hangs straight as judged by eye.

4.3.3 Characterization

At different stages of the commissioning process, several methods to characterize the status and success have been used. The first test on the quality of the suspension setup and alignment was measuring transfer functions using the BOSEMs to actuate and readout the upper mass motion. Resonance frequencies for the first three resonances for all degrees of freedom were extracted (for example longitudinal motion shown in figure 4.27) and compared to the results from the MATLAB-based state space model. The results are shown in table 4.1, showing not only good agreement on the level of 1 % for most resonances between the model and the suspensions, but more importantly even better agreement between both suspensions, helping with common mode suppression of longitudinal motion.

A second method to check the performance of the suspension, especially concerning seismic isolation, was to build an optical lever setup. There two laser beams are reflected from the test

DOF	TNIA	TNIB	model
Long	0.625 Hz	0.629 Hz	0.64 Hz
	1.373 Hz	1.371 Hz	1.39 Hz
	2.610 Hz	2.614 Hz	2.59 Hz
Pitch	0.960 Hz	0.992 Hz	0.98 Hz
	1.830 Hz	1.817 Hz	1.88 Hz
	5.750 Hz	5.680 Hz	5.20 Hz
Yaw	1.010 Hz	1.010 Hz	0.97 Hz
	1.805 Hz	1.820 Hz	2.30 Hz
	3.210 Hz	3.210 Hz	5.55 Hz
Vertical	0.988 Hz	0.984 Hz	1.24 Hz
	3.917 Hz	3.914 Hz	4.07 Hz
	17.82 Hz	17.82 Hz	18.62 Hz
Side	0.630 Hz	0.629 Hz	0.64 Hz
	1.378 Hz	1.371 Hz	1.39 Hz
	2.593 Hz	2.585 Hz	2.61 Hz
Roll	1.600 Hz	1.590 Hz	2.26 Hz
	8.61 Hz	8.61 Hz	9.12 Hz
	23.00 Hz	23.05 Hz	

Table 4.1: The resonance frequencies of both TNIA and TNIB suspension, sorted by degree of freedom. The measured frequencies are compared to those derived from a state space model.

mass mirror under a shallow angle of 21.5° and an acute angle of 51.6° and are subsequently detected on quadrant photodiodes. The angles are chosen such that a proper differentiation between longitudinal and rotational motion can be achieved. Combining signals from both QPDs provides information about pitch, yaw and longitudinal motion.

This measurement technique was combined with actuation at the top mass using BOSEMs, and test mass using the newly installed coil actuators, giving transfer functions from all degrees of freedom to longitudinal (shown in figure 4.28), pitch and yaw motion of the test mass. Furthermore, the presence and absence of BOSEM damping loops can be observed. The same transfer function was later measured in lock from BOSEM excitations to the TNI error signal. The result is shown in figure 4.29, corroborating the results obtained from optical lever measurements.

4.4 BOSEMs and damping

Damping of the fundamental resonances is a necessary prerequisite for the TNI to be able to acquire lock. The seismically excited motion on resonance, escpecially for the longitudinal modes of the suspension chain, is too large and fast for the coil actuators on the test mass, reaching amplitudes of more than 100 nm and velocities of 100 nm/s. In order to acquire lock they have to slow down motion enough for the cavity length to stay within the linear range of the error signal (roughly 10 pm) long enough, so that the lower mass coils can produce enough force to reverse the direction of motion and ultimately limit the residual motion to a less than a hundredth of the linewidth of the cavity.

In lock, feedback is strong enough to be able to keep the cavity locked even without damping, but only when the conditions are right, i.e. under vacuum with well controlled seismic isolation tables. Another issue with excess motion in the fundamental modes is nonlinear upconversion where the interaction of the moving mirror with light circulating inside the cavity produces oscillations in

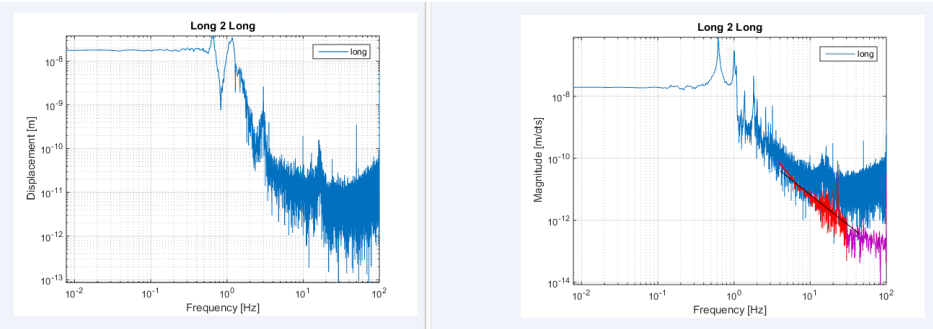

Figure 4.28: Measurement of the transfer function from excitations at the top mass to motion at the bottom mass, using BOSEMs as actuators and optical levers as sensors. The lowest longitudinal resonances are visible, followed by a steep drop due to the $\frac{1}{f^2}$ reduction per resonance. Measurements were taken with damping loops engaged (left) and disengaged (right).

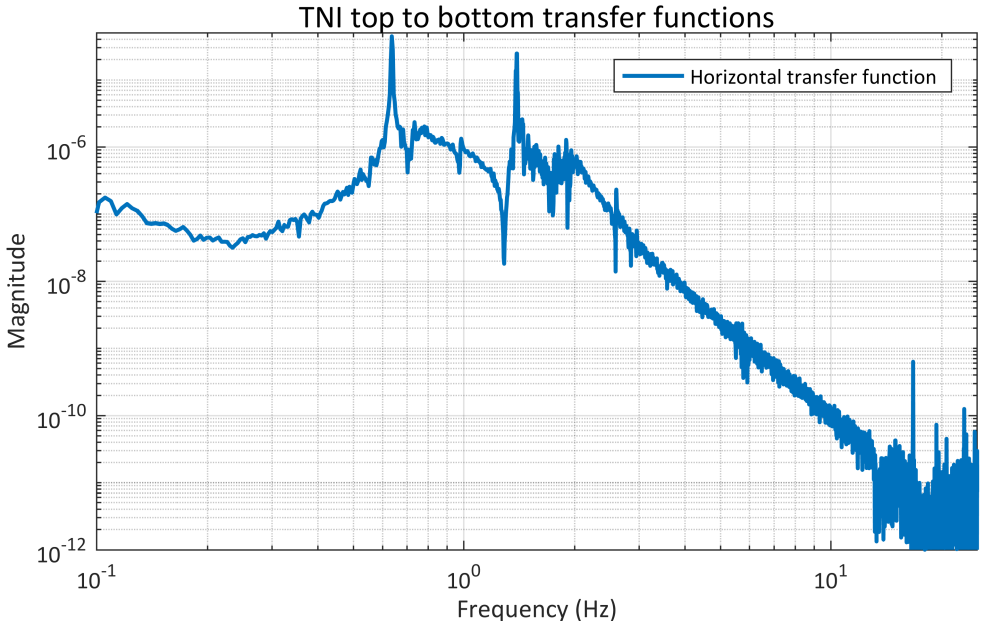

Figure 4.29: Measurement of the transfer function from excitations at the top mass to motion at the bottom mass, using BOSEMs as actuators and the TNI in-lock error signal as sensor. The lowest longitudinal resonances are visible, followed by a steep drop due to the $\frac{1}{f^2}$ reduction per resonance.

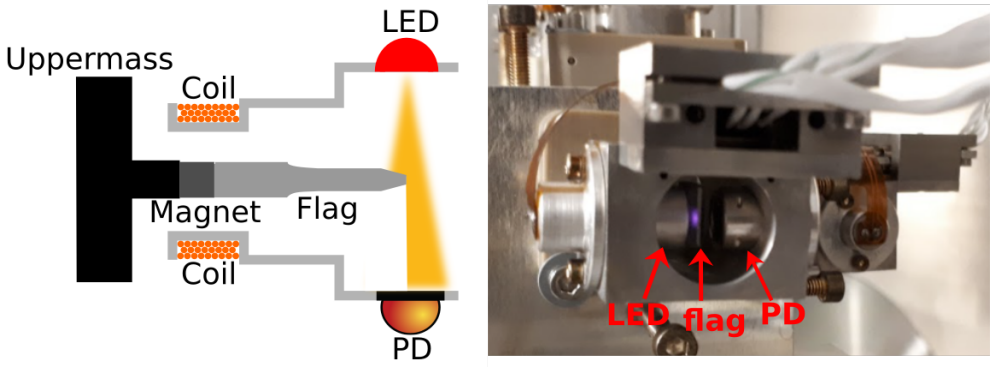

Figure 4.30: Basic operational principle of sensing and actuation of BOSEMs. Part of the light emitted from the LED is blocked by the flag, reducing the power sensed by the PD. Actuation is applied through a current in the coil, creating a magnetic force on the magnet, which is attached to the suspended mass.

the spectrum at frequencies above 1 kHz. Damping of these resonances can be achieved passively by using so called eddy-current dampers, which are copper cups surrounding magnets mounted on the mass to be damped. This induces velocity dependent damping through induction of eddy currents inside the copper by the motion of the magnet relative to the copper cup, counteracting the motion that produced them.

A more flexible approach consists of using a colocated pair of sensor and actuator, which in this case is called BOSEM (Birmingham Optical Sensor and Electro-Magnetic Actuator) [Ast11]. Sensor and actuator are used as parts of a digital feedback loop producing the desired level of damping while minimizing additional noise introduced in the measurement band. In the following subsections, the working principle and details about the BOSEMs are explained and the performance of the damping loops used are discussed.

4.4.1 BOSEMs

The BOSEM has been developed in Birmingham by Stuart Aston based on a design made by LIGO called OSEM. The basic sensing working principle is relying on a flag, mounted on the suspended mass, partly blocking the light path from an LED to a PD. The amount of light blocked corresponds to the position of the suspended mass. Actuation is applied by sending a current through a coil, creating a magnetic field, which in turn acts on a magnet attached to the suspended mass. A schematic representation of the setup is shown in figure 4.30.

BOSEMs consist of a vacuum compatible Kapton board to which the electronic parts are connected (shown in figure 4.31 on the right), and an aluminum piece which holds the photodiode, the LED and the coil in position (shown in figure 4.31 on the left). This aluminum structure is clamped into the upper mass catcher structure using PEEK clamps.

4.4.1.1 Sensing

The position sensing part of the BOSEM consists of an LED of type OP232 from Optek emitting light at 890 nm and a silicon PIN-PD of type BPX65 by Osram. The PD is placed opposite of the LED inside the aluminum holder, and without any obstacle, light from the LED illuminates the PD fully. In operation inside the suspension, the suspended mass has a flag attached (shown in figure 4.30), which blocks part of the light path from LED to PD, thereby creating a drop in the current registered by the PD. This is converted to a voltage through a transimpedance stage and

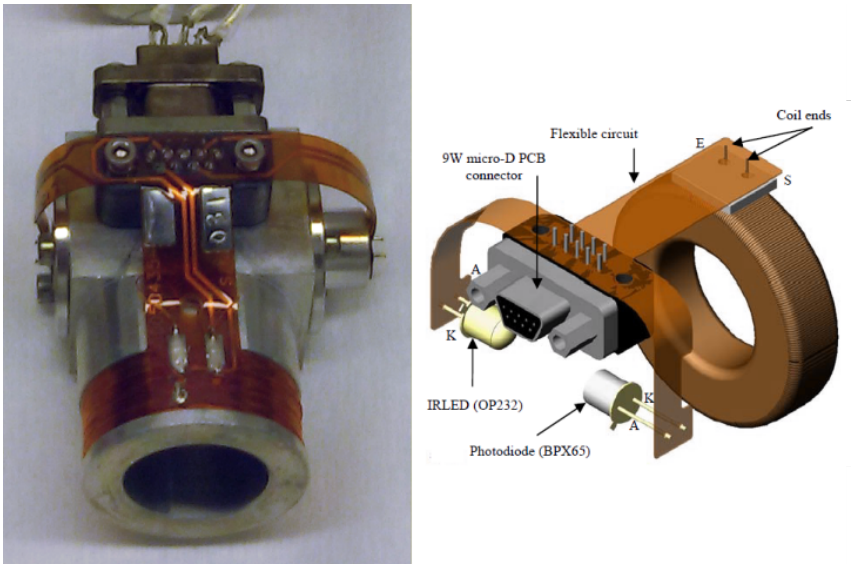

Figure 4.31: The right part is showing the electronic components of a BOSEM [Ast11]. The micro-D connector sends incoming actuator sinals through a capton sheet to the attached coil. The photodiode and LED are also connected via a capton sheet to the micro-D connector, which sends the signals to the CDS. The left side shows a fully assembled BOSEM with the components as detailed on the right. From the LED and PD, only the holder and soldered legs are visible.

digitized to be able to shape the signal using digital filters and feed it back to the actuators for damping.

This shadow sensor arrangement has a linear range of 800 µm as extracted from measurements in a test setup consisting of a translation stage moving the flag between the LED and PD (shown in figure 4.32). The measurement not only shows the extent of the linear range, but also gives a calibration factor in the form of the slope of the measurement (shown in figure 4.33). For this BOSEM, the slope was found to be 71 µm/V.

In the TNI, the linear range will stay constant as a mechanical property of the setup, but the slope will change with a change in the LED power and PD sensitivity. Regular recalibration has to be done by measuring the signal without the flag blocking any light and adapting the slope used for calibration. This is necessary as the shadow sensor has been observed to drift in the power sensed as well as showing a dependence on the temperature. A measurement over 12 days shows oscillations correlated to the laboratory temperature as well as a drift showing a degradation with time, presented in figure 4.35. The drift rate is 1.25 cts/d. Figure 4.34 shows the BOSEM sensor readout over a period of 24 h together with the temperaure at this time. A clear correlation is visible, showing the temperature dependence of the BOSEM sensors. From this, a temperature dependence of 26 cts/K is estimated.

An improvement from old flag designs was widening the flag to prevent sideways motion relative to the LED-PD-line to couple into the longitudinal signal. Using the test stand shows the difference in the sensitivtity to the sideways position (see figure 4.36 and figure 4.37).

4.4.2 BOSEM photodiode readout

The photodiodes of the BOSEMs, illuminated by LEDs at 890 nm, are supplied with a bias of −10 V at their anode. The resulting photocurrent is sent to the BOSEM readout electronics, where it is converted to a voltage by a transimpedance amplifier with a gain of 120 kV/A.

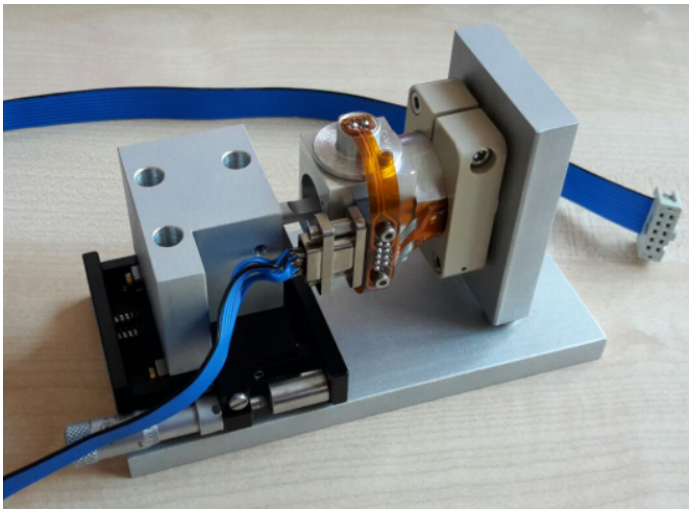

Figure 4.32: BOSEM test stand consisting of a mount holding the BOSEM and a translation stage with a micrometer screw moving the flag.

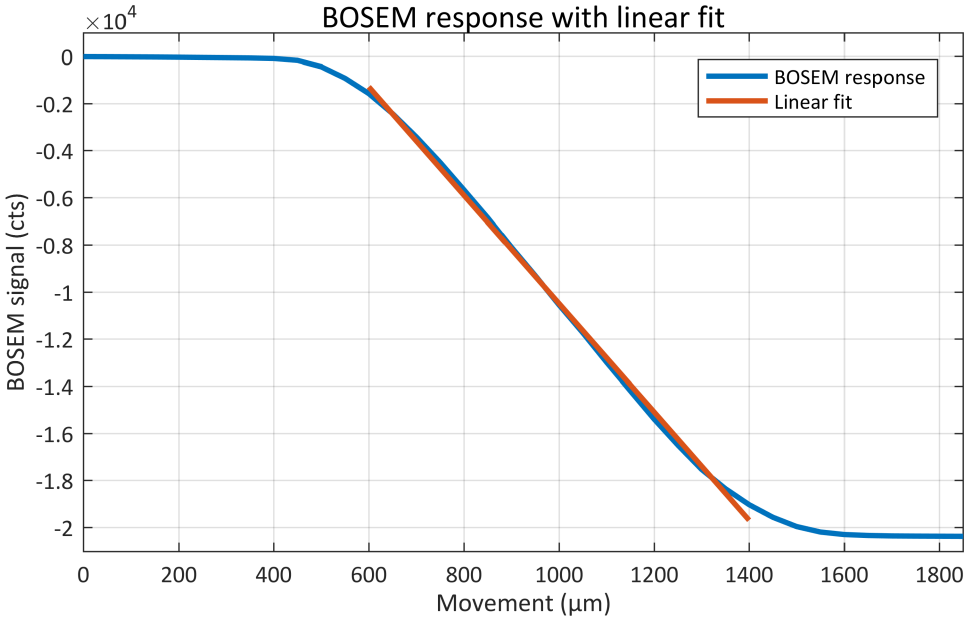

Figure 4.33: A measurement taken in the BOSEM test stand, showing the power sensed by the PD in cts against flag position in µm. The linear range of the measurement is highlighted by a straight line.

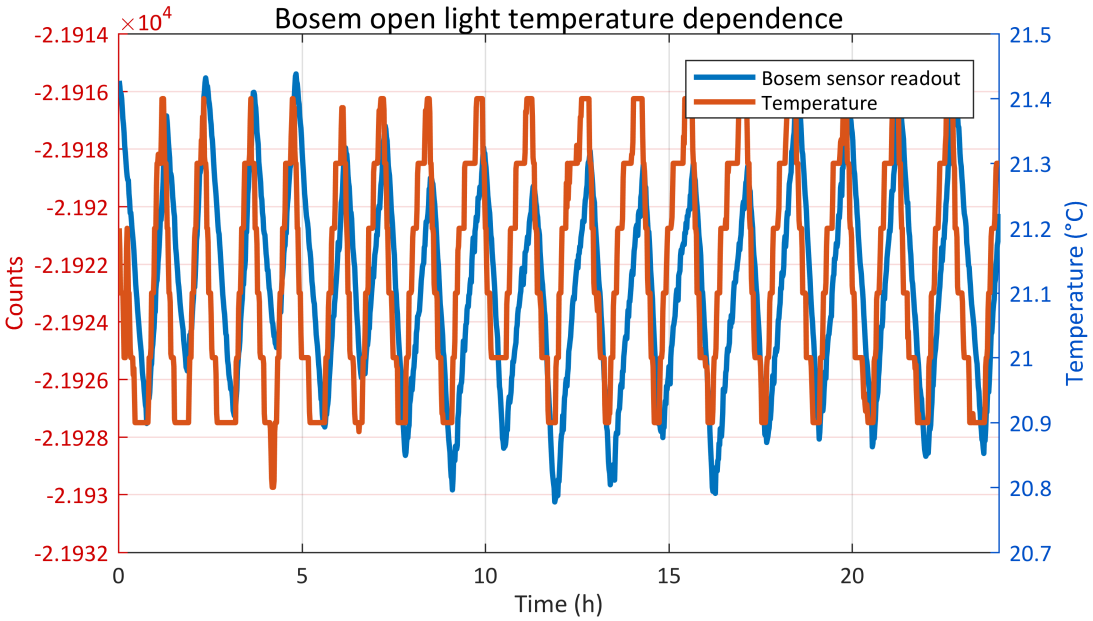

Figure 4.34: A measurement of the BOSEM output over 24 h. The fluctuations correspond to temperature changes in the lab, which is shown for comparison.

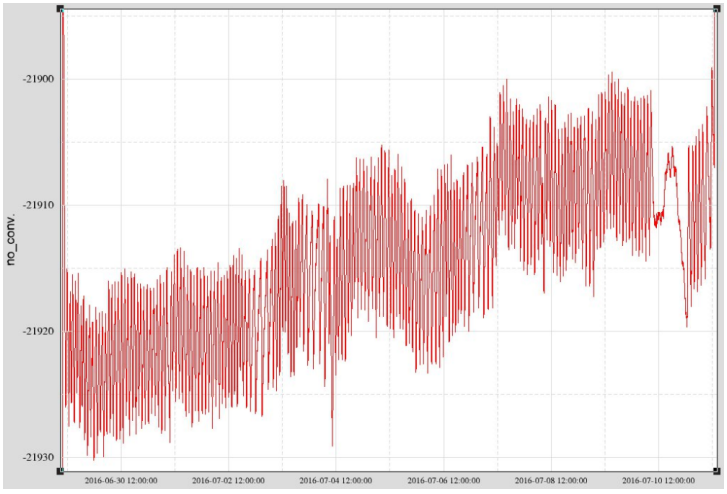

Figure 4.35: A measurement of the BOSEM output over 12 d. The short-term fluctuations correspond to temperature changes in the lab, the long-term drift is due to a slow degradation of the BOSEM sensor.

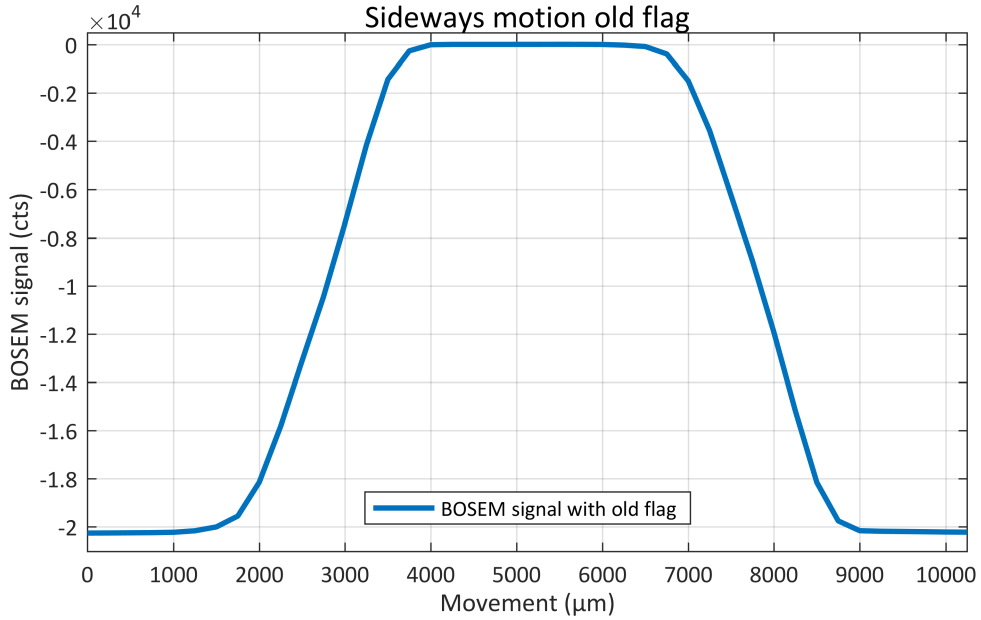

Figure 4.36: The power measured by the BOSEM as a function of the sideways flag position. In this plot, an old flag was used, having a width of 5 mm.

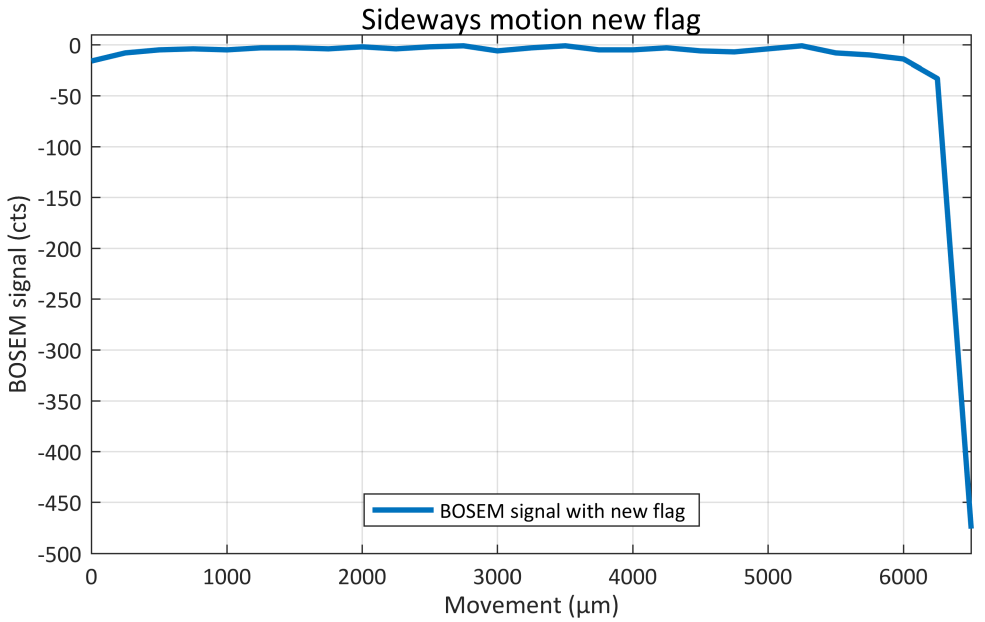

Figure 4.37: The power measured by the BOSEM as a function of the sideways flag position. In this plot, an new flag was used, having a width of 9 mm.

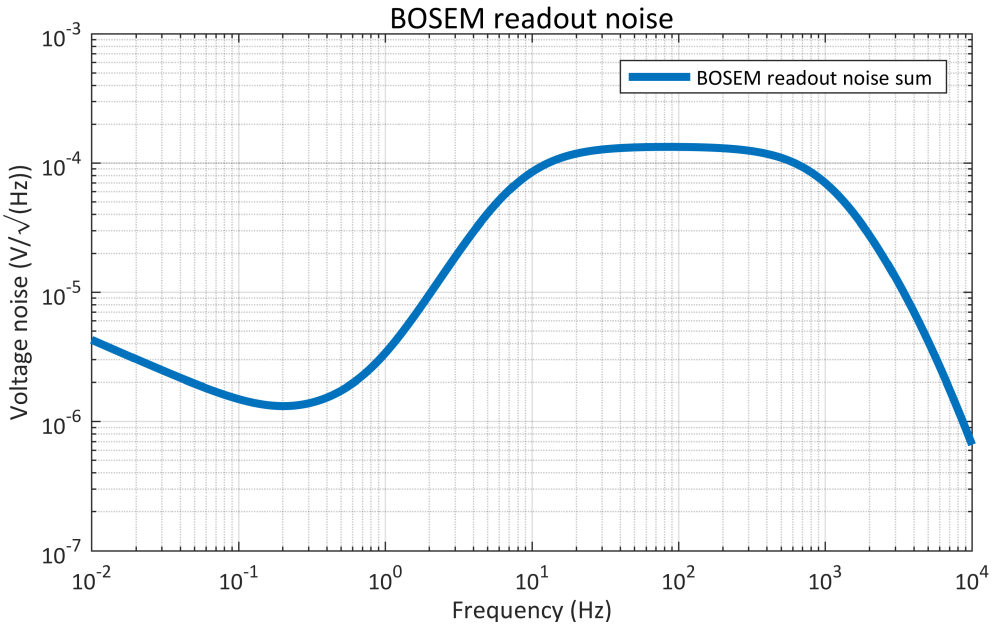

Figure 4.38: BOSEM readout noise as simulated using Zero.

Two possible signal paths follow, where one only consists of a differential sender with a lowpass with 10 kHz corner frequency, and the other one adds a whitening stage with two zeroes at 0.16 Hz and two poles at 8 Hz. Schematics and transfer functions of this electronic path can be found in Appendix B. Voltage noise, as calculated with the python-based tool Zero, developed by Sean Leavey (based on LISO by Gerhard Heinzel), is shown in figure 4.38. It is dominated by the transimpedance amplifier, as is shown in a more detailed noise plot in Appendix B.

4.4.2.1 Actuation

Actuation is supplied by the BOSEMs using a coil-magnet pair for each BOSEM. The coil is wound around the aluminum housing using 800 turns of Kapton coated wire of 0.15 mm diameter (shown in figure 4.31). This coil generates a magnetic field depending on the current flowing through it, which in turn is driven by a coil driver box.

The magnetic field then exerts a force onto a magnet glued to the bottom of the sensing flag. The position of the magnet relative to the coil is chosen such that it is at the point in the magnetic field where the sensitivity of the force to the relative position vanishes. This provides isolation against the coupling of seismic motion of the BOSEM to the suspension.

4.4.2.2 BOSEM coil driver

The BOSEM coil driver sends the actuation signal from CDS through a de-whitening-stage consisting of two poles at 0.16 Hz and two zeroes at 8 Hz. The current is then driven by an OP27, according to the voltage across a sensing resistor of 10 Ω. This value was chosen as the force required for the inital alignment is high. Improving the manual alignment by using the pushrods at the upper mass and intermediate mass can enable the use of larger sensing resistors.

The sensing resistor increases the output noise significantly, but the effect on the test mass is small due to the isolation by the triple suspension. Simulations are performed with Zero, giving the current noise (shown in figure 4.39) and the input-referred voltage noise (shown in figure 4.40).

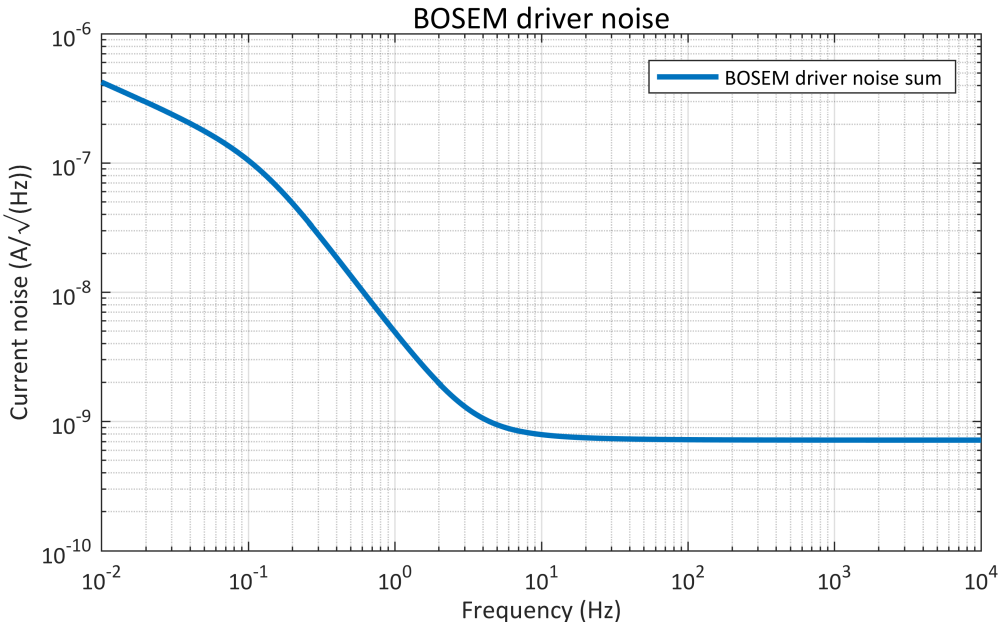

Figure 4.39: Current noise of the BOSEM coil driver.

Detailed noise plots along with the transfer function and schematics can be found in Appendix B.

4.4.3 Damping loops

Damping the lowest resonances of the suspensions is fundamental to reducing the rms motion of the test masses, thereby offloading the actuators used for locking. In the TNI, an active approach has been chosen to gain freedom in designing the feedback loop shape, which helps in reducing sensor and actuator noise coupling into the measurement band.

Each suspension has six BOSEMs located around the top mass, which sense all six degrees of freedom, so there are several choices for how to implement digital damping loops. They all have in common that the position signals sensed by the BOSEMs are digitized and sent through filters to shape the frequency response as desired before supplying the signals to analog coil drivers. These produce a current in the BOSEM coils acting onto the magnets attached to the upper mass.

The signal sensed by a single BOSEM can then be fed back to the same BOSEM, creating in total six SISO-systems, and this approach is currently being used in the TNI (shown in figure 4.41). A more complex approach would be using a matrix of damping filters which maps all the incoming BOSEM signals to all the BOSEM actuators. So called degree of freedom damping, where BOSEM signals are combined in physical degrees of freedom, is a special case of this approach. While this might offer slightly better performance, it has been shown that the TNI in its current state is sufficiently damped by the simpler approach and can even be operated without damping while being locked in vacuum (see section 6.11.2).

One damping loop shape has been adopted for all BOSEMs, making the loop gain the only variable part. The loop gain needs to be adjusted depending on the stiffness of the degrees of freedom on which this BOSEM acts. The shape of the filter is shown as a Bode Plot in figure 4.42. The performance has been evaluated in vacuum, where acoustic coupling and airflow are suppressed, on a seismically isolated table, as shown in figure 4.44. The influence of damping on the noise performance of the TNI is detailed in section 6.11.2.

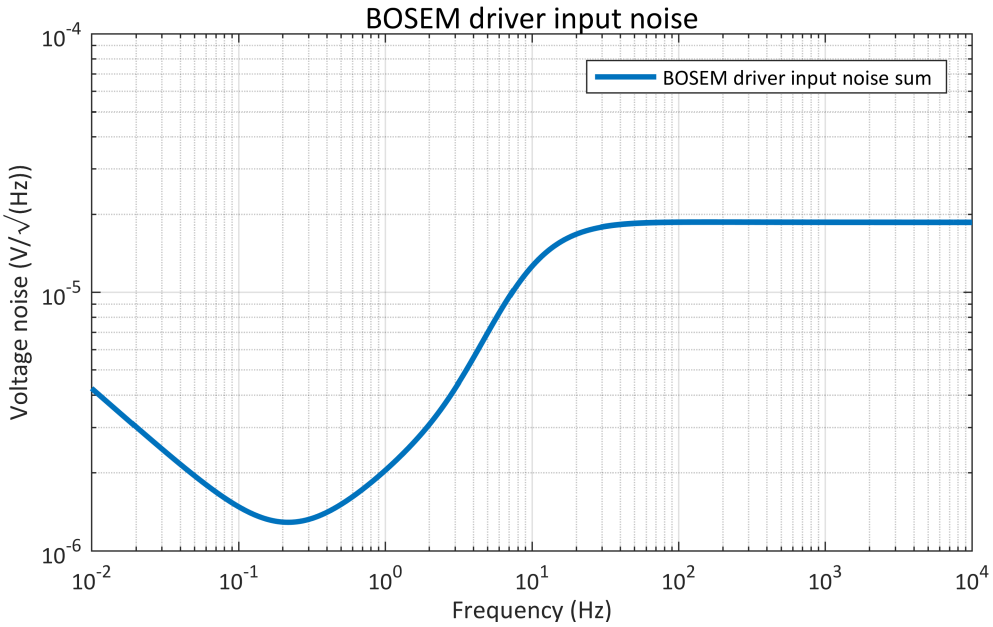

Figure 4.40: Voltage noise of the BOSEM coil driver as simulated by Zero.

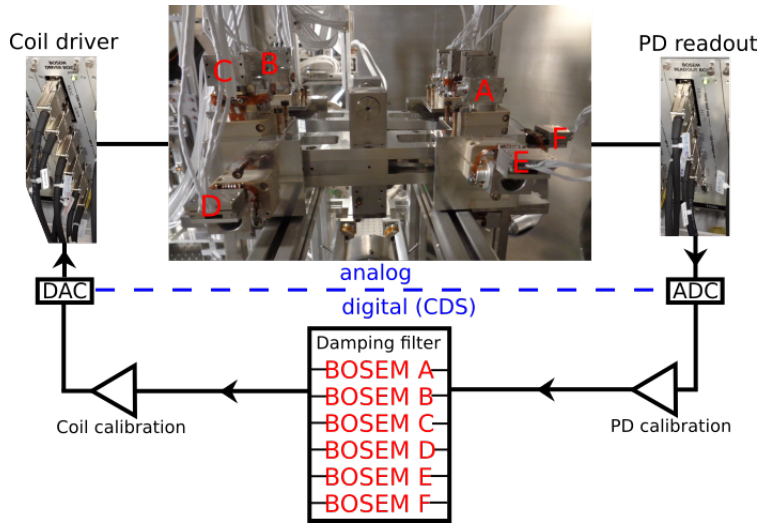

Figure 4.41: Diagrammatic representation of the BOSEM-to-BOSEM damping loops. The photodiodes of BOSEMS A-F sense the position, and the resulting signal is sent into digital damping filters through the PD readout electronics, the ADC and calibration filters. The resulting error signals again are sent through calibration filters before leaving the CDS through the DAC. In the coil driver electronics, the voltages from the CDS are translated into currents, which act on the suspension through the BOSEM coil-magnet pairs.

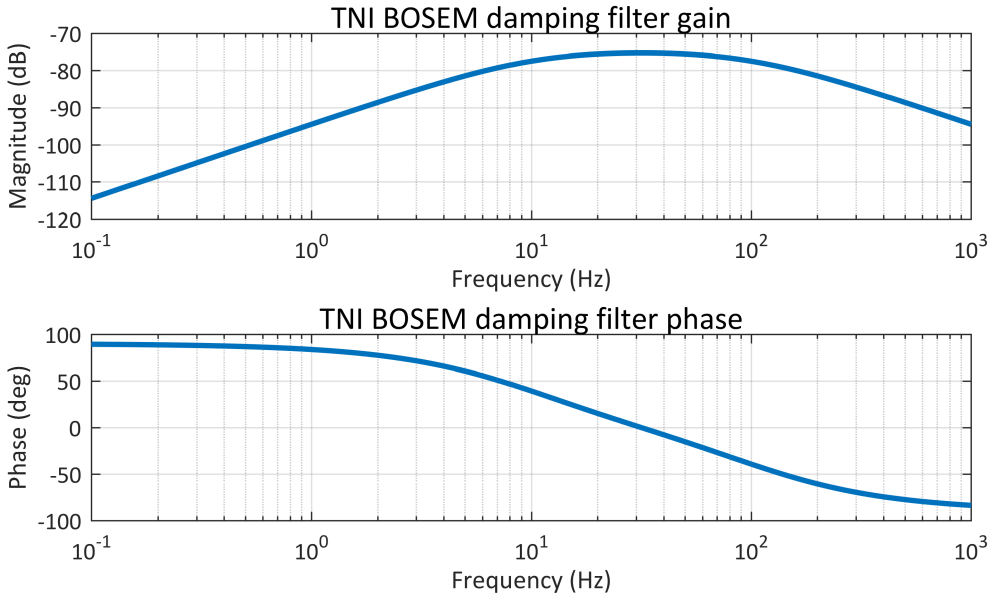

Figure 4.42: The transfer function for the filter used in the BOSEM damping loops. In the upper plot, the magnitude is shown. The bottom plot shows the corresponding phase response. Less phase loss at the suspension resonances was a main concern for the new design.

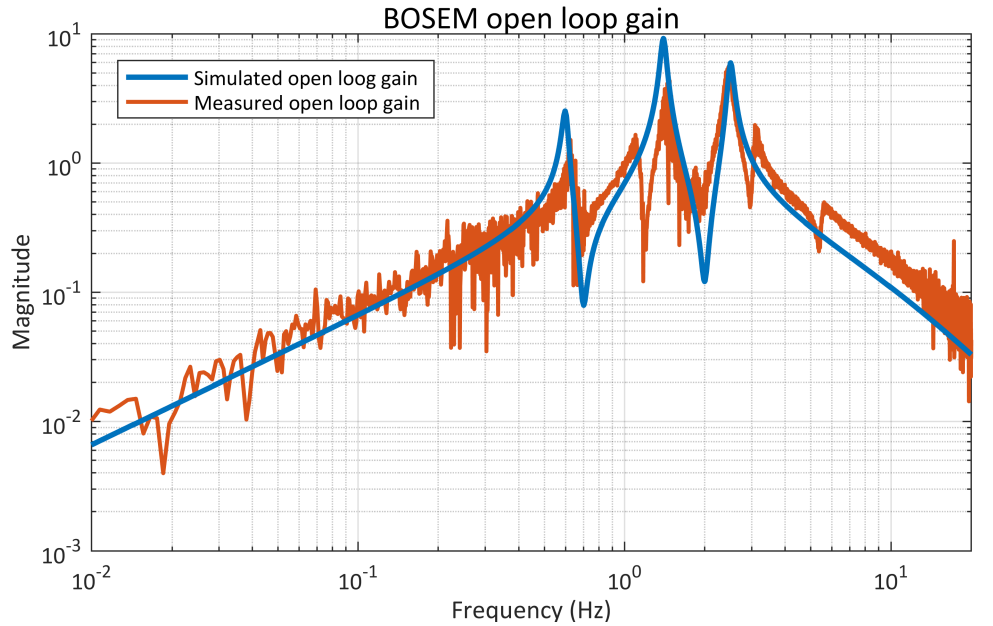

Figure 4.43: Open loop gain of the BOSEM damping loop. Shown are the calculated (blue) and measured (red) open loop gain for BOSEM D of suspension A. Differences arise mainly from cross-coupling neglected in the simplified modelling.

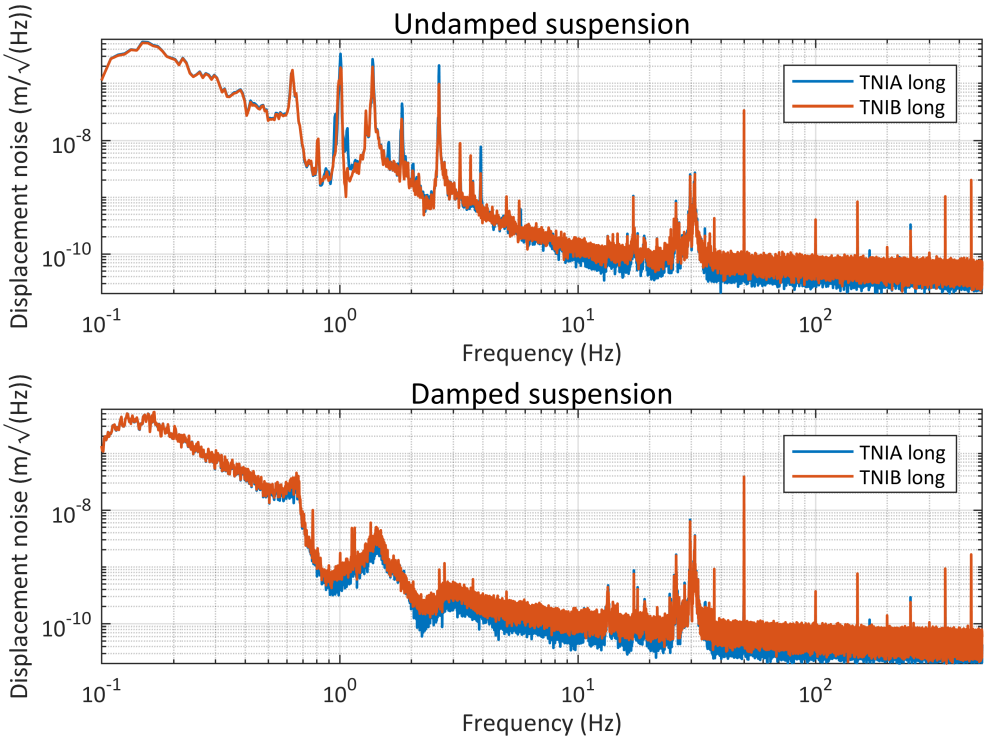

Figure 4.44: Spectra measured by the BOSEMs, without damping on the top and with damping on the bottom in the longitudinal degree of freedom for both suspensions. A clear reduction is visible at the fundamental resonances between 0.6 Hz and 6 Hz.

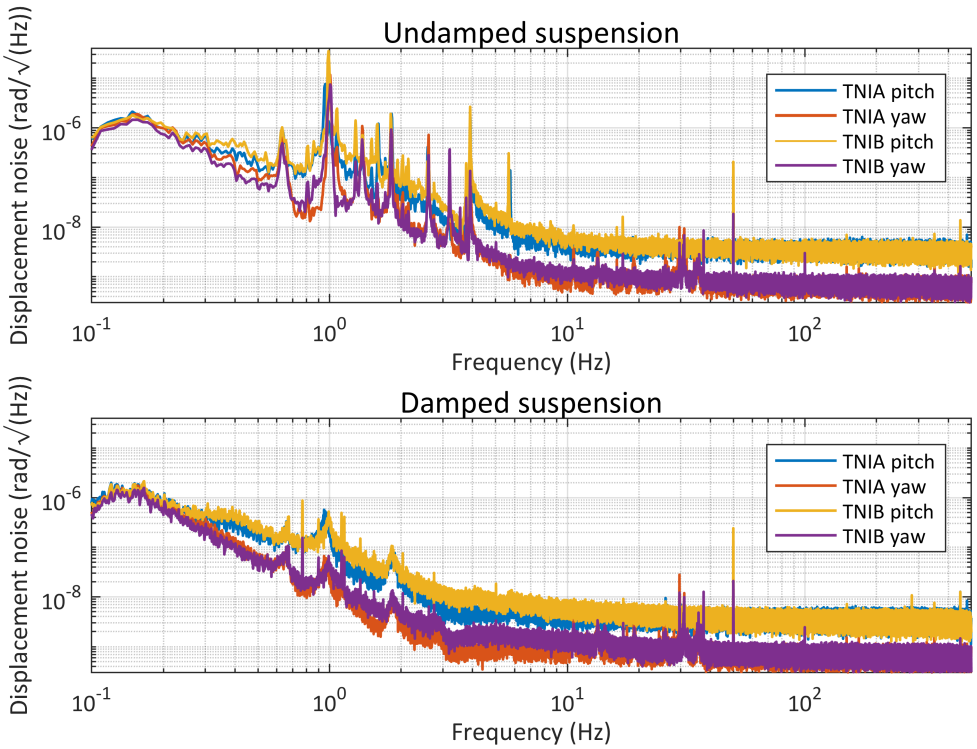

Figure 4.45: Spectra measured by the BOSEMs, without damping on the top and with damping on the bottom in the pitch and yaw degrees of freedom for both suspensions. A clear reduction is visible at the fundamental resonances between 0.6 Hz and 6 Hz.

Figure 4.46: The TNI cage sitting on the optical table in the south tank. It consists of aluminum profiles made by ITEM, which are screwed onto a baseplate.

4.5 Mechanical setup

There were two main design goals for the mechanical parts of the TNI including the cage, attached catchers and support structures as well as for the in-vacuum cabling. The first was to ensure mechanical stability while not compromising the seismic attenuation performance of the seismic attenuation tables and suspension. The second was to only use vacuum compatible components having outgassing rates low enough to not limit the quality of vacuum inside the AEI 10 m prototype vacuum system.

4.5.1 Cage

The TNI cage is constructed from vacuum compatible item aluminum profiles, providing the stability and attachment points required for mounting the two mirror suspensions (shown in figure 4.46).

4.5.2 Blade holders

Mounted to the uppermost part of the cage are two sliding structures ((1) in figure 4.47), which themselves hold the upper stage blades (4). The sliding structures are height adjustable (indicated by vertical red arrow) by using vertical screws (2) to enable vertical positioning of the suspension chains, making it possible to place the test masses at the beam height of 10 cm above the table. As the blades are mounted on top of the sliding structures, they exert torque onto their base, which inhibits the sliding motion while adjusting the longitudinal position (indicated by horizontal red arrow) of the suspension. Counteracting this torque is achieved by connecting two opposite sliding structures belonging to the same suspension using a rigid beam (3).

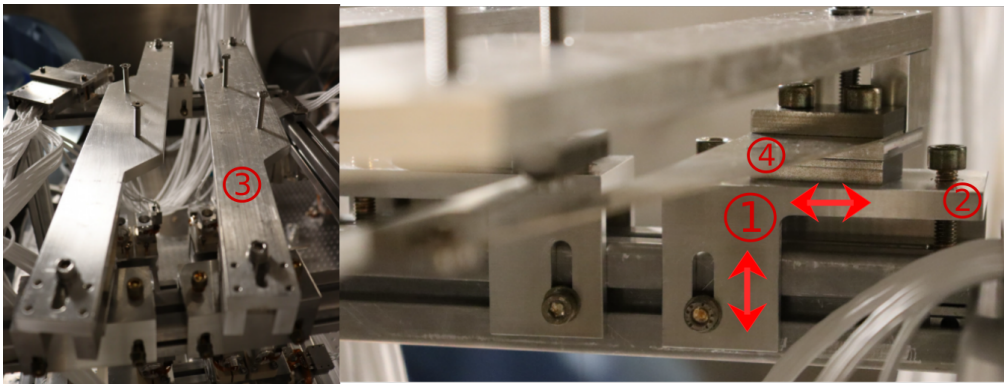

Figure 4.47: A blade holder made from aluminum (1) holds the steel blocks clamping the blade (4) in place. The blade holder itself can be moved along the ITEM profile (horizontal red arrow) to change the TNI cavity length. Two vertical screws (2) allow changing the mirror height above the table (vertical red arrow). To counter the torque created by the suspension at the blade holders, aluminum bars (3) rigidly connect opposing blade holders.

4.5.3 BOSEM holders

Around the upper mass, a cage composed of two parts is placed (shown as (1) and (2) in figure 4.48). This has been changed from a monolithic design to improve the adjustability of the BOSEM holder. Each of the two parts is connected to the item profile such that adjustability in three axes is realized (indicated by red arrows in right picture), based on parts screwed together via slot holes.

Apart from clamping the upper mass by screws for transport and mechanical work, the cage is designed to hold the BOSEMs in place. As the BOSEMs are used as a sensitive position sensor for the upper mass, they have to be adjustable to have the upper mass flags in the middle of their range without any mechanical short circuits. This requires individual sideways adjustability of each BOSEM (red arrow in left picture), as well as fine tuning the depth of the BOSEM inside its clamp (green arrow in left picture). Sideways adjustability is ensured by PEEK holders (5) with enlarged screw holes (4). The PEEK holders also allow adjusting the BOSEM depth by lowering the clamping force (releasing tension on the gap (3)) and pushing or pulling on the BOSEM.

4.5.4 Coil holders

The coil holders for the intermediate mass and lower mass have to fulfil the same requirements as the upper mass cage. They have to provide adjustability in three dimensions, moving the coil actuators relative to the magnets connected to the masses. Furthermore, clamping of the masses for transport and mechanical work has to be ensured, while also working as a catcher in case wires break.

This is achieved by an intricate holding structure, as shown in figure 4.49. The adjustability is provided by a screwing parts together via slot holes, and is indicated by the red arrows. The most important part of positioning is setting the distance between the coil and the magnet, defining the force per current acting on the mass. This positioning can be achieved with mm precision, limited by visual judgment of the distance. The other degrees of freedom have to be adjusted such that no risk of the magnet touching the coil prevails.

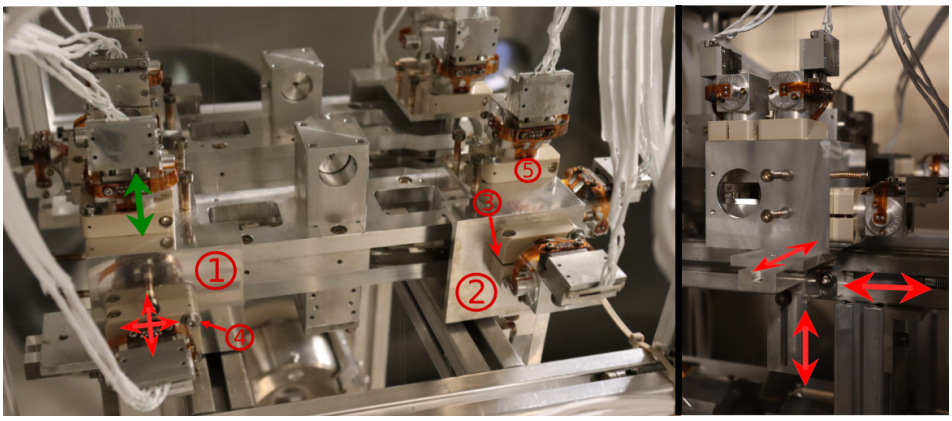

Figure 4.48: Aluminum structures holding the BOSEMs in place while serving as clamping structures for the uppermass ((1) and (2)). This is necessary when moving the cage and for shifting pushrods inside the uppermass for pitch and roll alignment. A clamp made of PEEK (5) for holding the BOSEMs is attached to this structure by enlarged screw holes (4) for lateral adjustment (red arrows in left picture). Untightening the clamping screw across the gap (3) allows positioning the BOSEM LED and PD relative to the flag (green arrow in left picture). The structure as a whole can be moved in three dimensions (indicated by red arrows in the right picture).

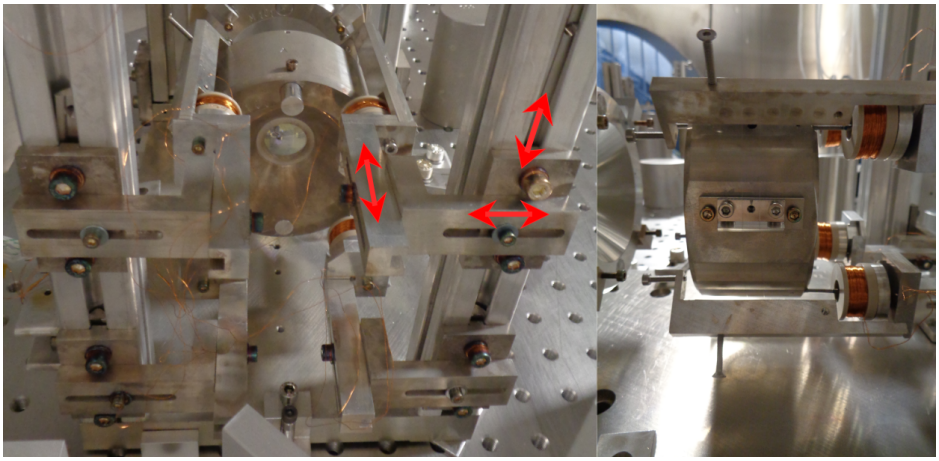

Figure 4.49: The coil holders are attached to aluminum parts, which enable individual positioning of the coils along three axes (indicated as red arrows). This is necessary to place the magnet in the sweet spot of the coil while keeping enough clearance.

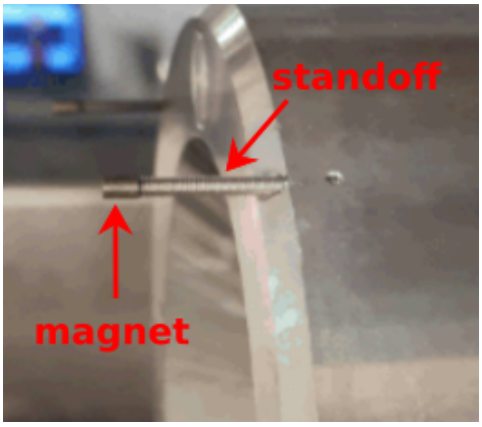

Figure 4.50: Threaded stainless steel standoff with the magnet used for test mass actuation glued on top. The standoff is tightly screwed into the aluminum test mass.

4.6 Length stabilization

The locking loop is a core part of the TNI, providing length stabilization and thereby keeping the cavity at its operating point inside the linear range of the error signal. This is needed to enable highly sensitive measurements of length changes. For this to be achieved, the feedback loop has to be stable and designed in such a way that it suppresses any excess motion while not introducing noise in the measurement band. Lock acquisition poses additional constraints on the loop used.

The basic scheme used for locking the TNI cavity is the so called Pound-Drever-Hall scheme (PDH, [Bla01]), which utilizes the phase difference between promptly reflected light and light interacting with the mirror surfaces to asses length changes of the cavity. A diagrammatic representation of the PDH scheme of the TNI with its main components is shown in figure 4.59.

In the subsequent subsections, the sensor (photodetector) and the actuator (coil-magnet pairs) are discussed in more detail, before describing the different evolutionary stages of locking loops used in the TNI.

4.6.1 Coil actuators

Actuation on the intermediate mass and test mass of the input suspension is achieved using coil-magnet actuators. The coils are mounted on adjustable holders as shown above. The magnets are glued onto threaded rods, which themselves are screwed into the suspended mass (shown in figure 4.50). This standoff structure helps positioning the magnet in the sweet spot of the coil while still maintaining a safe level of clearance between the mass and the coil. The cylindrical magnets used are made of a Samarium-Cobalt alloy with a diameter of 1 mm and a height of 1 mm. They have been chosen to be as small as possible while still offering enough actuation for locking with realistic currents inside the coils.

For each mass, four coil-magnet pairs are in use. The position of the magnet relative to the coil has been chosen to be in the sweet spot at 5.7 mm inside the coil, the position of minimal displacement dependence of the force. Sweet spot calculations are done using a Mathematica script written by Mark Barton [Bar], taking magnet and coil parameters as input and giving a force per current plot showing the extremal value and the slope around it (shown in figure 4.51). For the currently used Samarium-Cobalt magnet of length and diameter 1 mm and 400 turns for the coil wire, the resulting force per current is 0.001 39 N/A.

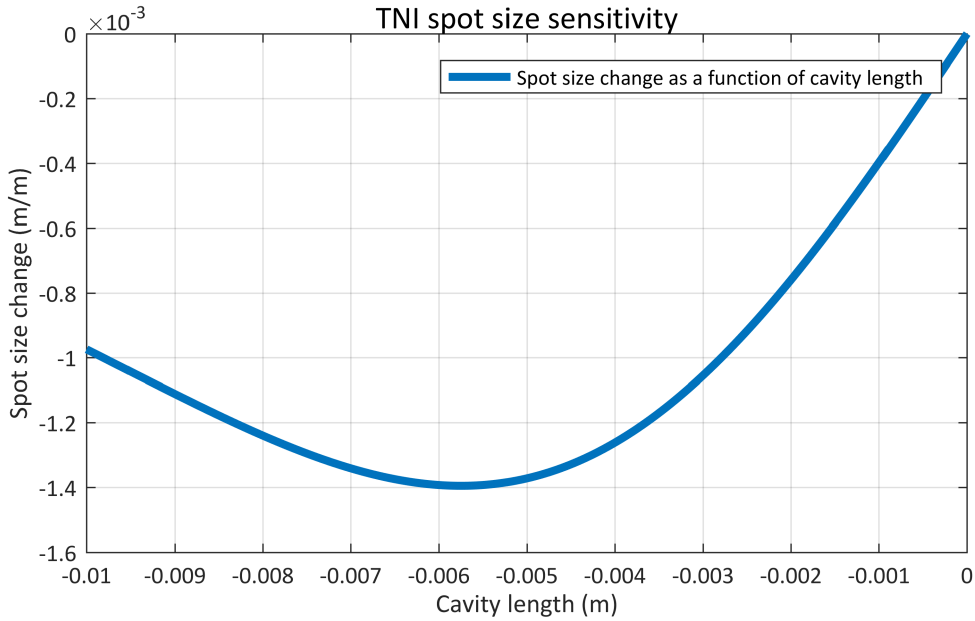

Figure 4.51: The force per current available for the coil-magnet pairs as a function of coi-magnet separation. At the extremum, the first derivative vanishes, reducing the sensitivity of the force to relative motion between magnet and coil.

4.6.1.1 Test mass coil driver

The coil driver for the test mass has been designed to provide low noise actuation. Its basic layout is shown in Appendix B. The input consists of a differential receiver as the signal coming from CDS through the DAC and AI-filter is sent differentially. Next in line is a de-whitening-stage having two poles at 1 Hz and two zeroes at 10 Hz, countering the whitening applied digitally in CDS. This is necessary as the high frequency response, being reduced by the free mass transfer function, has to be increased such that signals show up above the intrinsic DAC noise. After de-whitening, an OP27 drives the current according to the voltage drop across a sensing resistor of 499 Ω, with an amplifying BUF634 in series to supply up to 250 mA. With the current sensing resistor, the maximum current expected is 20 mA, sacrificing actuator strength for noise performance.

Using Zero, the current noise (shown in figure 4.52) as well as the input-referred voltage noise (shown in figure 4.53) are simulated. The input-referred voltage noise is close to the DAC-noise estimated to be at $9 \times 10^{-7}\,\mathrm{V}/\sqrt{\mathrm{Hz}}$. Creating electronics with less noise is not necessary as the DAC noise will then be the dominating contribution. The transfer function as well as more detailed noise plots can be found in Appendix B.

4.6.2 Photodetector

The photodetector used for locking the TNI is the most critical component in the locking loop regarding noise, as the sensor noise cannot be suppressed by the loop gain. This requires the photodetector to be shot noise limited at the light powers being used. The current locking PD in the TNI is based on a design by Henning Vahlbruch and Fabian Meylahn, having modified gain stages and filters to achieve shot noise limited performance at powers as low as 5 mW.

A simplified diagram is shown in figure 4.54, and the full schematic can be found in figure B.12 in B.

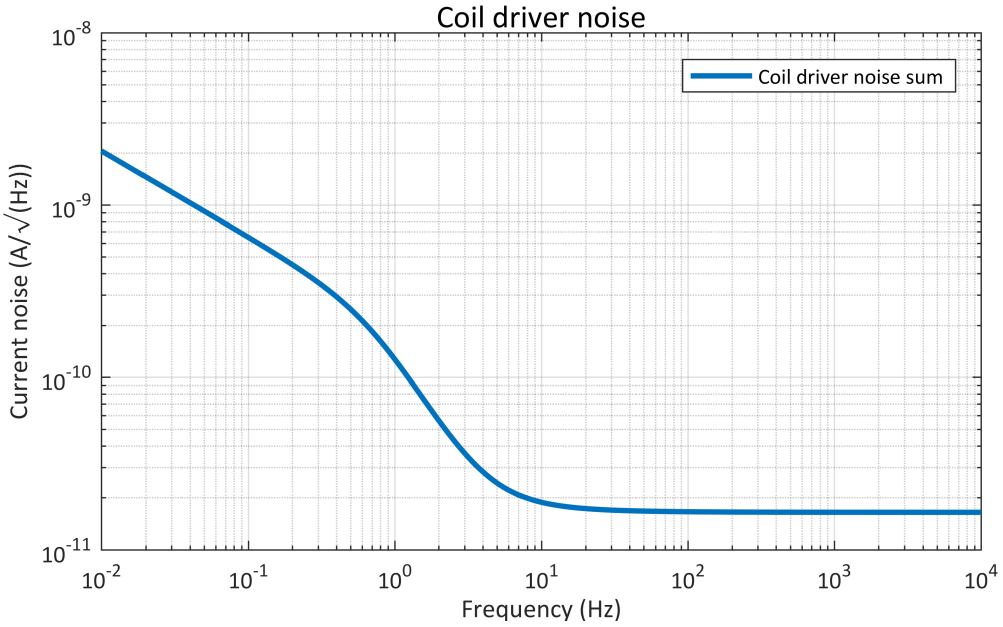

Figure 4.52: Current noise of the test mass coil driver as simulated by Zero. Johnson noise of the resistor dominates at higher frequencies, while current noise of the op amp dominates low frequencies.

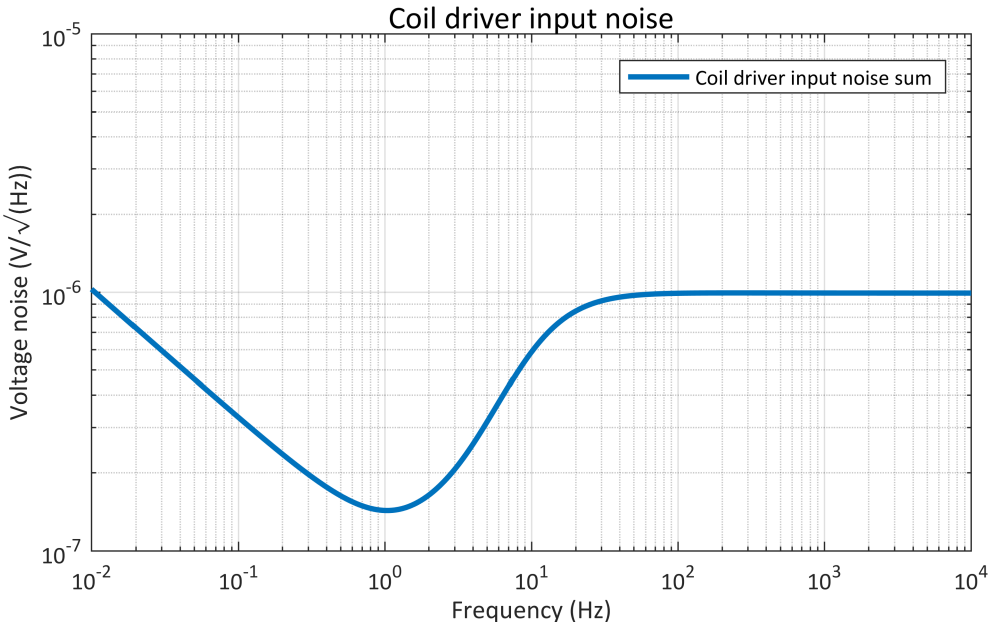

Figure 4.53: Voltage noise of the test mass coil driver as simulated by Zero.

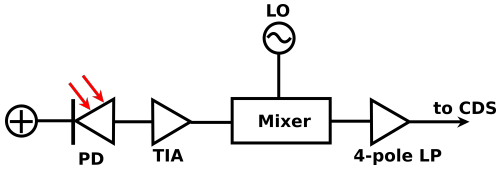

Figure 4.54: Schematic diagram of the locking PD electronics. The photodiode (PD) has the cathode connected to positive bias voltage. The resulting photocurrent is converted to a voltage in the transimpedance amplifier (TIA). Its output is demodulated in the mixer with the local oscillator (LO) signal. The result is amplified in a four pole low pass (4-pole LP) and sent differentially to the digital data acquisition system (CDS).

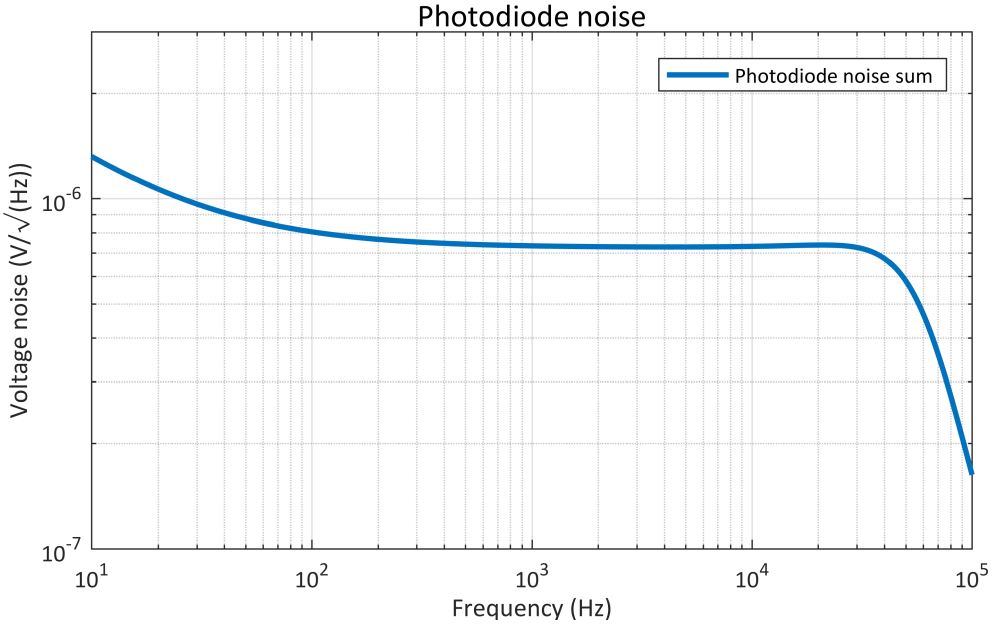

Figure 4.55: Total electronic noise of the locking PD as simulated in Zero.

The electronics consist of a transimpedance amplifier, converting the photocurrent to a voltage with a gain of 820 using a 330 Ω resistor. The signal is then mixed with the local oscillator running at the modulation frequency of 8.047 MHz, and finally encounters two more amplification stages containing two two-pole low pass filters with a gain of 25 each.

The resulting noise, simulated in Zero, is shown in figure 4.55, and a more detailed noise budget can be found in figure B.13 in B. This ensures that the noise is above CDS noise. Being designed to be shot noise limited thus enables the TNI to sense the shot noise in CDS. Furthermore, the design achieved the goal of not being saturated when the cavity is locked, although saturation is acceptable in the unlocked state.

4.6.3 Locking loops

There were several iterations of locking loops throughout the history of the TNI, catering to the needs at that time. The starting point after placing the TNI on an outside detection bench was a setup using the PZT as the primary feedback actuator and later adding the test mass coil actuators. This setup was used to characterize the suspensions and the coil actuators. From

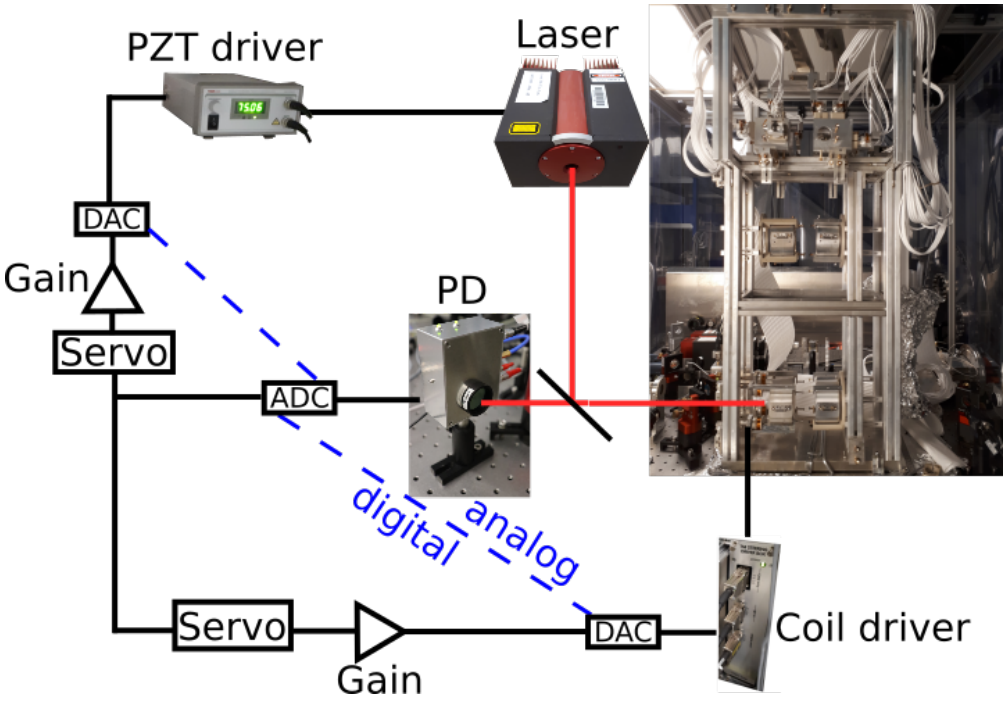

Figure 4.56: Schematic representation of the PZT and coil locking loop. The photodiode (PD) measures the frequency difference between the Laser and the cavity eigenmode. The derived error signal is fed back to the Laser PZT via a digital servo and an analog PZT driver. A second loop, operating at lower frequencies, acts on the coil-magnet pairs of the test mass via a digital servo and coil driver electronics.

the results obtained, locking loops incorporating the test mass coil actuators together with the laser PZT were developed and tested, resulting in the ability to make a complete transfer of the feedback actuation to the coil actuators in lock.

After the TNI returned into vacuum, lock acquisition and steady state operation using only the test mass coils were studied, resulting in the latest measurements with optimized loops to reduce the feedback forces used. A transfer to the intermediate mass coil actuators in lock was studied and achieved as well, which could in principle reduce noise coupling into the measurement band if feedback noise of the test mass actuators would be too high.

4.6.3.1 PZT and coil feedback

The first attempts in locking the TNI in the commissioning process were done outside of vacuum on a standard breadboard without any seismic isolation. Seismic excitation and air currents are the main disturbances, complicating the lock acquisition process. Light was supplied by a table-top NPRO laser running at 1064 nm (Innolight/Coherent Mephisto, output of 300 mW), and a broadband EOM of type 4004 by Newport was used to imprint the sidebands used in the PDH-scheme (shown in figure 4.56).

Feedback was supplied to the PZT pushing on the NPRO-crystal. The PZT was driven by a high voltage amplifier of type MDT694B made by Thorlabs and was used for lock acquisition and feedback at higher frequencies above 5 Hz, while the coils were used to keep the PZT in range, acting as an integrator. This setup was used to characterize the suspensions and optics, as well as identifying possible mechanical and optical problems.

One of the first short locks achieved using just the PZT path is shown in figure 4.57. The locked

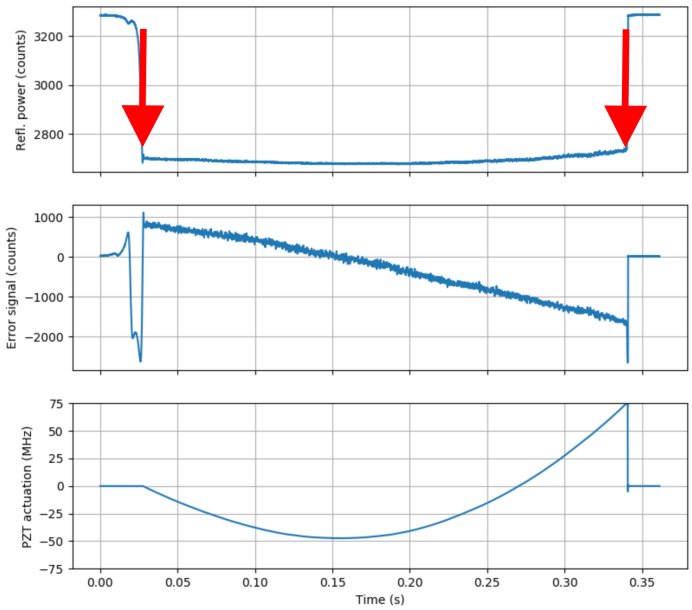

Figure 4.57: A short lock using the PZT as the actuator in the feedback loop.

state can be inferred from the drop in the reflected power, visible between the red arrows. A linear drift in the error signal is observed, which is countered by the PZT until the end of its dynamic range is reached. The lock is lost, and the need for an integrator with a larger dynamic range is obvious, subsequently realized by using coil actuators.

These first locks were done with lossy mirrors reducing the Finesse of the cavity, and thereby widening the linear range of the error signal, making lock acquisition relatively easy. After exchanging optics, the digital loop for the PZT was not sufficient for lock acquisition, so this part of the feedback was outsourced to an analog servo box triggered by digital signals.

4.6.3.2 First coils-only feedback

Starting with the locking procedure described above, the lower mass coil actuators were subsequently more and more integrated into the locking loop. By ramping up their gain, a crossover to the PZT actuation at 5 Hz was realized (shown in figure 4.58). Switching filters to achieve a stable coils-only loop enabled ramping down the gain of the PZT feedback loop. This lead to a stable lock only relying on coil feedback, stable over many hours, serving as the basis for lock acquisition using just the coils.

4.6.3.3 Low noise coil feedback

Locking the TNI in a low noise state to enable measurements of mirror thermal noise requires moving into vacuum onto a seismic isolation platform. In vacuum, the light is taken from the pre-stabilized main laser. This laser can not be frequency modulated for the TNI because it is already locked to the frequency reference cavity, so the TNI can only use its own coils to acquire lock. For lock acquisition, the damped cavity was pushed close to a resonance and left freely

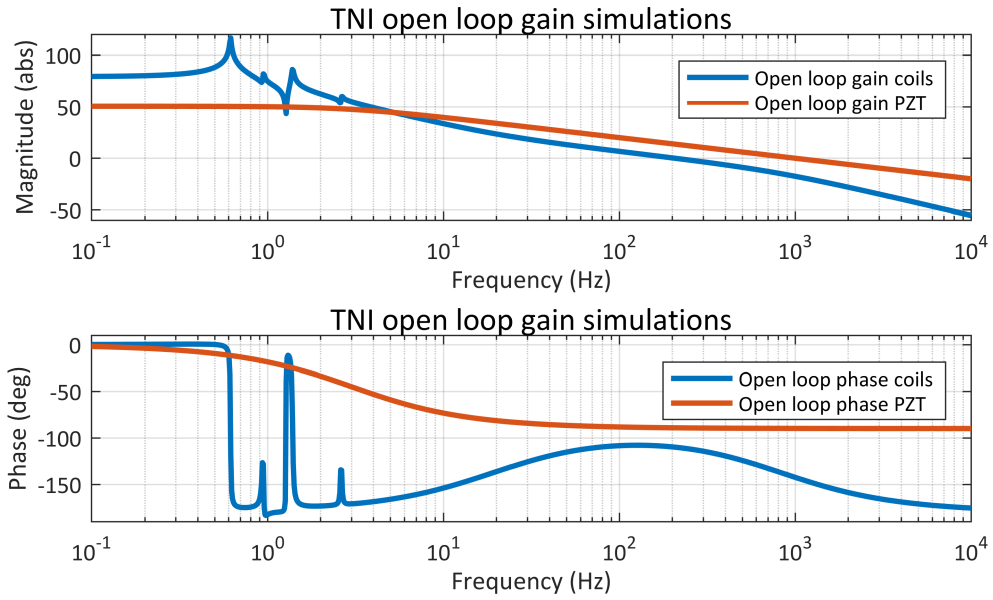

Figure 4.58: Open loop transfer function of the PZT feedback in red and the coil feedback in green. The upper plot shows the magnitude, where the crossover at 5 Hz is visible. The lower plot shows the phase, where the phase difference at the crossover frequency can be read as 110°, making the crossover stable.

swinging with the loop engaged without the integrator. When the conditions are right, lock is achieved and the integrator and low frequency boost can be engaged. A schematic diagram of the locking loop using only coils as actuators is shown in figure 4.59. The error signal generated by the photodiode is digitized, sent through a digital servo and then applied to the test mass coils via a coil driver.

Two types of servo loops were found to provide low noise feedback as well as repeatable lock acquisition. The more robust one can be tuned to have unity gain frequencies (UGF) between 20 Hz and a few hundred Hertz and consists of a loop gain, an integrator and a low frequency boost, shown in figure 4.60. With this loop, lock acquisition is robust, even with elevated levels of ground motion. The disadvantage is the possibility of coupling in actuator noise at frequencies where coating Brownian noise is expected to dominate.

A typical measured open loop gain is shown in figure 4.61, having a unity gain frequency of 54.3 Hz. To achieve unity gain frequencies between 10 Hz and 16 Hz, a modified loop was used, increasing the phase margin at the unity gain frequency of interest. The loop is shown in figure 4.62. With this loop, again reliable lock acquisition and stable locks were possible, although with more restrictions on the level of seismic motion. Noise introduced by the feedback loop should be restricted to frequencies around and below the unity gain frequency, not allowing inferences of the overall influence of feedback loop noise on the TNI spectrum in comparison to higher UGF locking loops, but also enabling the characterization of thermal noise down to lower frequencies.

4.6.3.4 Intermediate mass coil feedback

After having achieved low noise locks using the test mass coils with different unity gain frequencies, which fulfilled the requirements for measuring thermal noise, another configuration was studied, which could improve the noise performance if needed.

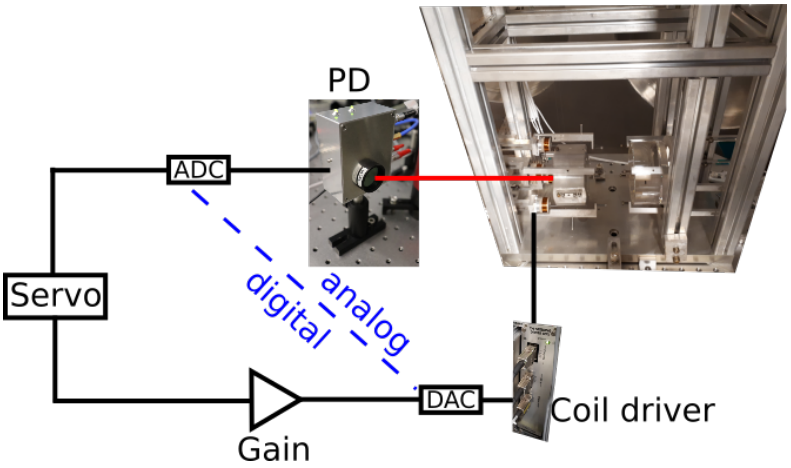

Figure 4.59: Schematic representation of the coils-only locking loop. Light reflected from the TNI is sensed by the photodiode, generating the error signal. This is digitized, sent through a servo and then applied to the test mass coils via a coil driver.

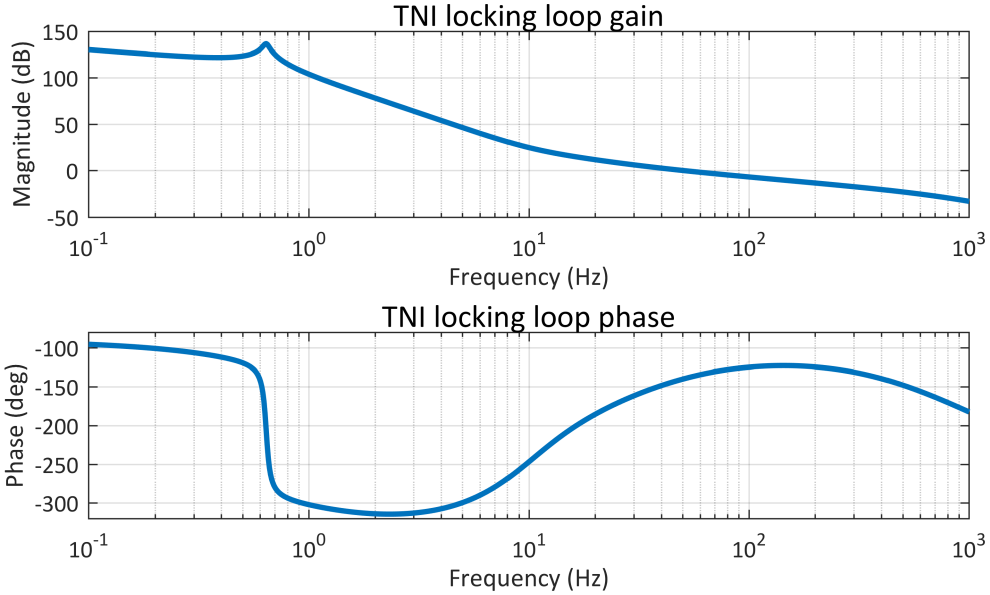

Figure 4.60: The open loop transfer function for the coils-only feedback loop used for all sensitive measurements in the TNI. The upper plot shows the magnitude, having the unity gain frequency at 80 Hz. There, the lower plot shows a phase margin of 50°.

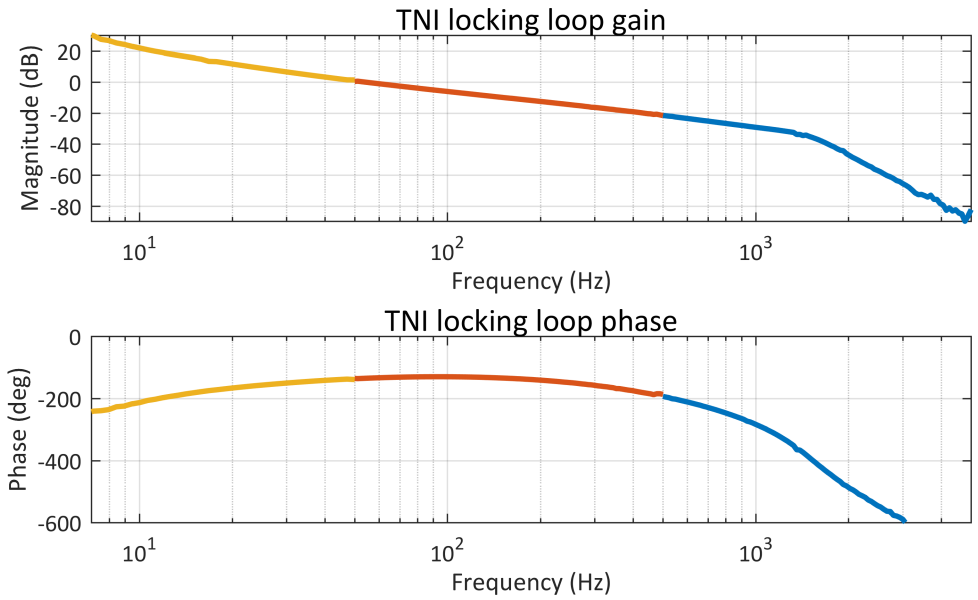

Figure 4.61: A typical measured open loop gain for feedback at the test mass coils. The unity gain frequency in this case is at 54.3 Hz.

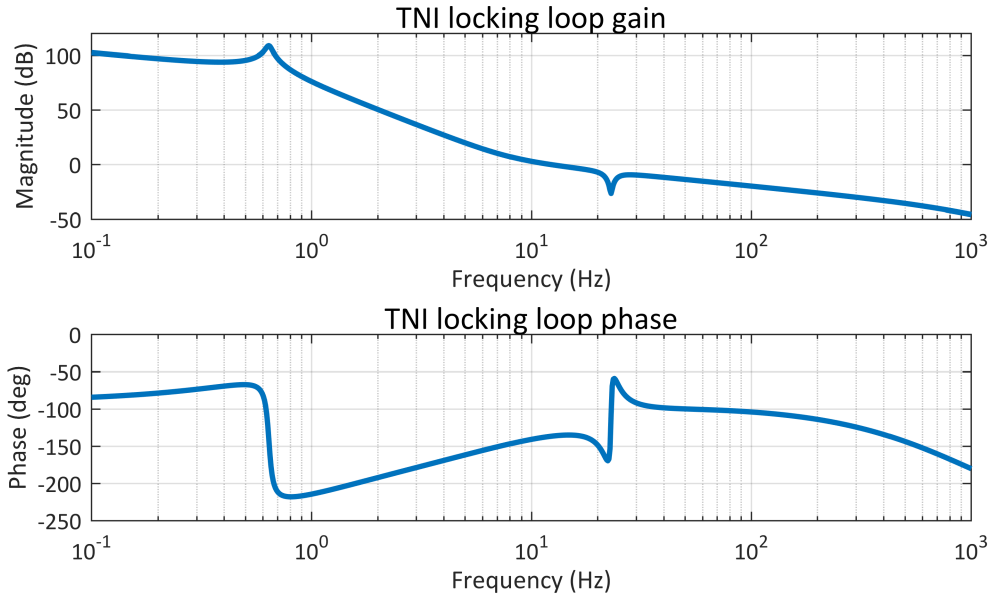

Figure 4.62: Open loop transfer function for a low unity gain frequency loop design. To achieve unity gain freuquencies around 12 Hz, the slope and phase response have to be changed compared to the standard loop in 4.60.

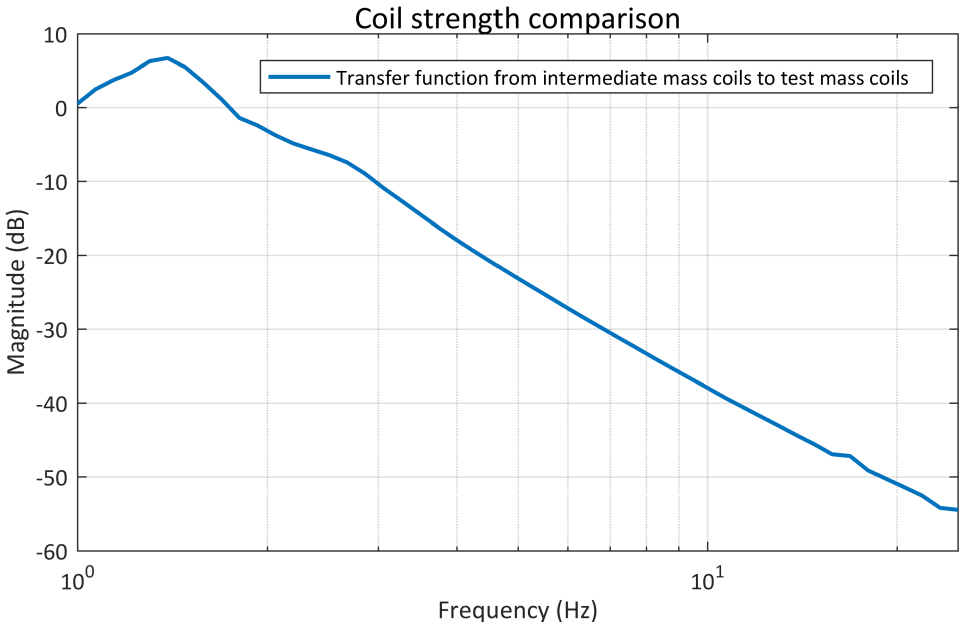

Figure 4.63: Measured transfer function from coil actuation at the intermediate mass to coil actuation at the test mass. This serves as the basis for creating a feedback loop blending test mass actuation and intermediate mass actuation.

Using only the intermediate mass coil actuators promises lower feedback noise coupling into the measurement band, as the last suspension stage acts as a filter with a $\frac{1}{f^2}$ slope above 2.6 Hz. It was not possible to acquire lock using only the intermediate mass coils because of limitations in high frequency actuation, so a hybrid scheme was used where the test mass coils acquire lock as explained before. After that, the gain for the intermediate mass coils are ramped up in a crossover configuration, and finally a handover is performed such that all feedback is supplied by the intermediate mass actuators.

The loop design was based on a comparison of the actuator transfer functions of lower mass coil actuators and intermediate mass coil actuators. This comparison was achieved by measuring the transfer function from an excitation on the intermediate mass to the actuation in lock of the lower mass coils, shown in figure 4.63. A stable crossover configuration was found, starting from the low UGF locking loop using just the lower mass coils (shown in figure 4.64). Ramping up the intermediate mass actuator loop gain was complicated by the excitation of the violin modes of the suspension wires. More than 50 notch filters had to be employed to avoid driving the resonances, making the lock stable. In this configuration, a change in the intermediate mass loop gain was possible to create a stable loop using only the intermediate mass coils (shown in figure 4.65).

The loop gain of the lower mass coils was then ramped down so that a stable lock using only the intermediate mass actuators was achieved and the noise of the TNI in this configuration was examined. Ideally, the lower mass coils would not only have been ramped down such that there is no signal sent to the coil driver electronics, but also would have been completely disconnected such that no DAC noise and coil driver noise could couple into the TNI. Although several approaches were tried to disconnect the coils while in lock, there was an unavoidable electronic spike kicking the TNI out of lock.

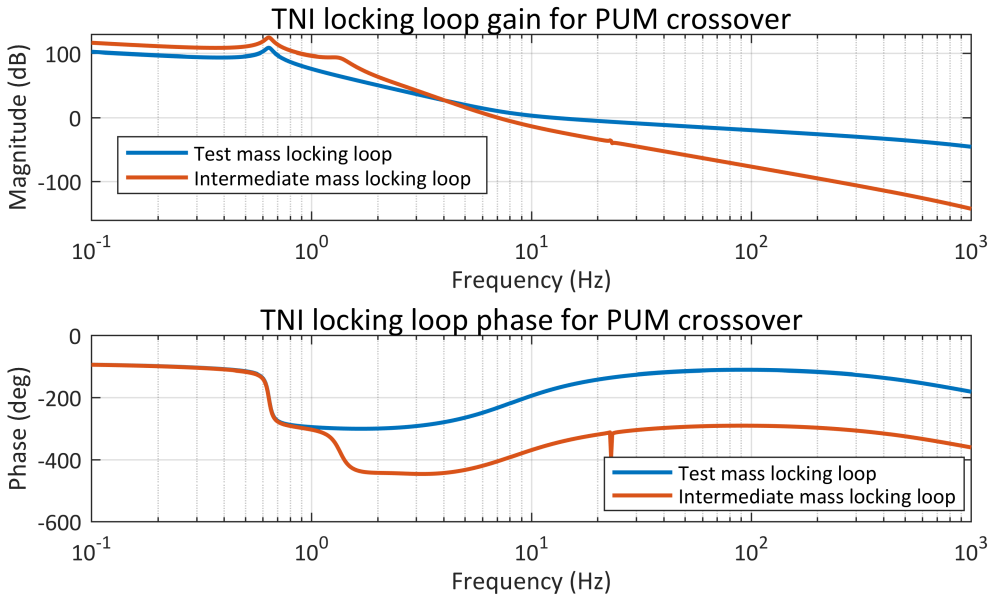

Figure 4.64: Open loop transfer function for blending intermediate mass feedback in red and lower mass feedback in blue. The crossover at 5 Hz is stable, because the phase response in the lower plot shows a difference of 150°.

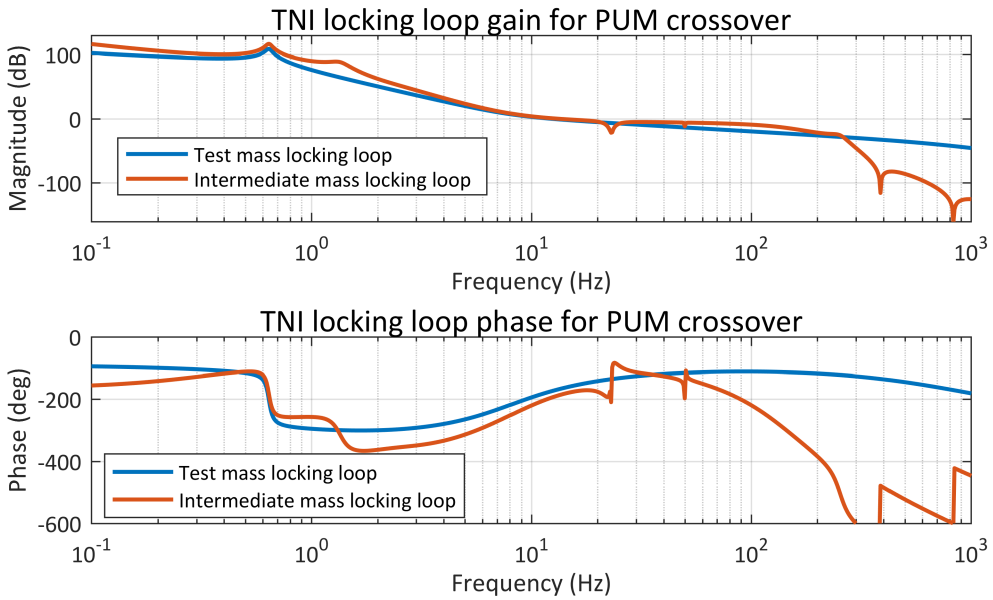

Figure 4.65: Open loop transfer function for intermediate mass only feedback. The intermediate mass feedback has to be stable on its own, while the test mass feedback is reduced and eventually turned off. At high frequencies, notch filters prevent excitation of violin modes.

4.7 Noise evolution

The displacement noise spectrum has been improved significantly over the last seven years (shown in figure 4.66). This has been achieved through commissioning described in section 4.3.2 and partly in chapter 6.

The starting point is the red trace, which shows a measurement done in 2014 before the start of this thesis. This measurement is dominated by frequency noise, and most probably suffers from seismic shortcuts in the suspension. This stems from the fact that the TNI had no length actuators at this point, relying on actuation on the main laser for locking. The reference cavity, also without length actuators, could not be locked simultaneously, leaving the frequency noise uncompensated. Furthermore, as significant work on the suspensions was found to be necessary, the seismic isolation performance before this thesis most likely was suboptimal.

After a long period of rebuilding the suspensions piece by piece outside of the vacuum, the TNI was moved back into vacuum in late 2019. The first measurement in vacuum in April 2020 is dominated by internal resonances of the aluminum holder-PEEK clamping screw-test mirror-system above 2 kHz. Glueing the mirrors into the aluminum holders led to a significant improvement, resulting in the yellow trace from September 2020.

Then, the spectrum was suffering from scattering at low frequencies. Improving the input and output path as well as the detection bench in terms of scattering removed the peaks at low frequencies, whereas the exchange of the old EOM and proper polarization control removed the peak close to 2 kHz. This led to the measured spectrum from May 2021 (green), which showed clear signs of thermal noise at frequencies above 100 Hz, at a level too high for coating Brownian thermal noise, which is shown in light blue.

Exchanging the composite test mass by a monolithic fused silica test mass led to the most recent measurements in May 2022 (blue), lowering the noise floor at high frequencies such that it now is best explained as coating Brownian thermal noise, shown here in dark red, starting from 100 Hz. This marks the goal of the commissioning of the TNI. The individual noise contributions to the latest spectrum are discussed in chapter 6.

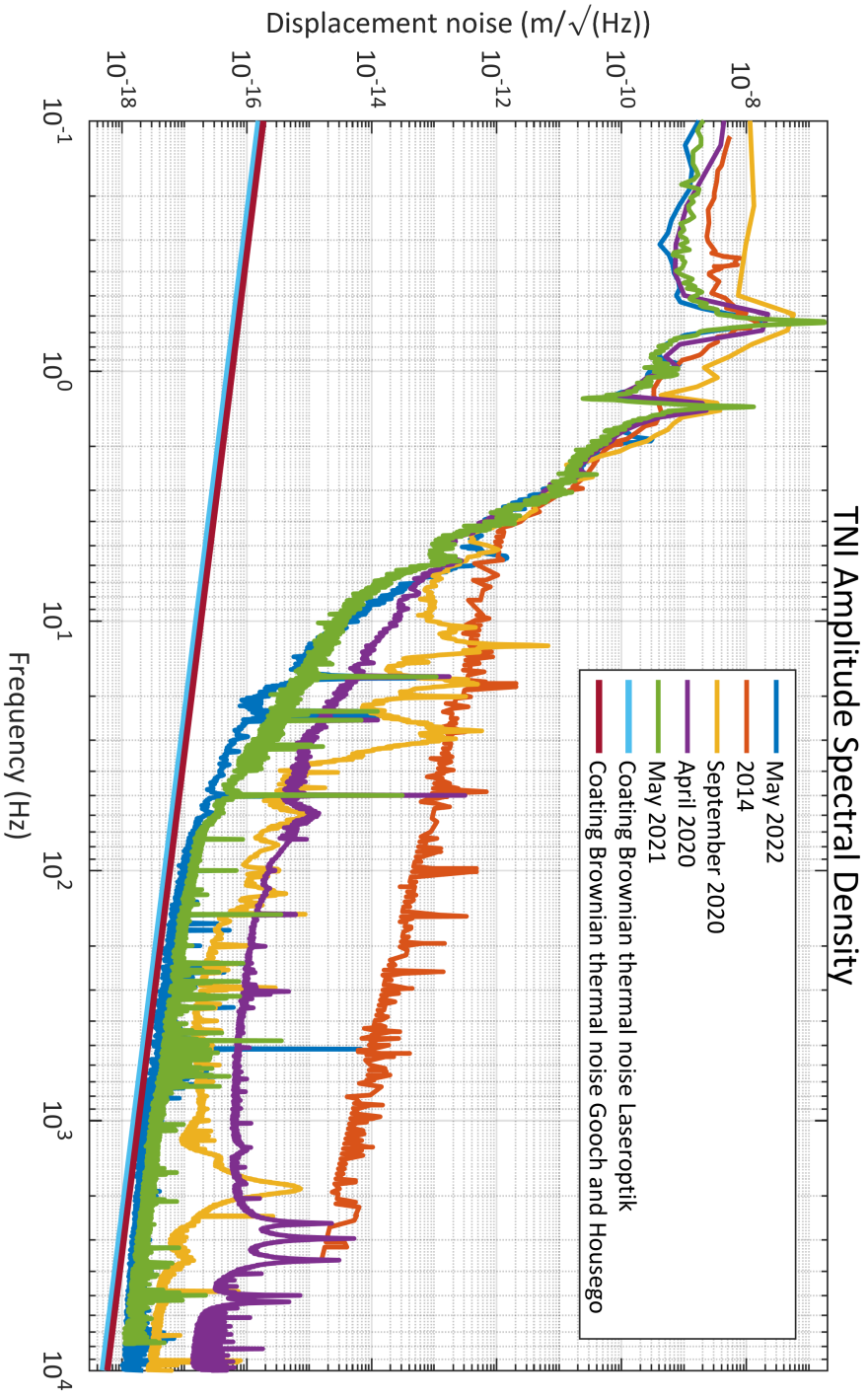

Figure 4.66: Evolution of the TNI readout noise over the last seven years. The data point from 2014 was reconstructed from measurements before the start of this thesis. An improvement of up to 3 orders of magnitude was achieved at frequencies above 5 Hz.

CHAPTER 5

Calibration of the thermal noise interferometer

One of the most fundamental aspects of every high sensitivity experiment is a reliable calibration of the readout variable. This is necessary to make any quantitative statements about the readout and factors influencing the readout. In gravitational wave detectors, this readout variable is either the test mass displacement or derived from it the strain.

Among several calibration methods in use is a photon pressure calibrator [Mos+06] and recently a gravitational calibrator [Ros+21] has been added. They use well known force couplings to the test mass such as radiation pressure and gravitation, and compare the readout signal to the expected signal.

In the TNI, a photon pressure calibrator is used as the most reliable way of calibrating the cavity mirror displacement, backed up by other methods such as analysing flashes of the free swinging cavity and comparing coil actuation with external references.

5.1 Photon pressure calibrator

Photon pressure has been used in gravitational wave detectors [Mos+06] to reliably calibrate the strain signal. This is done by modulating the power of a laser hitting one of the test masses under a shallow angle. The light transfers momentum upon reflection by the mirror proportional to the magnitude of the Poynting-vector, which itself corresponds to the power flux. The momentum transfer is a result of a change of direction of the photons through the interaction with the mirror.

As the test mass can be considered a free mass at frequencies well above the suspension resonance frequencies, the response to the radiation pressure will be inversely proportional to the mass M of the mirror and the cyclic frequency of modulation ω squared. Further modification comes from the angle of incidence α, which has to be large enough to not disturb the output path, but small enough to not reduce the actuation strength too much. The resulting equation for mirror displacement is then [Hil07]

$$x = \frac{2 \cdot P \cdot cos(\alpha)}{M \cdot c \cdot \omega^2} \,. \tag{5.1}$$

This shows that the light power is the most important parameter, whose uncertainty dominates the overall uncertainty in the calculation. The angle, which can be measured to within a few degress, does not couple strongly due to the cosine. Mirror mass is known well using a scale.

5.1.1 Setup

For the TNI, a photon pressure calibrator was realized in a simplified and robust setup. The starting point is a diode-pumped solid-state laser (DPSS) made by Roithner Lasertechnik, being

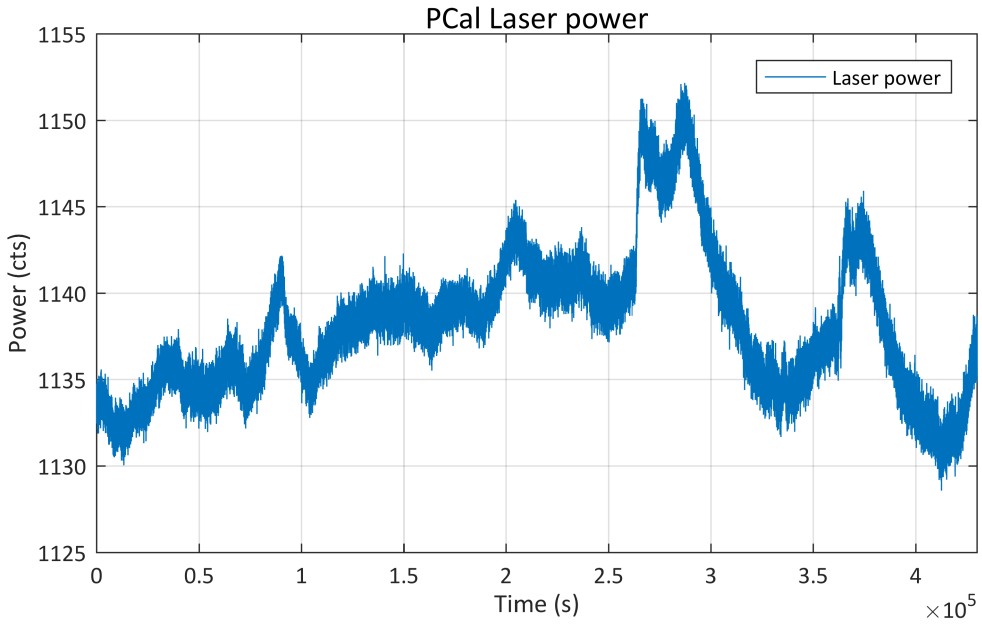

Figure 5.1: Mean power of the PCal laser measured over 5 d.

able to supply 350 mW at 1064 nm. The laser has a direct modulation input which is used to modulate the power up to full depth and up to frequencies of 5 kHz. Laser power has been monitored by a photodiode over a few days to assess its stability, as shown in figure 5.1.

The deviations of the mean power are less than 1.6 % over five days and short term fluctuations are close to 2 %. 25 mW of laser power are being steered into the vacuum chamber through a viewport, and sent onto the flat end mirror of the TNI using two steering mirrors, giving a spot size of 1.1 mm (shown in figure 5.2). Reflection occurs under an angle of 17°, judged by measuring distances on the optical table and calculating the opening angle. The reflection is sensed by a 3 mm InGaAs photodiode by Laser Components, which has been calibrated with a commercial power meter (Ophir Nova II) as shown in figure 5.3. The calibration factor has been determined as 0.79 cts/µW.

A typical power spectrum of the laser light modulated at 220 Hz is presented in figure 5.4 The line at 220 Hz is by far the strongest feature in the spectrum, but multiples of 50 Hz are clearly present and may be linked to grounding issues, which have been neglected for the calibration procedure as the analysis only focuses at the amplitude at the modulation frequency. Of course modulation frequencies can not be multiples of 50 Hz, but have to be chosen to not coincide with any sharp features in the spectrum.

For the first iterations, modulation was applied via a signal generator DG4102 by RIGOL, and two of the following results used this setup. The more recent version is based on generating the signals in CDS, allowing remote access to the calibration procedure. Furthermore, for a single frequency, an online calibration pipeline has been created, shown in figure 5.5. The modulation frequency, set in a CDS filter bank, is not only sent to the laser, but also used to demodulate the TNI error signal and the PCal photodiode signal. This is done in a I/Q-modulation scheme, and the resulting signals are incoherently added and divided, giving the calibration factor. This factor is then used to calibrate the TNI error signal.

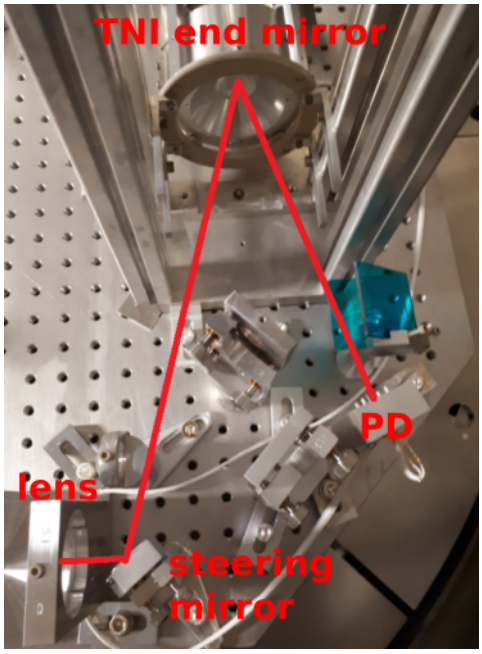

Figure 5.2: Setup of the PCal inside vacuum. The incoming beam is focused down using a lens. A steering mirror sends the beam onto the test mass, from where it is reflected onto a photodiode.

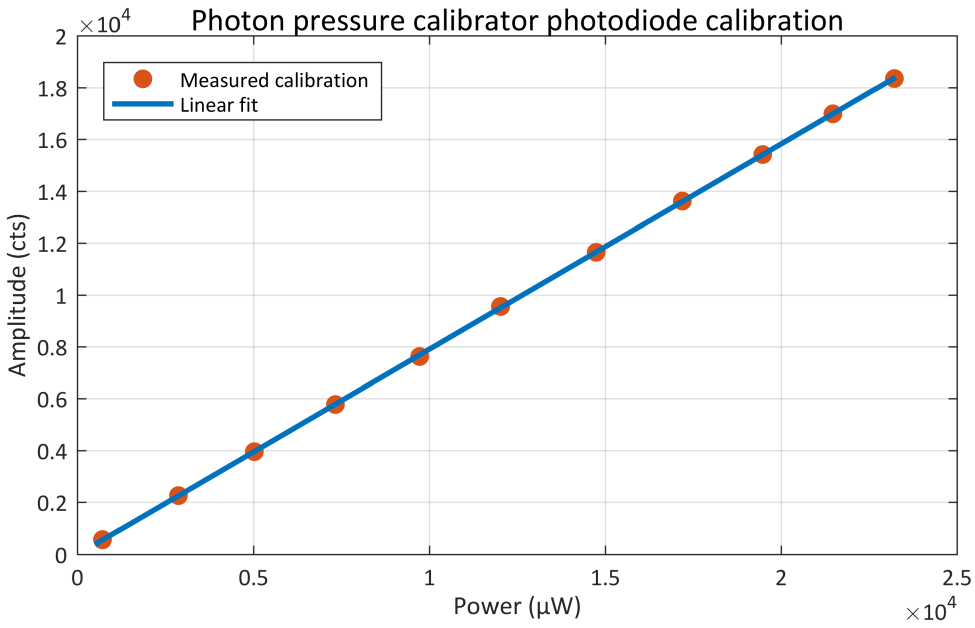

Figure 5.3: Calibration of the digital photodiode readout in cts as a function of power as measured by an optical powermeter.

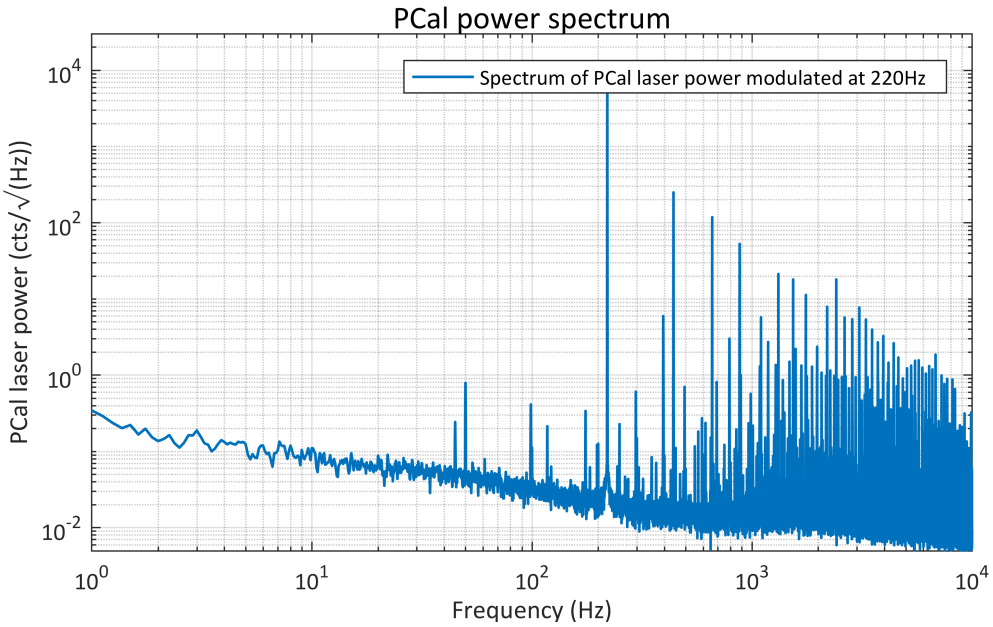

Figure 5.4: Spectrum of power fluctuations as measured by the photodiode. A modulation at 220 Hz is present on the laser. Multiples of this excitation are visible with reduced amplitudes.

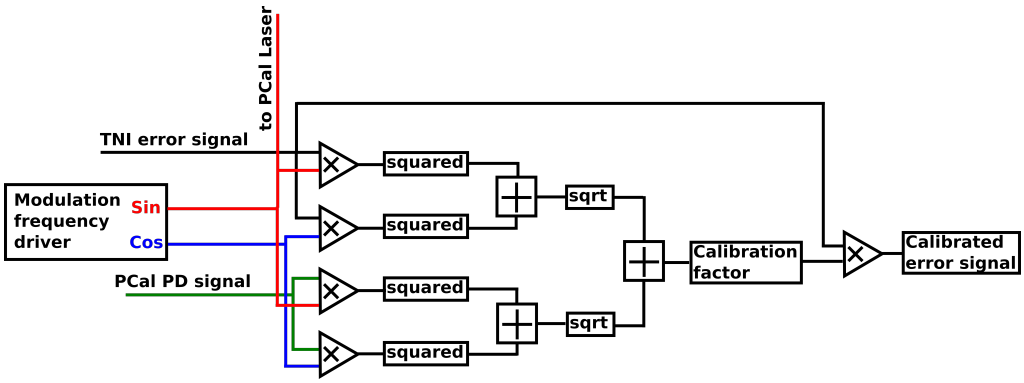

Figure 5.5: Block representation of the online calibration scheme. The raw error signal and the PCal photodiode signal are mixed down at the modulation frequency, using a I/Q-modulation scheme. Dividing the incoherently added quadratures gives the calibration coefficient, which is applied to the TNI error signal.

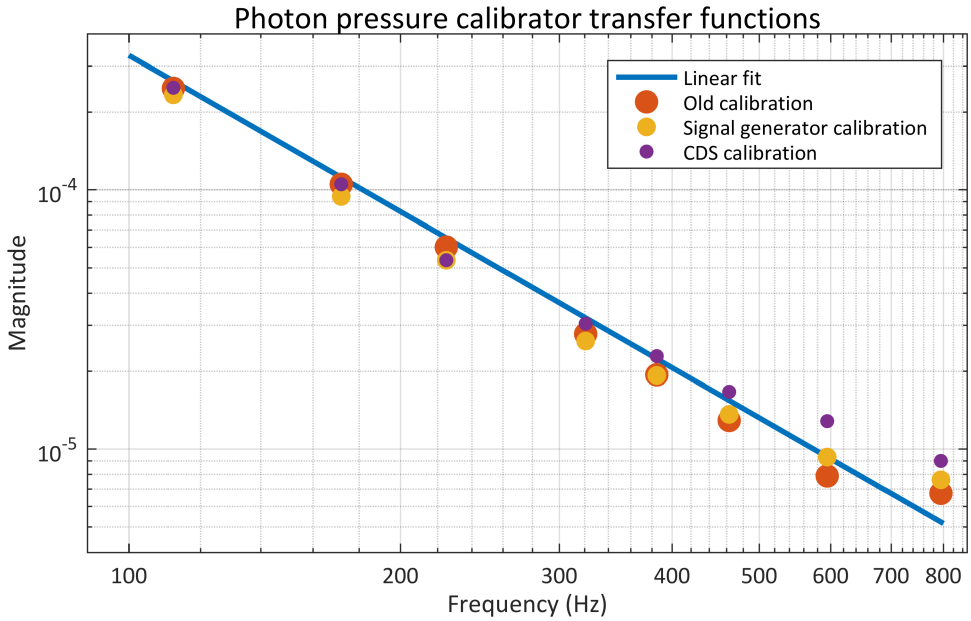

Figure 5.6: Transfer functions from the PCal modulation as sensed by the PCal PD to the error signal coming from the locking PD.

5.1.2 Results

While the TNI was locked, the laser was modulated at several frequencies between 112 Hz and 795 Hz. This corresponds to a frequency range where the suspension resonances are far below, allowing for a free mass response of the mirror. Due to the $\frac{1}{f^2}$ dependence for the free mass, there is not enough actuation achieved above 800 Hz to get a proper signal. Individual frequencies were then chosen to not conincide with large features in the spectrum to allow for maximum signal to noise ratio.

Furthermore, the chosen frequency range is well above the unity gain frequency. This ensures that the calibration is solely performed with the error signal. The coils can then be calibrated individually through measurements of the unity gain frequency and the requirement, that error signal and coil signal coincide at that frequency. Transfer functions between the error signal and the photodiode recording the modulated light in reflection as well as spectra were then taken, and the magnitudes of the transfer functions are shown in figure 5.6.

The blue line indicates a $\frac{1}{\omega^2}$ slope in agreement with the expectation of the response of a free mass to the radiation pressure force. The measurements labelled old and signal generator are from two iterations using a signal generator to modulate the laser. The data poins labelled CDS are using CDS to generate the modulation. The reliability of each data point can be estimated from the coherences of the transfer function measurements at the modulation frequency, which are shown in figure 5.7.

Especially at lower frequencies the coherences are close to 1, indicating that the measurement accurately represents the transfer function. An example transfer function is shown in figure 5.8.

Using the formula for the displacement due to the radiation pressure, the calibration factor for each data point in units of $\frac{m}{cts}$ was calculated. The resulting calibration factors are shown with their error bars in figure 5.9.

Errors are estimated as 2° for the angle, 20 g for the mass (the mirror has not been weighed before suspending) and 3×10^{-6} for the transfer function. The transfer function error is taken as

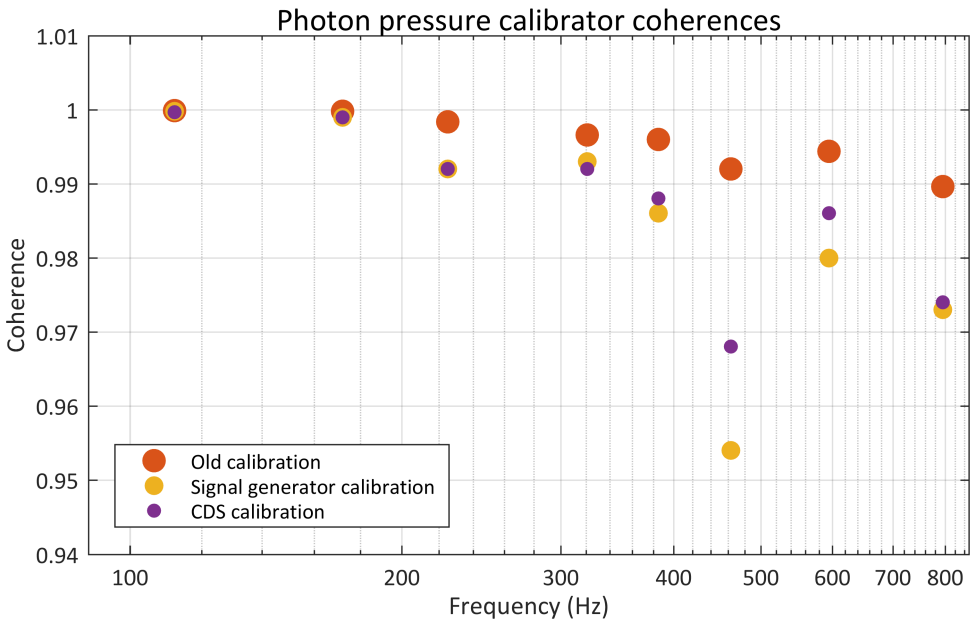

Figure 5.7: Coherences for the transfer functions shown in 5.6.

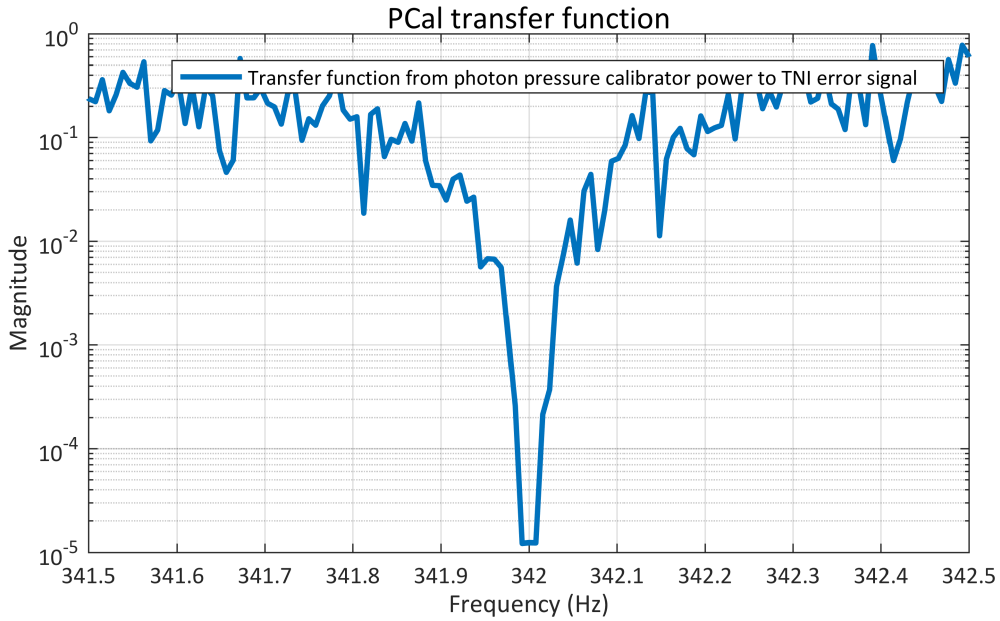

Figure 5.8: Measured example transfer function showing. Only at the modulation frequency there is enough coherence to give a proper signal.

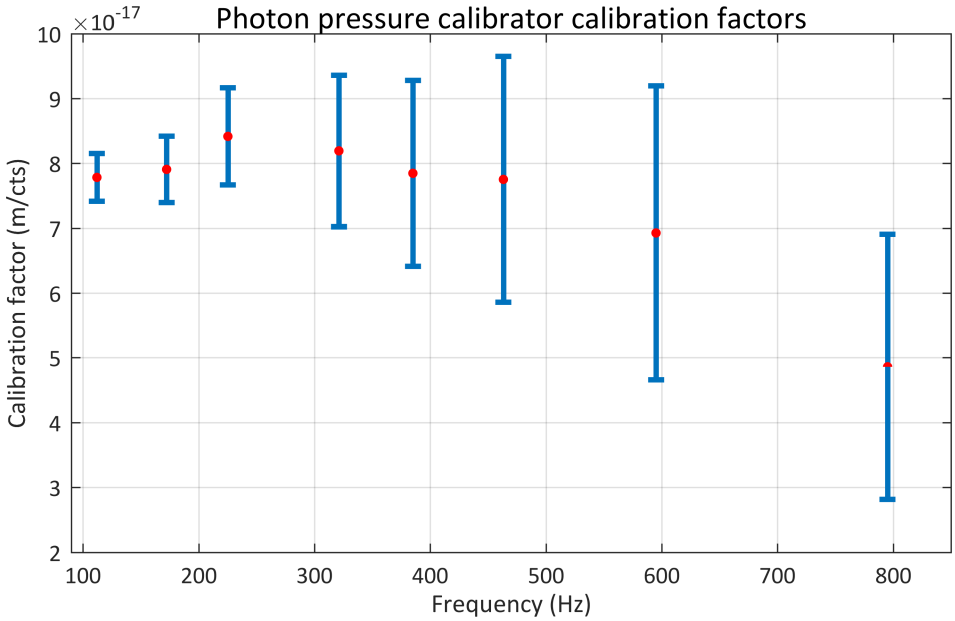

Figure 5.9: Calibration factors calculated from the transfer functions. The error bars assume an angle error of 2°, a mass error of 20 g and a transfer function error of 3×10^{-6}.

the ratio between the peak height at the modulation frequency in the PCal photodiode to the background level in the error signal of the TNI. The calibration factors measured at different frequencies are then averaged, and plotted with their standard deviation in figure 5.10. This is done for each iteration twice, once for the whole set of transfer functions and once for the first data points, restricting the analysis to transfer functions with the highest coherence.

In general, the calibration factors agree well with each other, and statistical analysis gives a mean value of 7.75×10^{-17} m/cts and a standard deviation of 5.1×10^{-18} m/cts. Spectra calibrated with this measurement agree well with the online calibration. This corresponds to an error from measurements at different times, averaged over the frequencies of 7 %. For individual frequencies, the uncertainty from the transfer function and to a lesser extent from the mass and angle uncertainty varies between 1 % at lower frequencies up to 40 % at higher frequencies, where the signal barely reaches above the noise floor.

This shows that the mechanical loss levels of coatings measured in the TNI can be inferred with an uncertainty of roughly 50 %, as the square root of the loss appears in the expression for the ASD of coating Brownian thermal noise.

5.2 Free swinging cavity

One of the simplest methods for calibration in a Pound-Drever-Hall locked cavity is the free swinging cavity method. As the name suggests, the cavity is left uncontrolled and swings through resonance. The recorded signal then shows the carrier and modulation sidebands as individual peaks in the reflected and transmitted photodiode time series, and the typical PDH-signal shape after the mixer, as shown in 5.11.

The separation between the carrier peak and each sideband peak corresponds to the phase modulation frequency of 8.047 MHz, which is produced by a stable oscillator. This calibrates the time axis of the recorded signals in units of frequency, and by relating this to the free spectral range of the cavity, which corresponds to half of the laser wavelength of 1064 nm, the time axis

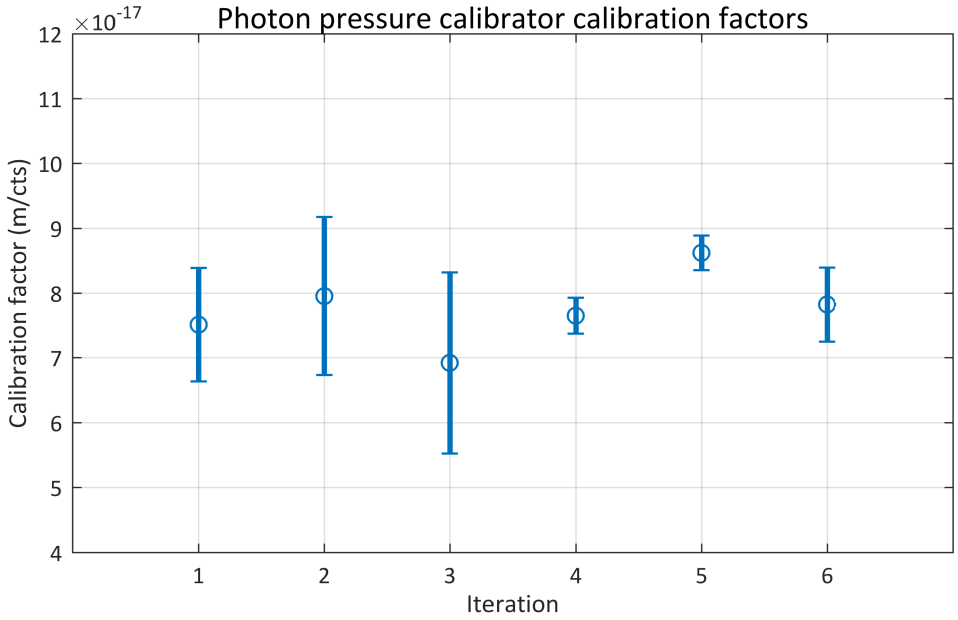

Figure 5.10: Averaged calibration factors calculated from each set of measurements. The average and standard deviation are shown for the two signal generator based measurements (1 and 2) and one CDS based measurement (3). For each, the first six data points have also been used alone restricting the analysis to measurements with high coherence (4 and 5 for signal generator and 6 for CDS).

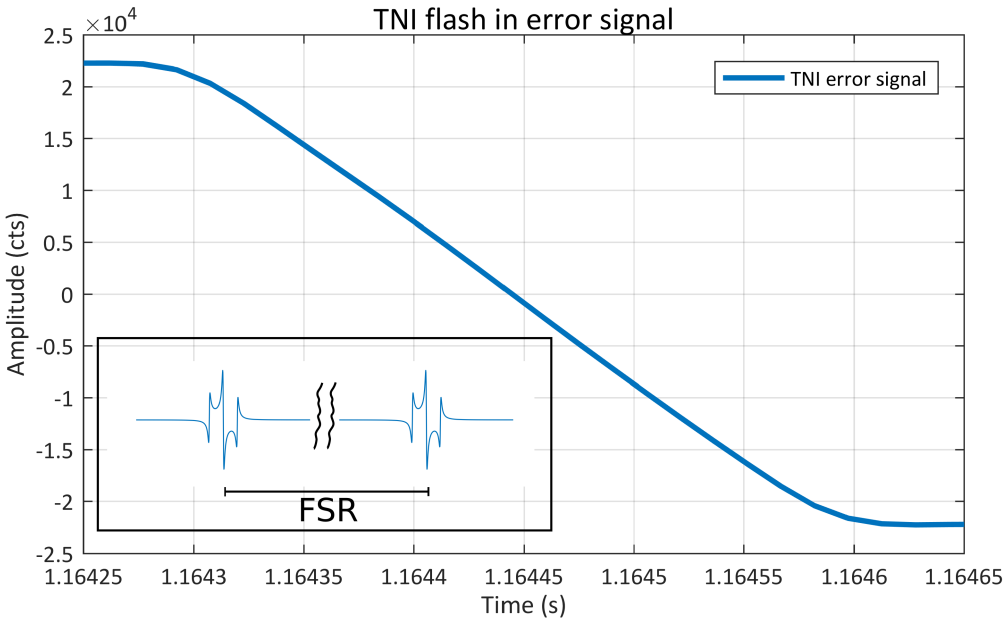

Figure 5.11: The trace of the error signal while the cavity goes through a flash. The slope is measured and converted to proper length units by taking the separation of the carrier and sidebands in the reflected PD signal as a reference for the timescale (from figure 5.12). The inset shows a simulation of the error signal over a free spectral range (FSR).

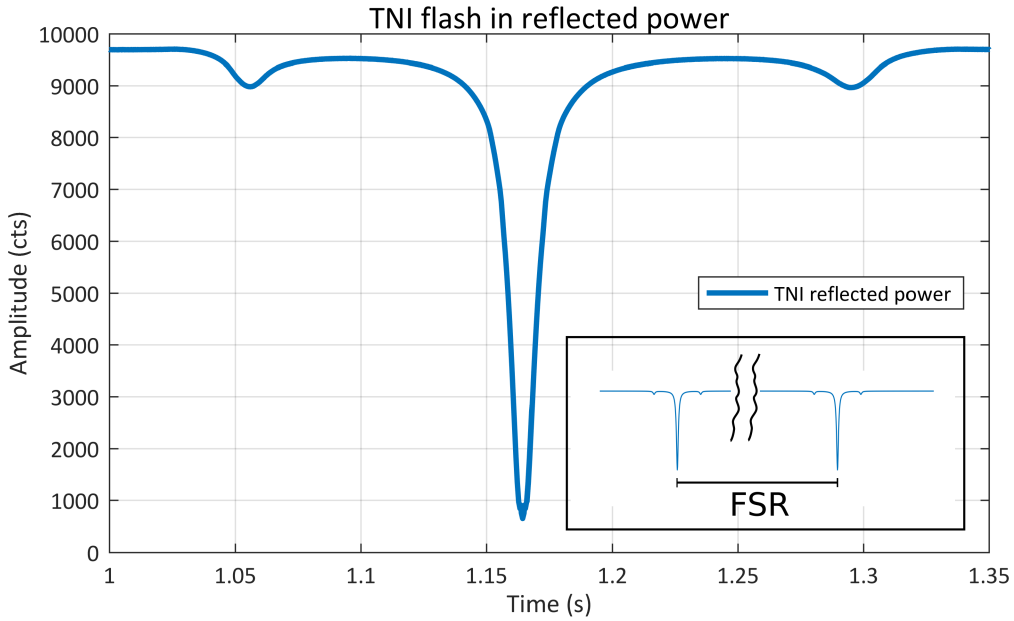

Figure 5.12: Time trace of a flash measured by the reflected PD. The separation between carrier and sidebands is taken as a reference, making the measurement of the full width at half maximum of the carrier possible. The Finesse is then estimated from the ratio of the FWHM and the calculated FSR. The inset shows a simulation of the reflected power over an FSR.

finally is calibrated in meter. The slope of the Pound-Drever-Hall signal can then be inferred in m/cts, which is the calibration factor for the error signal. This calibration factor was determined to be 1.5×10^{-16} m/cts.

This procedure gives a good estimate, but comes with non-negligible uncertainty. A source of error is the deviation from linearity of the central slope of the PDH-signal. Because the velocity of the free swinging mirrors is relatively high at the zero crossing, only few datapoints are available in the linear range to assess the slope. Furthermore, the calculations assume a constant speed, which is only approximately true for a swinging pendulum, and a steady state of the circulating power inside the cavity, which could otherwise lead to asymmetric flashes and artifacts. It is important to not take these measurements close to the turning points. Driving the mirror actively through the resonance can also help with the velocity, but leads again to the problem of not having enough data points in the linear range.

To test the accuracy of the free swinging cavity method, the same time series of the reflected signal was used to estimate the Finesse of the TNI. The result can then be compared to the Finesse calculated from the mirror reflectivity specifications. The measured time series are shown in 5.12. From the measured separation of the carrier peak position and the half maximum position, the FWHM can be estimated. The resulting Finesse of 2228 is in agreement with the Finesse of 2092 calculated from the specified mirror power reflectivities of 0.9985.

5.2.1 Coil feedback calibration

The former methods of calibration have used the error signal for calibration, which is only giving the proper displacement well above unity gain frequency. Below, the motion experienced by the cavity is suppressed and can be recovered from the actuator signal. In case of the TNI, this is the

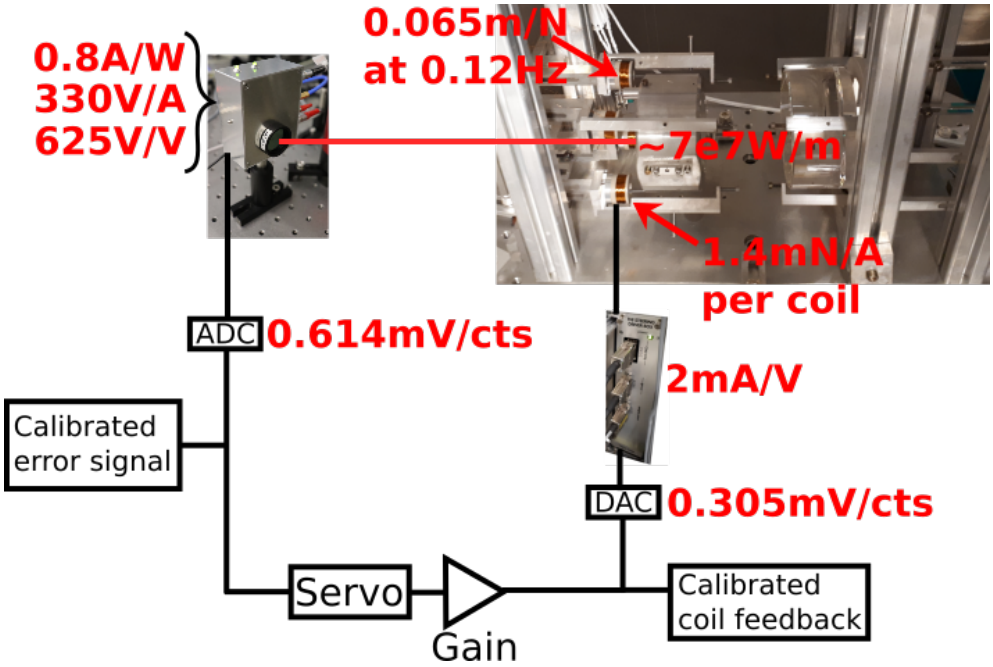

Figure 5.13: Schematic drawing of the coil locking loop of the TNI with conversion factors relevant for error signal calibration and coil feedback calibration calculations.

feedback current sent to the coils, which in turn actuate on magnets attached to the test mass. The strength of this actuation path can be evaluated in two ways: by a calculation using known and estimated transfer functions and conversion factors, and by measuring the actuation strength required to counteract actuation at the reference cavity below the first resonance, independently assessed by the PZT feedback used to lock the PMC to the laser.

Utilizing the coils gives an independent calibration below the unity gain frequency, increasing confidence in the error signal calibration using the photon pressure calibrator. A comparison between them can be done using the measured unity gain frequency as the point where error signal and feedback signal have to be equal. An actuator calibration procedure was used for example in the first successful TNI [Num+03] as well as in LIGO [Abb+17r].

5.2.1.1 Coil feedback calculation

The loop diagram containing known conversion factors and transfer functions is shown in 5.13. The channel which contains the calibrated coil signal is highlighted in red. In order to get the calibration factor the loop has to be traversed back from the mirror displacement to the coil calibration channel. This involves the frequency dependent force to displacement transfer function at the test mass as shown in 5.14. Further steps include the force to displacement below the resonances of 0.065 m/N, the current to force factor of the coil-magnet pair 1.4 mN/A, the sensing resistor of 500 Ω giving 2 mA/V connecting driving voltage to current through the coils and the DAC conversion factor 0.305 mV/cts.

All of this leads to a calibration factor of 5.5×10^{-11} m/cts This can be connected to the calibration factor for the error signal through a measurement of the unity gain frequency. At the unity gain frequency, the error signal has to be equal to the coil feedback signal, and so one calibration factor can fix the calibration for the other signal. Using this comparison for spectra calibrated by the PCal leads to an calibration factor of 5.1×10^{-11} m/cts.

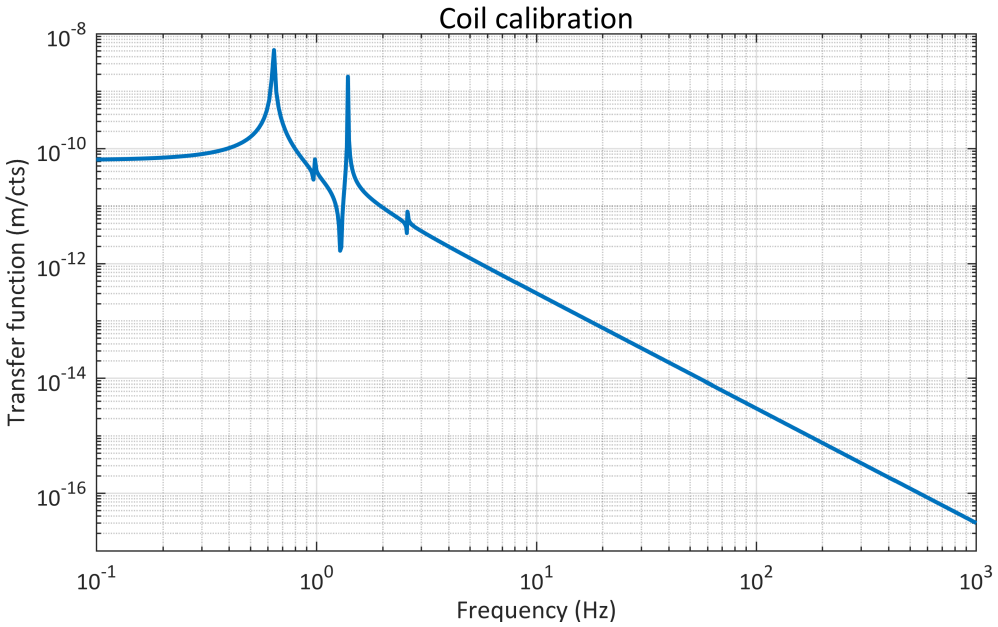

Figure 5.14: Transfer function from force at the coils to displacement of the test mass, used for calibration of the coil actuation.

This calibration factor is in good agreement with the calibration factor derived by the coil feedback calculations, increasing the confidence in the calibration procedures. For the error signal calibration, the ADC conversion factor of 0.614 mV/cts, the photodiode response consisiting of the efficiency of 0.8 A/W, the transimpedance resistor of 330 Ω and a gain of 625, and the cavity response of approximately 7×10^7 W/m from $\frac{16\sqrt{P_c P_s}\mathcal{F}}{\lambda}$ are used to arrive at a factor of 5.4×10^{-17} m/cts, compared to the value taken from the photon pressure calibrator of 7.5×10^{-17} m/cts.

5.2.1.2 Coil feedback measurement

The coil feedback calibration factor can be measured by actuating on the longitudinal BOSEMs of the end mirror of the reference cavity. This actuation is done at 0.12Hz, below the first resonance where the pendulum directly follows the actuation. The displacement of the reference cavity is translated into a frequency shift of the main laser as it is locked to the resonance of the frequency reference cavity. This frequency shift is then sensed by the TNI and the PMC, both tightly locked to the laser frequency.

The PMC feedback signal, as sensed in the high voltage driver path controlling the PZT length, has been calibrated to an iodine reference used for the SPI in the AEI 10 m prototype and is displayed in units of µm reference cavity length. The difference in length of the reference cavity of 10.6 m and the TNI of 0.095 m has to be taken into account to get the length change of the TNI in m. The corresponding measurement is shown in 5.15.

A calibration factor of 1.2×10^{-10} m/cts is the result. This deviates by a factor of 2 from all other calibrations, most probably stemming from observed long term drifts in the PMC feedback still under investigation.

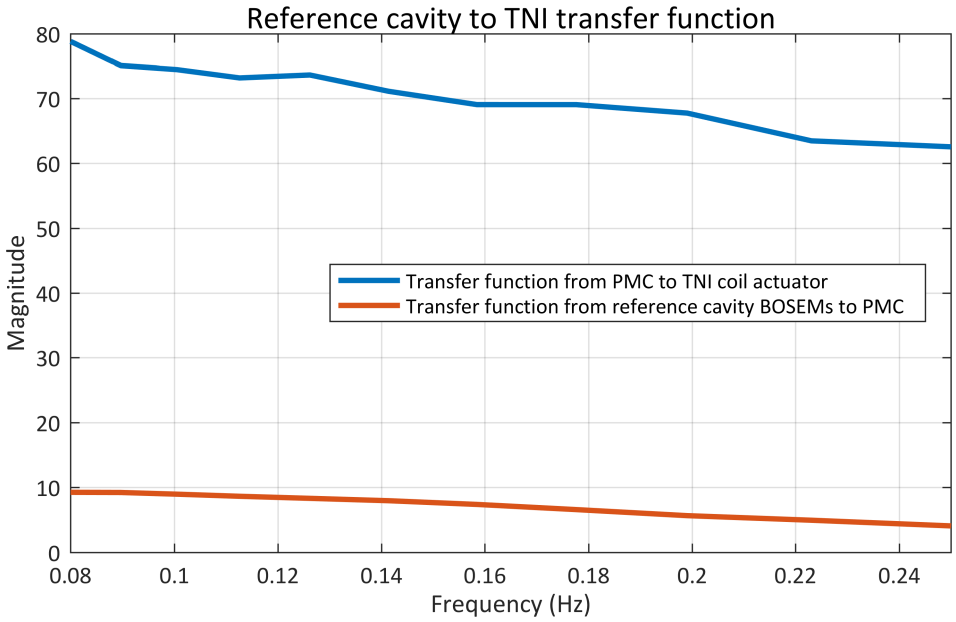

Figure 5.15: Transfer functions from actuation at the reference cavity suspension to the TNI coil actuation. Simultaneously, the transfer function from the reference cavity to the PMC is taken as a reference, as the PMC is supposed to be calibrated.

5.2.2 Laser frequency noise

An independent way of gaining confidence in the calibration results detailed above is to measure the frequency noise of the free running NPRO and compare this to the expected frequency noise typical for NPROs. In the manual and several papers [Mep], the level of frequency noise is cited as

$$S_{\Delta f} = 100 \frac{\mathrm{Hz}}{\sqrt{\mathrm{Hz}}} \qquad @100\mathrm{Hz}\,. \tag{5.2}$$

This method does not provide much accuracy as the laser noise is different from laser to laser and changes over time, but gives confidence that the calibration is correctly done by the other methods when the deviation from the nominal noise level is small.

The measurement is done with the TNI locked in the nominal state, but the frequency stabilization to the frequency reference cavity is disengaged. A power spectrum is shown in figure 6.19. The TNI spectrum is dominated by laser frequency noise in the range from 5 Hz to 10 kHz and the level of frequency noise at 1 kHz estimated from this measurement is $8\,\mathrm{Hz}/\sqrt{\mathrm{Hz}}$, which agrees well with the expected level of $10\,\mathrm{Hz}/\sqrt{\mathrm{Hz}}$. This shows that the calibration represents the actual displacement well.

CHAPTER 6

Noise budget of the thermal noise interferometer

In this chapter, all known and assumed noise sources are briefly discussed, and whenever possible an amplitude spectral density (ASD) is calculated or derived from measurements. The individual projections are compared against measurements of the TNI readout to gauge the impact of the noise source under investigation. For thermal noise, the discussions are kept short as the theory has been presented in chapter 2. Other noise sources are discussed in more detail.

All ASDs together, when summed up incoherently, represent the total expected readout noise of the TNI. This noise budget is compared to actual measurements in the following chapter, giving confidence in the claim of a direct measurement of mirror thermal noise.

6.1 Shot noise

Shot noise is a fundamental noise source in all experiments utilizing quantized information carriers like photons and electrons. In optical precision experiments, the signal under consideration usually is the result of counting photons in a defined time interval. As the number of photons passing a reference surface per time exhibits random fluctuations, the measured signal will be disturbed. Most interferometric experiments use lasers whose light can be best described by the so called coherent state, [GC08]

$$|\alpha\rangle = \mathrm{e}^{-\frac{|\alpha|^2}{2}} \sum_{n=0}^{\infty} \frac{\alpha^n}{\sqrt{n}} |n\rangle \,, \tag{6.1}$$

where $|n\rangle$ is the Fock-state of photon number n.

In this state, the number of photons through a surface per time

$$P_n = \mathrm{e}^{\overline{n}} \frac{\overline{n}^n}{n} \,, \tag{6.2}$$

is Poisson distributed, with the variance being proportional to the average photon number of the light

$$\overline{n} = \langle \alpha | a^\dagger a | \alpha \rangle = |\alpha|^2 \,. \tag{6.3}$$

The standard deviation is proportional to the square root of the variance and is frequency independent; and therefore the resulting spectral density of the noise will have the form of white noise. Because the measurements are conducted using photodiodes, which measure the power of the light, the resulting absolute noise will be proportional to the square root of the photon number or equivalently the square root of power. Naively, the solution to the reduction of shot noise in the context of cavity stabilization would be to lower the power or modify the statistics of light. The latter is called squeezing and is now reliably used in gravitational wave detectors to

combat the shot noise limit dominating at higher frequencies [Vah+10]. If analysed correctly, help comes from the fact that the signal in these optical experiments scales linearly with the power of the light, thereby improving the relevant signal to noise ratio in proportion to the square root of the light power.

To get the proper shot noise amplitude spectral density in the TNI, the signal has to be compared to the shot noise. The signal is derived using the Pound-Drever-Hall (PDH) locking scheme [Bla01]. Phase modulation sidebands are imprinted onto the laser light and are being used as the phase reference for judging the distance of the laser frequency from the cavity resonance. The sideband separation from the carrier is chosen large enough such that they are totally reflected from the cavity. As the photodiode in the PDH-scheme is located in reflection of the cavity, these sidebands together with carrier light leaking out determine the shot noise detected by the photodiode. On resonance in an impedance-matched cavity, no carrier is reflected and only the sideband power is relevant for the shot noise.

Further unwanted contributions, resulting in increased shot noise, stem from light being reflected because of improper mode matching, insufficient impedance matching or residual offsets of the locking point from the cavity resonance. Losses in the photodiode as well as its quantum efficiency also contribute to shot noise, reducing the measured signal. The signal will also suffer from losses inside the cavity, but will improve with increasing cavity Finesse, having the light probe the mirror separation more often, thereby increasing the signal per mirror motion. This results in the total shot noise of

$$S_x(f) = \frac{\hbar c \lambda}{128} \frac{\left(\frac{\mu \left| \frac{\sqrt{r_1}-\sqrt{r_2(1-t)}}{\sqrt{r_1 r_2(1-t)}-1} \right|^2}{J_1(\delta)^2} + \frac{1-\mu}{J_0(\delta)^2 J_1(\delta)^2} + \frac{2}{J_0(\delta)^2} \right)}{\left(\sqrt{P_{in}\mu} \frac{\pi \sqrt{\sqrt{r_1 r_2}}}{1-\sqrt{r_1 r_2}} \frac{(1-r_1)\sqrt{r_2(1-t)}}{(1-\sqrt{r_1 r_2(1-t)})\sqrt{\sqrt{r_1 r_2(1-t)}}} \right)^2} . \tag{6.4}$$

Here, J_0 is the Bessel function of the first kind of zeroth order, J_1 is the Bessel function of the first kind of first order, $r_{1,2}$ is the power reflectivity of the first respectively second mirror, t the round trip losses inside the cavity, μ is the mode matching efficiency, δ is the modulation depth of the sidebands and P_{in} is the power incident on the cavity.

It is instructive to analyze the scaling of the shot noise with impedance matching, mode matching and modulation depth, as these are parameters which can be adjusted in the experiment. Impedance matching is further divided into contributions from the input mirror reflectivity, the output mirror reflectivity and intracavity losses. The baseline parameters, taken from the TNI, are an input power of I =10 mW, a modulation depth of $\delta = 0.2$, a mode matching efficiency of $\mu = 97.8\%$, mirror reflectivities of $r_1 = r_2 = 0.9985$ and assumed intracavity losses of t =30 ppm.

For mode matching variations, the shot noise is shown in figure 6.1. This gives the required level of mode matching, which is aimed to be above 80 %, necessary for the shot noise to be below $1 \times 10^{-18}\,\mathrm{m}/\sqrt{\mathrm{Hz}}$, which would be close to the level of coating Brownian noise. This mode matching performance has been shown to be achievable using two mode matching lenses placed on sliding rails. The dependence on the modulation depth is shown in figure 6.2. The modulation depth is set by the voltage sent to the EOM, which is placed in the input path to all experiments in the AEI 10 m prototype. This can be increased if necessary, but for the TNI, the nominal depth of 0.2 is sufficient for sensitive measurements. Intracavity losses can only be changed by using well polished optics, as has been experienced in the TNI in the past (see chapter 4). Higher losses increase the shot noise approximately linearly (as shown in figure 6.3), and the aim is to keep losses as low as is possible.

In the case of varying input and output mirror reflectivities, the relation to shot noise becomes more complicated. For a fixed input mirror reflectivity, the output mirror reflectivity changes shot noise significantly if it becomes lower than the input mirror reflectivity, making the cavity undercoupled (as shown in figure 6.4). Having higher reflectivities does not change the shot noise significantly, which is important as test mirrors for thermal noise interferometers are in most cases

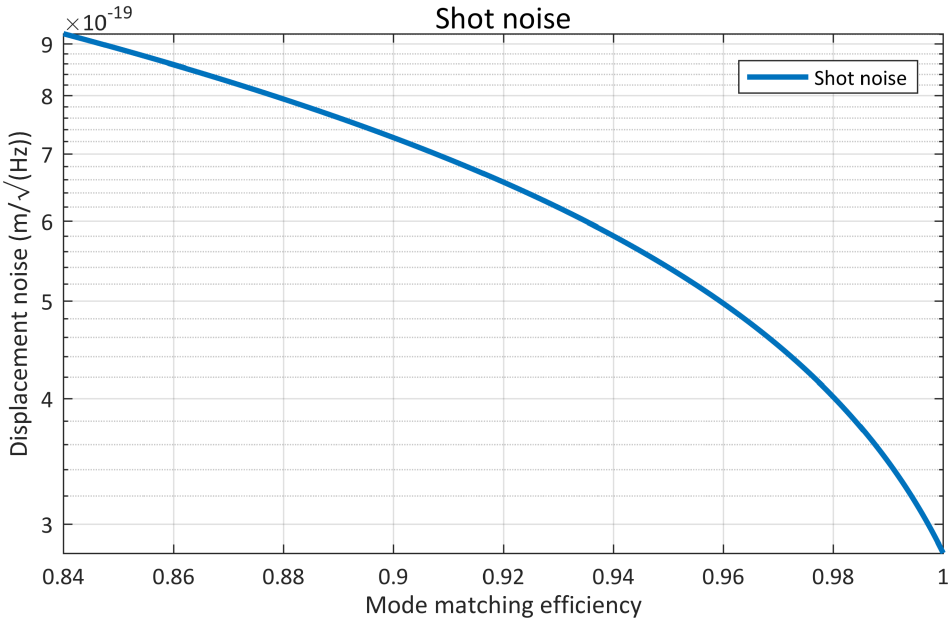

Figure 6.1: Influence of mode-matching efficiency on the shot noise of the TNI.

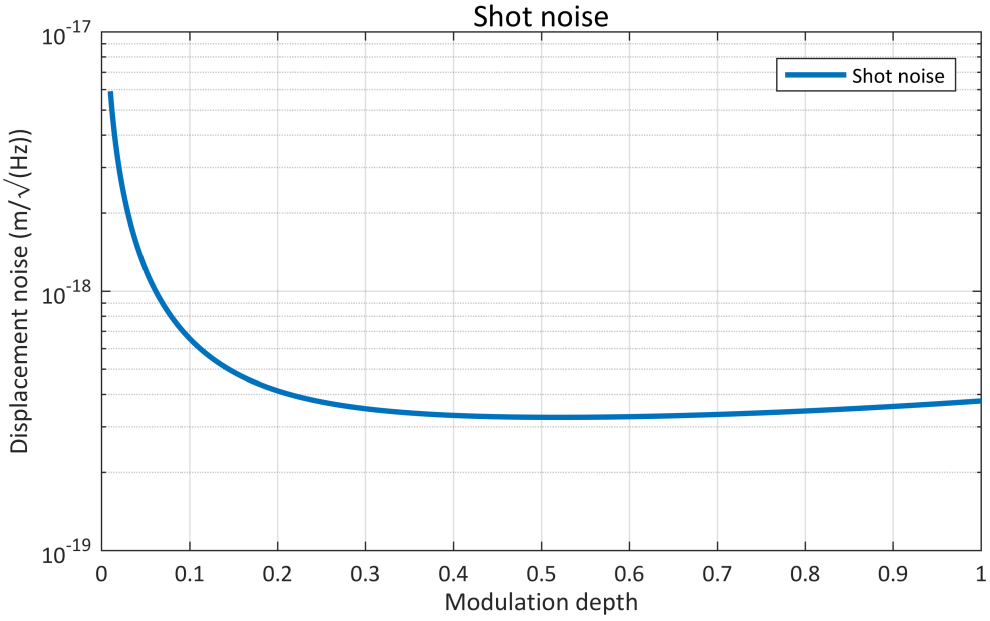

Figure 6.2: Influence of the EOM modulation depth on the shot noise of the TNI.

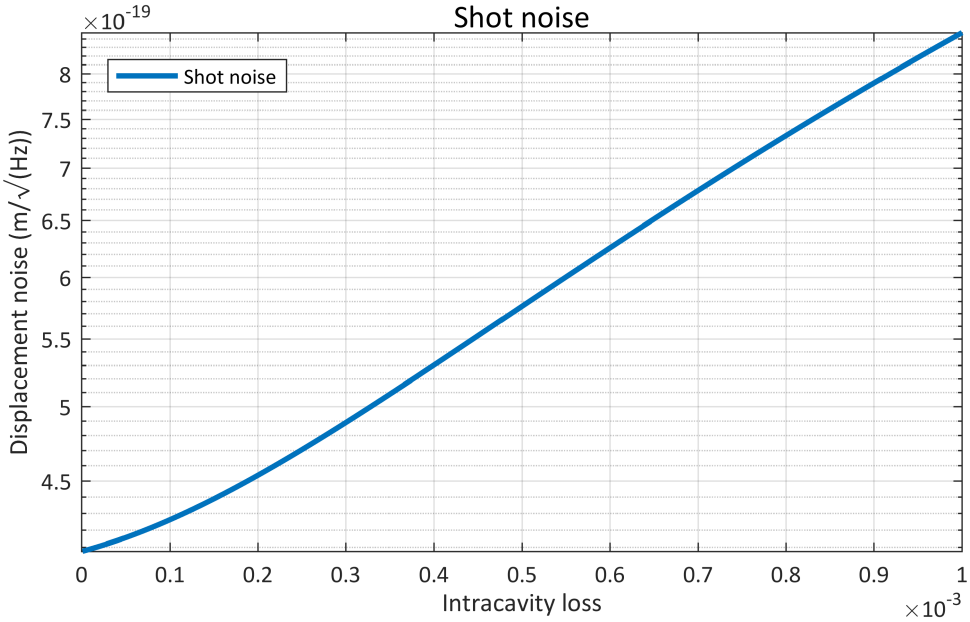

Figure 6.3: Influence of intracavity losses on the shot noise of the TNI.

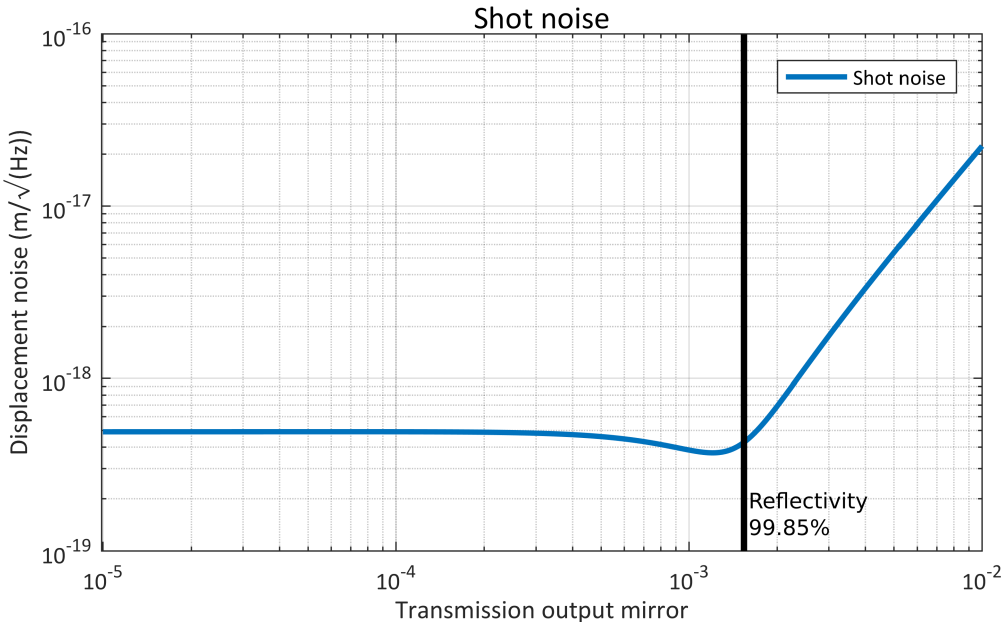

Figure 6.4: Influence of the output mirror transmissivity on the shot noise of the TNI. The input mirror has the nominal reflectivity of 99.85 %.

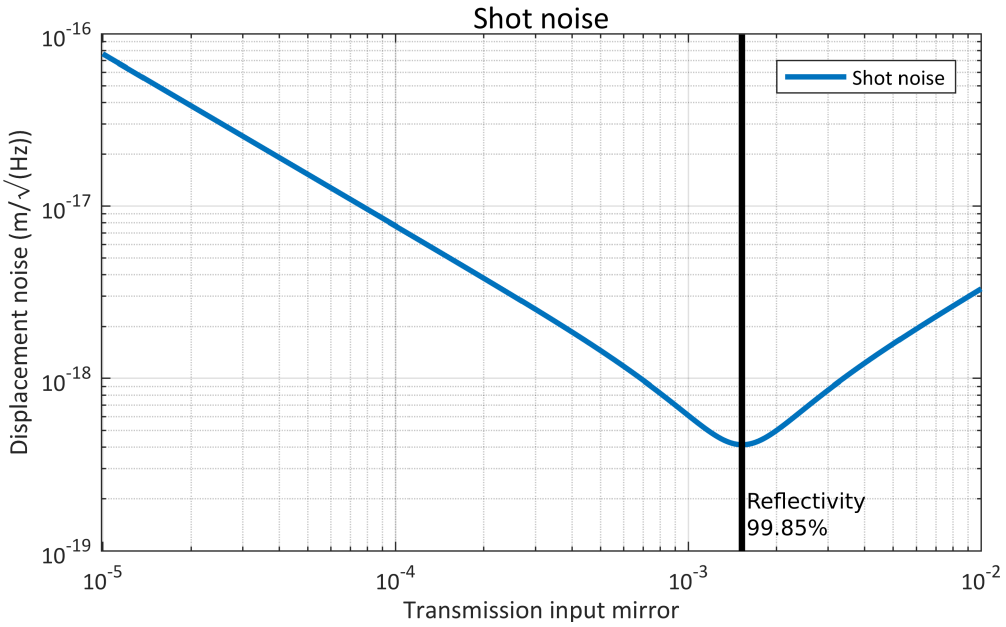

Figure 6.5: Influence of the input mirror transmissivity on the shot noise of the TNI. The output mirror has the nominal reflectivity of 99.85 %.

highly reflective and thus can be used with a fixed lower input mirror reflectivity. For a given output mirror reflectivity, the susceptibility of shot noise to the input mirror reflectivity is higher, as shown in figure 6.5. Thus, the absolute level of the reflectivity of the input mirror is important when considering shot noise, and care has to be taken when choosing the reflectivities for new monolithic input mirrors so that for the range of possible test mirrors, shot noise does not become the limiting factor.

The resulting shot noise for the nominal parameters shown above is plotted in comparison to the measured spectrum in figure 6.6. Shot noise starts limiting the measured spectrum at high frequencies, together with photodiode dark noise. The noise level has to be lowered in the future when measuring coatings with lower loss or fewer layers. This can be achieved by increasing the input power, where up to 50 mW is available. Because of the limited power handling capabilities of the locking photodiode in the unlocked state, this would require using separate photodiodes or gain settings for lock acquisition and in-lock measurements.

6.2 Seismic noise

The motion of the solid part of the earth is a limiting factor in most sensitive displacement measurements. There are many ways to reduce the influence of this seismic, but nevertheless the coupling will often dominate at low frequencies and a proper noise projection from ground motion through the isolation systems to the experimental readout has to be done.

Generally, the seismic spectrum will be highest at low frequencies and falls of with approximate $\frac{1}{f^2}$ at frequencies above 2 Hz (shown in figure 6.7). Aside from low frequency modes of the whole earth, main contributions stem from anthropogenic sources at a few Hz and the microseism at around 0.1 Hz and around 0.2 Hz [Hil+12]. Anthropogenic sources include traffic and the presence of people walking around, but also construction sites. There is a day/night-cycle because of working hours and quieter phases on weekends and holidays. One recurring example which is clearly visible in the lab is the Hannover Marathon, where thousands of people run past the

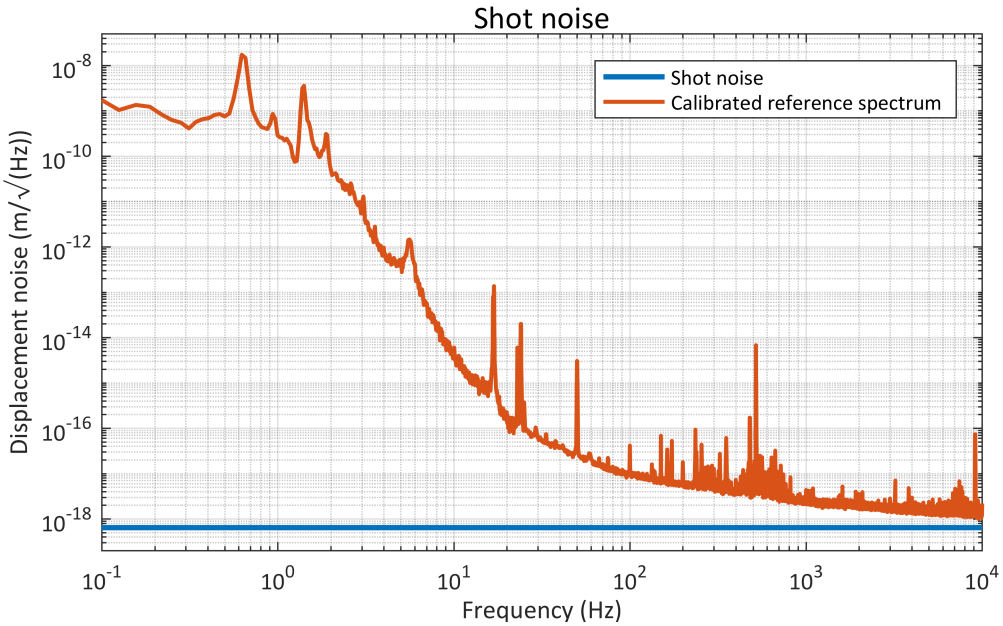

Figure 6.6: Comparison between the measured calibrated spectrum of the TNI length and the calculated shot noise, assuming an input power of 6.6 mW, mode matching efficiency of 85 %, modulation depth of 0.2, intracavity losses of 70 ppm, input mirror reflectivity of 0.9985 and output mirror reflectivity of 0.99999.

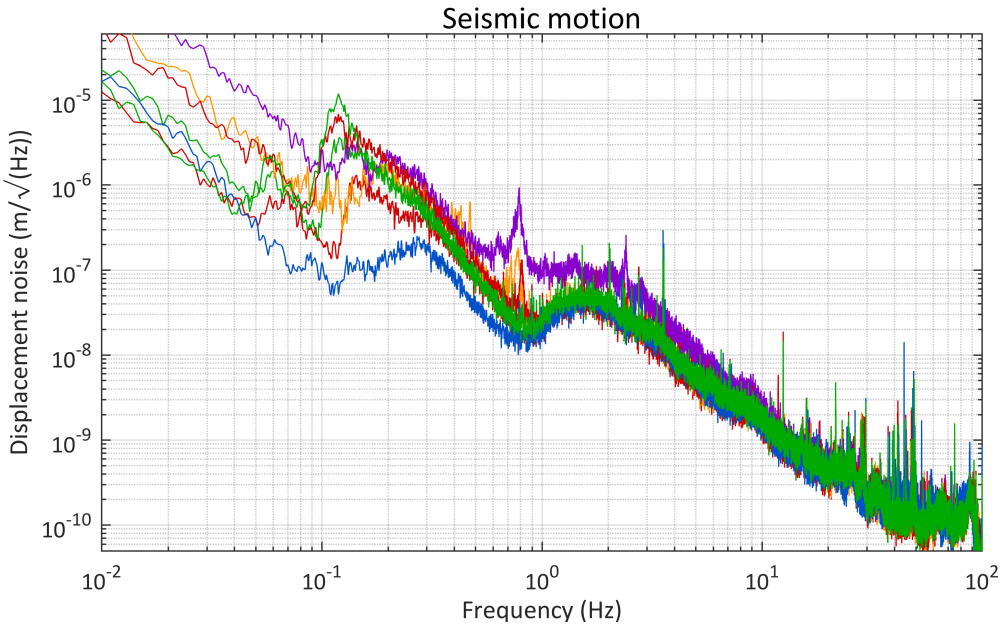

Figure 6.7: Seismic displacement spectra taken on different days in the AEI 10 m prototype lab by the STS-2 seismometer. Blue shows the spectrum taken on a calm summer day, purple was taken during a violent storm present in most of northern Europe.

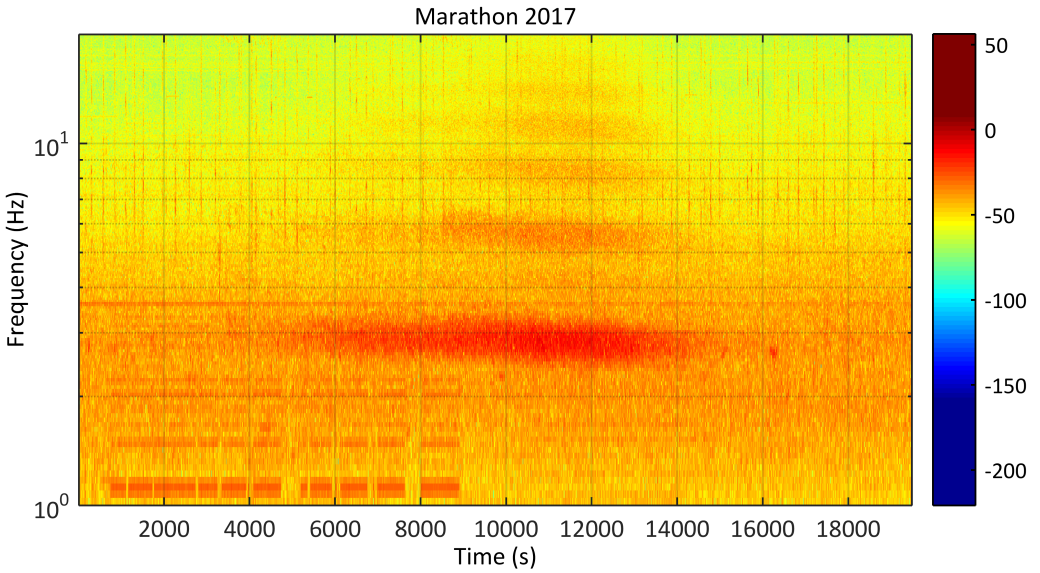

Figure 6.8: Spectrogram of the seismic during the Hannover Marathon.

institute and the seismic from their steps as well as a typical evolution of their step frequency can be seen in spectrograms taken around that time (shown in figure 6.8).

The microseismic peaks stem from ocean waves driven by storms in the north atlantic and north sea, interacting with the ocean floor and coastlines, transferring energy into ground motion in the process [Hil+12]. Microseism is highly variable and shows a strong dependence on the season, being highest in the storm season of autumn and winter. Exemplary spectromgrams from different times are shown in figure 6.9. Another external influence showing up in the seismic spectra are storms, not only driving the microseism, but also directly shaking nearby tall buildings. A comparison is shown in figure 6.10, where a calm summer day (red) is compared to a stormy day (blue), showing microseism at lower frequencies and a resonance of a building closeby at 0.8 Hz. Storms and microseism severly hinder locking the TNI when low-frequency ground motion is too high.

From time to time, earthquakes will send out seismic surface and body waves which can be measured in the lab and, if close enough or strong enough, will cause problems in aquiring lock in the suspended cavities. A time trace, showing ground motion of more than 1 mm is shown in figure 6.11, and a spectrum taken during an earthquake is shown in figure 6.12.

In the AEI 10 m prototype lab there are several sensors picking up seismic motion at different points in the seismic isolation system. An STS-2 seismometer monitors the motion of the ground under the vacuum tank. Accelerometers and geophones are placed inside and on top of the seismic attenuation system optical tables. They provide measurements of the residual seismic noise getting through to the table top where the thermal noise interferometer is located. From there, the transfer function of suspension with three stages in the horizontal and with two blade stages in the vertical has to be taken into account to project the seismic motion into displacement sensitivity.

6.2.1 Vertical seismic noise

For vertical seismic noise, a spectrum measured by vertical L4Cs on top of the seismic isolation table (shown in figure 6.13) is projected through the two vertical isolation stages of the TNI. The result is multiplied by the approximate vertical-to-horizontal coupling factor of 0.001 to get the

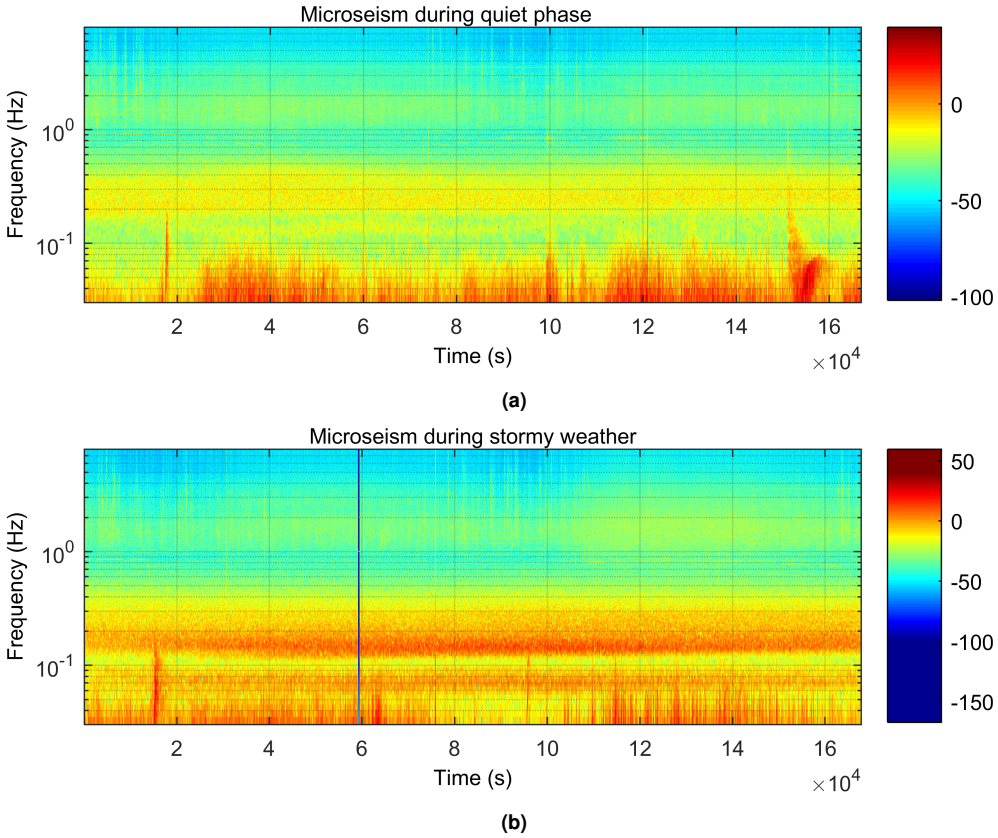

Figure 6.9: Spectrogram showing the presence (right) and absence (left) of microseism at frequencies around 0.2 Hz in the lab. Red indicates the highest ground motion, blue the lowest, as measured on a logarithmic scale. The main driving factor are storms over the north atlantic, creating wave fields, which in turn push the ocean floor creating the seismic.

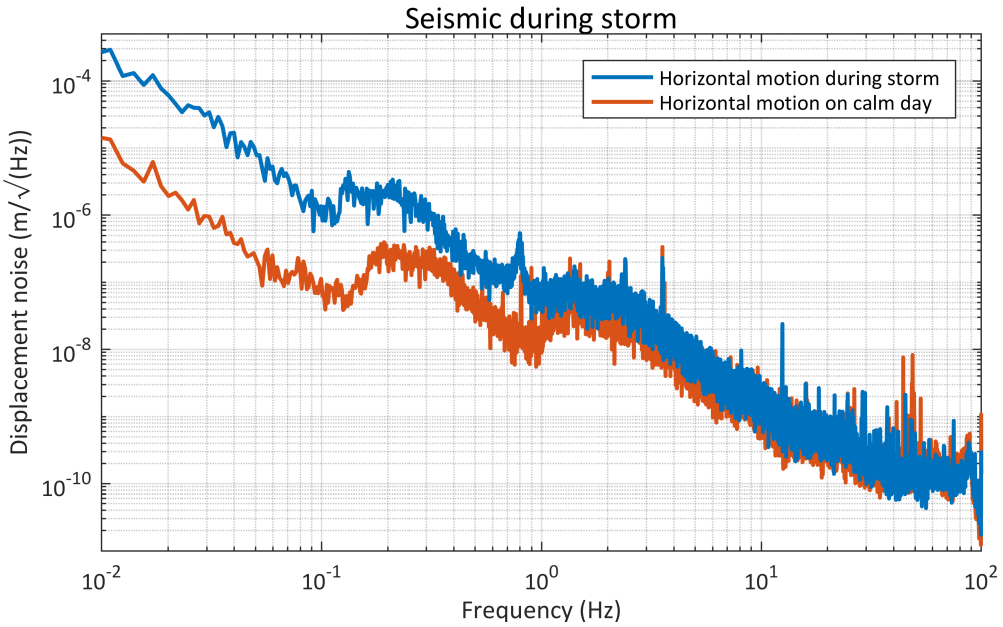

Figure 6.10: Spectrum of ground motion during a storm (blue) compared to a calm summer day (red). Apart from in increased microseism, a peak at 0.8 Hz and increased broadband noise up to 5 Hz appear.

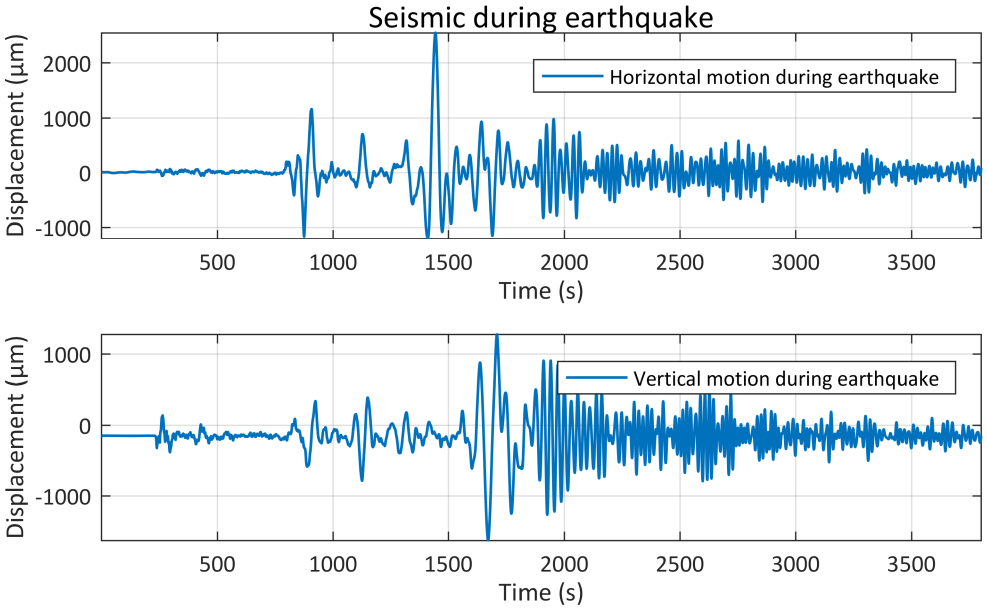

Figure 6.11: Horizontal and vertical ground motion as measured by the STS-2 seismometer of the AEI 10 m prototype during a large earthquake of magnitude 8.2 off the coast of Alaska. Significant ground motion of more than 1 mm prevents operation of the TNI.

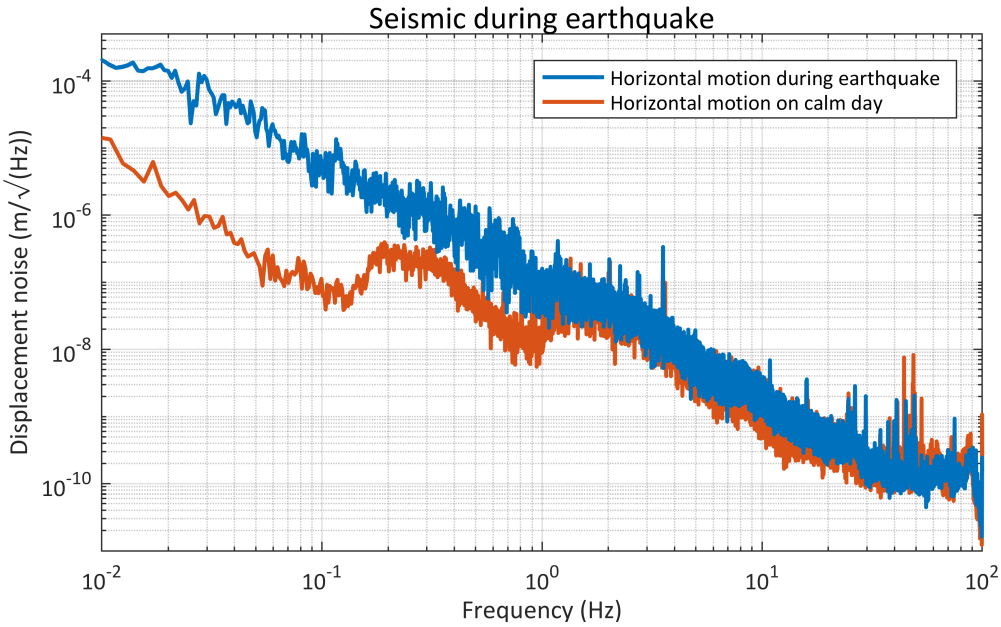

Figure 6.12: Spectrum of the ground motion during the earthquake from 6.11. Significant low frequency ground motion can be seen.

expected noise contribution (shown in figure 6.14).

The contribution to the fundamental longitudinal resonances most likely stems from cross-coupling of vertical excitation to horizontal motion in the transfer function. At 17 Hz, the vertical resonance is clearly explaining the peak observed in the spectrum. As the seismic motion in the horizontal and vertical are of the same order of magnitude, and the table transfer functions also do not differ drastically, the seismic as seen by the TNI topstage is comparable, making the vertical-to-horizontal coupling factor of 0.001 the reason for the low overall level of vertical seismic coupling into the TNI.

6.2.2 Horizontal seismic noise

Horizontal seismic noise is treated similary to vertical seismic noise, but here the horizontal transfer function of the triple suspension is used, projecting a measured table top L4C spectrum (shown in figure 6.15) to the readout of the TNI (shown in figure 6.16). It is evident that the horizontal seismic dominates the TNI readout below 20 Hz. A comparison to calculated transfer functions from topmass motion to TNI readout shows lower levels between resonance peaks and a steeper and earlier rolloff after the third longitudinal resonance. This is readily explained by electronic noise present in the transfer function measurements.

6.2.3 Coil actuator coupling

Another possible way for the seismic motion to couple into the displacement of the thermal noise interferometer is through the test mass coil actuators used for locking. The coils act on the magnets attached to the test mass by means of a variable magnetic field, created by driving a current through the coil. The force excerted onto the mass is dependent on the relative position of coil and magnet.

There is a force maximum where first order coupling is being suppressed - the sweet spot - but

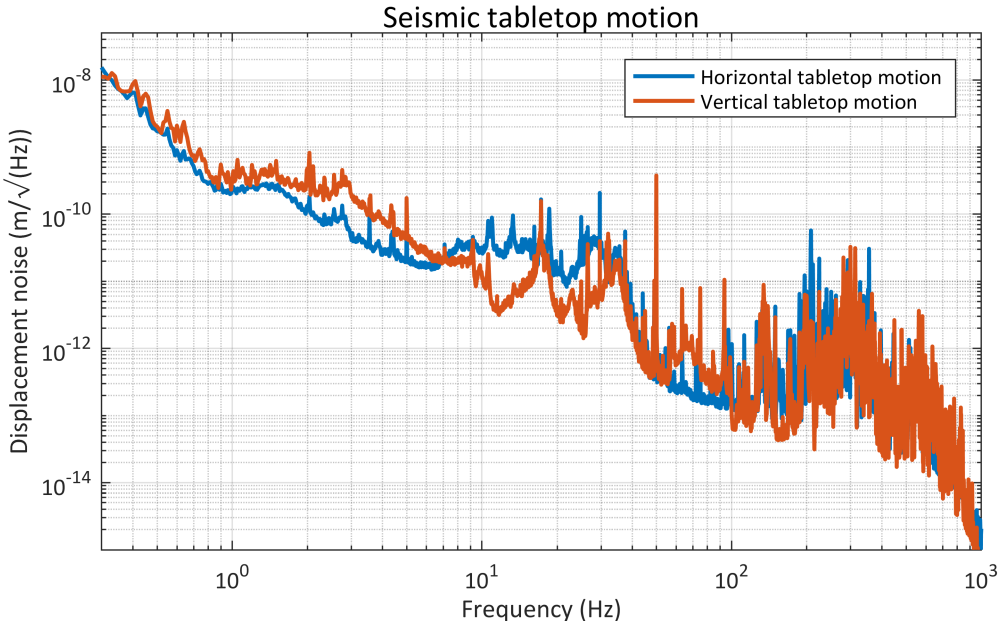

Figure 6.13: Spectrum of tabletop motion in horizontal and vertical, measured by L4C geophones.

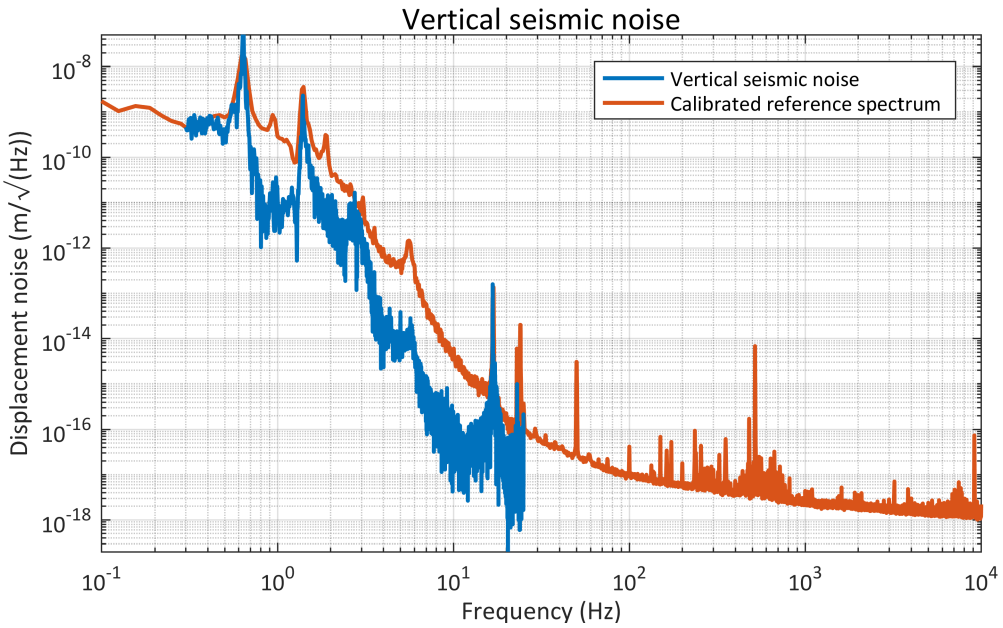

Figure 6.14: Projection of vertical seismic noise to the readout of the TNI. This is based on the measured table top motion propagated through measured transfer functions.

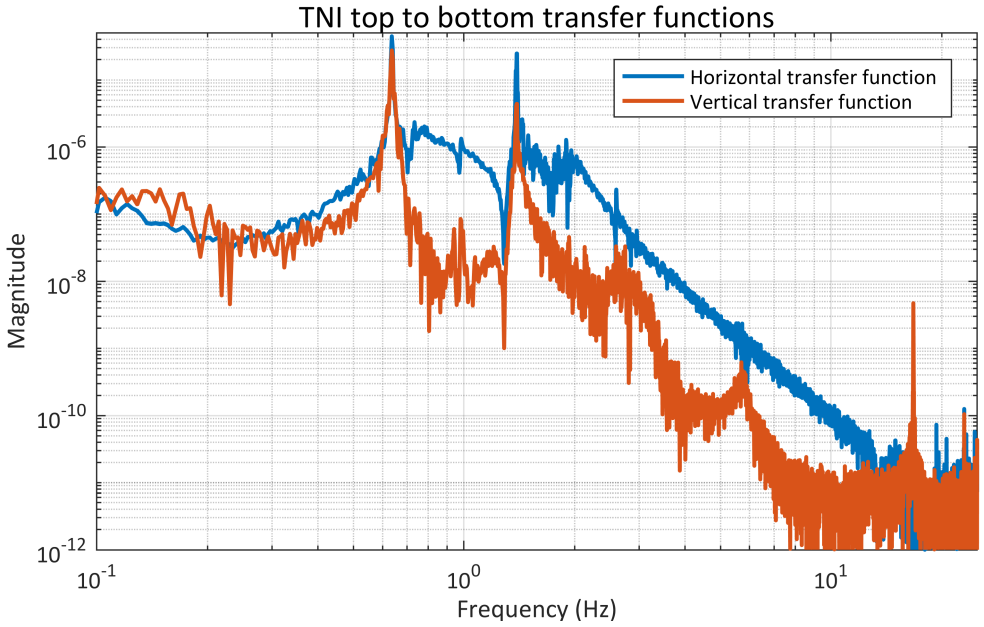

Figure 6.15: Transfer functions from top mass motion in horizontal and vertical to test mass motion.

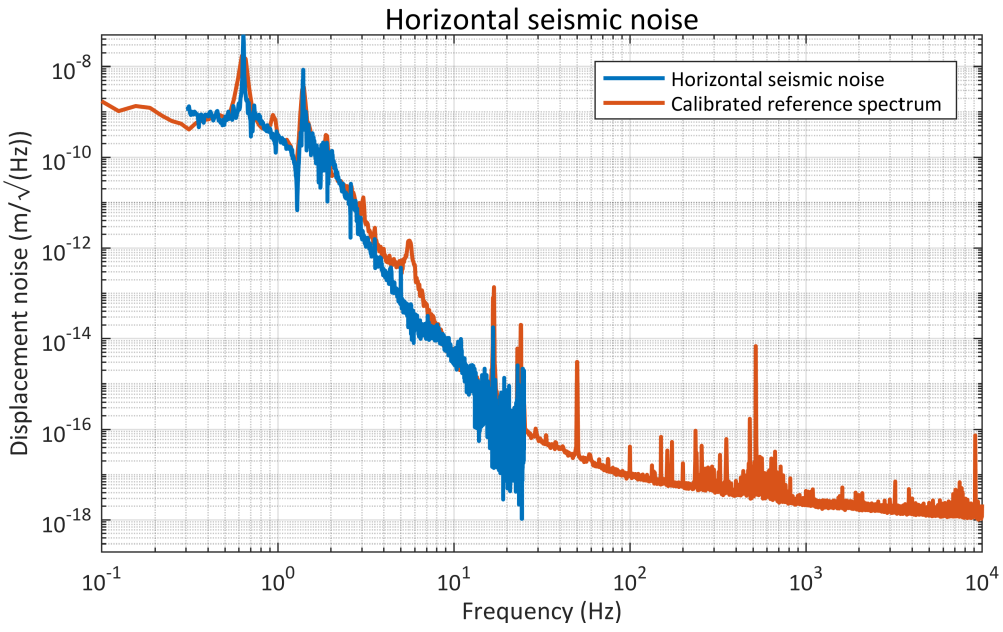

Figure 6.16: Projection of horizontal seismic noise to the readout of the TNI. This is based on the measured table top motion propagated through measured transfer functions.

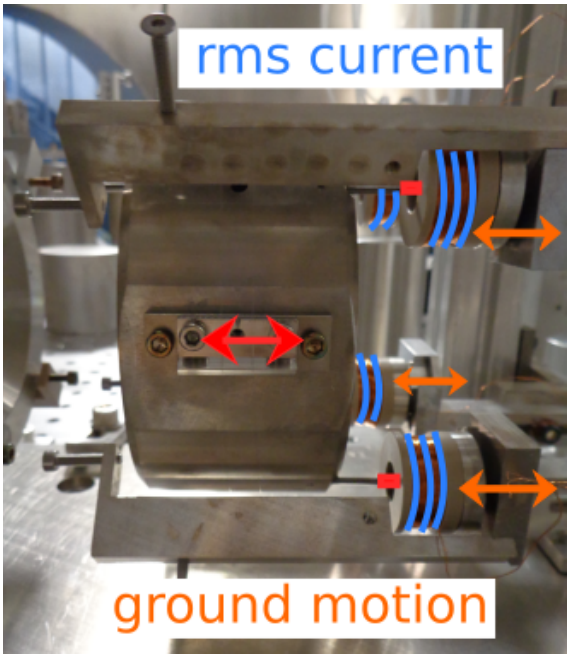

Figure 6.17: Seismic motion of the coils (yellow) varies their position relative to the test mass mounted magnets (red rectangles). As the actuation strength of the coil-magnet pairs depends on this separation, the rms-current (blue) present in lock will create a force noise (red arrow).

the alignment accuracy will always lead to a deviation from this sweet spot. Therefore, under the assumption of an offset from the sweet spot, a force noise will result, driven by seismically induced variation of the coil magnet separation (shown schematically in figure 6.17). The strength of this coupling depends on the rms current present in the feedback loop. The resulting projected noise is shown in figure 6.18.

6.3 Laser frequency noise

Every laser shows variations in the frequency they run at. This frequency noise depends strongly on the type of laser used, and the monolithic NPRO used in the AEI 10 m Prototype shows a good frequency stability without further stabilization, whereas for example external cavity diode lasers posess linewidths on the order of several MHz. The quoted noise of the NPRO is $100\,\mathrm{Hz}/\sqrt{\mathrm{Hz}}$ at 100 Hz and falling with $\frac{1}{f}$ [Mep].

Measurements with the TNI, when the frequency reference cavity is unlocked (shown in figure 6.19), agree well with this noise estimate. As frequency noise is indistinguishable from displacement in a cavity, it can limit the ability to observe thermal noise. Therefore, the frequency reference cavity is used to suppress laser frequency noise by up to seven orders of magnitude. The residual frequency noise is too low to be measured directly, so it has to be estimated from loop gain measurements of the frequency reference cavity or out of loop sensors like the single arm test or the PMC.

Because of the high gain needed for noise suppression to not limit the main sub-SQL interferometer, proper measurements of the loop gain are hard and often being limited by an insufficient dynamic range of measurement tools. At frequencies above 1 kHz, the loop gain is small enough to be extracted from the measurements and modelling shown in chapter 3. At low frequencies, the

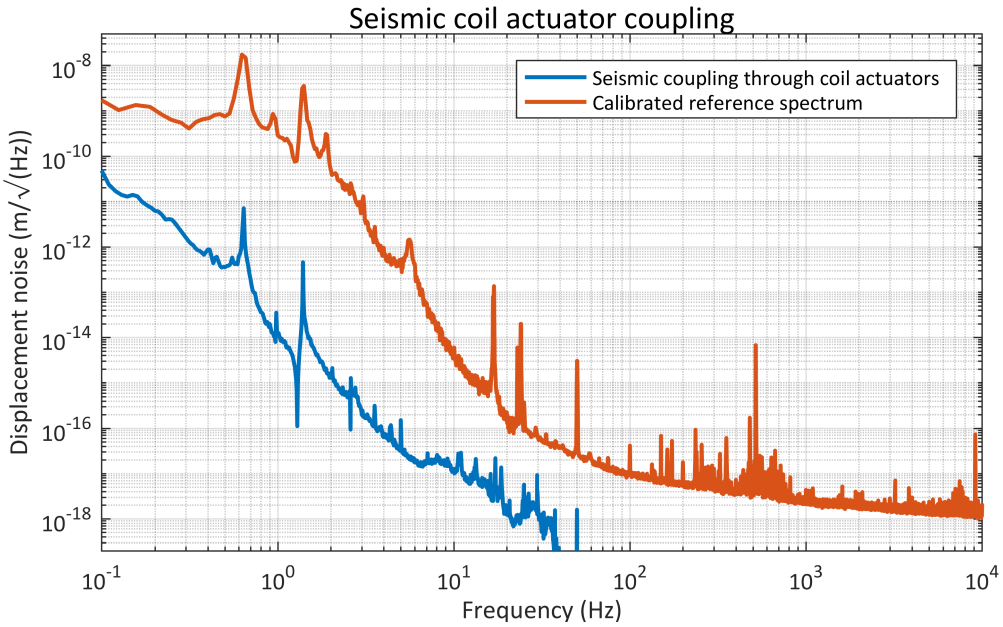

Figure 6.18: Projection of seismic noise coupling through the test mass coils, compared to a measured TNI spectrum. The position dependence of the current-to-force ratio of the coil-magnet pair enables relative motion to influence the actuation strength in lock.

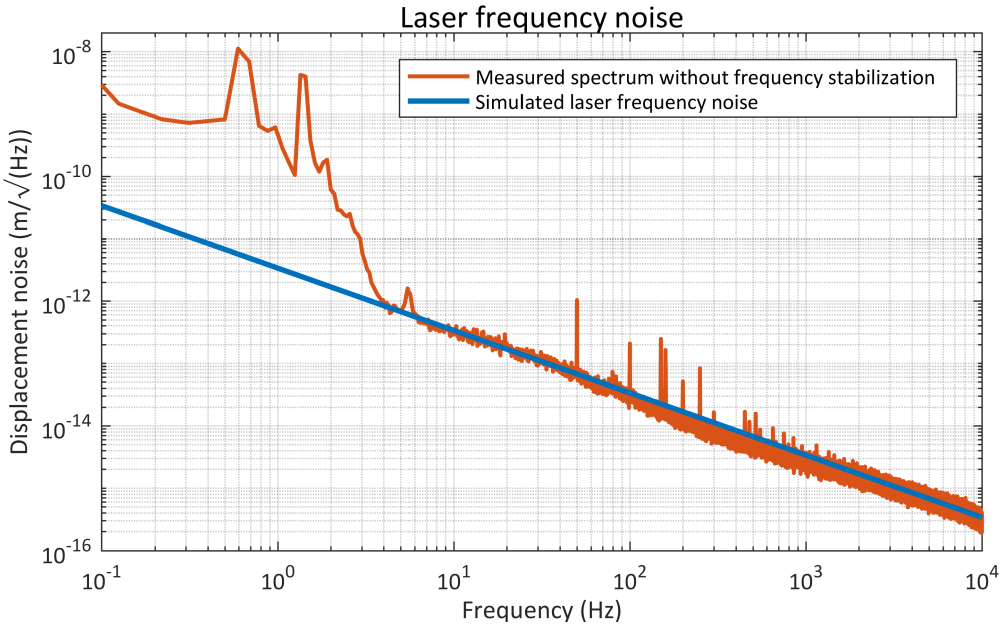

Figure 6.19: Laser frequency noise visible in the TNI readout without active frequency stabilization. The measurement agrees well with the expected frequency noise corresponding to $100\,\mathrm{Hz}/\sqrt{\mathrm{Hz}}$ at 100 Hz.

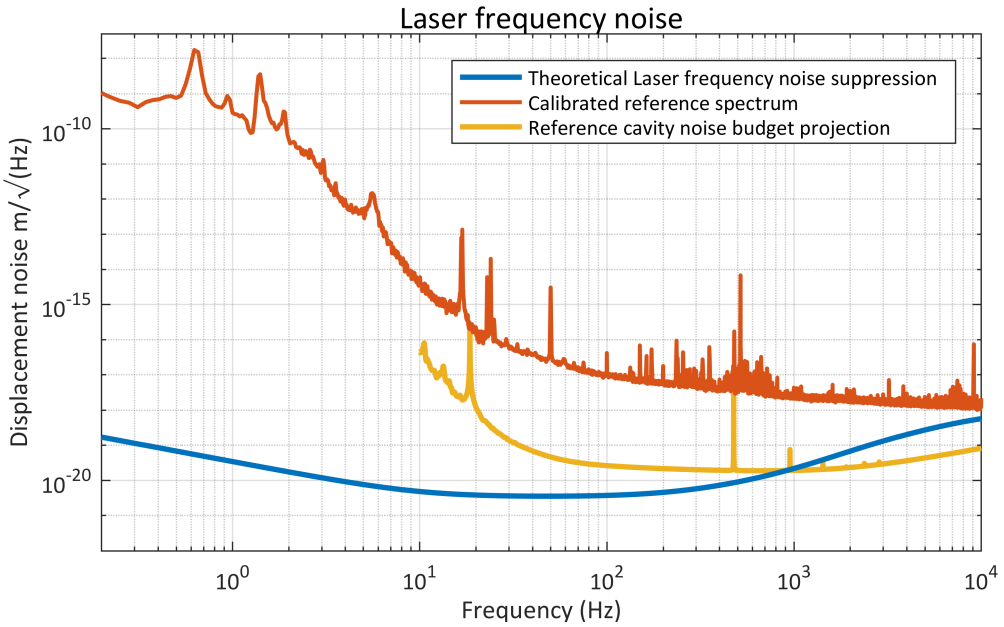

Figure 6.20: Estimate of the influence of suppressed laser frequency noise on the TNI readout. Because of the short cavity length of the TNI, the coupling of frequency noise is reduced by a factor of 100 compared to the SAT. At high frequencies, the level of frequency noise changes over time and can show up more strongly than in the reference measurements.

loop gain is high enough to suppress the frequency noise until the reference cavity noise limit is reached. Because frequency noise and displacement are related by

$$\frac{\Delta f}{f} = \frac{\Delta l}{l}\,, \tag{6.5}$$

shorter cavities are less susceptible to frequency noise. The frequency reference cavity has a round trip length of 21.2 m, the TNI has a length of less than 10 cm, so when the frequency noise is tied to the frequency reference cavity, it will be suppressed by a factor of 220 when sensed by the TNI.

This leads to the estimated frequency noise in the TNI, which is compared to the measured spectrum in figure 6.20. At low frequencies, the reference cavity noise (shown in yellow) is dominating the frequency noise, while at higher frequencies, insufficient gain suppresses the frequency noise to the level shown in blue. It has been observed that the reference cavity loop gain changes in different conditions and even has been reduced due to instability issues. This has been seen at frequencies above 4 kHz, although in the reference spectrum shown in red, the loop gain was sufficient to not be limited by frequency noise.

6.4 Quantum radiation pressure noise

Light emitted by a laser can be best described by a coherent state, giving a Poisson distribution of the photon number detected passing through a reference area. This is the case for suspended mirrors, which will experience a momentum transfer of magnitude $2\frac{\hbar}{k}$ from every photon encountered. In total, this interaction will show up as a radiation pressure, whose frequency dependence is the result of the photon number statistics and the free mass transfer function of the suspended mirror above resonance. The power spectral density can be written as [Han18]

$$S_{rp}(f) = \frac{\mathcal{F}\hbar P}{\pi^4 c\lambda m^2 (f^2 - f_0^2)^2}\,, \tag{6.6}$$

with the intracavity power P, the third longitudinal suspension resonance frequency f_0 and mirror mass m, and shows the $\frac{1}{f^2}$ dependence of the free mass. The photon number noise corresponds to white noise, as does the shot noise discussed before.

Radiation pressure noise is then mainly dependent on the light power, giving the total momentum transferred, and the mass of the mirror, determining the free mass transfer function. If the need arises to suppress quantum radiation pressure noise, non-classical light can be used changing the photon number distribution from Poissonian to sub-Poissonian, effectively homogenizing the arrival times of photons. Furthermore, optical or optomechanical elements with a response opposite to that of the free mirror, effectively acting as a negative mass, could be introduced to cancel out radiation pressure noise.

As the mirror mass in the TNI is high compared to the AEI 10 m prototype sub-SQL interferometer, which is designed to be limited by radiation pressure noise at lower frequencies, and the power is relatively low, the TNI will not be limited by quantum radiation pressure noise. This can be seen in figure 6.21, where quantum radiation pressure noise (dark blue) is close to the classical radiation pressure noise with the ISS fully engaged, and far below the TNI readout sensitivity. The ISS is designed to reduce the intensity noise to the shot noise level, so the agreement is expected.

6.5 Classical radiation pressure noise

The previous section described the impact of quantum radiation pressure noise onto the readout sensitivity of an interferometer with free test masses. This would only dominate when the laser power is shot noise limited. If instead classical laser power fluctuations are present and not sufficiently suppressed, they will induce a radiation pressure noise by the same mechanism as explained before, but the statistics of the photon number fluctuations will be different and strongly depend on the source of the laser power noise.

Figure 6.21 shows classical radiation pressure noise estimates without the ISS operating (green) and with the ISS running without the integrator (light blue). The corresponding TNI spectra are shown in red and yellow, suggesting that without the ISS radiation pressure noise can contribute between 10 Hz and 300 Hz.

6.6 Beam jitter

Beam jitter stems from moving optics in the input path of the TNI. This can be caused by seismic motion of the optical tables relative to each other, but is dominated by the internal resonances of rigidly mounted optics on the seismic isolation tables. This couples into the length signal of the TNI in a similar way as the misalignment of a single mirror of the Fabry-Perot cavity would.

The strength of the coupling depends on the offset of the beam from the center of roation of the mirrors. Beam jitter can be seen as a series of sharp resonance peaks between 200 Hz and 800 Hz (shown in figure 6.22). Identification of the optics responsible has been achieved by knocking

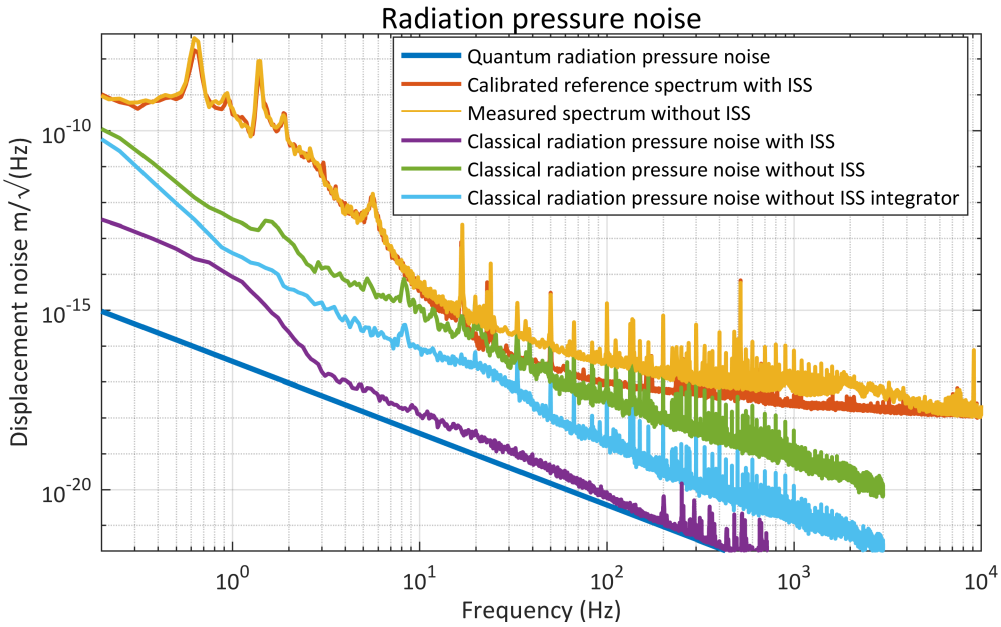

Figure 6.21: Projections of radiation pressure noise in the TNI readout. Distinguished are quantum radiation pressure noise originating from shot noise and classical radiation pressure noise originating from excess power fluctuations. Two measured spectra, with and without intensity stabilization, are shown for comparison.

individual optics while observing a running measurement of the readout spectrum. In vacuum, exciting the central table and south table individually, thereby driving the internal resonances of optics and their mounts provides information of the distribution of optics responsible between the central table and south table.

Driven measurements are shown in figure 6.23 and figure 6.24, where figure 6.24 also shows the coherence measured between table excitation and TNI readout, supporting the inferred connection. In figure 6.24, improvements in the common input path of the SAT and the TNI have been introduced, lowering the amount of jitter coupling into the TNI. Among these improvements are using less and more tightly clamped optics mounts, suspending as many optics as possible. Centering the beam on the cavity mirrors is another way of reducing the influence, and has been achieved to a level of a few 100 µm.

6.7 Scattering

Every optic scatters a fraction of the light impinging on it. The amount of scattering produced has a characteristic angular dependence and depends on the surface properties. Some of the scattered light is reflected or scattered back into the original beam path, and can be phase modulated in the process. This modulated light can then interfere with the readout light, creating a typical step-like structure in the measured spectrum (shown in figure 6.25 between 50 Hz and 150 Hz).

Reducing scattering, especially at small angles, involves choosing properly polished optical surfaces, cleaning optics thoroughly and hitting them under shallow angles away from the normal. Furthermore, reducing the number of optics and placing beam dumps in stray beam paths helps reducing the influence of scattering. Important culprits have been identified to be viewports of the vacuum chamber and beam splitters in the input path. All the signs of scattering visible in the old measurements of figure 6.25 are not obviously dominant anymore in recent TNI measurements.

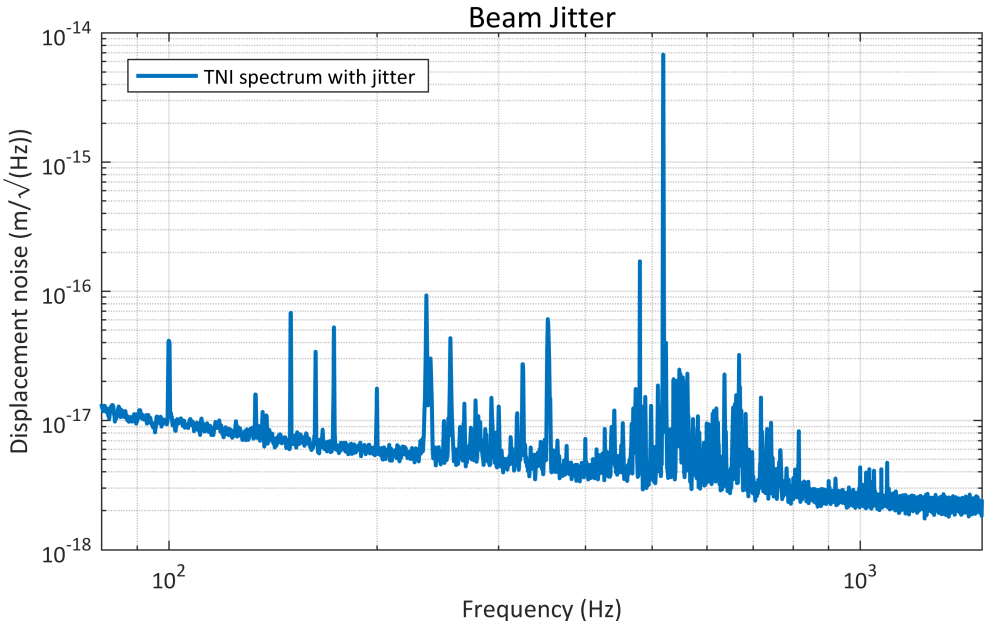

Figure 6.22: Beam jitter appearing in the TNI spectrum as a forest of sharp lines between 100 Hz and 1 kHz.

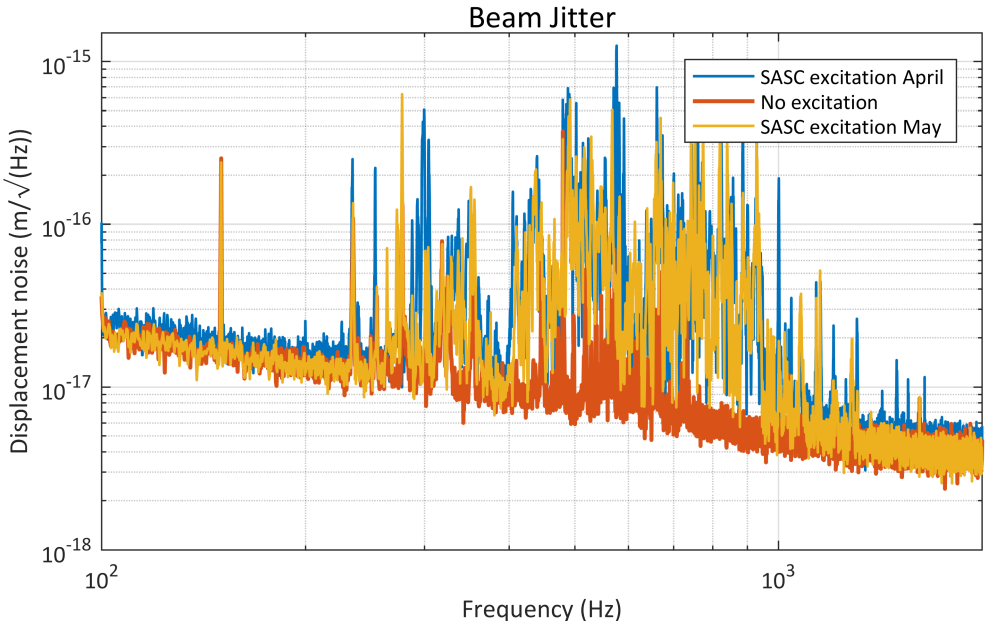

Figure 6.23: Beam jitter comparison between a reference measurement of the TNI error signal without any excitation (red) and measurements with central table excitation before (yellow) and after (blue) improvements in the input path.

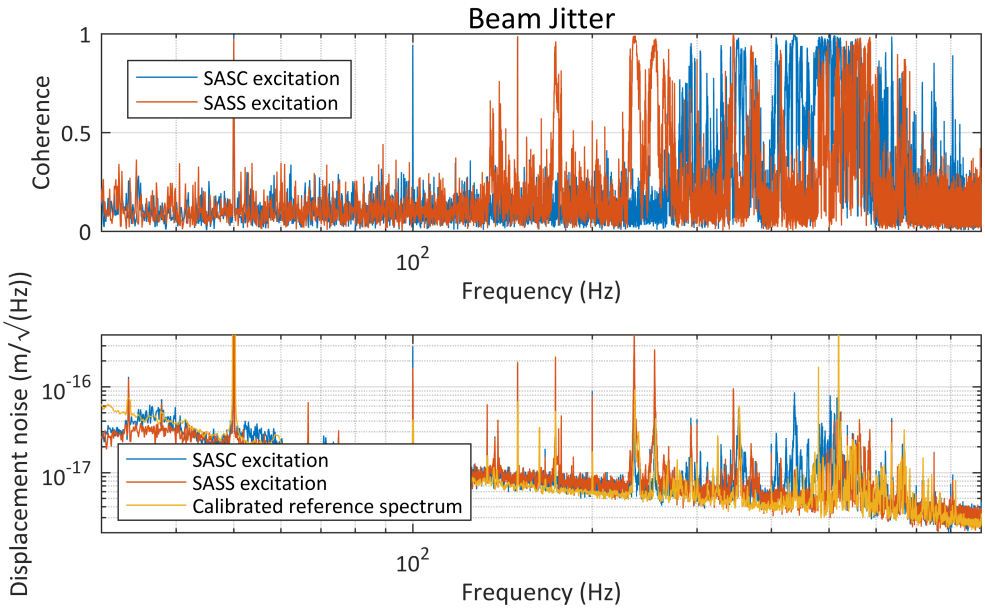

Figure 6.24: The same measurements as in 6.23 after improvements in the input path. The coherence between table excitations and TNI spectrum are shown, indicating the correlation between motion of optics on the corresponding table and the appearance of jitter peaks at this frequency.

Still, when looking at spectrograms with high enough time resolution, structures similar to scattering arches are visible up to a few hundred Hertz. This observation might explain excess noise between 8 Hz and 80 Hz.

6.8 Intensity noise

Intensity noise is ever present on the laser light and can couple into the TNI via a locking point offset. In order to characterize the susceptibility for a locking offset the TNI was locked with a digital offset corresponding to a locking point offset of 1×10^{-12} m or 0.2 % of the linewidth of the cavity. No change in the spectrum was visible, indicating low susceptibility to intensity noise.

This characterization was done in a state where the ISS stabilizes the intensity. Without this stabilization servo, the influence of intensity noise can clearly be seen in the TNI spectrum (shown in figure 6.26), and significant coherence with the ISS photodiodes is measurable between 10 Hz and 5 kHz. While the ISS is engaged, the coherence between measured intensity noise and the TNI error signal becomes negligible, showing that intensity noise does not contribute significantly to the TNI noise spectrum.

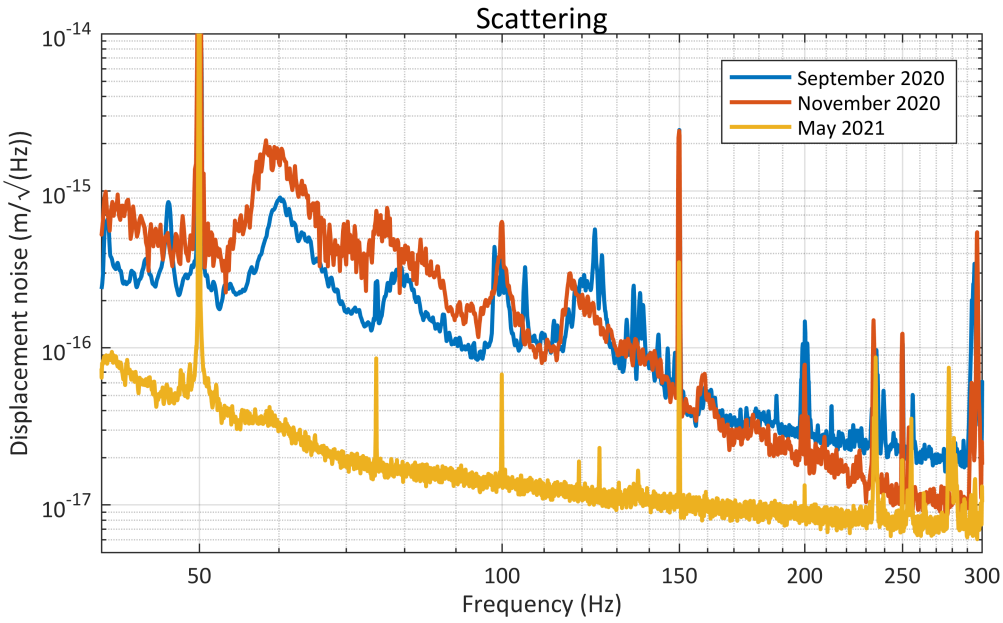

Figure 6.25: The effects of scattering in the measured spectra of the TNI. Typical is a sawtooth-like structure with several peaks, ending at 200 Hz. Removal of scattering sources between the autumn of 2020 and spring of 2021 has completely removed visible effects of scattering over the frequency range of interest.

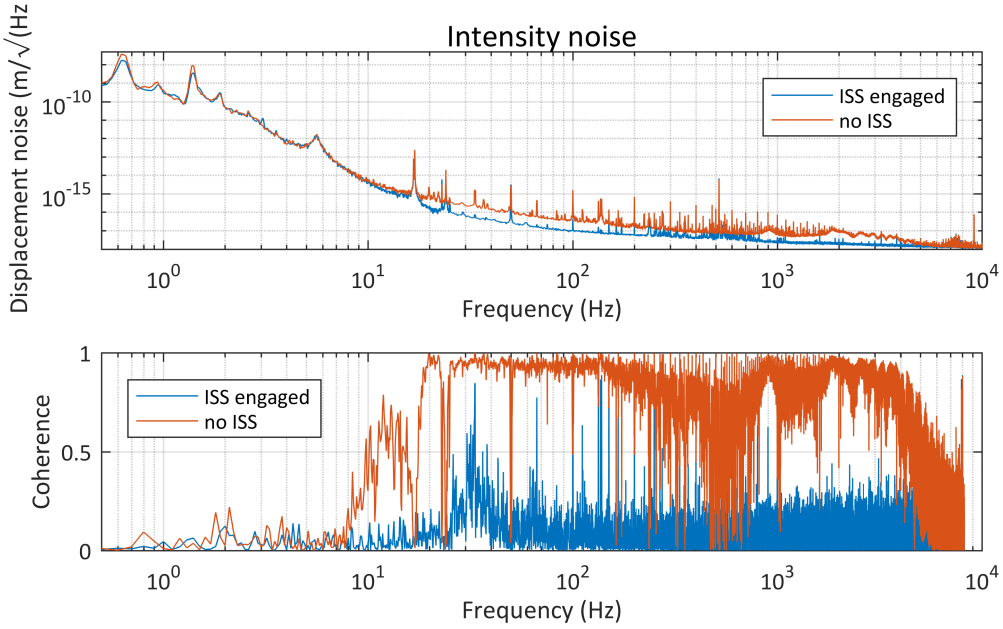

Figure 6.26: The coupling of intensity noise into the TNI is highlighted by taking measurements with and without the ISS engaged. A clear increase in the displacement noise coherent with the ISS photodiode readout is observed from 10 Hz to 5 kHz.

6.9 Residual amplitude modulation

Residual amplitude modulation is a by-product of phase modulation in the EOM used for the PDH-lock. When the polarization of the incoming light is not perfectly aligned to the corresponding crystal axis in the EOM, a small level of amplitude modulation is added to the otherwise perfect phase modulation. A remotely controllable rotation stage holding a half-wave plate in front of the EOM is used to align the polarization to a level of 5 µrad.

As crystal properties are temperature dependent, and the EOM temperature is not stabilized, the optimal orientation will change and the level of amplitude modulation will drift. This introduces offsets into the locking point of the TNI, making it susceptible to laser power noise. The level of residual amplitude modulation was measured to be 10^{-5}.

Coupling of residual amplitude modulation is expected to behave similar to intensity noise, depending on a locking point offset. As shown in section 6.8, no change in the spectrum is visible when changing the locking point offset, indicating negligible influence of residual amplitude modulation.

6.10 Magnetic noise

Magnetic fields can be found everywhere in the lab, originating from a variety of sources. The weakest and most homogeneous contribution comes from the earth magnetic field. The homogeneity can be influenced by nearby conducting structures, but because of the small magnitude and slow change will play no role for the TNI.

More problematic magnetic coupling comes from improperly shielded cables, but the strongest sources will be components specifically designed to produce magnetic fields strong enough to actuate on magnets attached to masses. These coil-magnet pairs are found in a number of places inside the vacuum tank, and stray fields of these can also apply a force to other magnets located on movable masses like the TNI input mirror.

A passive test of magnetic coupling to the test mass magnets of the TNI was performed using the magnetic field of the turbo pumps running at 485 Hz. Figure 6.21 shows a comparison between a spectrum taken when the turbo pump was running (red) and a spectrum when the turbo pump was shut down (blue). The line at 485 Hz vanishes, and the most probable coupling mechanism is magnetic as seismic at such a high frequency should be strongly suppressed.

Another way of gaugeing the sensitivity to magnetic fields is to deliberately excite magnetic fields at specific frequencies and measure a transfer function to the TNI readout. The coils of the LVDTs in the south table were chosen, and the signal of the SPI measuring inter-table motion was taken as a sensor for the strength of the LVDTs excitation (shown in figure 6.28). The overall level of coupling is small, but clearly measurable at frequencies between 20 Hz and 80 Hz. The reduction from red to blue and purple to yellow was achieved by replacing the test mass mounted magnets by smaller magnets. The order of magnitude reduction agrees well with the change in volume between the magnets. Placing the magnets in alternating orientations compared to a common orientation as before did not add a significant advantage. This can be explained by having inhomogeneous magnetic fields at the location of the test mass.

6.11 Electronic noise

All electronics show some level of noise, stemming from different mechanisms and components. Resistors for example show Brownian thermal noise of electron motion called Johnson noise. Operational amplifiers, used in most electronics in operation, show low levels of current and voltage noise, which can then influence the performance of sensing electronics as well as electronics driving actuators in feedback loops. The effects of noise of the most important electronic components

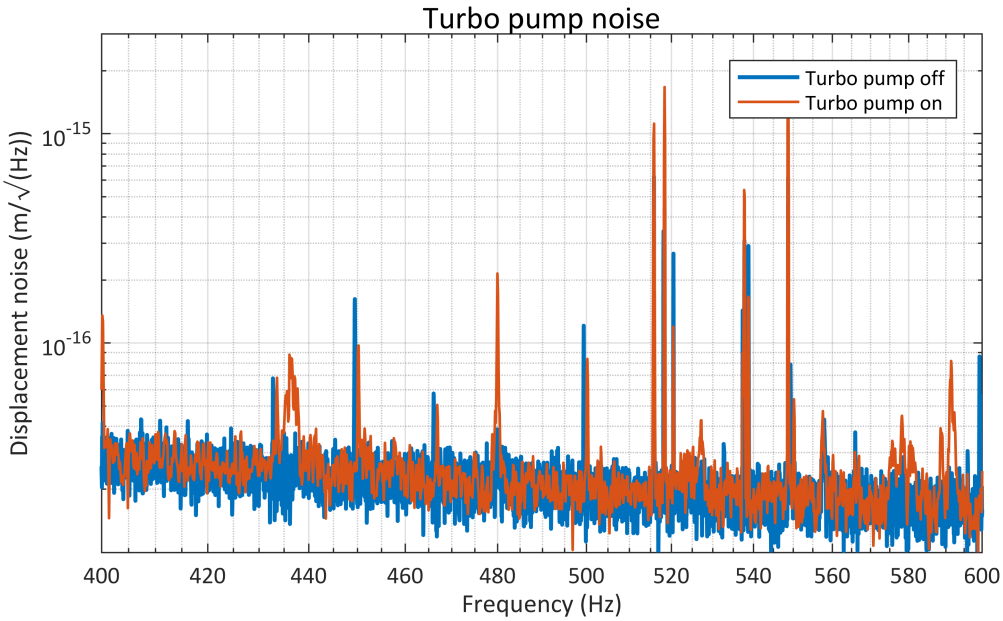

Figure 6.27: Noise originating from the turbo pump by magnetic coupling can be observed at 485 Hz in the orange spectrum. The absence of the peak without the turbo pumps running in the blue trace corroborates this finding.

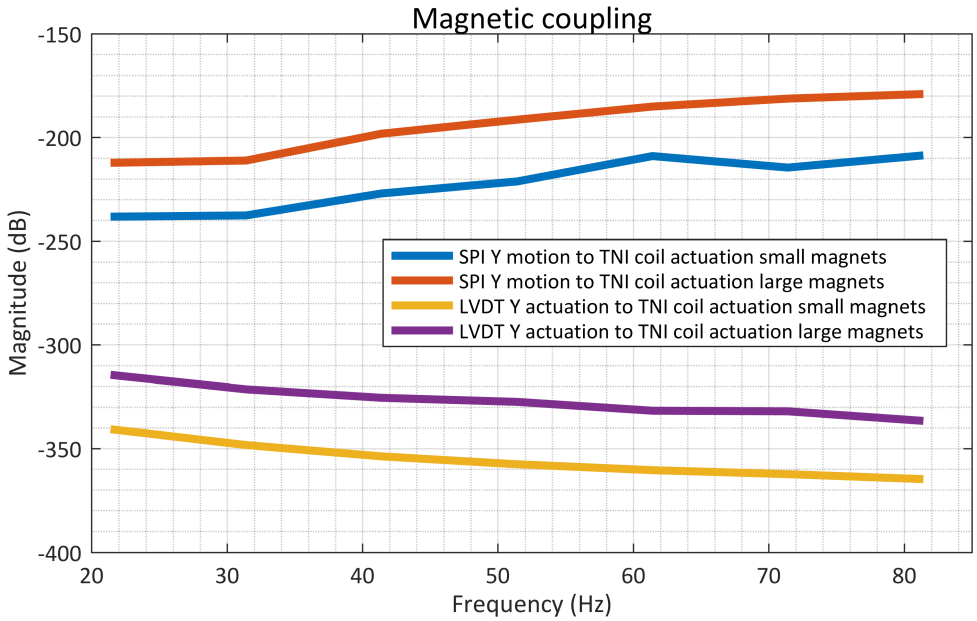

Figure 6.28: Measurement of the magnetic coupling from table coil actuators (LVDTs) to the TNI, with the old larger magnets (red and purple) and the new smaller magnets (blue and yellow) attached to the test mass. A clear reduction by more than an order of magnitude is visible, corresponding to the change in magnet volume.

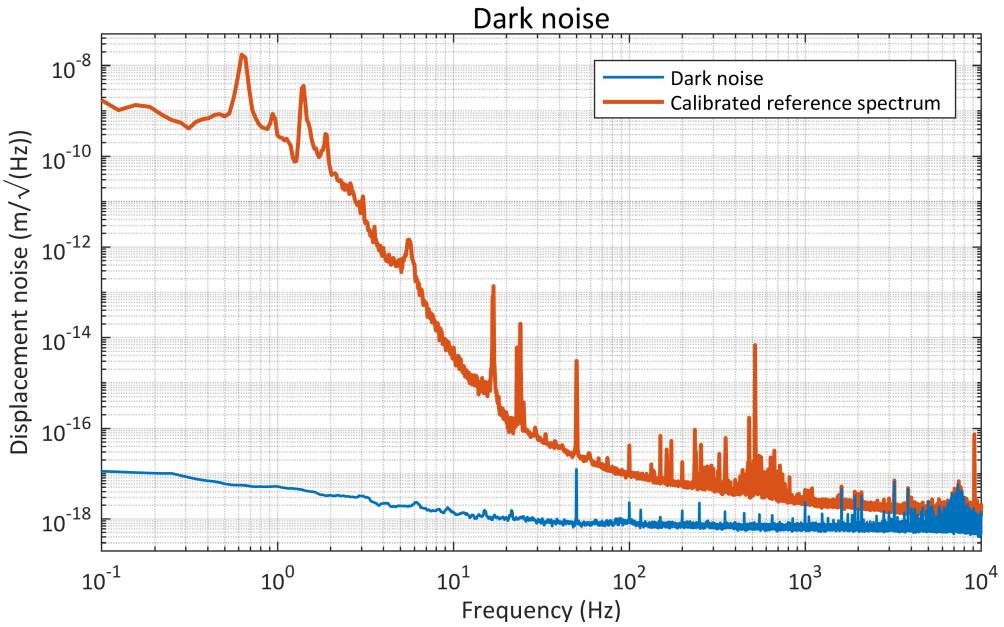

Figure 6.29: Noise measured in the TNI when no light impinges on the locking photodiode. This corresponds to the electronic noise of the photodiode and subsequent parts in the locking loop, limiting the readout sensitivity together with shot noise.

used in damping and locking loops will be analyzed in the following subsections.

6.11.1 Dark noise

The electronic noise produced by the photodiode and the amplifying electronics in the absence of light is called dark noise. It is estimated by projecting noise contributions, mainly from resistors and operational amplifiers, onto the output, where the error signal is sensed. This is compared to spectra taken while no light hits the photodetector. As the phototector electronics are designed to be shot noise limited at powers of 12 mW, the dark noise is not far below this level. In the case of half the power hitting the photodiode, as is currently the case in the TNI, the dark noise will be equal to the shot noise and make a significant contribution to the overall noise.

For the TNI calibrated with 6.6 mW of power on the locking photodiode, a spectrum without light is shown in figure 6.29. The corresponding spectrum in lock does not have much clearance at frequencies above 1 kHz and the dark noise contribution becomes substantial. Furthermore, a number of lines abover 1 kHz, especially a dense forest between 5 kHz and 10 kHz, coincide, showing the influence of the dark noise on the TNI spectrum. A reduction of this noise is necessary for future measurements with lower loss coatings.

6.11.2 BOSEM noise

Apart from projecting measured and estimated BOSEM noise onto test mass displacement, another way to estimate the influence of BOSEM damping onto the TNI sensitivity is through comparing spectra with and without damping. A spectrum for a locked TNI without longitudinal and yaw damping is shown in figure 6.30, a second spectrum showing the locked TNI without vertical and pitch damping in the output suspension is shown in figure 6.31 and finally a spectrum without any damping is shown in figure 6.32. These spectra were taken after ramping a zero gain filter in

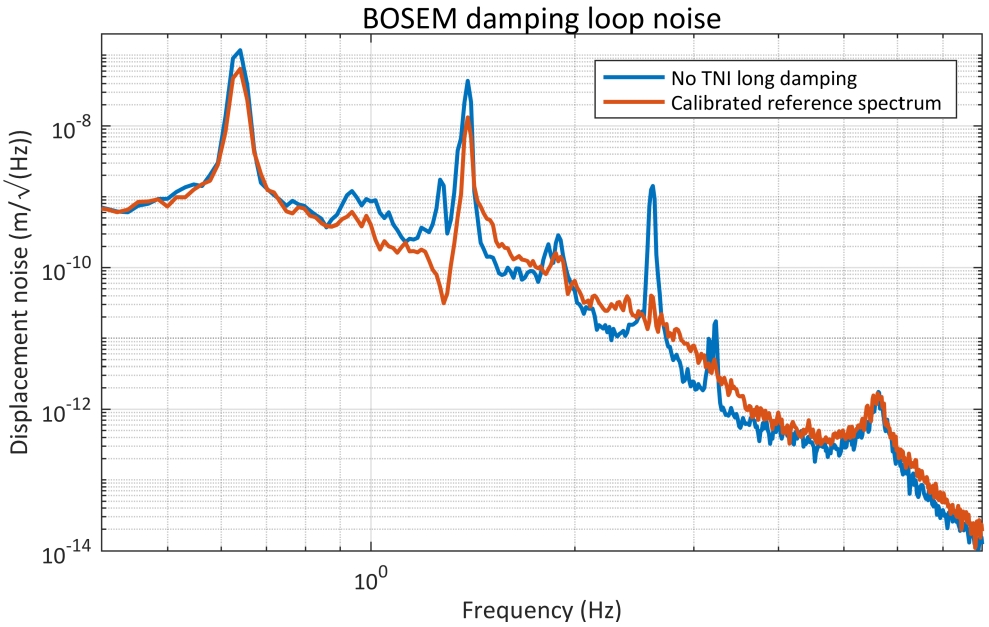

Figure 6.30: TNI spectrum with BOSEMs D and E turned off, providing no damping in longitudinal and yaw. The corresponding resonances show up more strongly, but the off-resonance noise floor is reduced, showing the influence of BOSEM sensor noise.

the BOSEM damping loops while the cavity was locked.

The most significant spectrum is the one taken without longitudinal and yaw damping, as these degrees of freedom couple most strongly into the TNI length readout. A clear reduction is visible between the longitudinal resonances at 0.63 Hz, 1.38 Hz and 2.62 Hz, while the resonances themselves are more strongly excited. Some level of damping of these resonances is provided by the locking loop.

Removing damping of the vertical and pitch degrees of freedom of the output suspension excites the pitch and vertical resonances, which become visible in the spectrum. No significant off-resonant noise reduction is visible, showing that damping loop noise from these degrees of freedom couples only weakly into the TNI readout.

Measuring the length noise without any damping removes any noise effects from the damping loops (shown in figure 6.32). On the other hand, the resonances are stronly excited by seismic and dominate the spectrum. A pronounced reduction is nevertheless visible between the resonances between 3 Hz and 6 Hz.

The strength of coupling noise through the damping loops is also assessed by changing the loop gain setting to higher values, increasing the effect of fed-back noise. In figure 6.33, spectra are shown for the nominal loop gain (yellow) in comparison with a doubled loop gain (red) and a tripled loop gain (blue). Especially between 1.5 Hz and 17 Hz, an increase in the noise related to increased gain is visible, confirming the finding from above that BOSEM loop noise dominates the spectrum between suspension resonances.

Finally, a comparison of the measured spectrum with calculated projections is done (shown in figure 6.34), where the ADC noise, the coil driver noise and sensing noise in the damping loop are considered. For the ADC noise and the coil driver noise, simulations discussed in chapter B, using Zero, are taken and projected into the TNI readout via measured transfer functions. Sensing noise is based on the open-light spectrum of the BOSEM readout, projected into the TNI length readout. While the coil driver noise contributes to the resonances, the dominating contribution

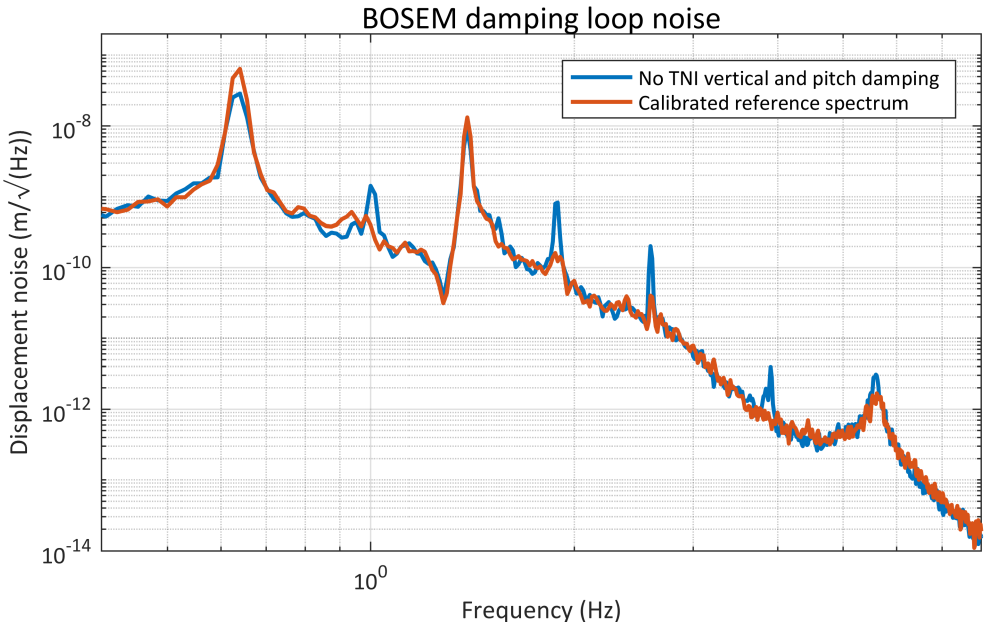

Figure 6.31: TNI spectrum with BOSEMs A, B and C turned off, providing no damping in vertical and pitch. The corresponding resonances show up more strongly, but the off-resonance noise floor is not reduced significantly, showing less noise coupling of BOSEM sensor noise through these degrees of freedom.

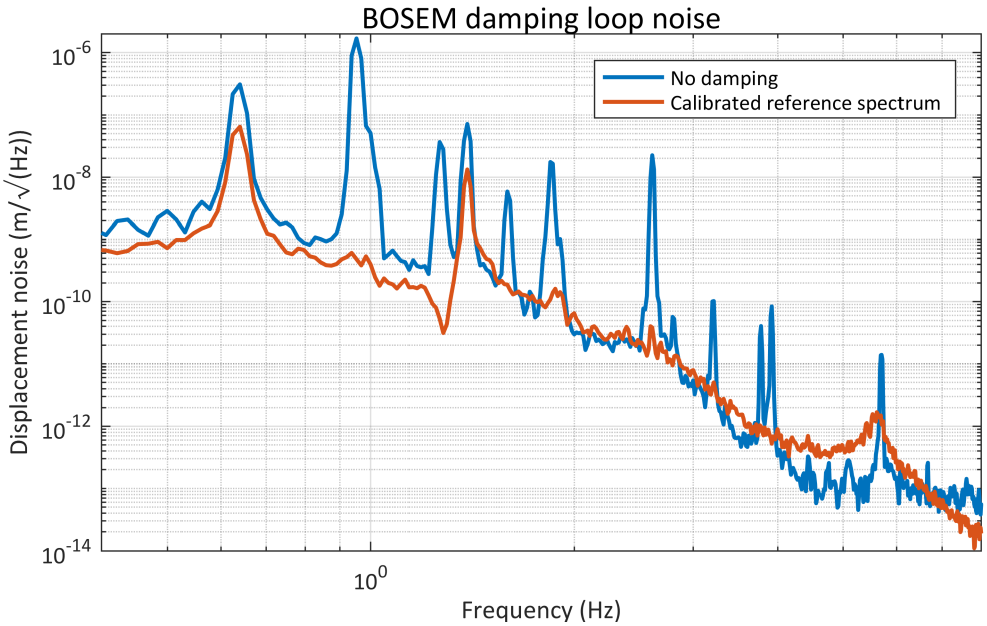

Figure 6.32: TNI spectrum with all BOSEMs turned off, providing no damping in any degree of freedom. All the suspension resonances show up more strongly, but the off-resonance noise floor is reduced, showing the influence of BOSEM sensor noise.

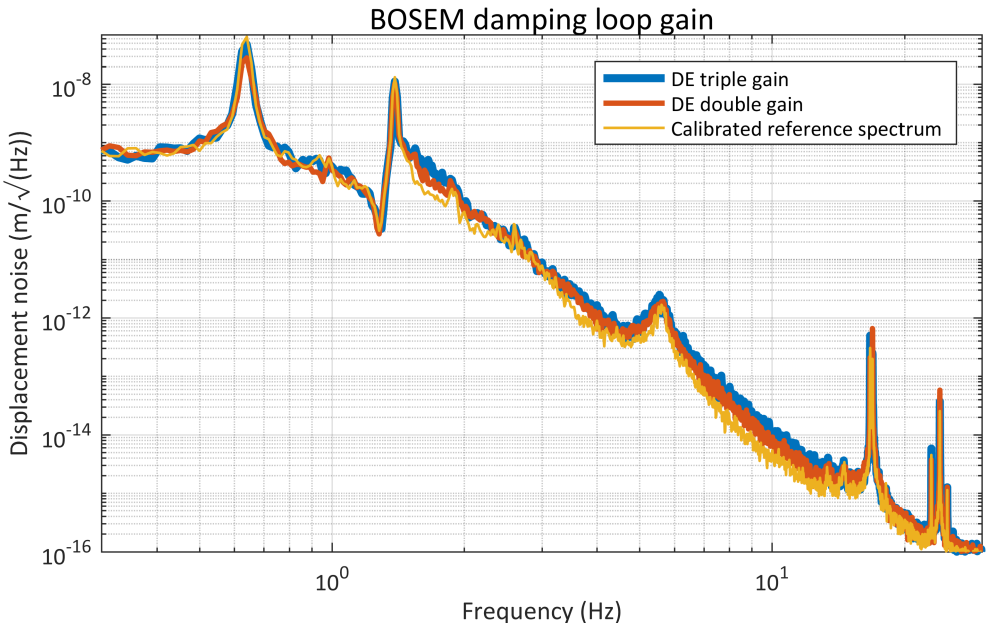

Figure 6.33: TNI spectra with different gain settings of the BOSEM damping loops. Increasing the gain by a factor of 2 (red) and 3 (blue) elevates the level of sensor noise being fed back into the TNI readout.

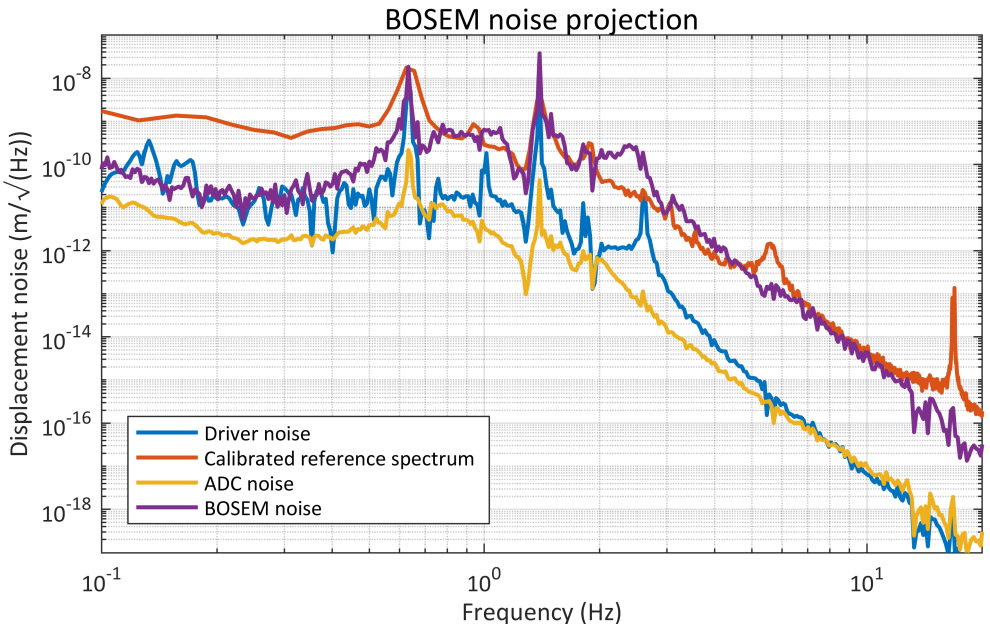

Figure 6.34: Projections of BOSEM noise into the TNI readout. The projected noise incorporates BOSEM sensor noise and electronic noise from the DAC and coil drivers.

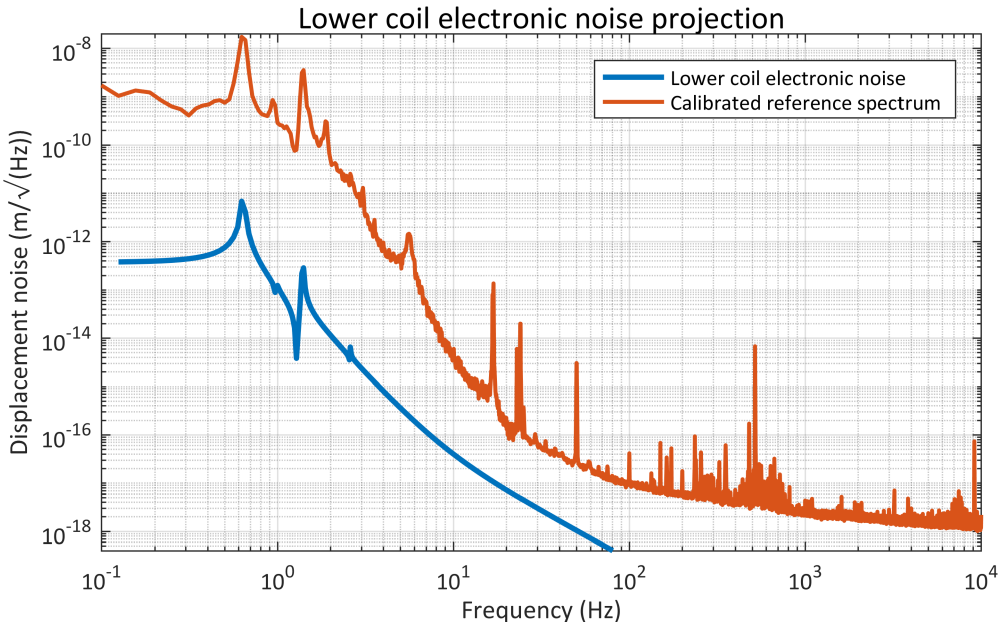

Figure 6.35: Electronic noise from the coil driver of the locking coils couples into the TNI readout. This electronic noise consists of contributions from voltage noise of the circuit, current noise of the circuit, digitization noise of the DAC and other voltage noise associated with the AI-filter.

comes from the sensing noise, limiting the TNI performance between resonances and up to 15 Hz.

6.11.3 Coil driver noise

The electronic noise originating in the coil driver directly couples to motion of the cavity input mirror through the coil actuators. An important part is the current noise, which is translated into a magnetic field inside the coil, acting on the magnet attached to the mirror. The level of current noise was simulated using ZERO.

There is also voltage noise present, simulated in the same way using ZERO. These two intrinsic noise sources inside the coil driver are complemented by DAC noise from CDS, creating an input to the current driver. Projections of these noise sources into the TNI readout via estimated conversion factors and transfer functions give an expected contribution more than an order of magnitude below the measured noise.

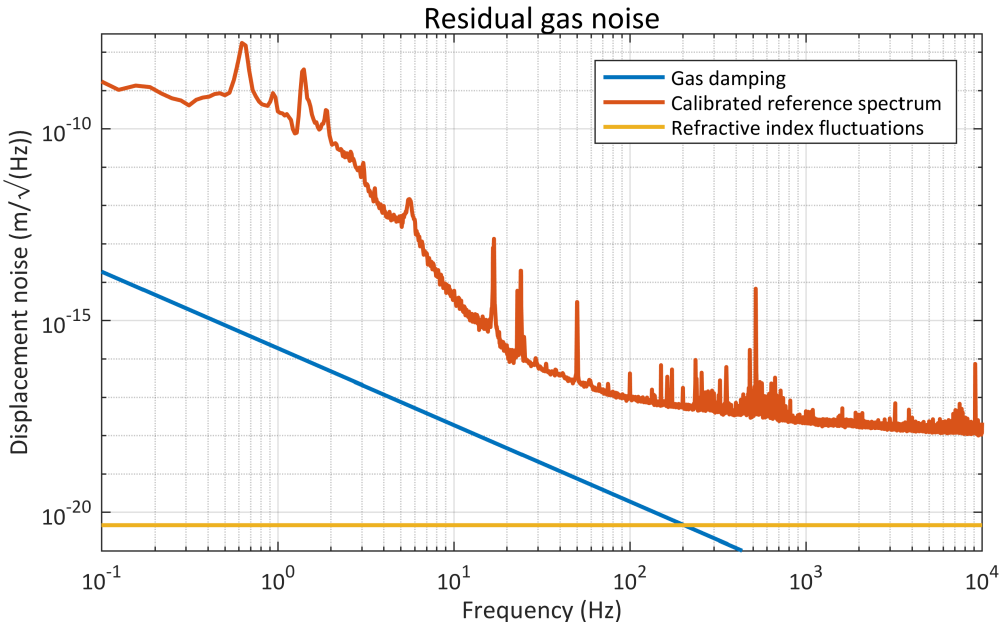

Figure 6.36: Calculation of the exptected readout noise from residual gas in the vacuum system. At a pressure of 2×10^{-7} mbar, refractive index fluctuations (yellow) and gas damping (blue) are negligible, where gas damping is calculated for water molecules making up the majority of the residual gas.

6.12 Residual gas noise

Although the experiment is placed inside a vacuum chamber pumped down to a pressure of less than 2×10^{-7} mbar, there are still 10^{15} particles per m^3. Most of these particles are water molecules, as inferred from residual gas analyzer scans. These particles interfere with the measurement in two ways. First, fluctuations in the residual gas density will change the refractive index, and second, the gas present will impart momentum randomly onto the mirrors.

Both calculated contributions are compared to the measured TNI noise spectrum in figure 6.36, and the contributions are discussed below in detail.

6.12.1 Refractive index noise

The residual gas at a pressure of 2×10^{-7} mbar provides an optical medium with a refractive index different from that of an ideal vacuum. Through random density fluctuations present in this residual gas, the refractive index will fluctuate along the path taken by the laser inside the TNI.

This in turn will change the optical path length, acting like displacement noise. As the noise is proportional to the beam path length and the residual pressure, the short cavity of the TNI and the low pressure in the vacuum chamber make this noise contribution negligible, as can be seen from the yellow trace in figure 6.36.

6.12.2 Background gas damping

Brownian motion was first observed by Robert Brown in 1827, when he observed pollen being moved aronud randomly in water [Bro28]. The same effect can be observed when the residual gas in the vacuum chamber imparts momentum onto the suspended mirrors randomly.

Another way to look at this is through the fluctuation-dissipation theorem, connecting the random motion with viscous damping experiend by the mirrors moving through the background gas. This damping can be modified when surfaces of the suspended mirrors are close to other surfaces, trapping volumes of residual gas in between.

Although with the pressure at 2×10^{-7} mbar, the system is considered to be in an ultra-high vacuum, considerable motion can be introduced, and it is mainly the high mirror mass of 850 g, which prevents the TNI from being gas damping limited up to a few hundred hertz (blue trace in figure 6.36).

6.13 Suspension thermal noise

Not only the mirrors experience fluctuations driven by the thermal bath, but also the wires and blades used in suspending the mirrors to isolate them from seismic motion. There are three main contributions, one from the longitudinal modes being driven by fluctuations close to the suspension points of the wires, the second from the violin modes of the wires, starting from a few hundred hertz, and the third vertical suspension thermal noise stemming from the blade springs and vertical bounce modes of the wires.

6.13.1 Longitudinal suspension thermal noise

Longitudinal modes of the suspension are excited by thermal energy, mostly coupled through losses in the wires close to the suspension points. The dominating contribution in the measurement band of the TNI comes from the lowest wire stage, which suspends the test mass from the intermediate mass. Contributions from the wire stages above are filtered out by the suspension transfer function above the resonances.

The amount of losses can be calculated using Levin´s approach [GH99], where an oscillatory force at the corresponding frequency pushes the suspension, and the stored deformational energy together with the losses present in the deformed volume give the total energy loss. There are two possibilies for the frequency dependence of the losses as well as different ways deformations can result in losses.

Main contributions stem from bulk losses and surface losses, the amount depending on the part of the wire where the loss happens. Each of these can be caused by internal friction, which will lead to Browninan motion, or thermoelastic damping, where deformations lead to temperature gradients, which in turn result in lossy heat flow, resulting in thermoelastic noise.

For the noise projection of the TNI, pygwinc was used to give a suspension thermal noise spectrum, including horizontal, vertical and violin mode contributions. The horizontal suspensions thermal noise in figure 6.37 consists mainly of the peaks below 10 Hz, corresponding to the longitudinal suspension resonances. They are well below the measured spectrum, making no siginificant contribution to the overall noise.

6.13.2 Vertical suspension thermal noise

Vertical suspension modes being excited by the thermal bath include bounce modes of the suspension wires and internal modes of the blade springs. Their influence on the TNI readout is diminished by the vertical to horizontal coupling factor of 0.001 [Pli+04]. In figure 6.37, the vertical resonance at 17 Hz is the result of the vertical suspension thermal noise, contributing to the TNI readout. There is a small offset between the vertical resonance frequency predicted by the model and the measured frequency.

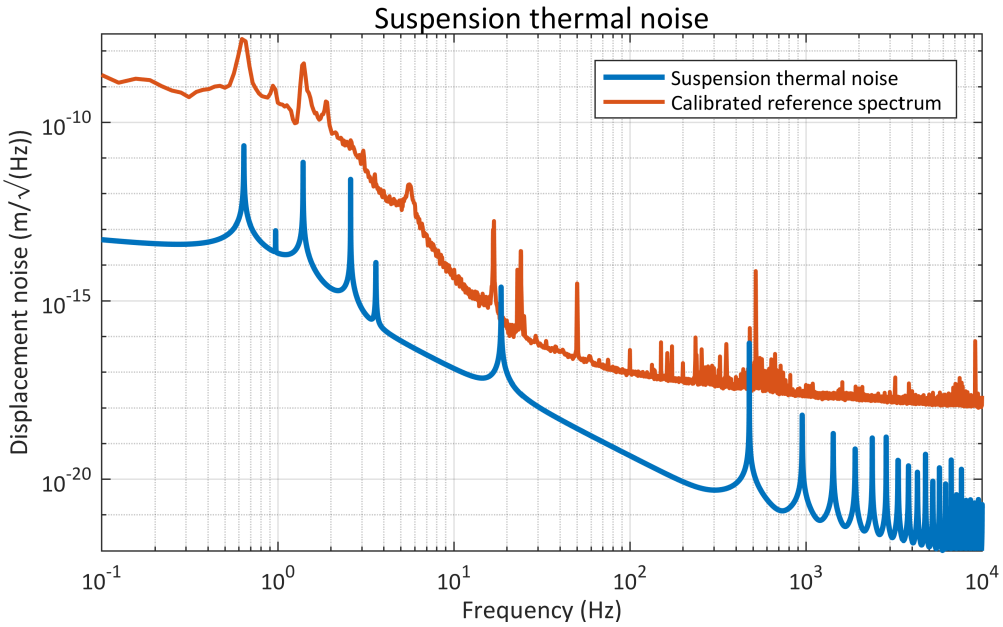

Figure 6.37: Projection of suspension thermal noise in the TNI readout. The contribution from horizontal suspension noise is dominated by the lowest stage wires bending at their upper breakoff point. Vertical contribution is mainly driven by the steel blades holding the top mass, but the blades in the upper mass and bounce modes of the wires contribute at higher frequencies. The forest of lines at high frequencies consists of violin modes of the lowest stage wires.

6.13.3 Violin modes

Violin modes are transversal oscillations of the wires, quite similar to an excited guitar string. They are mostly thermally excited, their strength depending on the loss in the wire and its spatial distribution. Where high loss and large modal amplitudes coincide, the coupling will be strong, whereas losses in the nodes of modes will not drive this mode strongly.

The frequencies of the violing modes depend on wire parameters such as length, thickness, loading and material parameters. Pygwinc, taking the suspension parameters, predicts the violin mode suspension noise as shown above 400 Hz in figure 6.37. Some resonances might be visible peaking through, but cannot be distinguished easily from jitter noise peaks. The modelled frequencies are also not perfectly matching observed violin mode frequencies. These have been measured while attempting to lock the TNI using the intermediate mass, which strongly excited a large number of modes. Among these was for example the first violin mode at 515 Hz.

6.14 Mirror thermal noise

The theory of thermal noise present in highly reflective mirrors is discussed in detail in 2.2, so this section only briefly discusses the different noise sources and their effect on the overall noise observed in the TNI. All noise curves are based on MATLAB-based simulations, as discussed in 2.3.

6.14.1 Coating Brownian noise

The most important noise contribution in the TNI comes from coating Brownian noise, as the amorphous coating material of the mirror under investigation is more lossy than the bulk material of the substrate. As the TNI has been designed to be limited by coating thermal noise, it is expected to dominate the noise budget. The exact level of the noise has a significant uncertainty stemming from imprecisely known coating parameters, especially the loss angle of the materials used. In the case of the reference cavity spare mirror used, the thickness of the coating is unknown as well and has been estimated based on the measured transmission.

The coating Brownian noise estimate for the old configuration of two mirrors of reflectivity 99.85 % made by Laseroptik is shown in figure 6.38, with the individual contributions of the input mirror (purple) and test mass (yellow dashed) calculated from the waist sizes of 384 µm and 86 µm respectively. The incoherent sum shows the same $\frac{1}{\sqrt{f}}$ frequency dependence as the measured spectrum, but is lower by more than a factor of two.

It is assumed, that the measured spectrum is dominated by thermal noise from the composite mass, masking the coating Brownian thermal noise contribution. The situation is different for the more recent configuration with a monolithic reference cavity mirror by Gooch and Housego as the test mirror. As the coating is approximately a factor of two thicker, the expected noise from the test mirror goes up. At the same time, the measured spectrum went down, such that the spectrum between 50 Hz and 10 kHz is showing coating Brownian noise of the monolithic end mirror (shown in figure 6.39).

6.14.2 Coating thermooptic noise

Another major coating thermal noise contribution, and one possibly dominating in crystalline AlGaAs-coatings, is thermo-optic noise. For the amorphous silica and tantala coatings under investigation, the contribution is insignificant due to the more beneficial thermal parameters of the amorphous materials.

In figure 6.40, the individual contributions from the input mirror and test mirror, both by

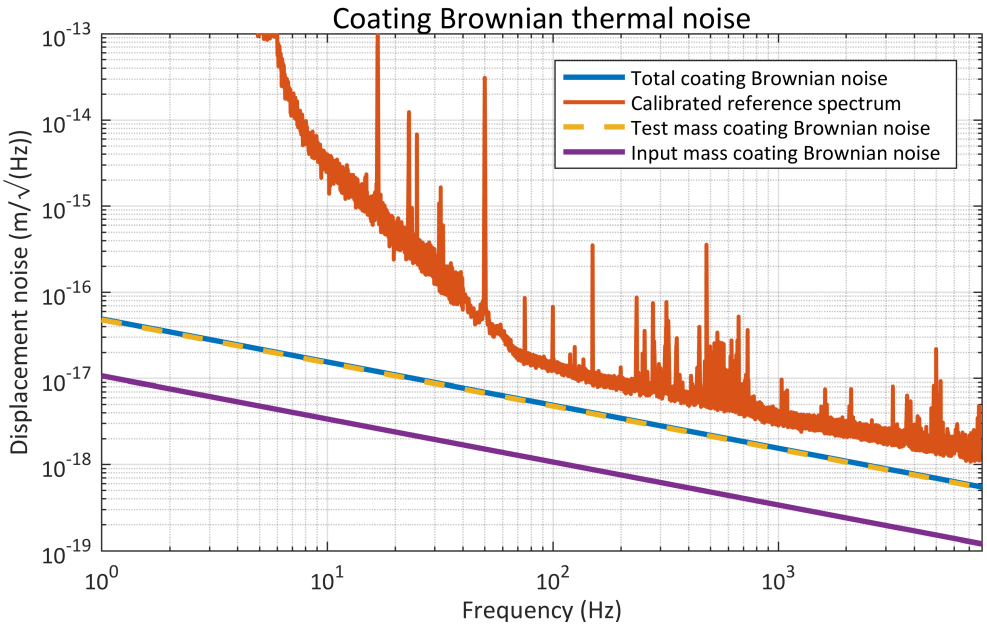

Figure 6.38: Coating Brownian thermal noise calculation for two Laseroptik mirrors with reflectivities of 99.85 % each. The noise is dominated by the test mirror contribution, as the small spot size of 86 µm enhances the measured thermal noise. The spectrum was measured at a time when these mirrors were installed, but the level seen can not be explained by coating Brownian thermal noise alone.

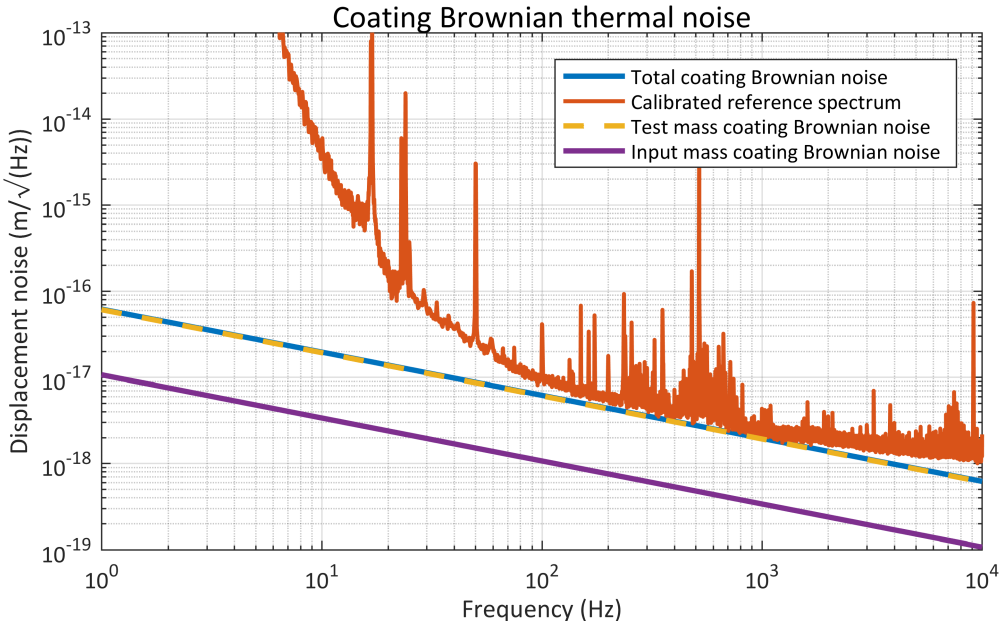

Figure 6.39: Coating Brownian thermal noise projection for a Laseroptik input mirror and the Gooch and Housego test mirror. The new mirror has a transmission estimated to be around 1 ppm, and its thermal noise dominates the readout. The measured spectrum, taken after the mirror installation, agrees well with the coating Brownian thermal noise estimate, especially considering uncertainties in material parameters.

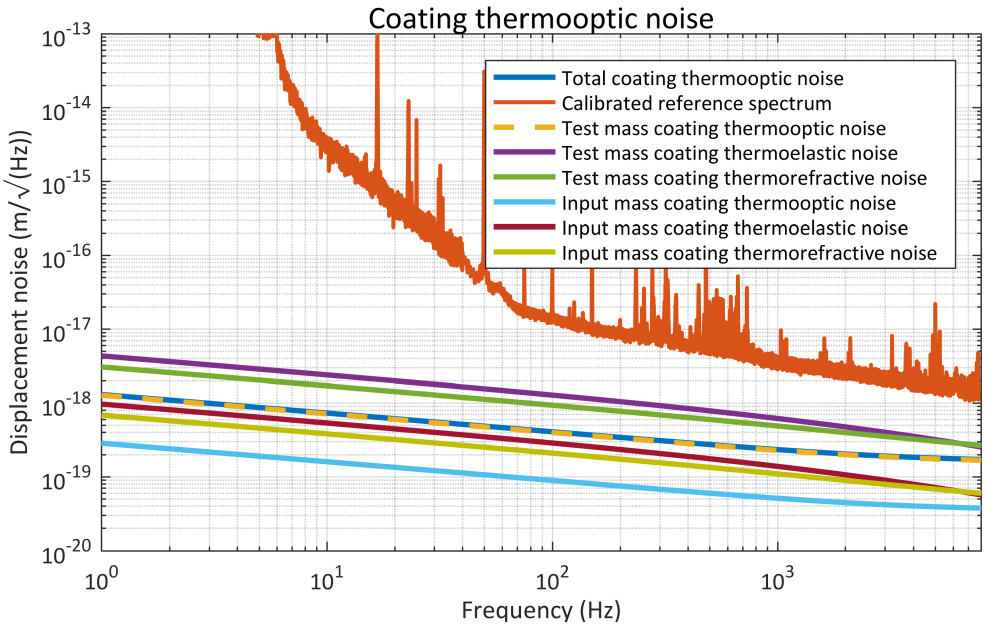

Figure 6.40: Coating thermooptic noise projection for the old Laseroptik mirrors. Contributions from thermoelastic and thermorefractive noise are shown for each individual mirror, and their coherent sums, thermooptic noise, are compared to the TNI readout. As expected for amorphous coating materials, the level of thermooptic noise is far below the readout sensitivity.

Laseroptik, to thermoelastic and thermorefractive noise are shown. These are then coherently combined for each mirror to get the measurable levels of thermooptic noise, which are about an order of magnitude below the measured spectrum of the TNI with these mirrors installed.

For the recent TNI configuration with the reference cavity spare mirror installed, the same noise curves as above are shown in figure 6.41, where the comparison is made to a recently measured spectrum. Again, the predicted levels of coating thermooptic noise are an order of magnitude below the measurement.

6.14.3 Coating photothermal noise

Photothermal noise behaves similar to coating thermo-optic noise, but is driven by laser power fluctuations, which lead to temperature flucuations in the coating through absorption. The level of laser power noise is taken from the characterizations of the ISS used in the AEI 10 m prototype. As the ISS significantly reduces the intensity noise, the contribution from coating photothermal noise is exptected to be well below the measured spectrum, even for a conservative absorption estimate of 50 ppm. For simplicity, figure 6.42 only shows the thermorefractive (yellow) and thermoelastic (blue) contributions, neglecting the coherent combination to thermooptic noise.

Even without coherent cancellation, coating photothermal noise is several orders of magnitude below the measured spectrum. Deliberate intensity modulation, using for example an AOM, could be used in the future to directly observe coating photothermal noise, as has been demonstrated in [Cha+16].

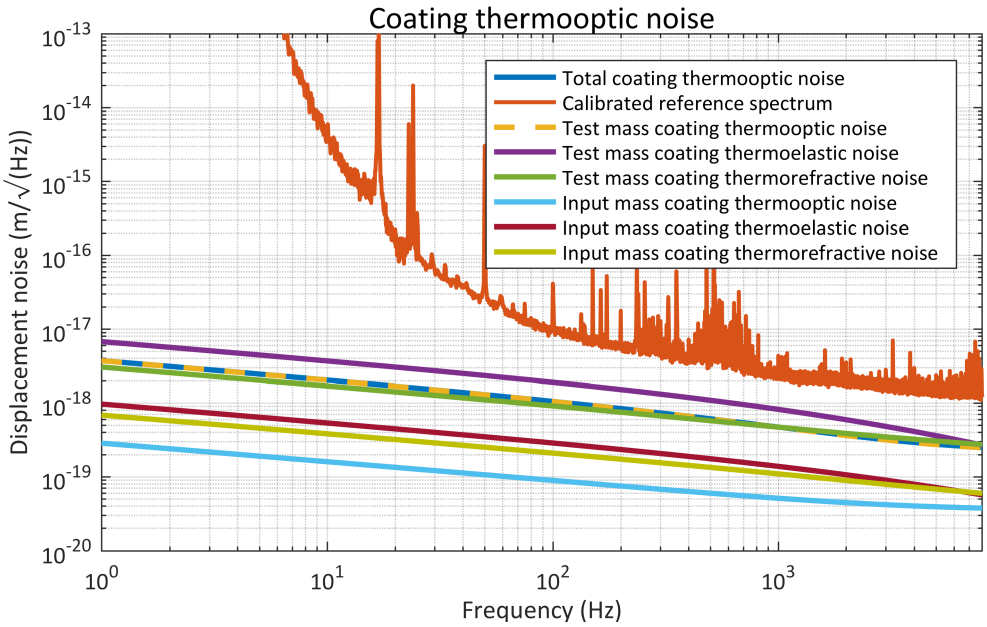

Figure 6.41: Coating thermooptic noise projection for the old Laseroptik input mirror and Gooch and Housego test mirror. Contributions from thermoelastic and thermorefractive noise are shown for each individual mirror, and their coherent sums, thermooptic noise, are compared to the TNI readout. As expected for amorphous coating materials, the level of thermooptic noise is far below the readout sensitivity.

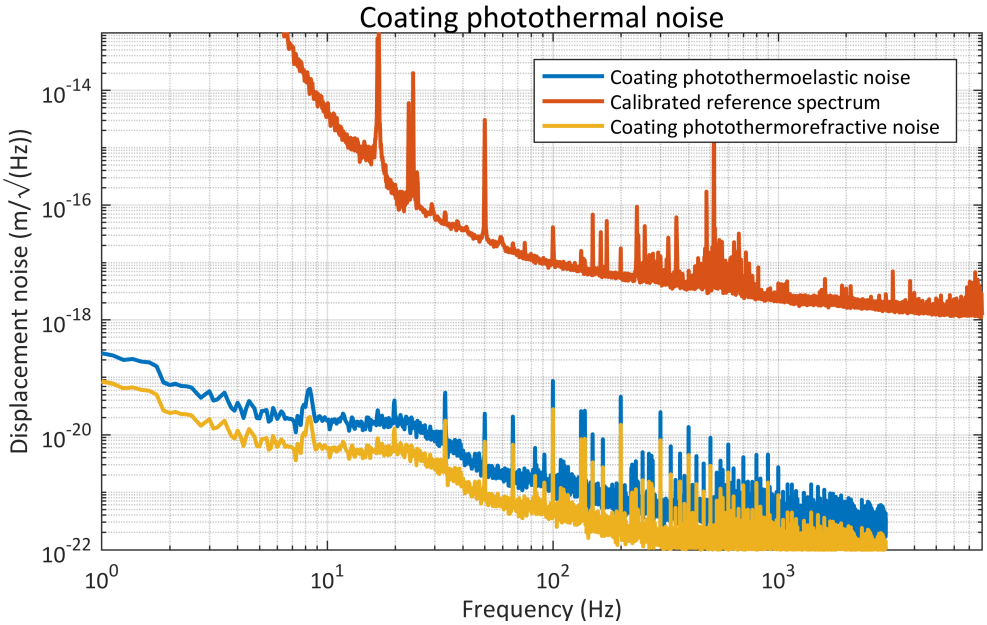

Figure 6.42: Projection of coating photothermal noise in the TNI. Measured intensity noise is propagated to coating thickness fluctuations (thermoelastic) and effective reflection point fluctuations (thermorefractive), assuming a very high level of absorption of 50 ppm. Even this conservative assumption and neglecting coherent cancellation of thermoelastic and thermorefractive contributions does not lead to a measurable contribution of the total noise.

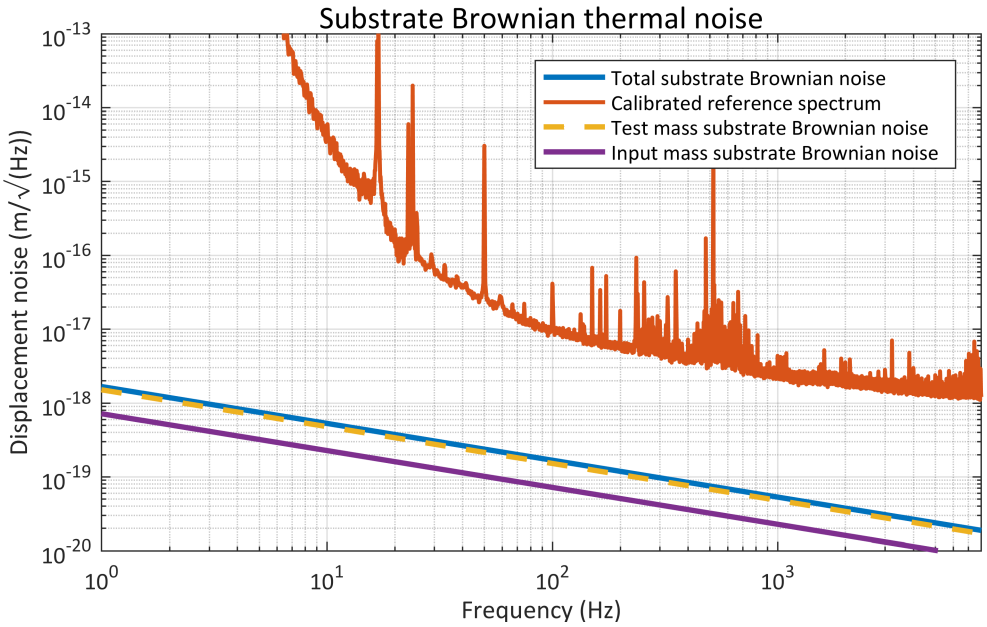

Figure 6.43: Projection of substrate Brownian noise to the TNI readout. The noise is dominated by the small spot size of the test mirror, but this contributions is well below the measured noise, as the mechanical loss of the used fused silica substrates is extremely low.

6.14.4 Substrate Brownian noise

Mechanical losses in the substrate influence the position of the mirror surface in a similar manner as mechanical losses in the coating, although the coupling into the readout variable is slightly different than for coating brownian noise, resulting in a $\frac{1}{w}$ dependence.

As the substrate material is chosen to be fused silica, which inherently has very low losses on the order of 10^{-8}, substrate thermal noise will be well below the measurement sensitivity of the TNI. This might not be true if a composite test mass is used, where the low loss mirror is glued into a larger aluminum structure. The aluminum mass might have higher intrinsical loss and together with losses from the glue might couple into the readout variable strongly. Here, only the fused silica part of the optic is taken into account, as there is no information about losses in the composite part of the input mass. As shown in figure 6.43, the expected noise is well below the measured noise.

6.14.5 Substrate thermoelastic noise

Temperature fluctuations not only appear in the coating, but also in the substrate. This leads to expansion of the substrate through the thermo-elastic effect, showing up in the readout of the TNI. Materials possessing large thermal conductivity and small specific heat capacity show a non-negligible contribution, but the fused silica used has a low thermal conductivity and therefore the contribution to the overall noise is negligible. This is evident in figure 6.44.

6.14.6 Substrate photothermoelastic noise

As with coating photothermal noise, temperature fluctuations arising from absorbed power fluctuations drive substrate expansion through the thermal expansion coefficient. Since the laser

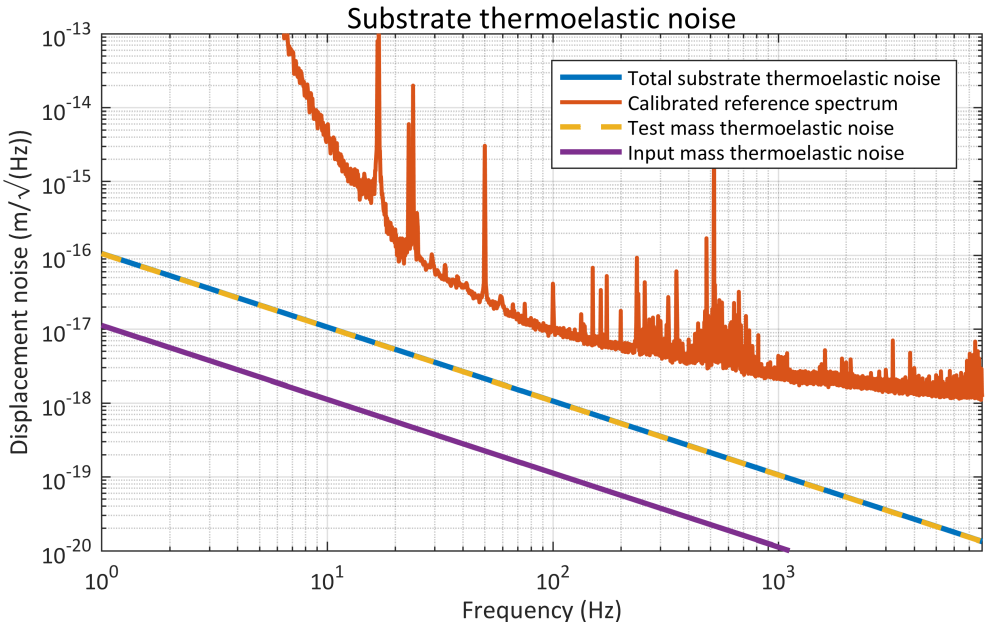

Figure 6.44: Projection of substrate thermoelastic noise to the TNI readout. The noise is strongly dominated by the test mirror contribution, and is only an order of magnitude below the measured noise, potentially impacting future low coating Brownian noise measurements.

power is actively stabilized, the expected level of substrate photothermoelastic noise is well below the sensitivity goal.

6.15 Total noise budget

Taking all the known and modeled noise sources shown above and adding them in quadrature gives the overall noise level expected in the TNI. This overall predicted noise is shown together with known individual contributions in figure 6.47, in comparison to the measured spectrum of the TNI.

This noise budget shows that the low frequency part of the spectrum is dominated by seismic noise and BOSEM noise, while suspension thermal noise is peaking through at the vertical resonance at 16.7 Hz and at the first violin mode at 515 Hz. Coating Brownian noise is dominating at frequencies above 80 Hz, with a margin explained by the input mass substrate thermal noise, as can be more clearly seen from the zoomed in version of the total noise budget in figure 6.46. Above 3.5 kHz, there is a non-negligible contribution from shot noise and dark noise of the photodetector.

In the range between 20 Hz and 80 Hz, there is an unmodeled noise excess. There are signs hinting at scattering as the source of this excess, especially the shape of features seen in the spectrogram. Additional contributions could stem from alternative coupling paths of actuator noise.

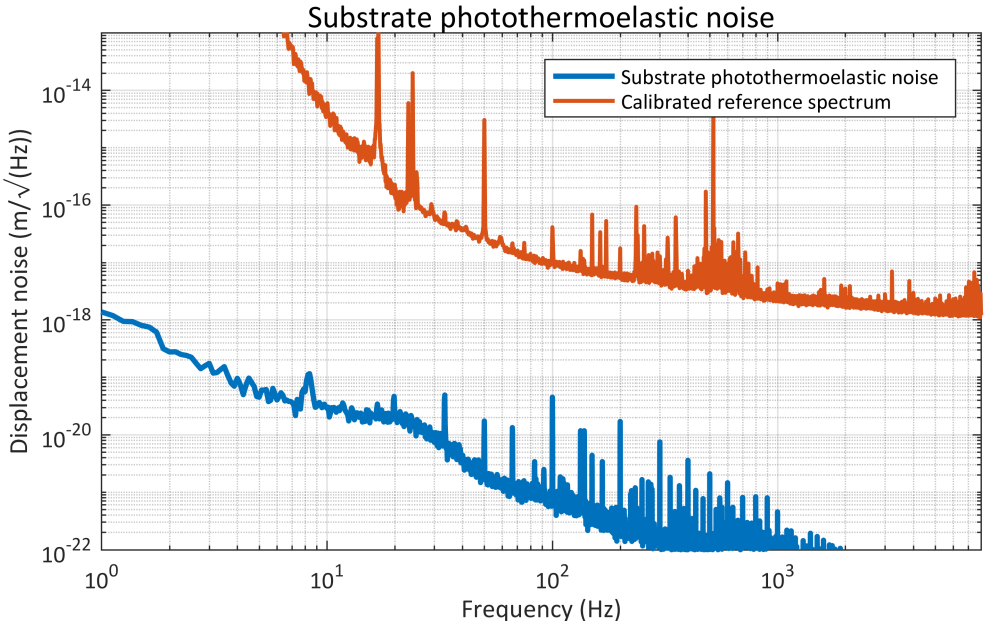

Figure 6.45: Projection of substrate photothermoelastic noise to the TNI readout. The noise is strongly dominated by the test mirror contribution, and is more than four orders of magnitude below the measured noise.

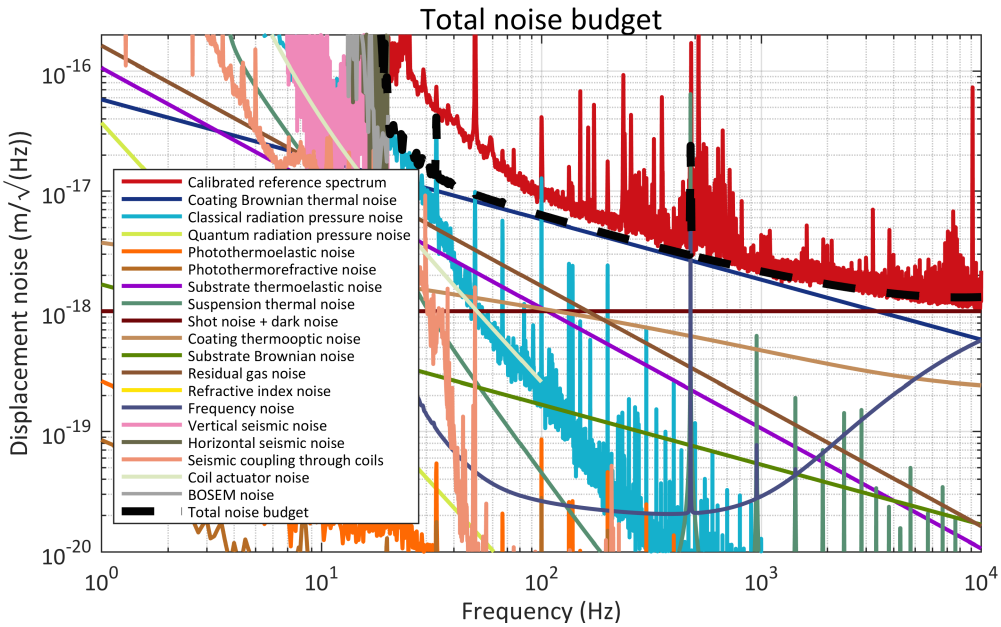

Figure 6.46: A zoomed in view of the total noise budget highlighting the part relevant for coating thermal noise measurements. It can be seen that the measured noise agrees well with the projection of coating Brownian noise, with shot noise and dark noise as well as to a lesser extent frequency noise coming in at high frequencies. The gap below 80 Hz is suspected to stem from scattering.

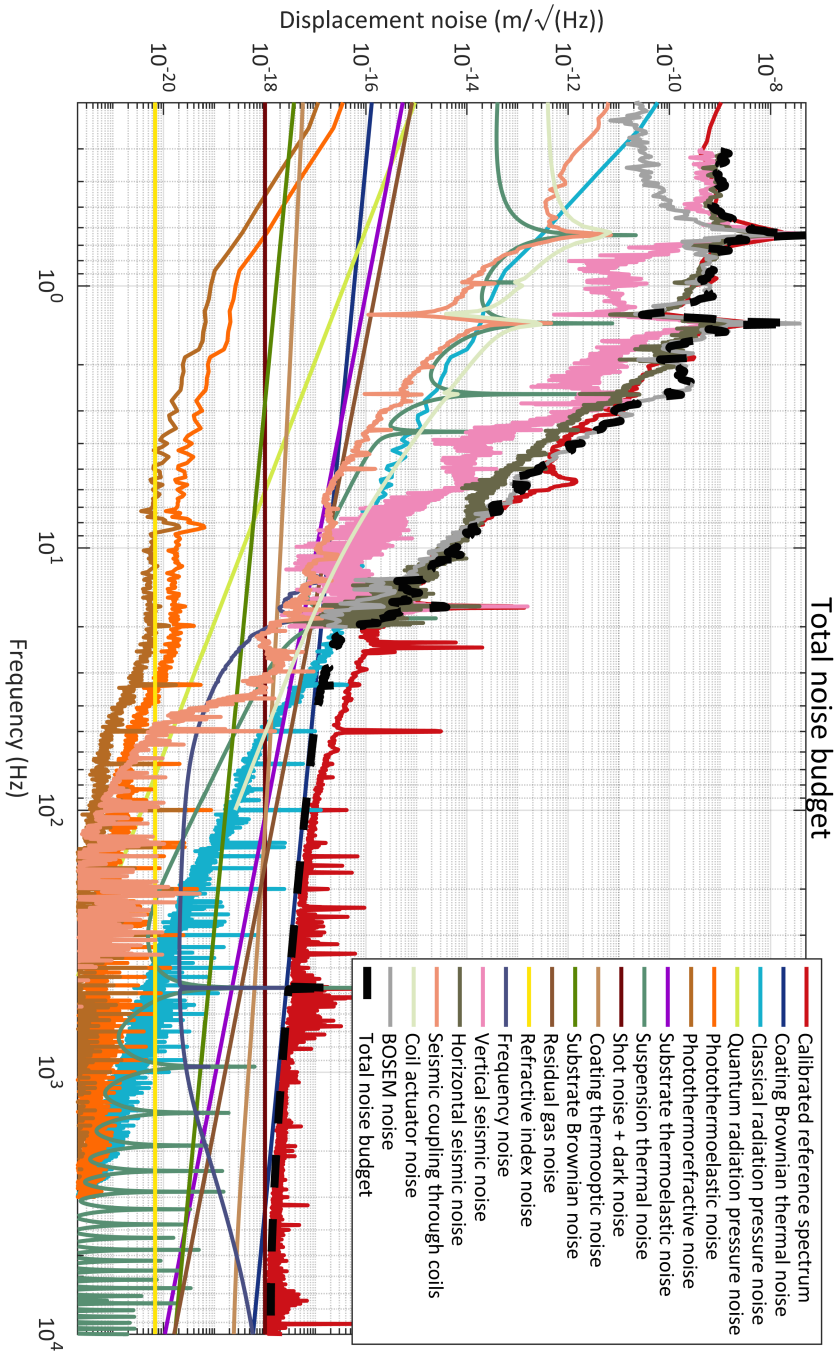

Figure 6.47: The total noise budget showing all individual contributions as well as their incoherent sum.

CHAPTER 7

Measurements of mirror thermal noise

After showing details of the design and commissioning process of the TNI in the last chapters, this chapter shows the results of measurements intended to show coating Brownian thermal noise. From these measurements, the loss angles of the coating materials are inferred, and a fitting procedure informs about the frequency dependence of the measured Brownian thermal noise.

7.1 Coating thermal noise measurement

The discussion of coating thermal noise measurments is focusing on the two latest iterations of the TNI. In both these configurations, the input 1" mirror with a radius of curvature of 10 cm is coated by Laseroptik Garbsen to have a reflectivity of 0.9985, and is glued into an aluminum holder. The end mirror in the first part is a flat 1"-mirror coated by Laseroptik Garbsen, with a reflectivity of 0.9985. For the second part, a spare mirror of the reference cavity made by Gooch and Housego, having a radius of curvature of 37.8 m and a transmission below 0.5 ppm, is used. The substrate is a monolithic fused silica mass with a thickness of 5 cm and a diameter of 10 cm.

Both these configurations showed a displacement spectrum with a slope consistent with thermal noise above about 100 Hz. As shown in section 6.14.1, the expected level of coating Brownian thermal noise for the first measurements is too far below the measured spectrum to properly explain the level observed. It is therefore assumed that the composite mirror holder introduces an effective substrate thermal noise with a large loss angle.

The second measurement shows a noise level close to the expected coating Brownian noise, adding photodiode dark noise and shot noise at high frequencies.Using the assumption, that the measured effective substrate Brownian noise from the first measurement behaves similarly in the input mass and output mass and has a spot size dependence similar to common substrate Brownian noise, a reduction from the first measurement by a factor of $\frac{\sqrt{(384\,\mu\mathrm{m})}}{\sqrt{(86\,\mu\mathrm{m})}} = 2.11$ is expected when only the composite input mass remains (shown in figure 7.1).

Taking the first measurement, which was dominated by this effective substrate Brownian noise of the test mass, and projecting it to the input test mass, its contribution to the overall noise can be estimated. When incoherently summing this substrate Brownian noise with shot noise, dark noise and the expected coating Brownian thermal noise, the observed spectrum with the monolithic test mirror is recreated to a high degree, as shown in figure 7.3. This shows that the best explanation for the noise limiting the TNI at high frequencies is coating Brownian thermal noise of the test mirror together with contributions of similar magnitude by the input mass substrate and readout noise, demonstrating the capabilities of the TNI to characterize the test mirror coating.

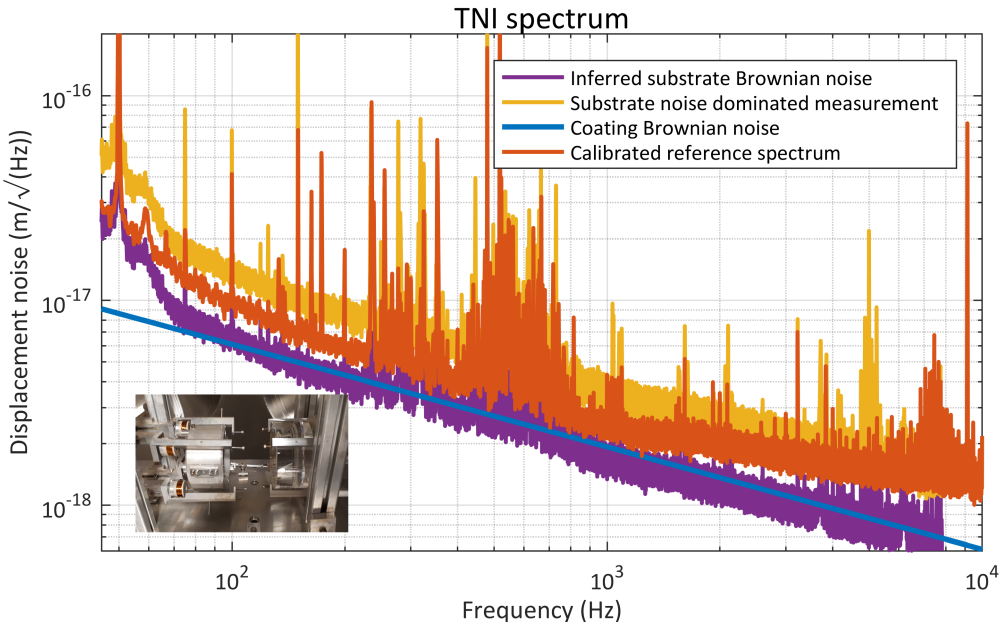

Figure 7.1: The measured spectrum is dominated by equal contributions from the expected coating Brownian thermal noise of the monolithic end mirror (blue) and the effective substrate thermal noise from the input mirror (purple). An estimate for the input mirror contribution has been calculated by taking the measurement dominated by the composite test mass substrate (yellow) and correcting for the spot size difference from test mass and input mass. The configuration of the mirrors in the TNI is shown in the inset.

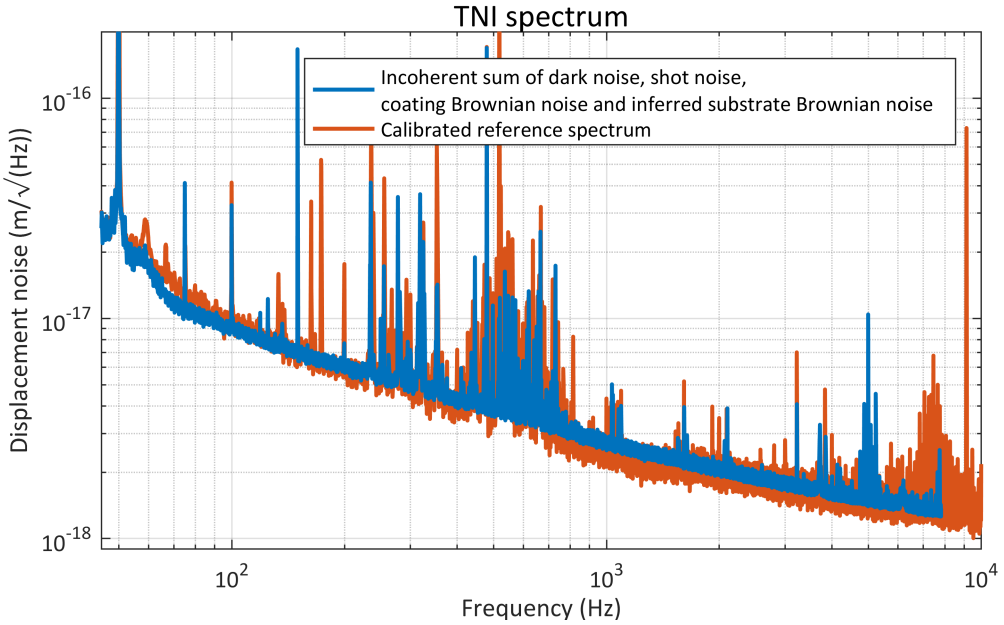

Figure 7.2: The incoherent sum of the contributions to the measured spectrum, coating Brownian thermal noise of the monolithic end mirror, effective substrate thermal noise from the input mirror as well as photodiode dark noise and shot noise, is compared to the measured spectrum. The agreement is profound, showing that the noise measured in the TNI is best explained by these contributions.

7.2 Frequency dependence and loss angle inference

Using the latest measurements discussed in the last section, a linear fit is performed on the logarithm of the spectrum to extract the slope of the frequency dependence (shown in figure 7.3). The resulting slope is found to be $-0.4911^{+0.0016}_{-0.0015}$ at two sigma when applying the linear fit to the full range from 100 Hz to 10 kHz after subtracting a level of $9.1 \times 10^{-19}\,\mathrm{m}/\sqrt{\mathrm{Hz}}$ for the combined measured dark noise and calculated shot noise.

This is close to the theoretical prediction of -0.5 [GHD12] and to measurements performed on the MIT thermal noise interferometer at -0.47 [GE18]. Considerable difficulty arises from the choice of the range of the spectrum used for the fit, as the result can strongly depend on this. One factor is the presence of peaks from jitter noise, which can be removed, the other the presence of contributions from the dark noise and possible contributions from nonlinearities.

As shown in the last section, the effective substrate Brownian noise and calculated coating Brownian noise together with dark noise and shot noise explain the observed spectrum well. This implies, that the values assumed for the loss angles of the coating materials, 4×10^{-5} for Silica and 3.8×10^{-4} for Tantala, describe the contribution of coating Brownian thermal noise well. These agree with loss angles extracted from the MIT TNI, given as 5×10^{-5} for Silica and 5.3×10^{-4} for Tantala [GE18].

For the effective substrate Brownian noise, assuming a homogeneous loss, a loss angle of 3.5×10^{-5} is inferred from the measurements dominated by this noise. This loss is comparable to the loss found in coating materials, but much higher than the bulk loss for fused silica substrate, which is quoted to be on the order of 5×10^{-9}. As the contribution from the substrate only scales with the square root of the spot size, a monolithic low loss input mass is the only way to achieve more sensitive measurements in the next iteration of the TNI, together with a more extreme spot

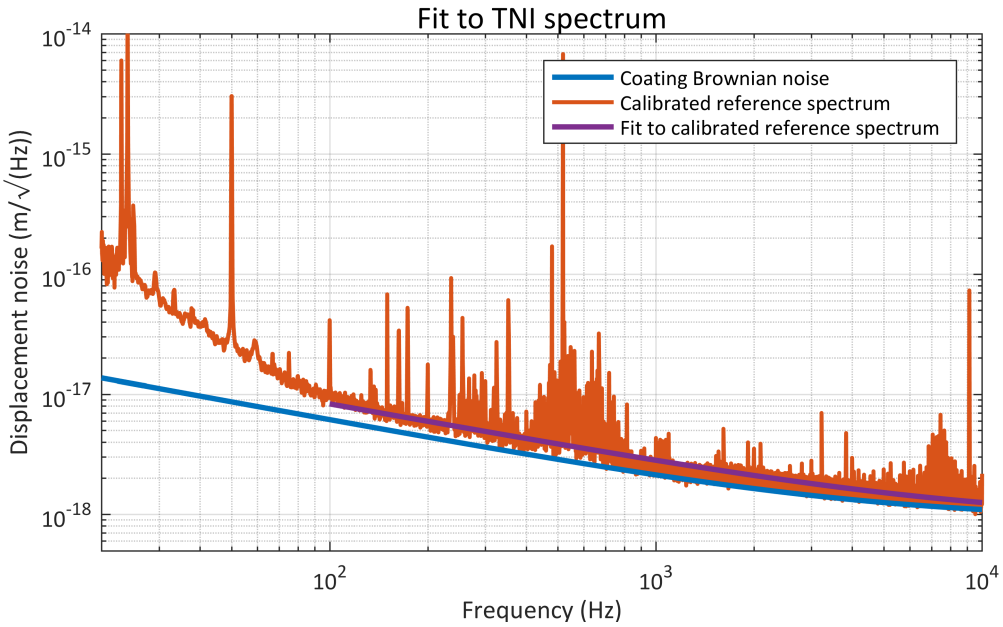

Figure 7.3: Linear fit performed on part of the TNI spectrum from 100 Hz to 10 kHz, which is expected to be dominated by thermal noise and photodiode noise. The measured photodiode dark noise and the inferred shot noise are subtracted before fitting, and are added in quadrature to the calculated thermal noise and linear fit. This is compared to the coating Brownian noise of the test mirror, which is below due to the contribution from the input mirror substrate thermal noise.

size ratio to not be limited by input mirror coating thermal noise.

7.3 Testing thermal noise

In order to increase confidence in the direct measurement of thermal noise, several alternative noise sources have been investigated and their possible influence tested. Furthermore, efforts were undertaken to characterize the spot size dependence, but without a conclusive result.

7.3.1 Alternative noise sources

Most known noise sources are described and calculated in chapter 6. Nevertheless, to exclude unknown couplings, measurements with the TNI have been taking in many different states, looking for changes in the thermal noise dominated part of the spectrum.

7.3.1.1 Seismic isolation system

Although the noise projections from ground motion to the TNI readout are calculated in section 6.2, there is some uncertainty in the amount of cross-coupling and spurious couplings. To assess the influence of different levels of table motion on the TNI readout, measurements were taken in the lowest table control state (LVDT integrated) and in high-gain state with optical levers, the SPI and the STS-2 engaged. No difference at the frequencies of interest are visible, although the height of the resonances at low frequencies changes.

Excitation of the tables increases the amount and height of the jitter peaks, as shown in section 6.6, but apart from that, no change is visible. In rare circumstances, where there is excessive motion, upconversion can be seen at high frequencies, showing a distinct pattern. Increasing the seismic attenuation system performance then brings back the noise level observed under all other circumstances.

7.3.1.2 Damping and BOSEMs

The influence of BOSEM noise and the gain of the damping loops has been shown in section 6.11.2. In any state tested, without damping and with increased damping loop gain, no difference was observable above 30 Hz.

7.3.1.3 Unity gain frequency, coil feedback location and sensing resistors

The locking loop has the potential to introduce unwanted noise into the TNI readout, both through electronic noise and through effects connected to the loop gain, characterized by the unity gain frequency. Measuring spectra and unity gain frequencies ranging from 12 Hz to 280 Hz only showed variation in the high unity gain frequency region, as the loop was not designed for these unity gain frequencies, and the small phase margin led to a servo bump.

To exclude the introduction of noise by acting directly at the test mass, an experiment was conducted where the intermediate mass coil actuators were added to the loop and a handover was performed, leaving only the intermediate mass actuators active (details in section 4.6.3.4). No difference was visible at high frequencies. One caveat was that it was not possible to unplug the lower coils completely to remove residual coupling, but the noise propagation in section 6.11.3 suggests, that the level is well below the measured spectrum.

Another factor possibly changing noise couplings are the sensing resistors in the coil drivers, defining the ratio of current produced for actuation per voltage applied. A larger sensing resistor reduces the amount of current per voltage, and thereby potentially reduces spurious couplings

originating between the CDS and the coil driver. Exchanging the default 499 Ω resistors with 2 kΩ resistors showed no change in the spectrum.

7.3.1.4 Locking photodiode

The locking photodiode is the most critical component in the locking loop, as noise introduced there cannot be suppressed by the loop. The dark noise was characterized in section 6.11.1, contributing significantly. Other noise couplings are possible, depending on the photodiode design and details of the assembly process. To test the influence of the photodiode, three different photodiodes were used for locking, where two of those are based on the same design. The dark noise floor is slightly different between the designs, but no other difference was visible, suggesting that no unknown effects contributed significantly.

7.3.2 Spot size dependence

The spot size dependence of coating Brownian thermal noise is known from theory to be proportional to $\frac{1}{w}$ for the ASD, with w the Gaussian beam radius. In order to vary the spot size, the separation of the mirrors in the hermispherical cavity has to be changed. Although it is in principle possible to move each suspension as a whole, this takes considerable effort and time, including a complete venting and pumping cycle for the large vacuum chamber. Furthermore, differences on the mirror surface when not sensing the exact same spot can induce changes masking the effect of spot size variation. Nevertheless, two approaches were taken to change the spot size without moving suspensions as a whole.

The first approach utilizes the BOSEMs at the uppermass, pushing the mirrors together until reaching the end of their sensing range, and afterwards pulling the mirrors apart until reaching the other end of their sensing range. This allows for a change in separation of 1065 µm, changing the spot size on the flat mirror by approximately 4.3 µm when starting at a separation of 9.5 cm. This leads to an expected change in the coating Brownian thermal noise of $0.47 \times 10^{-19}\,\mathrm{m}/\sqrt{\mathrm{Hz}}$ at 1 kHz, which is barely observable. In executing this procedure, problems arose from different optical properties of the mirrors encountered, leading to optical losses and thereby different optical gains. Although the online calibration using the PCal was employed, the uncertainty in this procedure is most likely larger than the expected shift in thermal noise and the results were inconclusive.

Another approach was locking the TNI to higher order TEM-modes, which have a different effective beam radius. Although locking to those modes was possible and measurements were taken, the coupling efficiency was greatly reduced, leading to photodiode noise and shot noise dominating the frequency range where thermal noise is expected. It was therefore not possible to see a change in the level of thermal noise with changing spot size. Part of the planned upgrades for the TNI is a more efficient way of coupling higher order modes into the TNI, using a mode cleaner with variable mode content in the input path to the TNI.

CHAPTER 8

Summary and outlook

8.1 Summary

The main goal of this thesis was the commissioning of the thermal noise interferometer (TNI) at the AEI 10 m prototype, making direct measurements of coating thermal noise possible. This required understanding and modelling thermal noise in precision interferometers, which has been discussed in detail. The insights have then been applied to another challenge, the design and optimization of crystalline coating structures for the AEI 10 m prototype sub-SQL interferometer. Optimization procedures, based on a genetic algorithm and particle swarm optimization, have been employed to find coatings with minimal overall thermal noise. It was found that quarter-wave coatings with two or three variable top layer thicknesses resulted in robust low noise coatings, coherently cancelling thermo-elastic and thermo-refractive noise while not spoiling Brownian thermal noise performance.

The scripts used for thermal noise calculations have also been used to generate a noise budget for the TNI. This was supplemented by projecting other known noise sources to the TNI length readout. The noise budget served as a guideline in the commissioning process. This process started with reassembling and characterizing the triple suspensions, from which the two TNI mirrors are suspended. Damping was reevaluated and the suspension was equipped with coil-magnet actuators for the intermediate mass and test mass of the input suspension.

The actuators were characterized with optical levers and, while an external laser was locked to the TNI, by transfer functions to the error signal. This served as the basis to bring the TNI into the vacuum chamber of the AEI 10 m prototype onto a seismically isolated optical table. Equipped with improved custom made optics, and with a newly designed mode matching telescope, first locks were achieved. In this state, measurements were used to inform about expected and unexpected noise source. Excess noise and performance limitations were subsequently identified and removed. This included photodiode dark noise, input path beam jitter noise, scattering from optical surfaces, optical losses in the cavity mirrors and thermally driven excitations of the composite mirror holders. Working on excess noise located in the composite mirror showed, that mirrors can be exchanged in a matter of days, having measurements mostly limited by the time to pump down the vacuum chamber and achieve thermal equilibrium.

To be able to get calibrated measurements, a photon pressure calibrator was designed and set up. Further calibration methods were employed to corroborate the calibration of the photon pressure calibrator. These efforts led to the first direct measurement of mirror thermal noise in Europe, which is also the first direct audio-band measurement in a single suspended cavity operating with the TEM_{00} mode. A sensitivity of $1.5\,\mathrm{am}/\sqrt{\mathrm{Hz}}$ at 5 kHz was achieved, marking an improvement of more than 3 orders of magnitude since the first locks of the TNI in the AEI 10 m prototype. It has thus been demonstrated, that direct measurements of mirror thermal noise are possible in the TNI, making it a useful testbed to characterize existing and future coatings.

8.2 Outlook

At the time of writing, the complete optical layout inside the AEI 10 m prototype is redone to accomodate the Fabry-Perot Michelson bound to reach the SQL. This also affects the TNI and presents the opportunity for improvements in the optical input path.

As jitter from fixed input optics still is strongly seen in the readout between 200 Hz and 800 Hz, redesigning the input path to use as many suspended optics as possible is the first step. This also enables the use of remotely controllable steering mirrors, which can be included into auto-alignment loops. Together with QPDs, serving as position and alignment references, ease of realignment after mirror exchanges is ensured.

Another important undertaking is the in-situ measurement of the spot size, which enables a better accuracy in the prediction of coating thermal noise. A viable option is to place knife-edges mounted to translation stages in the output path in front of the first collimating lens. Moving the knife-edges into the beam while locked in vacuum provides the data to reconstruct the spot size in the focus of the beam, which is located on the flat mirror.

Having shown that the losses in composite mirror holders potentially limit the noise performance of the TNI, monolithic curved input mirror substrates have been bought and will be coated with different HR-coatings, enabling close to impedance matched operation for a variety of output test mirrors. Equipping one of these new mirrors with breakoff prisms and suspending it for a thermal noise measurement is the next measurement planned for the TNI after input path rearrangement.

Employing an additional calibration procedure to cross-check currently used methods will also be incorporated in the general overhaul of the optical layout. Building a small Michelson interferometer, which uses the input mirror of the TNI as an end mirror, is able to characterize the actuator strength. This gives a direct method to assess the strength of the actuators, giving indepent confirmation of the PCal calibration.

Better alignment and damping performance can be achieved by employing additional sensors. These sensors can be optical levers reflected off of the test masses or intermediate masses, measuring angular shifts. Lateral motion can sensitively be detected by recently tested HOQIs, compact interferometric motion detectors with a large dynamic range. The derived signals can then be fed back into the existing damping and alignment loops, improving them at low frequencies. Reducing the actuator noise introduced by the coil-magnet pairs at the test mass can be achieved by adding an ESD. This would enable position-insensitive low-noise actuation without the presence of magnets, and has the potential to be switched off after handing off the lock to the intermediate mass coils without losing lock.

The long-term goal for the TNI is the characterization of thermal noise of different coating geometries and materials, especially crystalline coatings, and their dependence on the laser beam spot size on the mirror. This requires getting sample mirrors and bonding them to a monolithic substrate or directly coat large monolithic substrates. Care has to be taken that the input mirror coating is not limiting the readout noise, either by having a similarly performing coating as the test mirror, or by adjusting the spot size ratio. Among samples which could be tested, interesting coating geometries can be realized, which are dominated by different types of thermal noise, especially thermoelastic and thermorefractive noise. This can further inform about possible issues and ways of improvement for future coatings.

Appendices

APPENDIX A

Further theoretical calculations

A.1 Fluctuation Dissipation Theorem

Starting point for the derivation is the Hamiltonian of the perturbed system $\mathcal{H}$, where $\mathcal{H}_0$ is the Hamiltonian of the unperturbed system, V is taken to be the amplitude of the oscillating perturbation and Q is an operator coupling the perturbation to the system.
Expanding the wavefunction ψ of the state of the system into the basis of eigenfunctions of the unperturbed Hamiltonian and inserting it into the Schrödinger-equation leads through integration of the first-order differential equations for the coefficients of the expansion to an expression for the transition probability from state ψ_n to states separated by an energy $\hbar\omega$:

$$\frac{\pi}{2\hbar}V_0^2\{|\langle E_n+\hbar\omega|Q|E_n\rangle|^2\rho(E_n+\hbar\omega)+|\langle E_n-\hbar\omega|Q|E_n\rangle|^2\rho(E_n-\hbar\omega)\}\,. \tag{A.1}$$

The matrix elements of the operator Q are the main factors in this expression, accompanied by the densitiy of states $\rho(E)$ at energy E, and the corresponding change in energy can be calculated by multiplication with the energy difference $\hbar\omega$ of the states involved.
Using the initial occupation probability of a thermal system given by the Boltzmann distribution and integrating over the energy to get all contributions then gives the dissipated power

$$P=\frac{1}{2}\pi V_0^2\omega\int_0^\infty \rho(E)f(E)\{|\langle E+\hbar\omega|Q|E\rangle|^2\rho(E+\hbar\omega)-|\langle E-\hbar\omega|Q|E\rangle|^2\rho(E-\hbar\omega)\}dE\,. \tag{A.2}$$

This dissipated power can also be related to a generalized impedance $Z(\omega)$ and resistance $R(\omega)$, where the impedance is the complex proportionality factor between the force V and the rate of change $\dot{Q}$ of the Operator Q and the resistance is the real part of the impedance.
The dissipated power can then be written as

$$P=\frac{1}{2}\pi V_0^2\frac{R(\omega)}{|Z(\omega)|^2}\,. \tag{A.3}$$

From this follows the relation

$$\frac{R}{|Z^2|}=\pi\omega\int_0^\infty \rho(E)f(E)\{|\langle E+\hbar\omega|Q|E\rangle|^2\rho(E+\hbar\omega)-|\langle E-\hbar\omega|Q|E\rangle|^2\rho(E-\hbar\omega)\}dE\,. \tag{A.4}$$

To find the fluctuations in the force V, a simple approach is to first calculate fluctuations in the response $\dot{Q}$ and relate the force fluctuations V via the impedance.
Fluctuations are characterized by the expectation value of the squared operator under investigation $\langle\dot{Q}^2\rangle$, if this operator has a zero mean value. Expectation values are the diagonal matrix elements

of the operator, so in this case

$$\langle E_n|\dot{Q}^2|E_n\rangle = \sum_m \langle E_n|\dot{Q}|E_m\rangle\langle E_m|\dot{Q}|E_n\rangle = \frac{1}{\hbar^2}\sum_m (E_n - E_m)^2 |\langle E_m|Q|E_n\rangle|^2 \,. \tag{A.5}$$

Using common techniques from quantum mechanics such as inserting a one and defining a frequency ω through $\hbar\omega = |E_n - E_m|$ together with the Boltzmann distribution for the initial population and some integral magic lead to

$$\langle \dot{Q}^2 \rangle = \int_0^\infty \hbar\omega^2 \left[\int_0^\infty \rho(E) f(E) \{ |\langle E + \hbar\omega|Q|E\rangle|^2 \rho(E + \hbar\omega) - |\langle E - \hbar\omega|Q|E\rangle|^2 \rho(E - \hbar\omega) \} dE \right] d\omega \,. \tag{A.6}$$

and from there to

$$\langle V^2 \rangle = \int_0^\infty |Z|^2 \hbar\omega^2 \left[\int_0^\infty \rho(E) f(E) \{ |\langle E + \hbar\omega|Q|E\rangle|^2 \rho(E + \hbar\omega) - |\langle E - \hbar\omega|Q|E\rangle|^2 \rho(E - \hbar\omega) \} dE \right] d\omega \,. \tag{A.7}$$

Finally modifying these two results A.4 for driven dissipation and A.7 for spontanoues fluctuations while using some integration variable shifts and knowledge about vanishing quantities gives the updated equations

$$\frac{R}{|Z^2|} = \pi\omega(1 - \mathrm{e}^{-\frac{\hbar\omega}{kT}}) \int_0^\infty \rho(E) f(E) \{ |\langle E + \hbar\omega|Q|E\rangle|^2 \rho(E + \hbar\omega) dE \,, \tag{A.8}$$

and

$$\langle V^2 \rangle = \int_0^\infty |Z|^2 \hbar\omega^2 (1 + \mathrm{e}^{-\frac{\hbar\omega}{kT}}) \int_0^\infty \rho(E) f(E) \{ |\langle E + \hbar\omega|Q|E\rangle|^2 \rho(E + \hbar\omega) dE d\omega \,. \tag{A.9}$$

Combining both leads to the fluctuation-dissipation theorem

$$\langle V^2 \rangle = \frac{2}{\pi} \int_0^\infty R(\omega) E(\omega, T) d\omega \,. \tag{A.10}$$

with

$$E(\omega, T) = \frac{1}{2}\hbar\omega + \hbar\omega \left[\mathrm{e}^{\frac{\hbar\omega}{kT}} - 1 \right]^{-1} \,. \tag{A.11}$$

, which can be approximated at high temperatures by

$$\langle V^2 \rangle \simeq \frac{2}{\pi} kT \int_0^\infty R(\omega) d\omega \,. \tag{A.12}$$

APPENDIX B

Electronics

B.1 BOSEM readout electronics

The BOSEM readout electronics schematics are shown in figure B.1. Voltage noise is shown in detail in figure B.2, as calculated with Zero. The naming of each noise source is based on the schematics in figure B.1. The main contribution at high frequencies comes from the Johnson noise of the resistor (R20) of the transimpedance amplifier. This is followed by the current noise of the operational amplifier (N10) in the transimpedance part. At low frequencies, the current noise of the operational amplifier (N6A and N6B) in the de-whitening filter stage dominate the noise spectrum.

The total transfer function is shown in figure B.3, simulated in Zero.

B.2 BOSEM driver noise

The BOSEM driver electronics schematics are shown in figure B.4. Detailed current noise contributions are shown in figure B.5, and input-referred voltage noise is shown in figure B.6. The naming is based on figure B.4. At low frequencies, current noise from the operational amplifier (N20A and N20B) in the whitening filter dominate the noise spectrum. At high frequencies, Johnson noise from the resistor (R18) in the second stage of the whitening filter gives the main contribution. The total transfer function is shown in figure B.7.

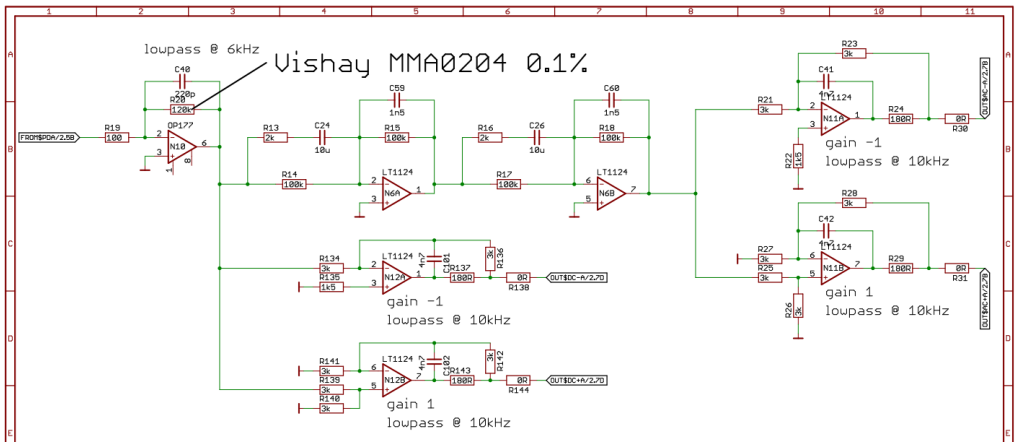

Figure B.1: Schematics of the BOSEM readout electronics.

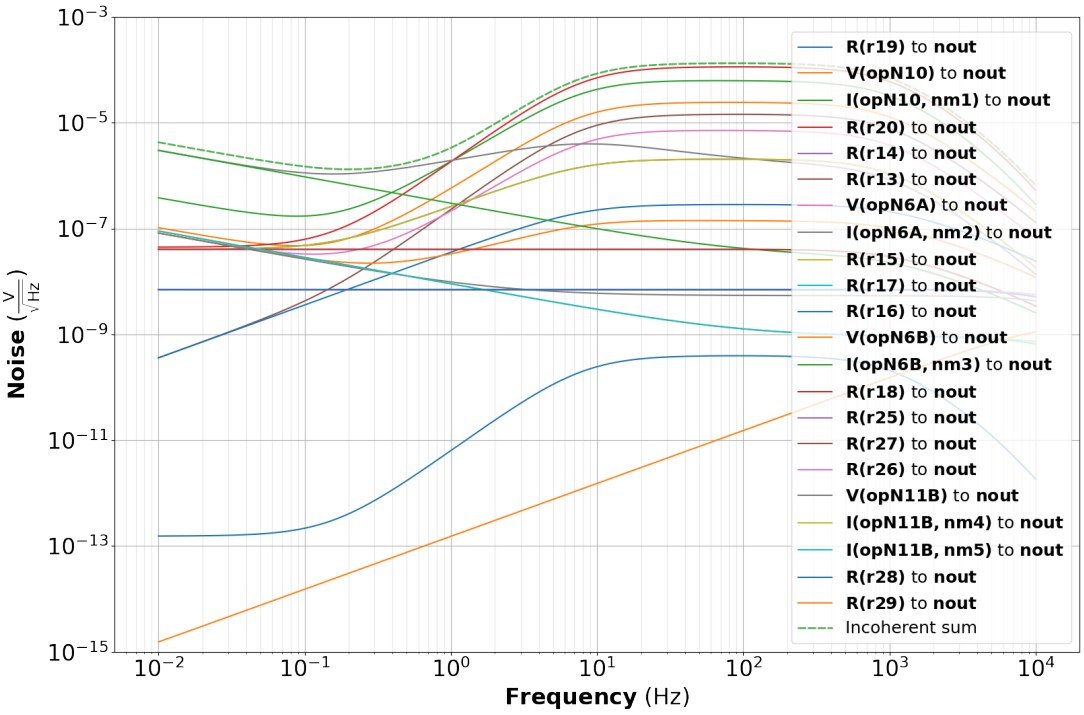

Figure B.2: BOSEM readout noise as simulated using Zero. The noise is dominated by Johnson noise of the resistor (R20) of the transimpedance amplifier at high frequencies. Down to 1 Hz, non-negligible contributions come from current noise of the operational amplifier (N10). At lower frequencies, current noise of the operational amplifier (OP6A and OP6B) of the dewhitening dominates the noise.

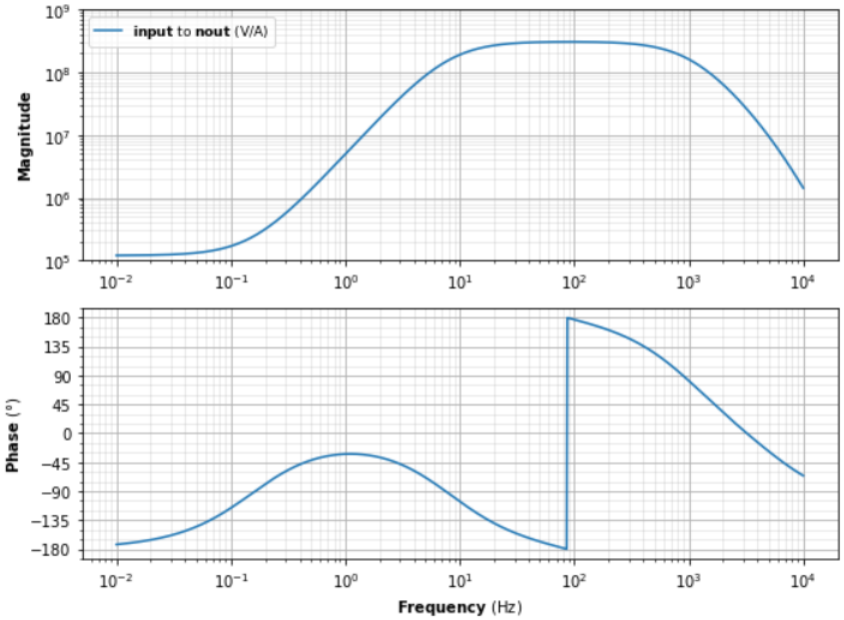

Figure B.3: The BOSEM readout transfer function as simulated in Zero.

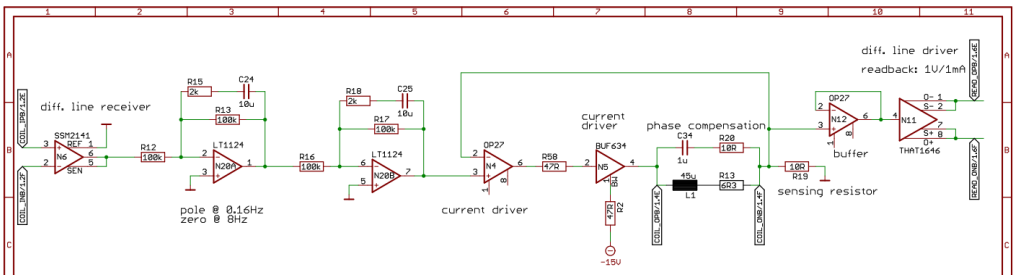

Figure B.4: Schematics of the BOSEM coil driver.

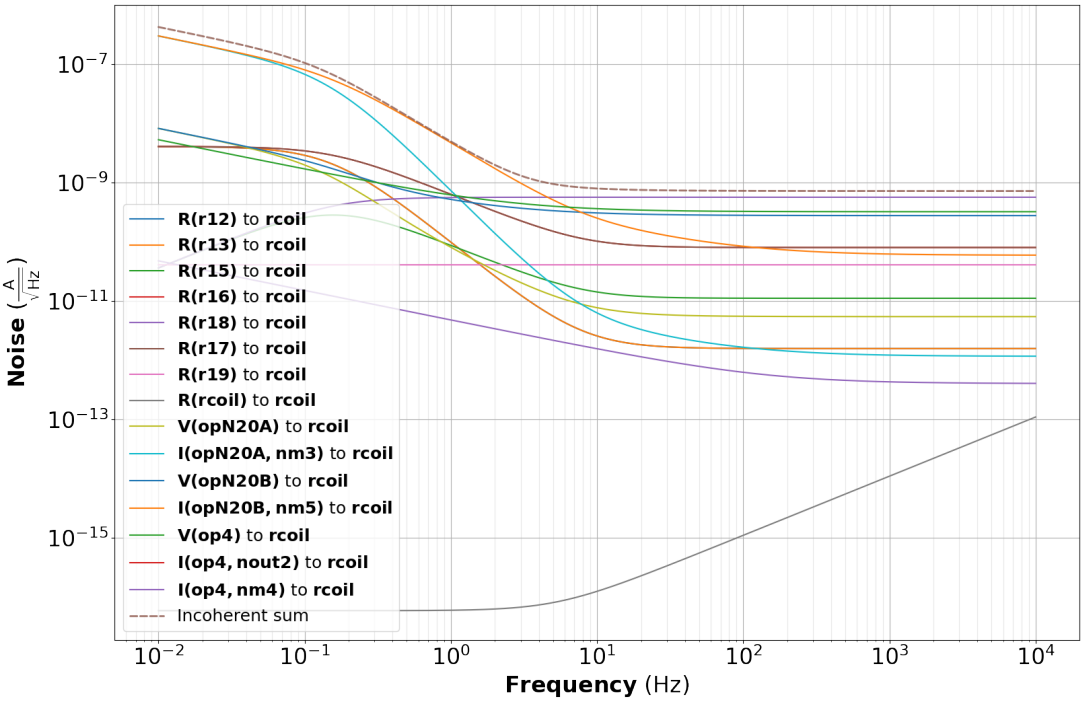

Figure B.5: Current noise of the BOSEM coil driver. At low frequencies, the noise is dominated by current noise of the operational amplifier (N20A and N20B) in the whitening path. For higher frequencies, Johnson noise of the resistor (R18) in the second stage of the whitening filter dominates.

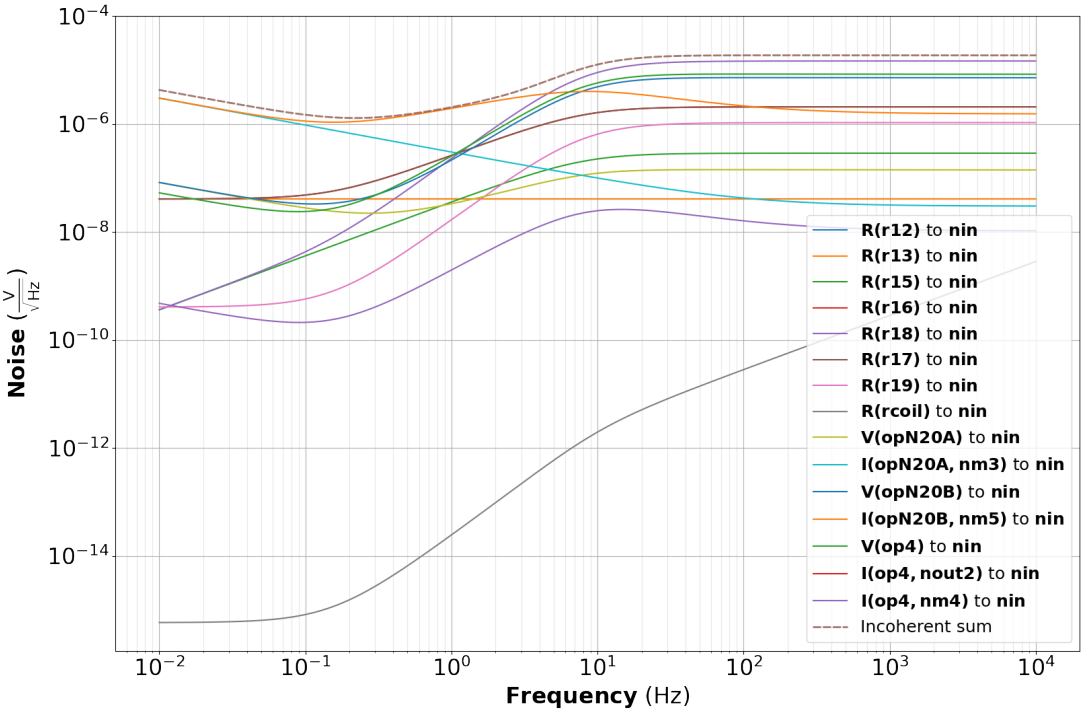

Figure B.6: Input referred voltage noise of the BOSEM coil driver as simulated by Zero.

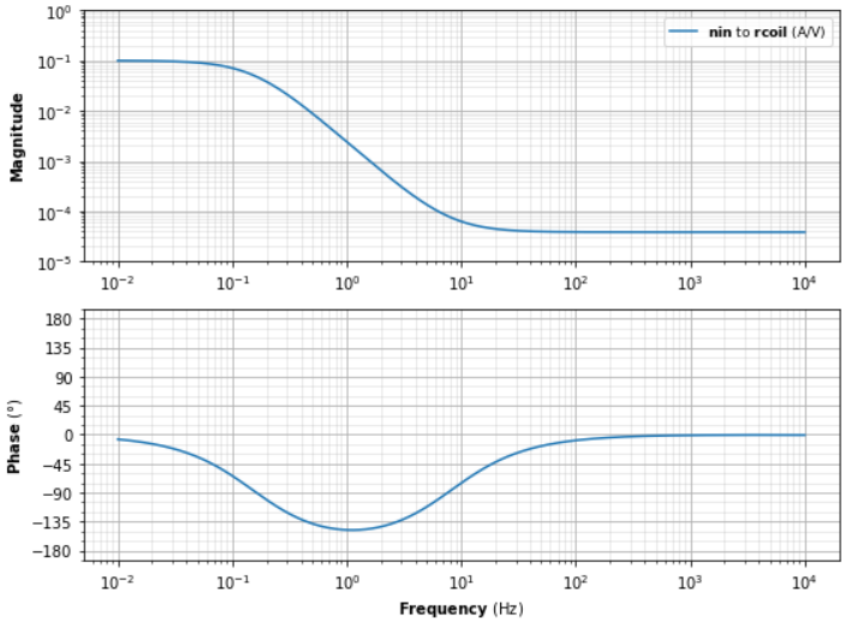

Figure B.7: Transfer function of the BOSEM coil driver as simulated by Zero. The upper plot shows the magnitude while the lower plot shows the phase.

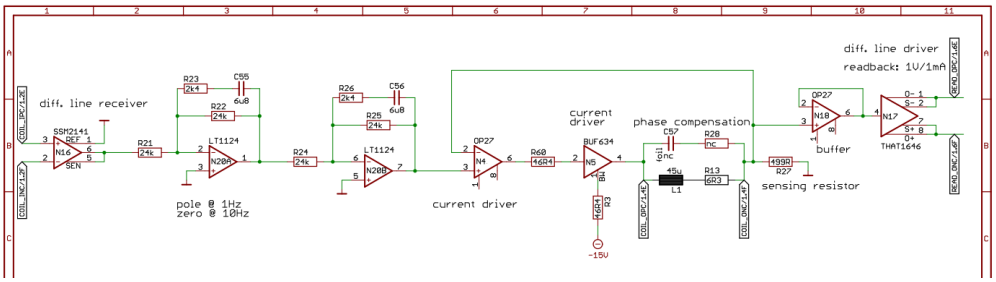

Figure B.8: Schematics of the test mass coil driver electronics.

B.3 Test mass coil driver

Schematics for the test mass coil driver are shown in figure B.8. The current noise, as simulated with Zero, is shown in figure B.9, and the input-referred voltage noise is shown in figure B.10. Naming is based on figure B.8. At low frequencies, current noise from the operational amplifier (N20A and N20B) in the whitening filter dominates the noise spectrum. At high frequencies, Johnson noise from the resistor (R26) in the second stage of the whitening filter gives the main contribution. The total transfer function is shown in figure B.11.

B.4 DAC

The DAC consits of a General Standards 16 bit PCIX card that can output $\pm 10\,\mathrm{V}$ differentially when driven by $\pm 32\,768\,\mathrm{cts}$ counts digitally. The noise has been modelled based on measurements, and has a level of $9 \times 10^{-7}\,\mathrm{V}/\sqrt{\mathrm{Hz}}$.

B.5 ADC

The ADC consists of a General Standards 16 bit PCIe card that can take up to $\pm 20\,\mathrm{V}$ differentially, which has been achieved by always connecting two channels to be used as one, reducing the total amount of channels from 64 to 32. This signal is converted to $\pm 32\,768\,\mathrm{cts}$ digitally. ADC noise is measured to be close to $2 \times 10^{-6}\,\mathrm{V}/\sqrt{\mathrm{Hz}}$.

B.6 Locking photodiode

The locking photodiode schematics of the signal path are shown in figure B.12. This schematic served as the basis for modelling the noise of the photodiode, starting from the mixer through to the output. The resulting noise contributions from the individual components as named in figure B.12 is shown in figure B.13, simulated with Zero.

The major contribution at low frequencies stems from voltage noise of the operational amplifier AD797 in the first stage of the four-pole low pass filter. At higher frequencies above 50 Hz, the Johnson noise of the resistor R13 in front of the AD797 is the dominant contribution.

The transfer function of the part after the mixer is simulated in Zero and shown in figure B.14.

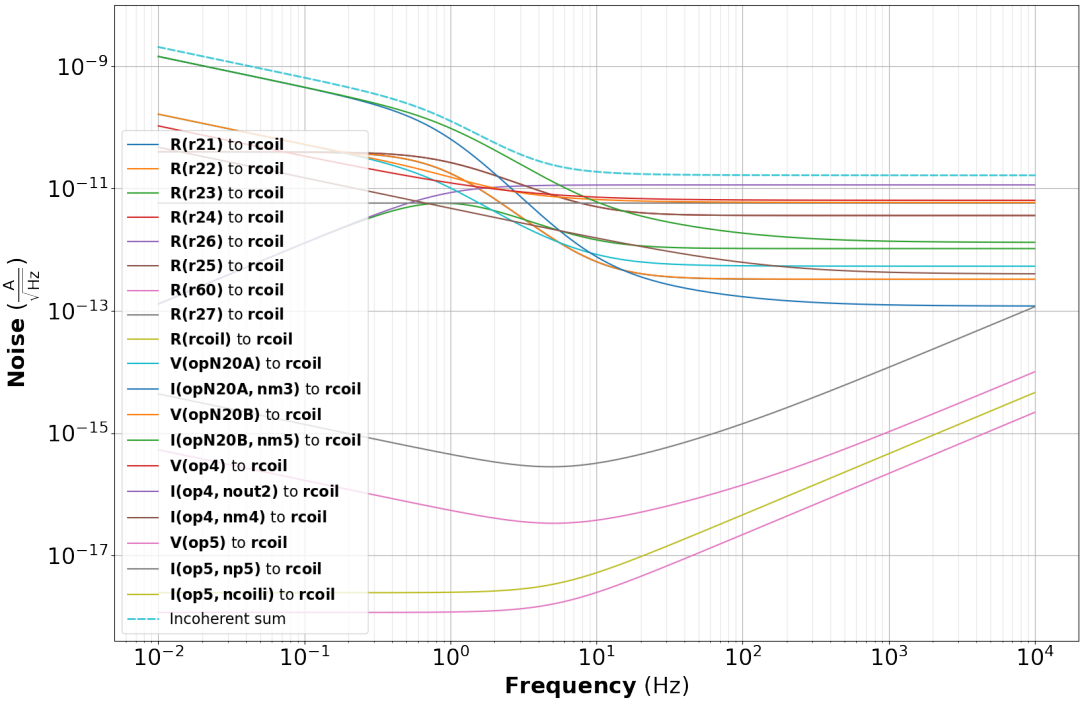

Figure B.9: Current noise of the test mass coil driver as simulated by Zero. Johnson noise of the resistor (R26) dominates at higher frequencies, while current noise of the op amp (N20A and N20B) dominates at low frequencies.

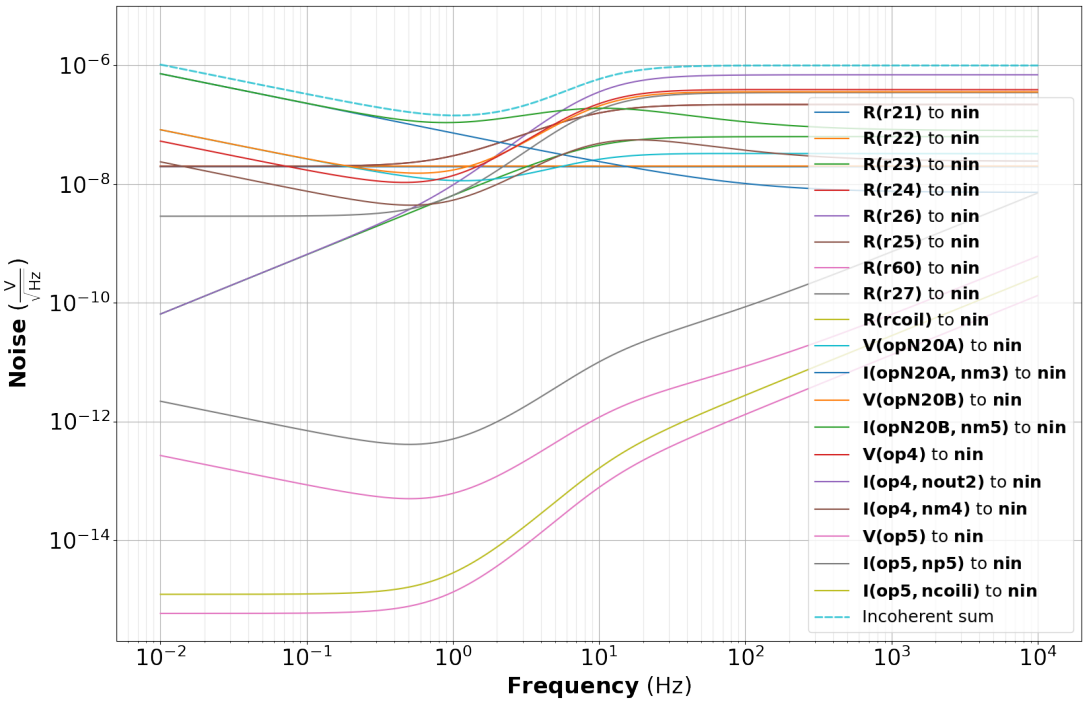

Figure B.10: Voltage noise of the test mass coil driver as simulated by Zero.

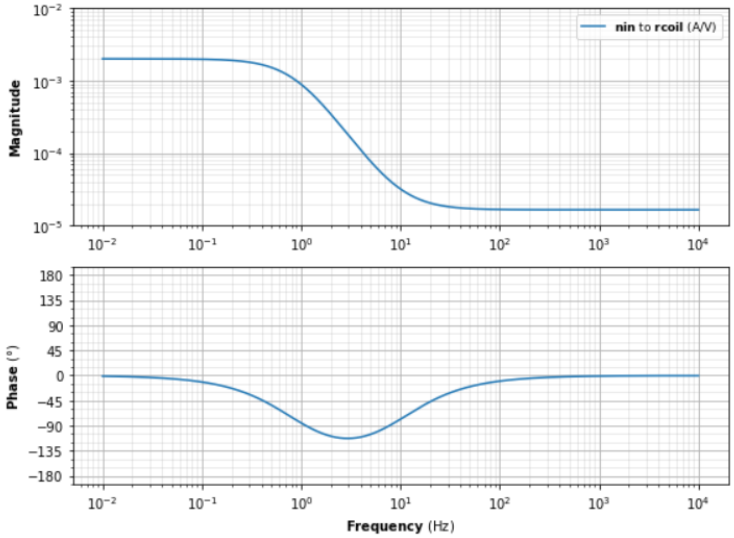

Figure B.11: Transfer function of the test mass coil driver as simulated using Zero. The upper plot shows the magnitude and the lower plot shows the phase.

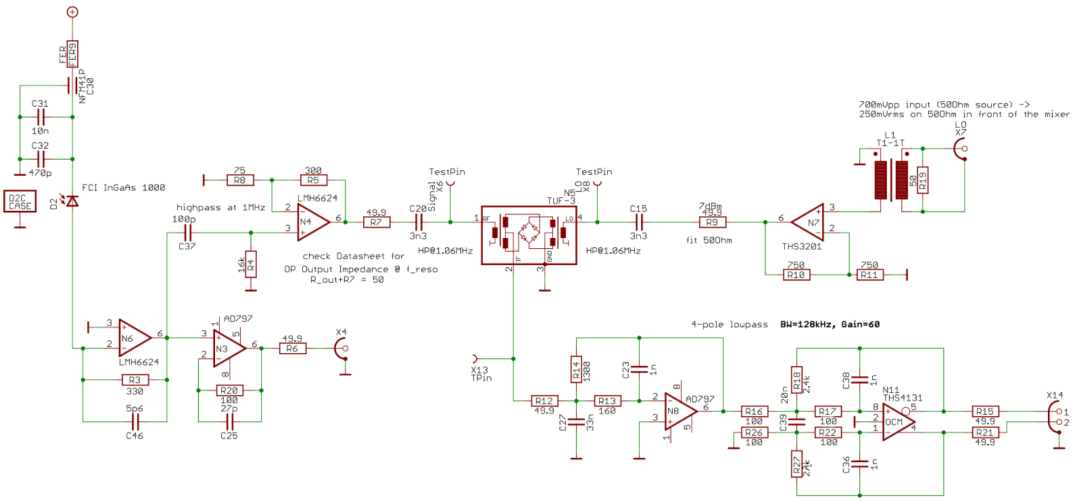

Figure B.12: Schematics of the locking PD electronics.

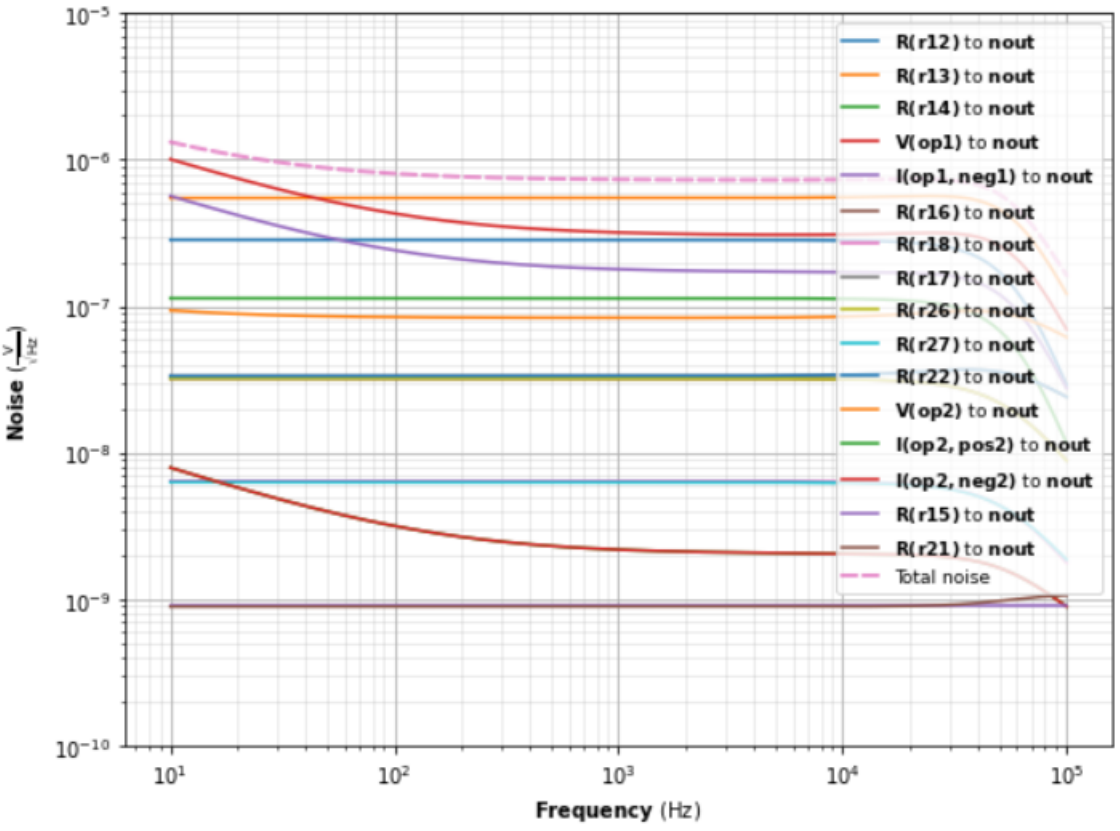

Figure B.13: Electronic noise budget of the locking PD as simulated in Zero. At low frequencies, voltage noise of the op amp AD797 dominates, whereas at higher frequencies Johnson noise of the resistor R13 in front of the AD797 is the major contribution.

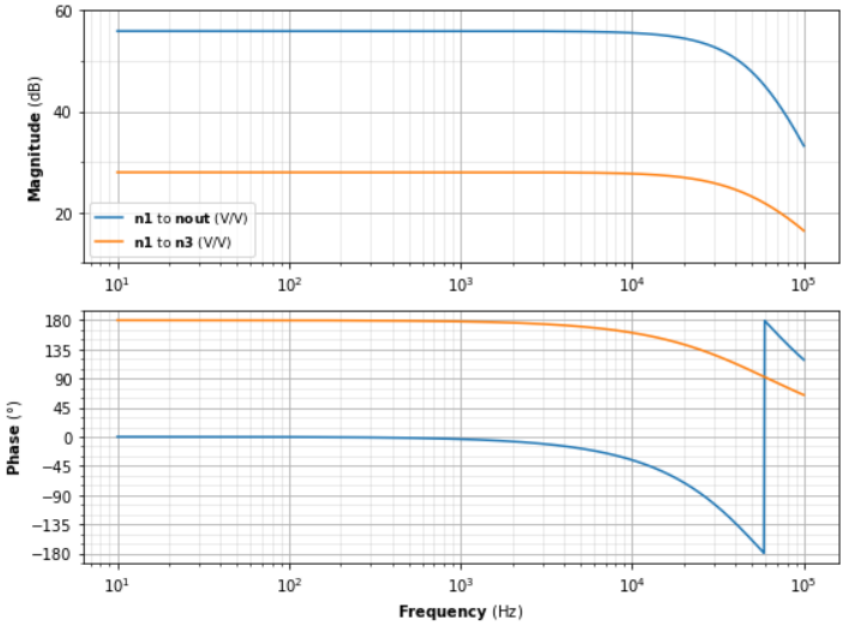

Figure B.14: Simulated transfer function of the locking PD using Zero. The corner frequency is at 30 kHz.

Bibliography

[Eic] .

[Cia] .

[Bar] .

[Abb+09] B Abbott et al. “Observation of a kilogram-scale oscillator near its quantum ground state”. In: *New Journal of Physics* 11.7 (2009), p. 073032.

[Abb+16a] B. P. Abbott et al. “Binary Black Hole Mergers in the First Advanced LIGO Observing Run”. In: *Physical Review X* 6.4 (2016).

[Abb+16b] B. P. Abbott et al. “Comprehensive all-sky search for periodic gravitational waves in the sixth science run LIGO data”. In: *Physical Review D* 94.4 (2016).

[Abb+16c] B. P. Abbott et al. “Directly comparing GW150914 with numerical solutions of Einstein’s equations for binary black hole coalescence”. In: *Physical Review D* 94.6 (2016).

[Abb+16d] B. P. Abbott et al. “GW151226: Observation of Gravitational Waves from a 22-Solar-Mass Binary Black Hole Coalescence”. In: *Physical Review Letters* 116.24 (2016).

[Abb+16e] B. P. Abbott et al. “Improved Analysis of GW150914 Using a Fully Spin-Precessing Waveform Model”. In: *Physical Review X* 6.4 (2016).

[Abb+16f] B. P. Abbott et al. “Results of the deepest all-sky survey for continuous gravitational waves on LIGO S6 data running on the Einstein@Home volunteer distributed computing project”. In: *Physical Review D* 94.10 (2016).

[Abb+16g] B. P. Abbott et al. “UPPER LIMITS ON THE RATES OF BINARY NEUTRON STAR AND NEUTRON STAR–BLACK HOLE MERGERS FROM ADVANCED LIGO’S FIRST OBSERVING RUN”. In: *The Astrophysical Journal* 832.2 (2016), p. L21.

[Abb+17a] B. P. Abbott et al. “All-sky search for periodic gravitational waves in the O1 LIGO data”. In: *Physical Review D* 96.6 (2017).

[Abb+17b] B. P. Abbott et al. “All-sky search for short gravitational-wave bursts in the first Advanced LIGO run”. In: *Physical Review D* 95.4 (2017).

[Abb+17c] B. P. Abbott et al. “Directional Limits on Persistent Gravitational Waves from Advanced LIGO’s First Observing Run”. In: *Physical Review Letters* 118.12 (2017).

[Abb+17d] B. P. Abbott et al. “Effects of waveform model systematics on the interpretation of GW150914”. In: *Classical and Quantum Gravity* 34.10 (2017), p. 104002.

[Abb+17e] B. P. Abbott et al. “Estimating the Contribution of Dynamical Ejecta in the Kilonova Associated with GW170817”. In: *The Astrophysical Journal* 850.2 (2017), p. L39.

[Abb+17f] B. P. Abbott et al. “Exploring the sensitivity of next generation gravitational wave detectors”. In: *Classical and Quantum Gravity* 34.4 (2017), p. 044001.

[Abb+17g] B. P. Abbott et al. “First low-frequency Einstein@Home all-sky search for continuous gravitational waves in Advanced LIGO data”. In: *Physical Review D* 96.12 (2017).

[Abb+17h] B. P. Abbott et al. “First narrow-band search for continuous gravitational waves from known pulsars in advanced detector data”. In: *Physical Review D* 96.12 (2017).

[Abb+17i] B. P. Abbott et al. “First Search for Gravitational Waves from Known Pulsars with Advanced LIGO”. In: *The Astrophysical Journal* 839.1 (2017), p. 12.

[Abb+17j] B. P. Abbott et al. “Gravitational Waves and Gamma-Rays from a Binary Neutron Star Merger: GW170817 and GRB 170817A”. In: *The Astrophysical Journal* 848.2 (2017), p. L13.

[Abb+17k] B. P. Abbott et al. “GW170104: Observation of a 50-Solar-Mass Binary Black Hole Coalescence at Redshift 0.2”. In: *Physical Review Letters* 118.22 (2017).

[Abb+17l] B. P. Abbott et al. “GW170608: Observation of a 19 Solar-mass Binary Black Hole Coalescence”. In: *The Astrophysical Journal* 851.2 (2017), p. L35.

[Abb+17m] B. P. Abbott et al. “GW170814: A Three-Detector Observation of Gravitational Waves from a Binary Black Hole Coalescence”. In: *Physical Review Letters* 119.14 (2017).

[Abb+17n] B. P. Abbott et al. “GW170817: Observation of Gravitational Waves from a Binary Neutron Star Inspiral”. In: *Physical Review Letters* 119.16 (2017).

[Abb+17o] B. P. Abbott et al. “Multi-messenger Observations of a Binary Neutron Star Merger”. In: *The Astrophysical Journal* 848.2 (2017), p. L12.

[Abb+17p] B. P. Abbott et al. “On the Progenitor of Binary Neutron Star Merger GW170817”. In: *The Astrophysical Journal* 850.2 (2017), p. L40.

[Abb+17q] B. P. Abbott et al. “Search for continuous gravitational waves from neutron stars in globular cluster NGC 6544”. In: *Physical Review D* 95.8 (2017).

[Abb+17r] B. P. Abbott et al. “Search for Gravitational Waves Associated with Gamma-Ray Bursts during the First Advanced LIGO Observing Run and Implications for the Origin of GRB 150906B”. In: *The Astrophysical Journal* 841.2 (2017), p. 89.

[Abb+17s] B. P. Abbott et al. “Search for gravitational waves from Scorpius X-1 in the first Advanced LIGO observing run with a hidden Markov model”. In: *Physical Review D* 95.12 (2017).

[Abb+17t] B. P. Abbott et al. “Search for intermediate mass black hole binaries in the first observing run of Advanced LIGO”. In: *Physical Review D* 96.2 (2017).

[Abb+17u] B. P. Abbott et al. “Search for Post-merger Gravitational Waves from the Remnant of the Binary Neutron Star Merger GW170817”. In: *The Astrophysical Journal* 851.1 (2017), p. L16.

[Abb+17v] B. P. Abbott et al. “Upper Limits on Gravitational Waves from Scorpius X-1 from a Model-based Cross-correlation Search in Advanced LIGO Data”. In: *The Astrophysical Journal* 847.1 (2017), p. 47.

[Abb+17w] B. P. Abbott et al. “Upper Limits on the Stochastic Gravitational-Wave Background from Advanced LIGO’s First Observing Run”. In: *Physical Review Letters* 118.12 (2017).

[Abb+18a] B. P. Abbott et al. “All-sky search for long-duration gravitational wave transients in the first Advanced LIGO observing run”. In: *Classical and Quantum Gravity* 35.6 (2018), p. 065009.

[Abb+18b] B. P. Abbott et al. “Constraints on cosmic strings using data from the first Advanced LIGO observing run”. In: *Physical Review D* 97.10 (2018).

[Abb+18c] B. P. Abbott et al. “Effects of data quality vetoes on a search for compact binary coalescences in Advanced LIGO’s first observing run”. In: *Classical and Quantum Gravity* 35.6 (2018), p. 065010.

[Abb+18d] B. P. Abbott et al. “First Search for Nontensorial Gravitational Waves from Known Pulsars”. In: *Physical Review Letters* 120.3 (2018).

[Abb+18e] B. P. Abbott et al. “Full band all-sky search for periodic gravitational waves in the O1 LIGO data”. In: *Physical Review D* 97.10 (2018).

[Abb+18f] B. P. Abbott et al. “GW170817: Implications for the Stochastic Gravitational-Wave Background from Compact Binary Coalescences”. In: *Physical Review Letters* 120.9 (2018).

[Abb+18g] B. P. Abbott et al. “GW170817: Measurements of Neutron Star Radii and Equation of State”. In: *Physical Review Letters* 121.16 (2018).

[Abb+18h] B. P. Abbott et al. “Prospects for observing and localizing gravitational-wave transients with Advanced LIGO, Advanced Virgo and KAGRA”. In: *Living Reviews in Relativity* 21.1 (2018).

[Abb+18i] B. P. Abbott et al. “Search for Subsolar-Mass Ultracompact Binaries in Advanced LIGO’s First Observing Run”. In: *Physical Review Letters* 121.23 (2018).

[Abb+18j] B. P. Abbott et al. “Search for Tensor, Vector, and Scalar Polarizations in the Stochastic Gravitational-Wave Background”. In: *Physical Review Letters* 120.20 (2018).

[Abb+19a] B. P. Abbott et al. “All-sky search for continuous gravitational waves from isolated neutron stars using Advanced LIGO O2 data”. In: *Physical Review D* 100.2 (2019).

[Abb+19b] B. P. Abbott et al. “All-sky search for long-duration gravitational-wave transients in the second Advanced LIGO observing run”. In: *Physical Review D* 99.10 (2019).

[Abb+19c] B. P. Abbott et al. “All-sky search for short gravitational-wave bursts in the second Advanced LIGO and Advanced Virgo run”. In: *Physical Review D* 100.2 (2019).

[Abb+19d] B. P. Abbott et al. “Binary Black Hole Population Properties Inferred from the First and Second Observing Runs of Advanced LIGO and Advanced Virgo”. In: *The Astrophysical Journal* 882.2 (2019), p. L24.

[Abb+19e] B. P. Abbott et al. “Constraining the p -Mode– g -Mode Tidal Instability with GW170817”. In: *Physical Review Letters* 122.6 (2019).

[Abb+19f] B. P. Abbott et al. “Directional limits on persistent gravitational waves using data from Advanced LIGO’s first two observing runs”. In: *Physical Review D* 100.6 (2019).

[Abb+19g] B. P. Abbott et al. “GWTC-1: A Gravitational-Wave Transient Catalog of Compact Binary Mergers Observed by LIGO and Virgo during the First and Second Observing Runs”. In: *Physical Review X* 9.3 (2019).

[Abb+19h] B. P. Abbott et al. “Low-latency Gravitational-wave Alerts for Multimessenger Astronomy during the Second Advanced LIGO and Virgo Observing Run”. In: *The Astrophysical Journal* 875.2 (2019), p. 161.

[Abb+19i] B. P. Abbott et al. “Narrow-band search for gravitational waves from known pulsars using the second LIGO observing run”. In: *Physical Review D* 99.12 (2019).

[Abb+19j] B. P. Abbott et al. “Properties of the Binary Neutron Star Merger GW170817”. In: *Physical Review X* 9.1 (2019).

[Abb+19k] B. P. Abbott et al. “Search for Eccentric Binary Black Hole Mergers with Advanced LIGO and Advanced Virgo during Their First and Second Observing Runs”. In: *The Astrophysical Journal* 883.2 (2019), p. 149.

[Abb+19l] B. P. Abbott et al. “Search for Gravitational-wave Signals Associated with Gamma-Ray Bursts during the Second Observing Run of Advanced LIGO and Advanced Virgo”. In: *The Astrophysical Journal* 886.1 (2019), p. 75.

[Abb+19m] B. P. Abbott et al. “Search for Gravitational Waves from a Long-lived Remnant of the Binary Neutron Star Merger GW170817”. In: *The Astrophysical Journal* 875.2 (2019), p. 160.

[Abb+19n] B. P. Abbott et al. “Search for gravitational waves from Scorpius X-1 in the second Advanced LIGO observing run with an improved hidden Markov model”. In: *Physical Review D* 100.12 (2019).

[Abb+19o] B. P. Abbott et al. “Search for intermediate mass black hole binaries in the first and second observing runs of the Advanced LIGO and Virgo network”. In: *Physical Review D* 100.6 (2019).

[Abb+19p] B. P. Abbott et al. “Search for Subsolar Mass Ultracompact Binaries in Advanced LIGO’s Second Observing Run”. In: *Physical Review Letters* 123.16 (2019).

[Abb+19q] B. P. Abbott et al. “Search for the isotropic stochastic background using data from Advanced LIGO’s second observing run”. In: *Physical Review D* 100.6 (2019).

[Abb+19r] B. P. Abbott et al. “Search for Transient Gravitational-wave Signals Associated with Magnetar Bursts during Advanced LIGO’s Second Observing Run”. In: *The Astrophysical Journal* 874.2 (2019), p. 163.

[Abb+19s] B. P. Abbott et al. “Searches for Continuous Gravitational Waves from 15 Supernova Remnants and Fomalhaut b with Advanced LIGO”. In: *The Astrophysical Journal* 875.2 (2019), p. 122.

[Abb+19t] B. P. Abbott et al. “Searches for Gravitational Waves from Known Pulsars at Two Harmonics in 2015–2017 LIGO Data”. In: *The Astrophysical Journal* 879.1 (2019), p. 10.

[Abb+19u] B. P. Abbott et al. “Tests of General Relativity with GW170817”. In: *Physical Review Letters* 123.1 (2019).

[Abb+19v] B. P. Abbott et al. “Tests of general relativity with the binary black hole signals from the LIGO-Virgo catalog GWTC-1”. In: *Physical Review D* 100.10 (2019).

[Abb+20a] B. P. Abbott et al. “A guide to LIGO–Virgo detector noise and extraction of transient gravitational-wave signals”. In: *Classical and Quantum Gravity* 37.5 (2020), p. 055002.

[Abb+20b] B. P. Abbott et al. “Erratum: “Searches for Gravitational Waves from Known Pulsars at Two Harmonics in 2015–2017 LIGO Data” (2019, ApJ, 879, 10)”. In: *The Astrophysical Journal* 899.2 (2020), p. 170.

[Abb+20c] B. P. Abbott et al. “GW190425: Observation of a Compact Binary Coalescence with Total Mass 3.4 M ⊙”. In: *The Astrophysical Journal Letters* 892.1 (2020), p. L3.

[Abb+20d] B. P. Abbott et al. “Model comparison from LIGO–Virgo data on GW170817’s binary components and consequences for the merger remnant”. In: *Classical and Quantum Gravity* 37.4 (2020), p. 045006.

[Abb+20e] B. P. Abbott et al. “Optically targeted search for gravitational waves emitted by core-collapse supernovae during the first and second observing runs of advanced LIGO and advanced Virgo”. In: *Physical Review D* 101.8 (2020).

[Abb+20f] B. P. Abbott et al. “Prospects for observing and localizing gravitational-wave transients with Advanced LIGO, Advanced Virgo and KAGRA”. In: *Living Reviews in Relativity* 23.1 (2020).

[Abb+21a] B. P. Abbott et al. “A Gravitational-wave Measurement of the Hubble Constant Following the Second Observing Run of Advanced LIGO and Virgo”. In: *The Astrophysical Journal* 909.2 (2021), p. 218.

[Abb+21b] B. P. Abbott et al. “Erratum: “A Gravitational-wave Measurement of the Hubble Constant Following the Second Observing Run of Advanced LIGO and Virgo” (2021, ApJ, 909, 218)”. In: *The Astrophysical Journal* 923.2 (2021), p. 279.

[Abb+21c] B. P. Abbott et al. “Erratum: “Searches for Continuous Gravitational Waves from 15 Supernova Remnants and Fomalhaut b with Advanced LIGO” (2019, ApJ, 875, 122) sup∗/*sup*”. In: *The Astrophysical Journal* 918.2 (2021), p. 91.

[Abb+20g] R. Abbott et al. “Gravitational-wave Constraints on the Equatorial Ellipticity of Millisecond Pulsars”. In: *The Astrophysical Journal Letters* 902.1 (2020), p. L21.

[Abb+20h] R. Abbott et al. “GW190412: Observation of a binary-black-hole coalescence with asymmetric masses”. In: *Physical Review D* 102.4 (2020).

[Abb+20i] R. Abbott et al. “GW190521: A Binary Black Hole Merger with a Total Mass of 150 M ⊙”. In: *Physical Review Letters* 125.10 (2020).

[Abb+20j] R. Abbott et al. “GW190814: Gravitational Waves from the Coalescence of a 23 Solar Mass Black Hole with a 2.6 Solar Mass Compact Object”. In: *The Astrophysical Journal Letters* 896.2 (2020), p. L44.

[Abb+20k] R. Abbott et al. “Properties and Astrophysical Implications of the 150 M ⊙ Binary Black Hole Merger GW190521”. In: *The Astrophysical Journal* 900.1 (2020), p. L13.

[Abb+21d] R. Abbott et al. “All-sky search for continuous gravitational waves from isolated neutron stars in the early O3 LIGO data”. In: *Physical Review D* 104.8 (2021).

[Abb+21e] R. Abbott et al. “All-sky search for long-duration gravitational-wave bursts in the third Advanced LIGO and Advanced Virgo run”. In: *Physical Review D* 104.10 (2021).

[Abb+21f] R. Abbott et al. “All-sky search for short gravitational-wave bursts in the third Advanced LIGO and Advanced Virgo run”. In: *Physical Review D* 104.12 (2021).

[Abb+21g] R. Abbott et al. “All-sky search in early O3 LIGO data for continuous gravitational-wave signals from unknown neutron stars in binary systems”. In: *Physical Review D* 103.6 (2021).

[Abb+21h] R. Abbott et al. “Constraints from LIGO O3 Data on Gravitational-wave Emission Due to R-modes in the Glitching Pulsar PSR J0537–6910”. In: *The Astrophysical Journal* 922.1 (2021), p. 71.

[Abb+21i] R. Abbott et al. “Constraints on Cosmic Strings Using Data from the Third Advanced LIGO–Virgo Observing Run”. In: *Physical Review Letters* 126.24 (2021).

[Abb+21j] R. Abbott et al. “Diving below the Spin-down Limit: Constraints on Gravitational Waves from the Energetic Young Pulsar PSR J0537-6910”. In: *The Astrophysical Journal Letters* 913.2 (2021), p. L27.

[Abb+21k] R. Abbott et al. “GWTC-2: Compact Binary Coalescences Observed by LIGO and Virgo during the First Half of the Third Observing Run”. In: *Physical Review X* 11.2 (2021).

[Abb+21l] R. Abbott et al. “Observation of Gravitational Waves from Two Neutron Star–Black Hole Coalescences”. In: *The Astrophysical Journal Letters* 915.1 (2021), p. L5.

[Abb+21m] R. Abbott et al. “Population Properties of Compact Objects from the Second LIGO–Virgo Gravitational-Wave Transient Catalog”. In: *The Astrophysical Journal Letters* 913.1 (2021), p. L7.

[Abb+21n] R. Abbott et al. “Search for anisotropic gravitational-wave backgrounds using data from Advanced LIGO and Advanced Virgo’s first three observing runs”. In: *Physical Review D* 104.2 (2021).

[Abb+21o] R. Abbott et al. “Search for Gravitational Waves Associated with Gamma-Ray Bursts Detected by Fermi and Swift during the LIGO–Virgo Run O3a”. In: *The Astrophysical Journal* 915.2 (2021), p. 86.

[Abb+21p] R. Abbott et al. “Searches for Continuous Gravitational Waves from Young Supernova Remnants in the Early Third Observing Run of Advanced LIGO and Virgo”. In: *The Astrophysical Journal* 921.1 (2021), p. 80.

[Abb+21q] R. Abbott et al. “Tests of general relativity with binary black holes from the second LIGO-Virgo gravitational-wave transient catalog”. In: *Physical Review D* 103.12 (2021).

[AAA21] R. Abbott et al. “Upper limits on the isotropic gravitational-wave background from Advanced LIGO and Advanced Virgo’s third observing run”. In: *Physical Review D* 104.2 (2021).

[Abb+22a] R. Abbott et al. “All-sky, all-frequency directional search for persistent gravitational waves from Advanced LIGO’s and Advanced Virgo’s first three observing runs”. In: *Physical Review D* 105.12 (2022).

[Abb+22b] R. Abbott et al. “All-sky search for gravitational wave emission from scalar boson clouds around spinning black holes in LIGO O3 data”. In: *Physical Review D* 105.10 (2022).

[Abb+22c] R. Abbott et al. “Constraints on dark photon dark matter using data from LIGO’s and Virgo’s third observing run”. In: *Physical Review D* 105.6 (2022).

[Abb+22d] R. Abbott et al. “Narrowband Searches for Continuous and Long-duration Transient Gravitational Waves from Known Pulsars in the LIGO-Virgo Third Observing Run”. In: *The Astrophysical Journal* 932.2 (2022), p. 133.

[Abb+22e] R. Abbott et al. “Search for continuous gravitational wave emission from the Milky Way center in O3 LIGO-Virgo data”. In: *Physical Review D* 106.4 (2022).

[Abb+22f] R. Abbott et al. “Search for continuous gravitational waves from 20 accreting millisecond x-ray pulsars in O3 LIGO data”. In: *Physical Review D* 105.2 (2022).

[Abb+22g] R. Abbott et al. “Search for Gravitational Waves Associated with Gamma-Ray Bursts Detected by Fermi and Swift during the LIGO–Virgo Run O3b”. In: *The Astrophysical Journal* 928.2 (2022), p. 186.

[Abb+22h] R. Abbott et al. “Search for intermediate-mass black hole binaries in the third observing run of Advanced LIGO and Advanced Virgo”. In: *Astronomy Astrophysics* 659 (2022), A84.

[Abb+22i] R. Abbott et al. “Search of the early O3 LIGO data for continuous gravitational waves from the Cassiopeia A and Vela Jr. supernova remnants”. In: *Physical Review D* 105.8 (2022).

[Abb+21r] R. Abbott et al. “Open data from the first and second observing runs of Advanced LIGO and Advanced Virgo”. In: *SoftwareX* 13 (2021), p. 100658.

[Abe+18] M. Abernathy et al. “Bulk and shear mechanical loss of titania-doped tantala”. In: *Physics Letters A* 382.33 (2018), pp. 2282–2288.

[AO83] S. Adachi et al. “Internal strain and photoelastic effects in Ga1-xAlxAs/GaAs and In1-xGax AsyP1-y/InP crystals”. In: *Journal of Applied Physics* 54.11 (1983), pp. 6620–6627.

[Age+04] A. Ageev et al. “Very high quality factor measured in annealed fused silica”. In: *Classical and Quantum Gravity* 21.16 (2004), pp. 3887–3892.

[Agr+06] J. Agresti et al. “Optimized multilayer dielectric mirror coatings for gravitational wave interferometers”. In: (2006). Ed. by M. J. Ellison.

[Aku+18] T Akutsu et al. “Construction of KAGRA: an underground gravitational-wave observatory”. In: *Progress of Theoretical and Experimental Physics* 2018.1 (2018).

[Aku+20] T. Akutsu et al. “The status of KAGRA underground cryogenic gravitational wave telescope”. In: *Journal of Physics: Conference Series* 1342.1 (2020), p. 012014.

[Alb+17a] A. Albert et al. “Search for High-energy Neutrinos from Binary Neutron Star Merger GW170817 with ANTARES, IceCube, and the Pierre Auger Observatory”. In: *The Astrophysical Journal* 850.2 (2017), p. L35.

[Alb+17b] A. Albert et al. “Search for high-energy neutrinos from gravitational wave event GW151226 and candidate LVT151012 with ANTARES and IceCube”. In: *Physical Review D* 96.2 (2017).

[Alb+19] A. Albert et al. “Search for Multimessenger Sources of Gravitational Waves and High-energy Neutrinos with Advanced LIGO during Its First Observing Run, ANTARES, and IceCube”. In: *The Astrophysical Journal* 870.2 (2019), p. 134.

[Ali13] T. Alig. “Charakterisierung und Unterdrückung der Strahlgeometriefluktuationen des fasergekoppelten 35W Lasers für das AEI 10m Prototypinterferometer”. MA thesis. Gottfried Wilhelm Leibniz Universität Hannover, 2013.

[Aln+08] J. Alnis et al. “Subhertz linewidth diode lasers by stabilization to vibrationally and thermally compensated ultralow-expansion glass Fabry-Pérot cavities”. In: *Physical Review A* 77.5 (2008).

[Aln+11] J. Alnis et al. “Thermal-noise-limited crystalline whispering-gallery-mode resonator for laser stabilization”. In: *Physical Review A* 84.1 (2011).

[Ama+13] S. Amairi et al. “Reducing the effect of thermal noise in optical cavities”. In: *Applied Physics B* 113.2 (2013), pp. 233–242.

[Ama+21] A. Amato et al. “Optical and mechanical properties of ion-beam-sputtered Nb2O5 and TiO2-Nb2O5 thin films for gravitational-wave interferometers and an improved measurement of coating thermal noise in Advanced LIGO”. In: *Physical Review D* 103.7 (2021).

[Ama19] A. Amato. “Low Thermal Noise Coating for New Generation Gravitational-Wave Detectors”. PhD thesis. Université Claude Bernard Lyon 1, 2019.

[Ama+18] A. Amato et al. “High-Reflection Coatings for Gravitational-Wave Detectors State of The Art and Future Developments”. In: *Journal of Physics: Conference Series* 957 (2018), p. 012006.

[Ast+12] S. M. Aston et al. “Update on quadruple suspension design for Advanced LIGO”. In: *Classical and Quantum Gravity* 29.23 (2012), p. 235004.

[Ast11] S. M. Aston. “Optical Read-out Techniques for the Control of Test-masses in Gravitational Wave Observatories”. PhD thesis. University of Birmingham, 2011.

[BPA+16] and B. P. Abbott et al. “The basic physics of the binary black hole merger GW150914”. In: *Annalen der Physik* 529.1-2 (2016), p. 1600209.

[BPA+17] and B. P. Abbott et al. “A gravitational-wave standard siren measurement of the Hubble constant”. In: *Nature* 551.7678 (2017), pp. 85–88.

[Bak+14] C. Baker et al. “Photoelastic coupling in gallium arsenide optomechanical disk resonators”. In: *Optics Express* 22.12 (2014), p. 14072.

[Bal+14] K. C. Balram et al. “Moving boundary and photoelastic coupling in GaAs optomechanical resonators”. In: *Optica* 1.6 (2014), p. 414.

[Bar06] L. Barsotti. “The control of the Virgo interferometer for gravitational wave detection”. PhD thesis. Universitá degli Studi di Pisa, 2006.

[Bas+10] R Bassiri et al. “Probing the atomic structure of amorphous Ta2O5mirror coatings for advanced gravitational wave detectors using transmission electron microscopy”. In: *Journal of Physics: Conference Series* 241 (2010), p. 012070.

[Bas+13] R. Bassiri et al. “Correlations between the mechanical loss and atomic structure of amorphous TiO2-doped Ta2O5 coatings”. In: *Acta Materialia* 61.4 (2013), pp. 1070–1077.

[Bas+16] R. Bassiri et al. “Order, disorder and mixing: The atomic structure of amorphous mixtures of titania and tantala”. In: *Journal of Non-Crystalline Solids* 438 (2016), pp. 59–66.

[Bel+14] C. J. Bell et al. “Experimental results for nulling the effective thermal expansion coefficient of fused silica fibres under a static stress”. In: *Classical and Quantum Gravity* 31.6 (2014), p. 065010.

[BL09] B. Benthem et al. “Thermorefractive and thermochemical noise in the beamsplitter of the GEO600 gravitational-wave interferometer”. In: *Physical Review D* 80.6 (2009).

[Bla01] E. D. Black. “An introduction to Pound–Drever–Hall laser frequency stabilization”. In: *American Journal of Physics* 69.1 (2001), pp. 79–87.

[Bla+04a] E. D. Black et al. “Direct observation of broadband coating thermal noise in a suspended interferometer”. In: *Physics Letters A* 328.1 (2004), pp. 1–5.

[Bla+04b] E. D. Black et al. “Enhanced photothermal displacement spectroscopy for thin-film characterization using a Fabry-Perot resonator”. In: *Journal of Applied Physics* 95.12 (2004), pp. 7655–7659.

[BVL04] E. D. Black et al. “Thermoelastic-Damping Noise from Sapphire Mirrors in a Fundamental-Noise-Limited Interferometer”. In: *Physical Review Letters* 93.24 (2004).

[Bon96] F. Bondu. “Étude du bruit thermique et stabilisation en fréquence du laser du détecteur interférométrique d’ondes gravitationnelles VIRGO”. PhD thesis. Université de Paris-Sud, 1996.

[BHV98] F. Bondu et al. “Thermal noise in mirrors of interferometric gravitational wave antennas”. In: *Physics Letters A* 246.3-4 (1998), pp. 227–236.

[BLV99] V. B. Braginsky et al. “How to reduce suspension thermal noise in LIGO without improving the Q of the pendulum and violin modes”. In: *Measurement Science and Technology* 10.7 (1999), pp. 598–606.

[BGV99] V. Braginsky et al. “Thermodynamical fluctuations and photo-thermal shot noise in gravitational wave antennae”. In: *Physics Letters A* 264.1 (1999), pp. 1–10.

[BGV00] V. Braginsky et al. “Thermo-refractive noise in gravitational wave antennae”. In: *Physics Letters A* 271.5-6 (2000), pp. 303–307.

[BV03] V. Braginsky et al. “Thermodynamical fluctuations in optical mirror coatings”. In: *Physics Letters A* 312.3-4 (2003), pp. 244–255.

[BV04] V. Braginsky et al. “Corner reflectors and quantum-non-demolition measurements in gravitational wave antennae”. In: *Physics Letters A* 324.5-6 (2004), pp. 345–360.

[BRV06a] V. Braginsky et al. “Limitations in quantum measurements resolution created by cosmic rays”. In: *Physics Letters A* 359.2 (2006), pp. 86–89.

[BRV06b] V. Braginsky et al. “Notes about noise in gravitational wave antennas created by cosmic rays”. In: *Physics Letters A* 350.1-2 (2006), pp. 1–4.

[Bro28] R. Brown. “A brief account of microscopical observations made on the particles contained in the pollen of plants”. In: *Philosophical Magazine* 4 (1828), pp. 161–173.

[Bru+10] F. Bruckner et al. “Realization of a Monolithic High-Reflectivity Cavity Mirror from a Single Silicon Crystal”. In: *Physical Review Letters* 104.16 (2010).

[Bru+20] F. Bruns et al. “Thermal charge carrier driven noise in transmissive semiconductor optics”. In: *Physical Review D* 102.2 (2020).

[Bur+19] E. Burns et al. “A Fermi Gamma-Ray Burst Monitor Search for Electromagnetic Signals Coincident with Gravitational-wave Candidates in Advanced LIGO's First Observing Run”. In: *The Astrophysical Journal* 871.1 (2019), p. 90.

[Cag+18] G. Cagnoli et al. “Mode-dependent mechanical losses in disc resonators”. In: *Physics Letters A* 382.33 (2018), pp. 2165–2173.

[CW51] H. B. Callen et al. “Irreversibility and Generalized Noise”. In: *Physical Review* 83.1 (1951), pp. 34–40.

[Cel18] G. Cella. “Thermal noise correlations and subtraction”. In: *Physics Letters A* 382.33 (2018), pp. 2269–2274.

[Cer+01] M. Cerdonio et al. “Thermoelastic effects at low temperatures and quantum limits in displacement measurements”. In: *Physical Review D* 63.8 (2001).

[Cha+14] T. Chalermsongsak et al. “Broadband measurement of coating thermal noise in rigid Fabry–Pérot cavities”. In: *Metrologia* 52.1 (2014), pp. 17–30.

[Cha+16] T. Chalermsongsak et al. “Coherent cancellation of photothermal noise in GaAs-Al0.92Ga0.08As Bragg mirrors”. In: *Metrologia* 53.2 (2016), pp. 860–868.

[CHF09] S. Chelkowski et al. “Prospects of higher-order Laguerre-Gauss modes in future gravitational wave detectors”. In: *Physical Review D* 79.12 (2009).

[Col12] G. D. Cole. “Cavity optomechanics with low-noise crystalline mirrors”. In: (2012). Ed. by K. Dholakia et al.

[Col+13a] G. D. Cole et al. “Substrate-transferred crystalline coatings”. In: (2013).

[Col+13b] G. D. Cole et al. “Tenfold reduction of Brownian noise in high-reflectivity optical coatings”. In: *Nature Photonics* 7.8 (2013), pp. 644–650.

[Col+16] G. D. Cole et al. “High-performance near- and mid-infrared crystalline coatings”. In: *Optica* 3.6 (2016), p. 647.

[Col+04] T. V. Collaboration et al. “The VIRGO large mirrors: a challenge for low loss coatings”. In: *Classical and Quantum Gravity* 21.5 (2004), S935–S945.

[Cro+02] D. R. M. Crooks et al. “Excess mechanical loss associated with dielectric mirror coatings on test masses in interferometric gravitational wave detectors”. In: *Classical and Quantum Gravity* 19.5 (2002), pp. 883–896.

[Cro+04] D. R. M. Crooks et al. “Experimental measurements of coating mechanical loss factors”. In: *Classical and Quantum Gravity* 21.5 (2004), S1059–S1065.

[Cro+06] D. R. M. Crooks et al. “Experimental measurements of mechanical dissipation associated with dielectric coatings formed using SiO2, Ta2O5 and Al2O3”. In: *Classical and Quantum Gravity* 23.15 (2006), pp. 4953–4965.

[Cum+09] A Cumming et al. “Finite element modelling of the mechanical loss of silica suspension fibres for advanced gravitational wave detectors”. In: *Classical and Quantum Gravity* 26.21 (2009), p. 215012.

[Cum+12] A. V. Cumming et al. “Design and development of the advanced LIGO monolithic fused silica suspension”. In: *Classical and Quantum Gravity* 29.3 (2012), p. 035003.

[Cum+20] A. V. Cumming et al. “Lowest observed surface and weld losses in fused silica fibres for gravitational wave detectors”. In: *Classical and Quantum Gravity* 37.19 (2020), p. 195019.

[Cum08] A. V. Cumming. "Aspects of mirrors and suspensions for advanced gravitational wave detectors". PhD thesis. University of Glasgow, 2008.

[Dan+15] S. L. Danilishin et al. "Quantum noise of non-ideal Sagnac speed meter interferometer with asymmetries". In: *New Journal of Physics* 17.4 (2015), p. 043031.

[DR+17] J. Davila-Rodriguez et al. "Compact, thermal-noise-limited reference cavity for ultra-low-noise microwave generation". In: *Optics Letters* 42.7 (2017), p. 1277.

[Dic21] J. Dickmann. "Thermal noise computation of arbitrary masses in optical interferometers from first principles". In: *Optics Express* 29.22 (2021), p. 36546.

[DK18] J. Dickmann et al. "Highly reflective low-noise etalon-based meta-mirror". In: *Physical Review D* 98.8 (2018).

[Dic+18] J. Dickmann et al. "Thermal noise of beam splitters in laser gravitational wave detectors". In: *Physical Review D* 98.8 (2018).

[Dix67] R. W. Dixon. "Photoelastic Properties of Selected Materials and Their Relevance for Applications to Acoustic Light Modulators and Scanners". In: *Journal of Applied Physics* 38.13 (1967), pp. 5149–5153.

[DB14] S. Dwyer et al. "Radiative thermal noise for transmissive optics in gravitational-wave detectors". In: *Physical Review D* 90.4 (2014).

[Edg11] M. P. Edgar. "Experimental investigations into diffractive optics and optomechanical systems for future gravitational wave detectors". PhD thesis. University of Glasgow, 2011.

[Eva+08] M. Evans et al. "Thermo-optic noise in coated mirrors for high-precision optical measurements". In: *Physical Review D* 78.10 (2008).

[Far+12] A. Farsi et al. "Photothermal and thermo-refractive effects in high reflectivity mirrors at room and cryogenic temperature". In: *Journal of Applied Physics* 111.4 (2012), p. 043101.

[Faz+20] M. A. Fazio et al. "Structure and morphology of low mechanical loss TiO2-doped Ta2O5". In: *Optical Materials Express* 10.7 (2020), p. 1687.

[Fej+04] M. M. Fejer et al. "Thermoelastic dissipation in inhomogeneous media: loss measurements and displacement noise in coated test masses for interferometric gravitational wave detectors". In: *Physical Review D* 70.8 (2004).

[Fla+10] R Flaminio et al. "A study of coating mechanical and optical losses in view of reducing mirror thermal noise in gravitational wave detectors". In: *Classical and Quantum Gravity* 27.8 (2010), p. 084030.

[Fri+11] D. Friedrich et al. "Waveguide grating mirror in a fully suspended 10 meter Fabry-Perot cavity". In: *Optics Express* 19.16 (2011), p. 14955.

[Ful+12] P Fulda et al. "Review of the Laguerre-Gauss mode technology research program at Birmingham". In: *Journal of Physics: Conference Series* 363 (2012), p. 012010.

[GC08] J. Garrison et al. "Quantum Optics". Oxford University Press, 2008.

[GR93] A Gillespie et al. "Thermal noise in the test mass suspensions of a laser interferometer gravitational-wave detector prototype". In: *Physics Letters A* 178.5-6 (1993), pp. 357–363.

[GP81] K. S. Gilroy et al. "An asymmetric double-well potential model for structural relaxation processes in amorphous materials". In: *Philosophical Magazine B* 43.5 (1981), pp. 735–746.

[Glo+18] L. Glover et al. “Optical scattering measurements and implications on thermal noise in Gravitational Wave detectors test-mass coatings”. In: *Physics Letters A* 382.33 (2018), pp. 2259–2264.

[Gon00] G. González. “Suspensions thermal noise in the LIGO gravitational wave detector”. In: *Classical and Quantum Gravity* 17.21 (2000), pp. 4409–4435.

[GS94] G. I. González et al. “Brownian motion of a mass suspended by an anelastic wire”. In: *The Journal of the Acoustical Society of America* 96.1 (1994), pp. 207–212.

[GS95] G. I. González et al. “Brownian motion of a torsion pendulum with internal friction”. In: *Physics Letters A* 201.1 (1995), pp. 12–18.

[Gor08a] M. L. Gorodetsky. “Thermal noises and noise compensation in high-reflection multilayer coating”. In: (2nd Sept. 2008). arXiv: `0809.0438v1 [cond-mat.mtrl-sci]`.

[Gor08b] M. L. Gorodetsky. “Thermal noises and noise compensation in high-reflection multilayer coating”. In: *Physics Letters A* 372.46 (2008), pp. 6813–6822.

[Goß+10] S Goßler et al. “The AEI 10 m prototype interferometer”. In: *Classical and Quantum Gravity* 27.8 (2010), p. 084023.

[Gos04] S. Gossler. “The suspension systems of the interferometric gravitational-wave detector GEO600”. PhD thesis. Universität Hannover, 2004.

[Goß+07] S. Goßler et al. “Coating-free mirrors for high precision interferometric experiments”. In: *Physical Review A* 76.5 (2007).

[Gra13] C. Graef. “Optical Design and Numerical Modeling of the AEI 10m Prototype sub-SQL Interferometer”. PhD thesis. Gottfried Wilhelm Leibniz Universität Hannover, 2013.

[Gra+19] M. Granata et al. “Progress in the measurement and reduction of thermal noise in optical coatings for gravitational-wave detectors”. In: (2019).

[Gra+16] M. Granata et al. “Mechanical loss in state-of-the-art amorphous optical coatings”. In: *Physical Review D* 93.1 (2016).

[Gra+17] S. Gras et al. “Audio-band coating thermal noise measurement for Advanced LIGO with a multimode optical resonator”. In: *Physical Review D* 95.2 (2017).

[GE18] S. Gras et al. “Direct measurement of coating thermal noise in optical resonators”. In: *Physical Review D* 98.12 (2018).

[Gra00] M. B. Gray. “The ANU thermal noise experiment”. In: (2000).

[GHD12] T. P. B. Gregory Harry et al. “Optical Coatings and Thermal Noise in Precision Measurement”. CAMBRIDGE, 15th Jan. 2012. 344 pp. ISBN: 1107003385. URL: `https://www.ebook.de/de/product/15567993/optical_coatings_and_thermal_noise_in_precision_measurement.html`.

[GH99] A. M. Gretarsson et al. “Dissipation of mechanical energy in fused silica fibers”. In: *Review of Scientific Instruments* 70.10 (1999), pp. 4081–4087.

[Gre+00] A. M. Gretarsson et al. “Pendulum mode thermal noise in advanced interferometers: a comparison of fused silica fibers and ribbons in the presence of surface loss”. In: *Physics Letters A* 270.3-4 (2000), pp. 108–114.

[GG18] E. M. Gretarsson et al. “Three methods for characterizing thermo-optic noise in optical cavities”. In: *Physical Review D* 98.12 (2018).

[Gur10] A. G. Gurkovsky. “Investigation of Brownian coating noise in laser interferometric gravitational antennas”. In: *Optics and Spectroscopy* 109.1 (2010), pp. 48–53.

[GV10] A. Gurkovsky et al. “The thermal noise in multilayer coating”. In: *Physics Letters A* 374.33 (2010), pp. 3267–3274.

[Gur+11] A. G. Gurkovsky et al. “Reducing thermal noise in future gravitational wave detectors by employing Khalili etalons”. In: *Physics Letters A* 375.46 (2011), pp. 4147–4157.

[Had+99] Y Hadjar et al. “High-sensitivity optical measurement of mechanical Brownian motion”. In: *Europhysics Letters (EPL)* 47.5 (1999), pp. 545–551.

[Ham+20] R. Hamburg et al. “A Joint Fermi-GBM and LIGO/Virgo Analysis of Compact Binary Mergers from the First and Second Gravitational-wave Observing Runs”. In: *The Astrophysical Journal* 893.2 (2020), p. 100.

[Ham+12] G. D. Hammond et al. “Reducing the suspension thermal noise of advanced gravitational wave detectors”. In: *Classical and Quantum Gravity* 29.12 (2012), p. 124009.

[Han18] M. M. Hanke. “Laser Frequency Stabilization for the Sub-SQL Interferometer”. PhD thesis. Gottfried Wilhelm Leibniz Universität Hannover, 2018.

[Har+02] G. M. Harry et al. “Thermal noise in interferometric gravitational wave detectors due to dielectric optical coatings”. In: *Classical and Quantum Gravity* 19.5 (2002), pp. 897–917.

[Har+06a] G. M. Harry et al. “Thermal noise from optical coatings in gravitational wave detectors”. In: *Applied Optics* 45.7 (2006), p. 1569.

[Har+06b] G. M. Harry et al. “Titania-doped tantala/silica coatings for gravitational-wave detection”. In: *Classical and Quantum Gravity* 24.2 (2006), pp. 405–415.

[Har+16] M. J. Hart et al. “Medium range structural order in amorphous tantala spatially resolved with changes to atomic structure by thermal annealing”. In: *Journal of Non-Crystalline Solids* 438 (2016), pp. 10–17.

[Har17] M. J. Hart. “Amorphous Mirror Coatings for Ultra-High Precision Interferometry”. PhD thesis. University of Glasgow, 2017.

[Har15] M. T. Hartman. “Measurement of Thermal Noise in Dielectric Mirrors and Parallel Phase Modulation for Gravitational-wave Detectors”. PhD thesis. University of Florida, 2015.

[Hei+13] D. Heinert et al. “Calculation of thermal noise in grating reflectors”. In: *Physical Review D* 88.4 (2013).

[HHN14] D. Heinert et al. “Fluctuation Dissipation at work: Thermal noise in reflective optical coatings for GW detectors”. In: (2014).

[Hew+07] M Hewitson et al. “Charge measurement and mitigation for the main test masses of the GEO 600 gravitational wave observatory”. In: *Classical and Quantum Gravity* 24.24 (2007), pp. 6379–6391.

[Hil07] S. Hild. “Beyond the first Generation: Extending the Science Range of the Gravitational Wave Detector GEO600”. PhD thesis. Gottfried Wilhelm Leibniz Universität Hannover, 2007.

[Hil+06] S. Hild et al. “Measurement of a low-absorption sample of OH-reduced fused silica”. In: *Applied Optics* 45.28 (2006), p. 7269.

[Hil+12] G. Hillers et al. “Global oceanic microseism sources as seen by seismic arrays and predicted by wave action models”. In: *Geochemistry, Geophysics, Geosystems* 13.1 (2012), n/a–n/a.

[Hon+13] T. Hong et al. “Brownian thermal noise in multilayer coated mirrors”. In: *Physical Review D* 87.8 (2013).

[Jac+99] K. Jacobs et al. “Quantum noise in the position measurement of a cavity mirror undergoing Brownian motion”. In: *Physical Review A* 60.1 (1999), pp. 538–548.

[Jen98] O. Jennrich. “Das Quantenlimit der Interferometrie”. PhD thesis. Universität Hannover, 1998.

[Jia+11] Y. Y. Jiang et al. “Making optical atomic clocks more stable with 10-16-level laser stabilization”. In: *Nature Photonics* 5.3 (2011), pp. 158–161.

[Jun16] J. Junker. “Laser Power Stabilization for the AEI 10m Prototype”. MA thesis. Gottfried Wilhelm Leibniz Universität Hannover, 2016.

[KP03] N. Kaiser et al., eds. “Optical Interference Coatings”. Springer Berlin Heidelberg, 2003.

[Kaj+99] M. Kajima et al. “Wide-band measurement of mechanical thermal noise using a laser interferometer”. In: *Physics Letters A* 264.4 (1999), pp. 251–256.

[Kar19] S. Karki. “Accurate and Precise Calibration of Advanced LIGO Detectors in the Era of Gravitational Wave Astronomy”. PhD thesis. University of Oregon, 2019.

[Kaw98] K. Kawabe. “Development of a 3-meter Fabry-Perot-Michelson Interferometer for Gravitational Wave Detection”. PhD thesis. University of Tokyo, 1998.

[KLS11] T. Kessler et al. “Thermal noise in optical cavities revisited”. In: *Journal of the Optical Society of America B* 29.1 (2011), p. 178.

[Kes+12] T. Kessler et al. “A sub-40 mHz laser based on a silicon single-crystal optical cavity”. In: (2012).

[Kha05] F. Khalili. “Reducing the mirrors coating noise in laser gravitational-wave antennae by means of double mirrors”. In: *Physics Letters A* 334.1 (2005), pp. 67–72.

[Kö18] S. M. Köhlenbeck. “Towards the SQL Interferometer Length Stabilization at the AEI 10m-Prototype”. PhD thesis. Gottfried Wilhelm Leibniz Universität Hannover, 2018.

[KLY08] H. J. Kimble et al. “Optical Interferometers with Reduced Sensitivity to Thermal Noise”. In: *Physical Review Letters* 101.26 (2008).

[KH+16] M. Kinley-Hanlon et al. “The effect of time on optical coating mechanical loss and implications for LIGO-India”. In: *Classical and Quantum Gravity* 33.14 (2016), p. 147001.

[Kir+17] R Kirchhoff et al. “Huddle test measurement of a near Johnson noise limited geophone”. In: *AIP - Review of Scientific Instruments* 88.11 (Nov. 2017), p. 115008.

[Kir+20] R Kirchhoff et al. “Local active isolation of the AEI-SAS for the AEI 10 m prototype facility”. In: *Classical and Quantum Gravity* 37.11 (2020), p. 115004.

[Kir21] R. Kirchhoff. “Implementation of an active seismic isolation system for the AEI 10m prototype”. PhD thesis. Gottfried Wilhelm Leibniz Universität Hannover, 2021.

[Klo+22] Y. Y. Klochkov et al. “Using silicon disk resonators to measure mechanical losses caused by an electric field”. In: *Review of Scientific Instruments* 93.1 (2022), p. 014501.

[Koc+19] P. Koch et al. “Thickness uniformity measurements and damage threshold tests of large-area GaAs/AlGaAs crystalline coatings for precision interferometry”. In: *Optics Express* 27.25 (2019), p. 36731.

[Koc22] P. Koch. “Design, Suspension and Optical Characterization of the Beam Splitter and Output Mode Cleaner for the AEI 10 m Prototype”. PhD thesis. Gottfried Wilhelm Leibniz Universität Hannover, 2022.

[Kok+13] K. Kokeyama et al. “Residual amplitude modulation in interferometric gravitational wave detectors”. In: *Journal of the Optical Society of America A* 31.1 (2013), p. 81.

[Kom+18] K. Komori et al. “Direct approach for the fluctuation-dissipation theorem under nonequilibrium steady-state conditions”. In: *Physical Review D* 97.10 (2018).

[KGG11] N. M. Kondratiev et al. “Thermal noise and coating optimization in multilayer dielectric mirrors”. In: *Physical Review D* 84.2 (2011).

[Kon+15] N. Kondratiev et al. “Spontaneous crystallization noise in mirrors of gravitational wave detectors”. In: *Physical Review D* 92.4 (2015).

[KG16] N. Kondratiev et al. “Viscosity of fused silica and thermal noise from the standard linear solid model”. In: *Physical Review D* 94.8 (2016).

[Kro+17] S. Kroker et al. “Brownian thermal noise in functional optical surfaces”. In: *Physical Review D* 96.2 (2017).

[Kum08] R. Kumar. “Finite element analysis of suspension elements for gravitational wave detectors”. MA thesis. University of Glasgow, 2008.

[Kwe+14] P. Kwee et al. “Decoherence and degradation of squeezed states in quantum filter cavities”. In: *Physical Review D* 90.6 (2014).

[Kwe10] P. Kwee. “Laser Characterization and Stabilization for Precision Interferometry”. PhD thesis. Gottfried Wilhelm Leibniz Universität Hannover, 2010.

[Lal+21] É. Lalande et al. “Zirconia-titania-doped tantala optical coatings for low mechanical loss Bragg mirrors”. In: *Journal of Vacuum Science Technology A* 39.4 (2021), p. 043416.

[Lü+04] H Lück et al. “Thermal correction of the radii of curvature of mirrors for GEO 600”. In: *Classical and Quantum Gravity* 21.5 (2004), S985–S989.

[Lü+08] H Lück et al. “Opto-mechanical frequency shifting of scattered light”. In: *Journal of Optics A: Pure and Applied Optics* 10.8 (2008), p. 085004.

[Leg+17] T. Legero et al. “1.5 mu Lasers with sub 10 mHz Linewidth”. In: (2017).

[Leh14] J. Lehmann. “Aufbau und Test der Dreifach-Aufhängung für das SQL Interferometer am AEI 10m-Prototypen”. Bachelor’s Thesis. Gottfried Wilhelm Leibniz Universität Hannover, 2014.

[Leo+02] V Leonhardt et al. “Towards measuring the off-resonant thermal noise of a pendulum mirror”. In: *Classical and Quantum Gravity* 19.7 (2002), pp. 1717–1721.

[Leo+04] V Leonhardt et al. “The Hannover thermal noise experiment”. In: *Classical and Quantum Gravity* 21.5 (2004), S1127–S1131.

[Leo03] V. Leonhardt. “Displacement measurements on suspended mirrors for off-resonant thermal noise detection”. PhD thesis. Universität Hannover, 2003.

[Lev98] Y. Levin. “Internal thermal noise in the LIGO test masses: A direct approach”. In: *Physical Review D* 57.2 (1998), pp. 659–663.

[Lev08] Y. Levin. “Fluctuation–dissipation theorem for thermo-refractive noise”. In: *Physics Letters A* 372.12 (2008), pp. 1941–1944.

[Li+14] T. Li et al. “Measurements of mechanical thermal noise and energy dissipation in optical dielectric coatings”. In: *Physical Review D* 89.9 (2014).

[LT00] Y. T. Liu et al. “Thermoelastic noise and homogeneous thermal noise in finite sized gravitational-wave test masses”. In: *Physical Review D* 62.12 (2000).

[LDK17] G. Lovelace et al. “Numerically modeling Brownian thermal noise in amorphous and crystalline thin coatings”. In: *Classical and Quantum Gravity* 35.2 (2017), p. 025017.

[Lud+07] A. D. Ludlow et al. “Compact, thermal-noise-limited optical cavity for diode laser stabilization at 10-15”. In: *Optics Letters* 32.6 (2007), p. 641.

[Lun+08] A. P. Lundgren et al. “Finite mirror effects in advanced interferometric gravitational wave detectors”. In: *Physical Review D* 77.4 (2008).

[Mac14] J. Macarthur. “Towards Surpassing the Standard Quantum Limit Using Optical Springs”. PhD thesis. University of Glasgow, 2014.

[Mac19] I. A. O. MacMillan. “Brownian Thermal Noise in AlGaAs and Its Implications for LIGO’s Sensitivity”. Bachelor’s Thesis. Georgetown University, 2019.

[Mar+09] I. W. Martin et al. “Comparison of the temperature dependence of the mechanical dissipation in thin films of Ta2O5 and Ta2O5 doped with TiO2”. In: *Classical and Quantum Gravity* 26.15 (2009), p. 155012.

[Mar+10] I. W. Martin et al. “Effect of heat treatment on mechanical dissipation in Ta2O5 coatings”. In: *Classical and Quantum Gravity* 27.22 (2010), p. 225020.

[Mar+14] I. W. Martin et al. “Low temperature mechanical dissipation of an ion-beam sputtered silica film”. In: *Classical and Quantum Gravity* 31.3 (2014), p. 035019.

[Mar13] M. J. Martin. “Quantum Metrology and Many-Body Physics: Pushing the Frontier of the Optical Lattice Clock”. PhD thesis. University of Colorado, 2013.

[Mar15] D. Martynov. “Lock Acquisition and Sensitivity Analysis of Advanced LIGO Interferometers”. PhD thesis. California Institute of Technology, 2015.

[Mep] “Mephisto Laser Operator’s Manual”.

[Mer08] L. Merrill. “A Study of Thermal Noise for Enhanced Laser Interferometer Gravitational Wave Observatory”. MA thesis. Simmons College, 2008.

[Mes17] D. Meschede. “Optics, Light and Lasers”. Wiley-VCH GmbH, 5th Apr. 2017. ISBN: 3527413316. URL: `https://www.ebook.de/de/product/26153804/dieter_meschede_optics_light_and_lasers.html`.

[Met19] B. D. Metzger. “Kilonovae”. In: *Living Reviews in Relativity* 23.1 (2019).

[Mil+09] J. Millo et al. “Ultrastable lasers based on vibration insensitive cavities”. In: *Physical Review A* 79.5 (2009).

[Mos+06] K. Mossavi et al. “A photon pressure calibrator for the GEO 600 gravitational wave detector”. In: *Physics Letters A* 353.1 (2006), pp. 1–3.

[Mul12] A. J. Mullavey. “Arm Length Stabilisation for Advanced Gravitational Wave Detectors”. PhD thesis. Australian National University, 2012.

[Nak+02] N. Nakagawa et al. “Thermal noise in half-infinite mirrors with nonuniform loss: A slab of excess loss in a half-infinite mirror”. In: *Physical Review D* 65.10 (2002).

[Naw+10] R. Nawrodt et al. “Challenges in thermal noise for 3rd generation of gravitational wave detectors”. In: *General Relativity and Gravitation* 43.2 (2010), pp. 593–622.

[Neb+12] A. R. Neben et al. “Structural thermal noise in gram-scale mirror oscillators”. In: *New Journal of Physics* 14.11 (2012), p. 115008.

[NL70] D. F. Nelson et al. “New Symmetry for Acousto-Optic Scattering”. In: *Physical Review Letters* 24.8 (1970), pp. 379–380.

[Ner21] M. T. Nery. “Laser power stabilization via radiation pressure”. PhD thesis. Gottfried Wilhelm Leibniz Universität Hannover, 2021.

[Ngu+15] T. T.-H. Nguyen et al. “Frequency dependence of thermal noise in gram-scale cantilever flexures”. In: *Physical Review D* 92.11 (2015).

[Not+06] M. Notcutt et al. “Contribution of thermal noise to frequency stability of rigid optical cavity via Hertz-linewidth lasers”. In: *Physical Review A* 73.3 (2006).

[Num+02] K. Numata et al. “Intrinsic losses in various kinds of fused silica”. In: *Classical and Quantum Gravity* 19.7 (2002), pp. 1697–1702.

[Num+03] K. Numata et al. “Wide-Band Direct Measurement of Thermal Fluctuations in an Interferometer”. In: *Physical Review Letters* 91.26 (2003).

[NKC04] K. Numata et al. “Thermal-Noise Limit in the Frequency Stabilization of Lasers with Rigid Cavities”. In: *Physical Review Letters* 93.25 (2004).

[Ogi+16] G. H. Ogin et al. “Measuring the Thermo-Optic Response of Dielectric Stack Mirrors”. In: (2016).

[Opp17] P. Oppermann. “Characterization and Stabilization of a High Power Fiber Amplifier Laser”. PhD thesis. Gottfried Wilhelm Leibniz Universität Hannover, 2017.

[OH05] B. Orr et al. “Cavity ringdown spectroscopy with widely tunable swept-frequency lasers”. In: (2005).

[O’S06] R O’Shaughnessy. “A note on coating thermal noise for arbitrary-shaped beams”. In: *Classical and Quantum Gravity* 23.24 (2006), pp. 7627–7630.

[Pac+20] S. D. Pace et al. “Thermal noise study of a radiation pressure noise limited optical cavity with fused silica mirror suspensions”. In: *The European Physical Journal D* 74.11 (2020).

[Pag+18] M. Page et al. “Ultra-low dissipation resonators for improving the sensitivity of gravitational wave detectors”. In: *Physics Letters A* 382.33 (2018), pp. 2174–2180.

[Pan+18] H.-W. Pan et al. “Silicon nitride and silica quarter-wave stacks for low-thermal-noise mirror coatings”. In: *Physical Review D* 98.10 (2018).

[Pen+01] S. D. Penn et al. “High quality factor measured in fused silica”. In: *Review of Scientific Instruments* 72.9 (2001), pp. 3670–3673.

[Pen+03] S. D. Penn et al. “Mechanical loss in tantala/silica dielectric mirror coatings”. In: *Classical and Quantum Gravity* 20.13 (2003), pp. 2917–2928.

[Pen+06] S. D. Penn et al. “Frequency and surface dependence of the mechanical loss in fused silica”. In: *Physics Letters A* 352.1-2 (2006), pp. 3–6.

[Pen+19] S. D. Penn et al. “Mechanical ringdown studies of large-area substrate-transferred GaAs/AlGaAs crystalline coatings”. In: *Journal of the Optical Society of America B* 36.4 (2019), p. C15.

[Pie+19] V. Pierro et al. “On the performance limits of coatings for gravitational wave detectors made of alternating layers of two materials”. In: *Optical Materials* 96 (2019), p. 109269.

[Pli+04] M. V. Plissi et al. “An investigation of eddy-current damping of multi-stage pendulum suspensions for use in interferometric gravitational wave detectors”. In: *Review of Scientific Instruments* 75.11 (2004), pp. 4516–4522.

[Pri+15] M. Principe et al. “Material loss angles from direct measurements of broadband thermal noise”. In: *Physical Review D* 91.2 (2015).

[Pro+18] L. Prokhorov et al. “Upper limits on the mechanical loss of silicate bonds in a silicon tuning fork oscillator”. In: *Physics Letters A* 382.33 (2018), pp. 2186–2191.

[Qi+08] H. Qi et al. “Investigation on damage process of GaAs induced by 1064nm continuous laser”. In: *Journal of Applied Physics* 103.3 (2008), p. 033106.

[RA22a] F. A. K. A. N. A. R. Abbott H. Abe. “First joint observation by the underground gravitational-wave detector KAGRA with GEO 600”. In: *Progress of Theoretical and Experimental Physics* 6 (June 2022).

[RA22b] F. A. K. A. N. A. R. Abbott H. Abe. “Searches for Gravitational Waves from Known Pulsars at Two Harmonics in the Second and Third LIGO-Virgo Observing Runs”. In: *The Astrophysical Journal* 935.1 (May 2022).

[RHV11] A. A. Rakhubovsky et al. “Stable double-resonance optical spring in laser gravitational-wave detectors”. In: *Physical Review D* 84.6 (2011).

[Rao03] S. R. Rao. “Mirror Thermal Noise in Interferometric Gravitational Wave Detectors”. PhD thesis. California Institute of Technology, 2003.

[RM16] S. Reid et al. “Development of Mirror Coatings for Gravitational Wave Detectors”. In: *Coatings* 6.4 (2016), p. 61.

[Rob+02] N. A. Robertson et al. “Quadruple suspension design for Advanced LIGO”. In: *Classical and Quantum Gravity* 19.15 (2002), pp. 4043–4058.

[Ros+02] M. D. Rosa et al. “Experimental Measurement of the Dynamic Photothermal Effect in Fabry-Perot Cavities for Gravitational Wave Detectors”. In: *Physical Review Letters* 89.23 (2002).

[Ros+06] M. D. Rosa et al. “Experimental investigation of dynamic photo-thermal effect”. In: *Classical and Quantum Gravity* 23.8 (2006), S259–S266.

[Ros+21] M. P. Ross et al. “Initial results from the LIGO Newtonian calibrator”. In: *Physical Review D* 104.8 (2021).

[RHC05] S. Rowan et al. “Thermal noise and material issues for gravitational wave detectors”. In: *Physics Letters A* 347.1-3 (2005), pp. 25–32.

[SHH88] C. Salomon et al. “Laser stabilization at the millihertz level”. In: *Journal of the Optical Society of America B* 5.8 (1988), p. 1576.

[SL01] D. H. Santamore et al. “Eliminating thermal violin spikes from LIGO noise”. In: *Physical Review D* 64.4 (2001).

[Sau90] P. R. Saulson. “Thermal noise in mechanical experiments”. In: *Physical Review D* 42.8 (1990), pp. 2437–2445.

[Sha12] B. N. Shapiro. “Adaptive Model Damping for Advanced LIGO Suspensions”. PhD thesis. Massachusetts Institute of Technology, 2012.

[Sha+20] S. Sharifi et al. “Design of microresonators to minimize thermal noise below the standard quantum limit”. In: *Review of Scientific Instruments* 91.5 (2020), p. 054504.

[SC+06] W. Shi-Chen et al. “Photo-thermal Shot Noise in End Mirrors of LIGO due to Correlation of Power Fluctuation”. In: *Chinese Physics Letters* 23.12 (2006), pp. 3173–3175.

[Smi+03] J. R. Smith et al. “Mechanical loss associated with silicate bonding of fused silica”. In: *Classical and Quantum Gravity* 20.23 (2003), pp. 5039–5047.

[SS+19] M. Soares-Santos et al. “First Measurement of the Hubble Constant from a Dark Standard Siren using the Dark Energy Survey Galaxies and the LIGO/Virgo Binary–Black-hole Merger GW170814”. In: *The Astrophysical Journal* 876.1 (2019), p. L7.

[Som09] K. Somiya. “Reduction and Possible Elimination of Coating Thermal Noise Using a Rigidly Controlled Cavity with a Quantum-Nondemolition Technique”. In: *Physical Review Letters* 102.23 (2009).

[SY09] K. Somiya et al. “Coating thermal noise of a finite-size cylindrical mirror”. In: *Physical Review D* 79.10 (2009).

[Som+11] K. Somiya et al. “Reduction of coating thermal noise by using an etalon”. In: *Physics Letters A* 375.11 (2011), pp. 1363–1374.

[Ste+15a] J. Steinlechner et al. “Mapping the optical absorption of a substrate-transferred crystalline AlGaAs coating at 1.5 mu”. In: *Classical and Quantum Gravity* 32.10 (2015), p. 105008.

[Ste+15b] J. Steinlechner et al. “Thermal noise reduction and absorption optimization via multimaterial coatings”. In: *Physical Review D* 91.4 (2015).

[SM19] J. Steinlechner et al. “Thermal noise from icy mirrors in gravitational wave detectors”. In: *Physical Review Research* 1.1 (2019).

[Ste14] O. Stenzel. “Optical Coatings”. Springer Berlin Heidelberg, 2014.

[Ste+09] U. Sterr et al. “Ultrastable lasers: new developments and applications”. In: (2009). Ed. by T. Ido et al.

[Sto88] J. Stone. “Stress-optic effects, birefringence, and reduction of birefringence by annealing in fiber Fabry-Perot interferometers”. In: *Journal of Lightwave Technology* 6.7 (1988), pp. 1245–1248.

[Tai+20] S. C. Tait et al. “Demonstration of the Multimaterial Coating Concept to Reduce Thermal Noise in Gravitational-Wave Detectors”. In: *Physical Review Letters* 125.1 (2020).

[Tay08] J. R. Taylor. “Interferometric Experiments Towards Advanced Gravitational Wave Detectors”. PhD thesis. University of Glasgow, 2008.

[Tor99] C. I. E. Torrie. “Development of Suspensions for the GEO 600 Gravitational Wave Detector”. PhD thesis. University of Glasgow, 1999.

[Tra98] S. Traeger. “Thermisches Rauschen - Eine Empfindlichkeitsgrenze der Interferometrie”. PhD thesis. Universität Hannover, 1998.

[TLV18] M. Tugolukov et al. “Thermal noise computation in gravitational wave interferometers from first principles”. In: *Physics Letters A* 382.33 (2018), pp. 2181–2185.

[Vah+10] H. Vahlbruch et al. “The GEO600 squeezed light source”. In: *Classical and Quantum Gravity* 27.8 (2010), p. 084027.

[Vaj+20] G. Vajente et al. “Method for the experimental measurement of bulk and shear loss angles in amorphous thin films”. In: *Physical Review D* 101.4 (2020).

[Vaj+21] G. Vajente et al. “Low Mechanical Loss TiO2GeO2 Coatings for Reduced Thermal Noise in Gravitational Wave Interferometers”. In: *Physical Review Letters* 127.7 (2021).

[Vil+10] A. E. Villar et al. “Measurement of thermal noise in multilayer coatings with optimized layer thickness”. In: *Physical Review D* 81.12 (2010).

[Vin09a] J.-Y. Vinet. “On Special Optical Modes and Thermal Issues in Advanced Gravitational Wave Interferometric Detectors”. In: *Living Reviews in Relativity* 12.1 (2009).

[Vin09b] J.-Y. Vinet. “On Special Optical Modes and Thermal Issues in Advanced Gravitational Wave Interferometric Detectors”. In: *Living Reviews in Relativity* 12.1 (2009).

[VZS80] K. M. van Vliet et al. “Temperature-fluctuation noise of thin films supported by a substrate”. In: *Journal of Applied Physics* 51.6 (1980), pp. 2947–2956.

[VM81] K. M. V. Vliet et al. “Theory of Transport Noise in Semiconductors”. In: *physica status solidi (b)* 106.1 (1981), pp. 11–30.

[Vya20] S. Vyatchanin. “The loss in reflecting coating induced by polarization”. In: *Physics Letters A* 384.34 (2020), p. 126878.

[Wan+18] H. Wang et al. “Feasibility of near-unstable cavities for future gravitational wave detectors”. In: *Physical Review D* 97.2 (2018).

[War10] R. L. Ward. “Length Sensing and Control of a Prototype Advanced Interferometric Gravitational Wave Detector”. PhD thesis. California Institute of Technology, 2010.

[Web+08] S. A. Webster et al. “Thermal-noise-limited optical cavity”. In: *Physical Review A* 77.3 (2008).

[Wes16] T. Westphal. “A Coating Thermal Noise Interferometer for the AEI 10m Prototype facility”. PhD thesis. Gottfried Wilhelm Leibniz Universität Hannover, 2016.

[WGB85] E. A. Whittaker et al. “Residual amplitude modulation in laser electro-optic phase modulation”. In: *Journal of the Optical Society of America B* 2.8 (1985), p. 1320.

[Wit15] H. Wittel. “Active and passive reduction of high order modes in the gravitational wave detector GEO600”. PhD thesis. Gottfried Wilhelm Leibniz Universität Hannover, 2015.

[WH85] N. C. Wong et al. “Servo control of amplitude modulation in frequency-modulation spectroscopy: demonstration of shot-noise-limited detection”. In: *Journal of the Optical Society of America B* 2.9 (1985), p. 1527.

[YGE15] W. Yam et al. “Multimaterial coatings with reduced thermal noise”. In: *Physical Review D* 91.4 (2015).

[Yam00] K. Yamamoto. “Study of the thermal noise caused by inhomogeneously distributed loss”. PhD thesis. University of Tokyo, 2000.

[Yam+06] K. Yamamoto et al. “Measurement of the mechanical loss of a cooled reflective coating for gravitational wave detection”. In: *Physical Review D* 74.2 (2006).

[You+99] B. C. Young et al. “Visible Lasers with Subhertz Linewidths”. In: *Physical Review Letters* 82.19 (1999), pp. 3799–3802.

[Zen+18] X. Y. Zeng et al. “Thermal-noise-limited higher-order mode locking of a reference cavity”. In: *Optics Letters* 43.8 (2018), p. 1690.

[Zha+17] W. Zhang et al. “Ultrastable Silicon Cavity in a Continuously Operating Closed-Cycle Cryostat at 4 K”. In: *Physical Review Letters* 119.24 (2017).

Acknowledgements

First and foremost I would like to thank Karsten Danzmann for creating such a great environment, making research in an open and friendly group of colleagues possible, and always giving us students all the support we could ask for.

Further I would like to thank Harald Lück for the opportunity to join the best 10 m prototype group, for all the support I needed, and for sending me to the Grawiton lecture weeks all across europe.

Thanks to Michele and Benno for being there whenever help is needed, to Ken for all the helpful comments on every problem I encountered, and to Stefan for getting me enough dinner to survive.

I would like to give special thanks to all the members of the AEI10 m prototype group, Johannes for the music and fighting suspensions, Manu, Vaishali and Juliane for being the best office buddies, Philip for the squash matches, Robin for the bouldering trips, Matteo for suffering through noise budgets, David for always being a group leader, Sean for understanding my english, Paddy for fighting for what is right, Sara for joining long lab nights, Luise for the coffee, and Connor for teaching me so much about lab work.

Also thanks to all the people I spent time with on several lecture weeks around Europe, for making these trips not only educational, but also so much fun.

A lot of thanks to the rest of the institute for always being friendly and accesible, especially Marina for all the pizza, Aparna for the tea, Kanioar for suffering playing squash, Dennis for the fame, Justus for the glass table, Holger and Emil for being wedding pals, Fabian for my photodiodes, Henk for squeezing light, Nina for keeping the chiller cool, Gerrit for suffering from my creative computer problems, and the Lasergroup for accepting me as one of theirs.

I am especially thankful to Kirsten, Sandra and all the other secretaries for guarding me from administration hell.

Thanks to Sina and the High-QG folks for the fun trips to Jena and all the support.

Arigatō gozaimashita to Kentaro for having me in his group and showing me around Tokyo and Kagra.

Many thanks to Ronny for the self-made ice cream in Jena.

I would also like to thank Josh for helping me solve the optical mysteries of the TNI.

Thanks also to the electronics workshop, Andreas, Philipp and Jörg for making electronic voodoo fun.

A special thank you to all the members of the mechanical workshop, especially Jan, Philipp and Stefan for creating impossible constructions while being available for a quick chat.

Acknowledgements

Many thanks to my parents, who were always supportive and made this whole adventure possible in the first place.

Na záver, chcem ďakovať Alicka, ktorá mi podporovala v každom situácie.